Seismic retrofitting of masonry walls with flexible deep mounted CFRP strips

PROEFSCHRIFT

ter verkrijging van de graad van doctor
aan de Technische Universiteit Eindhoven,
op gezag van de rector magnificus prof. dr. ir. F.P.T. Baaijens,
voor een commissie aangewezen door het College voor Promoties,
in het openbaar te verdedigen op
dinsdag 17 november 2020 om 11:00 uur

door

Ömer Serhat Türkmen

geboren te Rotterdam

Dit proefschrift is goedgekeurd door de promotoren en de samenstelling van de promotiecommissie is als volgt:

voorzitter:	prof. dr. ir. M.C.J. Hornikx
1e promotor:	prof. ir. S.N.M. Wijte
2e promotor:	prof. J.M. Ingham (University of Auckland)
co-promotor:	dr. ir. A.T. Vermeltfoort (gepensioneerd UHD)
leden:	prof. dr. ir. T.A.M. Salet prof. dr. G. Magenes (University of Pavia) prof. dr. ir. J.G. Rots (Technische Universiteit Delft)
adviseur(s):	dr. I.E. Bal (Hanzehogeschool Groningen)

Het onderzoek of ontwerp dat in dit proefschrift wordt beschreven is uitgevoerd in overeenstemming met de TU/e Gedragscode Wetenschapsbeoefening.

A catalogue record is available from the Eindhoven University of Technology Library
ISBN: 978-90-386-5156-9
Bouwstenen: 302

Cover photo by Boy Tobias de Vries
Printed by Dereumaux, Eindhoven

Copyright © Ömer Serhat Türkmen, 2020
No part of this document may be reproduced, stored in a retrieval system or transmitted in any form by any means electronic, mechanical, photocopying, recording or otherwise, without the prior written permission of the author.

The work in this dissertation has been funded by Koninklijke Oosterhof Holman, SealteQ Group and QuakeShield.

Acknowledgements

This doctoral journey has been a five-year-long, intense and profound experience for me as a PhD student at Eindhoven University of Technology. I would like to express my sincere gratitude to many people who, either directly or indirectly, have kindly contributed to this final result.

Firstly I would like to thank my first promotor, prof. Simon Wijte. I am deeply grateful for the dedicated support and guidance you have shown throughout the last five years. Your knowledge of concrete and masonry structures and experience in practice-oriented (experimental) research was of great help and highly improved the quality of this work.

Secondly, I would like to like to express my sincere gratitude to my daily supervisor, dr. Ad Vermeltfoort. For every problem I was facing within this PhD research, you would always take your time to provide me with a detailed explanation in a very relaxed way. Your guidance and sincere involvement are much, much appreciated. I wish you a long and joyous retirement.

My sincere thanks to my second promotor, prof. Jason Ingham from the University of Auckland, New Zealand. Your expertise and guidance on mainly earthquake engineering related topics were a significant contribution to this work despite the geographical distance. I wish to express my gratitude to my colleague researcher dr. Jaroslav Vaculik from the University of Adelaide (Australia), for the many online discussions and his valued contribution to the comparative studies. I would also like to thank prof. Dirk Martens for his involvement at the beginning of my PhD research.

I would like to offer my special thanks to Peter Westra and Martin van der Leest for their pro-active and leading role in the seismic retrofitting challenge Groningen was facing. I can still remember like it was yesterday when we did the first small scale experiments back in 2013, and were completely surprised with the promising outcome. Two years later, in 2015, you challenged me to continue the preliminary research we started despite the many challenges that would lie ahead for all of us. Your innovation-driven and entrepreneurial mindsets made a significant difference.

A special thanks goes to a wonderful colleague and friend from QuakeShield, Boy de Vries, for his highly appreciated assistance at every stage of the research project. I sincerely hope that our scientific collaboration is just the beginning of a long and dynamic journey. I also would like to thank the rest of the QuakeShield team: Peter Schultinga, Ben Keizer, Jan Folkert de Vries and Jolanda van der Vaart. Working with all of you is a pleasure.

I am very grateful for the support of the staff of Royal Oosterhof Holman and SealteQ, and the technical assistance of the colleagues at TU/e Structures Laboratory. The experimental campaigns in this research would not have been possible without your valued help and feedback. I would like to thank all the colleagues at floor 9 of Vertigo for the pleasant working/developing atmosphere. I would also like to express my gratitude to the engineers/researchers of former Centrum Veilig Wonen, Royal Haskoning DHV, BAM, Econstruct, W2N, ABT, Arcadis and Delft University of Technology for the many fruitful discussions.

I am deeply grateful to the support I received from my family and friends. I would like to express my sincere gratitude to my mother and father. Despite the many challenges you faced, you have always given your unconditional support in every way, just for us to get the most out of life. Words can't express my love and respect for you. I would also like to thank my sisters, Aslı and Gülsüm, for their help and support. I am so proud of you and all your accomplishments.

Zühal, the past five years you have shown nothing but unconditional love and support. Even with the many evenings, nights and weekends I was hidden behind my laptop, you were patient and understanding. From my side, I will show nothing less in your pursuit of becoming the most awesome general practitioner in the world. Love you.

The combination of parenthood with my doctoral study was by far the most challenging part in the past five years. Halil Ibrahim, nearly 1.5 years into the PhD research our family was blessed with you. Despite the many challenges, you have made me stronger, better and more fulfilled than I could have ever imagined. I sincerely appreciated the numerous times you have forcefully shut down my laptop to claim your time with me.

I wish everyone health and all the best for the future.

Ömer Serhat Türkmen
Rotterdam, October 2020

Summary

Seismic retrofitting of masonry walls with flexible deep mounted CFRP strips

There is a growing awareness worldwide of the need to structurally improve the existing building stock to protect communities in the event of earthquakes. This includes the induced seismicity in Groningen, a region in the Netherlands where the building stock comprises mainly single- and two-story buildings with unreinforced masonry (URM) walls, designed without any seismic considerations. The need to warrant a sufficient level of structural safety for buildings in seismic active zones has led to the broad use of fibre-reinforced polymer (FRP) as retrofit material. The deep mounting of carbon FRP (CFRP) strips to masonry using a flexible adhesive was developed as a minimally-invasive and cost-effective out-of-plane seismic retrofitting technique for URM walls. With this novel retrofitting technique deep grooves are cut in the masonry, after which CFRP strips are installed at the center of the wall, thus reinforcing the wall for both lateral loading directions. To account for the failure of the masonry and consequent underutilization of the CFRP, a flexible adhesive instead of a conventional stiff adhesive is used for bonding the CFRP to the masonry. For combined in-plane and out-of-plane retrofitting, the proposed flexible deep mounted (FDM) CFRP strip retrofit is combined with a single-sided fabric reinforced cementitious matrix (FRCM) overlay to form a hybrid retrofit solution. The FRCM system consists of a carbon fiber mesh embedded in a polymer-modified mortar.

Preliminary experiments showed a strong increase in both moment- and deformation capacity for URM wallettes retrofitted with FDM CFRP strips, without significantly damaging the masonry. The effectiveness of this novel strengthening system was examined in depth in this doctoral research. The three main topics covered in the thesis are the experimental characterization and modelling of: i) the bond behaviour between CFRP strips and masonry when the flexible adhesive is used, ii) the out-of-plane behaviour of masonry walls retrofitted with FDM CFRP strips, both with and without the single-sided FRCM overlay, and iii) the in-plane behaviour of masonry walls retrofitted with FDM CFRP strips, with and without a single-sided FRCM overlay.

The effectiveness of any FRP retrofit system largely depends on the ability to develop shear transfer across the FRP-to-masonry bond. It was thus considered essential to investigate the bond behaviour of masonry retrofitted with FDM CFRP strips. An experimental campaign was initiated to determine the high-speed pullout behaviour of deep-mounted CFRP strips bonded with a flexible, visco-elasto-plastic adhesive to clay brick masonry. Test results showed that for anchorage lengths over 1 meter the utilization of the tensile capacity of the CFRP strip was 100%. Multiple bond-slip correlations were developed, generalized and simplified to a global, multi-linear bond-slip relation. The accuracy of the proposed partial-interaction model was validated. This experimental campaign showed that the application of a flexible adhesive results in higher interfacial fracture energy and higher debonding slip, when compared to conventional stiff adhesive systems gathered from the global database of FRP-to-masonry bond tests.

Through an extensive experimental campaign on full-scale FDM CFRP strip retrofitted masonry walls, more in-depth knowledge was obtained regarding the out-of-plane behaviour. The full-scale wall specimens were subjected high-speed cyclic loading conditions using a novel, cyclic bending test setup. Experimental results confirmed the significant increase in the out-of-plane lateral resistance and deformation capacity for the FDM CFRP strip retrofitted specimens with respect to the URM specimens. The lateral moment resistance of the wall was increased with 133% with the installation of two FDM CFRP strips. For the mean mid-span displacement corresponding to the lateral resistance, an increase with roughly a factor 90 was achieved for given axial load. By implementing a scenario where multiple bed joint-cracks can form and cyclic degradation of the masonry is included, the proposed mechanical model provided a good fit with the experimentally obtained moment – mid-span displacement relationship. A cross-section analysis using non-linear material models resulted in an overestimation of the moment capacity for higher displacement levels, because the slip of the embedded CFRP strips was significant in the real situation.

The mechanical behaviour of the FRCM overlay on clay brick masonry was characterized by means of double-shear bond tests, tensile tests, beam tests and full-scale out-of-plane bending tests. Material models were proposed where, in addition to existing design models, the influence of the cementitious matrix was also considered in the cross-section analysis. Using the modified tensile test results as input parameters for the model, a good estimation of the strength and deflection levels of the beam tests was obtained. The accuracy of the proposed (non)-linear material models and the cross-section analysis was validated with the full-scale out-of-plane experiments. The full-scale out-of-plane bending tests on the hybrid retrofitted walls showed that the single-sided FRCM overlay was able to cooperate effectively with the FDM CFRP strips, enhancing the moment resistance for both lateral loading directions. The mean lateral moment resistance of the hybrid retrofitted walls with respect to the walls retrofitted with solely FDM

CFRP strips was found to be 120% (FRCM in compression) and 320% (FRCM in tension) higher. The inclusion of the contribution of FRCM in compression for the lateral moment resistance was justified. The hybrid retrofitted walls showed a significant decline in lateral moment resistance after CFRP mesh rupture.

The in-plane behaviour of hybrid retrofitted walls was experimentally characterized under cyclic quasi-static loading conditions. A total of nine full-scale reinforced masonry walls with three different geometries were tested under three different axial load levels. None of the specimens showed shear failure on either the reinforced side or the as-built side of the wall surface. An additional experimental program was undertaken in which clay brick masonry wallettes were subjected to the diagonal compression test to assess the effectiveness of the hybrid strengthening system on the in-plane shear behaviour. The FRCM overlay increased the shear capacity with 80%, compared to the unstrengthened control specimens. In contrast to the URM specimens, retrofitting a wallette with a FDM CFRP strip alone did not affect the in-plane strength of masonry wallettes and prevented the disintegration after reaching the failure load. The analytical model showed good correspondence with the experimental values for both failure mechanism and failure load.

Multiple valorization projects using the FDM CFRP retrofit were realized over the course of this doctoral research. The process and challenges regarding groove cutting, FDM CFRP strip installation, and FRCM overlay installation were presented and discussed. Finally, five completed retrofit projects in Groningen were briefly reviewed.

Samenvatting

Seismisch versterken van metselwerk muren met flexibel en verdiept gemonteerde koolstofvezel strips

Wereldwijd groeit het bewustzijn van de noodzaak om het bestaande gebouwenbestand constructief te verbeteren om gemeenschappen te beschermen tegen aardbevingen. Zo ook in Groningen, waar sinds de jaren negentig meer dan duizend geïnduceerde aardbevingen hebben plaatsgevonden. De bestaande gebouwen in Groningen hebben voornamelijk één of twee verdiepingen en wanden van ongewapend metselwerk (URM). Deze wanden zijn ontworpen en gebouwd zonder seismische overwegingen. De noodzaak om de constructieve veiligheid van gebouwen in seismisch actieve gebieden te waarborgen, heeft geleid tot de brede toepassing van vezelversterkte polymeren, oftewel FRP (fibre reinforced polymer). Bij een combinatie van FRP en metselwerk ontstaat er bij het bezwijken van het metselwerk vaak ook een bros bezwijken van de aanhechting tussen het FRP en het metselwerk. Om deze reden wordt in plaats van een conventionele stijve lijm, een flexibele lijm gebruikt om het CFRP component aan het metselwerk te verlijmen. Zo is een minimaal invasieve seismische versterkingstechniek ontwikkeld om onversterkte metselwerk (URM) wanden te versterken tegen uit-het-vlak (buig) belastingen. Met deze innovatieve versterkingstechniek worden diepe sleuven in het metselwerk gefreesd, waarin een flexibele lijm en koolstof-FRP (CFRP) strips worden aangebracht. Deze aanbrengmethode van CFRP strips wordt aangeduid als FDM (flexible deep mounted). Door de CFRP strip in het hart van de doorsnede van de wand aan te brengen, wordt de wand versterkt tegen beide uit-het-vlak belastingsrichtingen. Voor gecombineerde in-het-vlak (afschuiving) en uit-het-vlak belastingen wordt de voorgestelde versterkingsmethode gecombineerd met een enkelzijdige textielgewapende mortellaag, oftewel fabric reinforced cementitious matrix (FRCM), om een hybride versterkingssysteem te vormen. Het FRCM systeem bestaat uit een met koolstofvezelgaas ingebedde polymeer gemodificeerde mortel.

Inleidende experimenten zijn uitgevoerd op metselwerk proefstukken die versterkt zijn met FDM CFRP strips. Deze versterking resulteerde in een sterke toename in zowel moment- als vervormingscapaciteit van de geteste proefstukken. De effectiviteit van dit nieuwe versterkingssysteem is in dit promotieonderzoek onderzocht. De drie belangrijkste onderwerpen die in dit proefschrift aan bod komen zijn de experimentele karakterisering en modellering van: i) het hechtgedrag van FDM CFRP strips aan metselwerk wanneer een flexibele lijm wordt toegepast, ii) het uit-het-vlak gedrag van metselwerk muren die achteraf zijn versterkt met FDM CFRP strips, zowel met als zonder enkelzijdige FRCM laag, en iii) het in-het-vlak gedrag van metselwerk muren die achteraf zijn versterkt met FDM CFRP strips, zowel met als zonder enkelzijdige FRCM laag.

De effectiviteit van een FRP versterkingssysteem hangt grotendeels af van het vermogen van het systeem om schuifspanningen over te dragen aan het substraat metselwerk. Onderzoek naar het hechtgedrag van FDM CFRP strips aan metselwerk was mede hierdoor een essentieel onderdeel van dit promotieonderzoek. Het uittrekgedrag van FDM CFRP strips werd bepaald door uittrekproeven uitgevoerd bij een hoge snelheid. De testresultaten toonden aan dat voor verankeringslengtes van meer dan één meter de treksterkte van de CFRP strip volledig kan worden benut. Meerdere hecht-slip-correlaties zijn geconstrueerd, gegeneraliseerd en vereenvoudigd tot een algemene multi-lineaire hecht-slip-relatie, waarmee de nauwkeurigheid van het partial-interaction model is gevalideerd. Deze testresultaten zijn vergeleken met data uit een wereldwijde database van uittrekproeven op FRP-versterkt metselwerk. Op basis hiervan is geconcludeerd dat de toepassing van een flexibele lijm resulteert in een hogere grensvlak-breukenergie en een hogere onthechtingsslip dan systemen met conventionele stijve lijmen.

Om meer inzicht te verkrijgen in uit-het-vlak gedrag van FDM CFRP strip versterkte metselwerk-muren, is een uitgebreid experimenteel testprogramma opgezet. Met behulp van een nieuw ontwikkelde buigtestopstelling zijn in dit testprogramma wanden op ware grootte, met hoge snelheid, onderworpen aan cyclische belastingen. De testresultaten tonen een significante toename aan in zowel momentweerstand als vervormingscapaciteit van de door de installatie van twee FDM CFRP strips versterkte wanden. De maximale momentweerstand en bijbehorende gemiddelde verplaatsing in het midden van de overspanning van de versterkte testmuren was respectievelijk een factor 1.3 en 90 hoger dan de onbehandelde referentiemuren. Het ontwikkelde mechanisch model, waar meervoudige scheuren in de lintvoegen en cyclische degradatie van het metselwerk zijn meegenomen, resulteerde in een goede benadering van de moment–doorbuigingsrelatie die volgen uit de experimenten. Een dwarsdoorsnede-analyse met niet-lineaire materiaalmodellen resulteerde in een overschatting van de momentweerstand. Dit gebeurde vooral bij grotere doorbuigingen, waarbij de slip van de ingebedde CFRP strips niet meer verwaarloosd kan worden.

Door middel van hechtproeven, trekproeven, en buigproeven op grote en kleine schaal zijn de mechanische eigenschappen van de FRCM laag op baksteen metselwerk vastgesteld. Op basis van de uitkomsten van het experimenteel onderzoek zijn materiaalmodellen opgesteld, die in tegenstelling tot bestaande modellen ook rekening houden met de invloed van de betonmatrix. Met het model kon het constructieve gedrag van de kleine testmuren worden beschreven. De opgezette materiaalmodellen en de voorgestelde rekenmethode zijn vervolgens gevalideerd door buigproeven op versterkte testmuren op ware grootte. Deze buigproeven op testmuren voorzien van de hybride versterkingsmethode toonden aan dat de enkelzijdige FRCM laag effectief kon samenwerken met de FDM CFRP strips. De momentweerstand van wanden met een hybride versterking bleek een factor 1.2 (FRCM laag in drukzone) en 3.2 (FRCM laag in trekzone) hoger te ligger dan wanden enkel versterkt met FDM CFRP strips. De muren met hybride versterking vertoonden een significante afname in laterale momentweerstand na het scheuren van het koolstofvezel wapeningsnet in de FRCM laag.

Het in-het-vlak gedrag van hybride versterkte muren is vastgesteld aan de hand van experimenten onder cyclische, quasi-statische belasting condities. In totaal zijn negen hybride versterkte metselwerk muren getest, met drie verschillende wandgeometrieën en drie verschillende bovenbelastingen. De geteste muren vertoonden geen dwarskracht bezwijken op de versterkte of onbehandelde muuroppervlakten. In een aanvullend experimenteel programma, waarin vierkante metselwerkpanelen zijn onderworpen aan de diagonale compressietest, is de effectiviteit van het hybride versterkingssysteem op het in-het-vlak schuifgedrag beoordeeld. De enkelzijdige FRCM laag zorgde voor een verhoging van de afschuifsterkte met 80% vergeleken met de niet-versterkte referentie panelen. Het aanbrengen van enkel een FDM CFRP strip had geen invloed op de in-het-vlak sterkte van de metselwerk panelen, maar voorkwam wel het uit elkaar vallen van het proefstuk na het bereiken van de bezwijklast. Tot slot zijn analytische modellen ontwikkeld en gevalideerd door middel van de in-het-vlak experimenten. De analytische modellen bleken goed in staat zowel de bezwijklast als het bezwijkmechanisme van wanden te voorspellen.

Gedurende dit promotieonderzoek zijn meerdere valorisatieprojecten gerealiseerd met het FDM CFRP versterkingssysteem. Het proces en de uitdagingen met betrekking tot het frezen van de sleuven, het installeren van FDM CFRP strips en het aanbrengen van de enkelzijdige FRCM laag zijn in deze dissertatie gepresenteerd. Ter afsluiting zijn vijf afgeronde versterkingsprojecten in Groningen beschreven.

Contents

Dedicated to my beloved family


BOUWPLAATS

Chapter 1

Introduction

Masonry structures represent the highest proportion of the building stock worldwide. There is a growing awareness worldwide of the need to improve the existing building stock to protect communities in the event of future earthquakes. This development, mainly driven by the need to warrant a sufficient level of safety, has led to the development of multiple seismic retrofit techniques. This dissertation provides fundamental research on a novel, minimally-invasive and cost-effective seismic retrofitting technique for masonry buildings.

1.1 Context

Discovered in 1959, the Groningen gas field in the north of the Netherlands has for a long time been one of Europe's main suppliers of natural gas. In the decades since the discovery, this natural gas had brought economic welfare and prosperity to the Netherlands. Gas extraction operations occurred in Groningen for 20 years without any induced earthquakes, until 26th of December 1986, where an earthquake with magnitude 2.8 struck Assen. The accumulated extraction of natural gas caused the reservoir to compact, increasing the stresses on pre-existing geological faults. When the shear traction at these faults becomes sufficient to overcome frictional resistance on the fault surface, fault slip occurs leading to seismic events [1]. With only three induced earthquakes between 1986 and 1990, the recorded earthquakes were relatively rare at first. However, starting from the 90's, over 1,600 induced earthquakes were recorded (Fig. 1.1) until now. The heaviest induced earthquake took place in 2012, with a magnitude of 3.6. Although the magnitude of these induced earthquakes is relatively low, the earthquakes have a big impact on the buildings in the region due the soft surface soils in the area, the shallow depth (3 km beneath earth's surface) of the hypocentre [2] and the regional building typology.

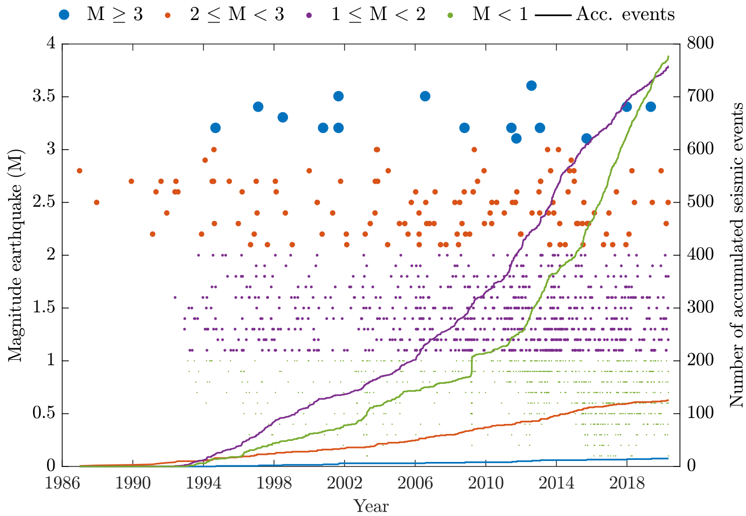

Figure 1.1: Magnitude and number of accumulated events of the earthquakes in Groningen between 1986 and 2020, divided in 4 groups: M≥3 (blue), 2≤M<3 (orange), 1≤M<2 (purple) and M<1 (green) [3].

As an area not prone to tectonic earthquakes, buildings in Groningen were not designed to withstand seismic actions, consequently making these buildings highly vulnerable to earthquake events. Approximately 70% of the building stock in Groningen is composed of unreinforced masonry buildings [4]. Façades of these buildings typically consist of cavity walls with masonry leaves of 100 mm in thickness divided by a 30-80 mm wide cavity and connected by a limited number of steel wall ties. Generally, the inner leaves are constructed from either clay-brick masonry or calcium-silicate masonry while clay-brick masonry is most commonly used for the outer leaves. The slenderness of the load-bearing inner leaves is one of the main reasons these buildings are highly vulnerable for seismic actions. The minimum effective thickness for masonry shear walls as provided in Eurocode 8 [5] is 170 mm in cases of low seismicity.

After the 2012 Huizinge earthquake, a program of inspection began to assess the earthquake risk of the buildings in the area, from public buildings, such as schools and hospitals, to private dwellings [6]. In 2014 the Dutch Minister of Economic Affairs announced several measures to ensure the safety of those living above the Groningen natural gas field. Next to the reduction of natural gas production in Groningen over the following three years, a total of nearly €1.2 billion was made available to retrofit homes and other buildings, strengthen infrastructure, and improve quality of life in the region over the following five years [7]. In 2018 the Dutch government announced that the natural gas extraction from the Groningen gas field will eventually be terminated [8].

The Dutch State Supervision of Mines reported in 2019 that the magnitude of the retrofitting task was estimated at approximately 26,000 addresses. From the 15,300 addresses that had been inspected until the beginning of 2020, 1,000 addresses were retrofitted, and 900 were in the process of being retrofitted. Due to the magnitude and needed pace of the retroffitting task, cost-effective, minimally invasive and easy to install (in order to mobilize contractors at large scale) retrofit configurations were needed.

1.2 Out-of-plane retrofitting techniques

During an earthquake a wall is subject to simultaneous in-plane and out-of-plane actions. In-plane refers to the loading condition along the axis of a surface of the considered wall, whereas out-of-plane refers to the loading condition perpendicular to the surface to the considered wall, as depicted in Fig. 1.2. One of the most critical deficiencies of historic clay brick masonry buildings is out-of-plane (OOP) failure induced by lateral earthquake loads [9–11]. Even though this failure mechanism is inhibited via the addition of adequate wall-diaphragm connections at the building's roof and floor levels [12], the sudden and unstable out-of-plane failure of walls acting in either one-way or two-way bending endangers their vertical load bearing capacity. Hence, the out-of-plane failure mechanism can result in extensive damage and potential catastrophic collapse, posing a significant life-safety hazard to both building occupants and nearby pedestrians [13].

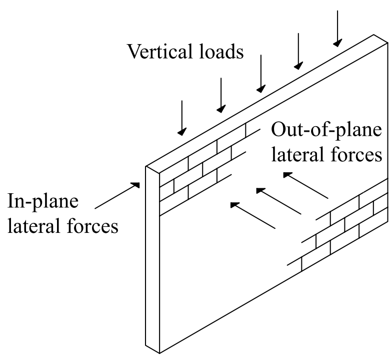

Figure 1.2: In-plane and out-of-plane loading directions on a masonry wall

A major part of the retrofitting task in Groningen consists of out-of-plane strengthening of masonry walls. Traditional strengthening techniques for enhancing the OOP structural performance of masonry walls such as steel plate bonding, steel or timber frame works and shotcrete jacketing have major disadvantages such as adding considerable mass to the structure, being labour intensive and impinging the aesthetics of a building [9].

Researchers in New-Zealand developed a cost-effective and light timber retrofit solution, consisting of a number of vertical timber members (termed as strong-backs) installed on the internal surface of the inner loadbearing masonry leaf [14]. In a series of shake-table tests involving timber strong-back retrofitting of both masonry walls [14] and a terraced house [15] an increase in sustained maximum peak ground acceleration (PGA) values with respect to the unreinforced situation was reported. Even though using strong-backs may provide a cost-effective retrofit solution, trade-offs need to be made with the living floor space. Using 90x45 mm timber strong backs combined with an oriented strand board of 18 mm thick on the internal surface of the inner loadbearing masonry leaf would move the wall of the domestic space roughly 110 mm inward.

The use of fibre reinforced polymers (FRP) for seismic retrofitting of masonry has gained a lot of interest over the past decades. The disadvantages of the traditional strengthening techniques for masonry led to the idea of using FRP composites for strengthening of masonry. Typically, these materials are made of Carbon (CFRP), Glass (GFRP), Basalt (BFRP) or Aramid (AFRP) fibres bonded together by an epoxy-resin. The main advantages of FRP include high strength, high stiffness, low weight and immunity to corrosion [16]. Initially FRP was used in the form of Externally Bonded (EB) sheets for both in-plane and out-of-plane strengthening of masonry. In this method firstly the surface of the substrate (concrete or masonry) is prepared by removing contamination and weak surface layers, after which a FRP sheet is adhesively bonded to the substrate by means of an organic resin. This strengthening system has proven to be highly effective in enhancing both the shear capacity, the flexural capacity and the ductility of masonry walls. The main disadvantages of this method were however found to be vulnerability to environmental influences, vulnerability to fire, high cost of epoxies, lack of vapor permeability, inability to install the system on damp substrates and poor behaviour of the epoxy-resin at temperatures above the glass transition temperature [17–19].

Over the last decade the near surface mounted (NSM) technique has been raised as a promising alternative. With this technique, FRP strips or rods are placed in a layer of epoxy in pre-cut grooves perpendicular to the surface of the wall. Near surface mounting offers several advantages over EB FRP such as higher strain at debonding and therefore more efficient use of the FRP, reduced aesthetic impact, reduced installation time and superior protection from fire and environmental influences [13, 20, 21]. Both the EB and NSM technique however, require double-sided application for seismic retrofitting of masonry walls for reversed cyclic loading. In case of strengthening load-bearing inner leaves of cavity walls, both the EB and NSM technique would require both stripping the wall from the inside and the removal of the outer leaf of the façade, consequently leading to considerable additional expenses. If the FRP strips were to be installed at the center-depth of the brick by milling deeper grooves perpendicular to the surface of the wall, reinforcing the inner loadbearing masonry from only one face would be sufficient, effectively decreasing the total retrofit expenses. As the required retrofit would be installed inside the inner loadbearing masonry wall, the living floor space would remain unaffected. However, in an experimental study on the behaviour of NSM CFRP strips bonded to vintage solid clay brick masonry [13], it was observed that increasing the depth of the groove led to under-utilisation of adhesive material and the initiation of premature brick splitting. Therefore, *Dizhur et al.* [13] recommended that the groove depth should be no greater than is required to accommodate the CFRP strip and that at least 5 mm of adhesive cover should be provided for minimal protection of the CFRP strip from fire, vandalism and exposure to environmental elements. This under-utilization and premature-failure mechanism, i.e. the obstruction for placing the FRP strip deeper, was linked to the mechanical properties of the adhesive component used for installing FRP on masonry [22].

1.3 Importance of the adhesive

Several previously conducted research studies underline the essence of the adhesive component for installing FRP reinforcement on masonry/concrete substrates. *Sharaky et al.* [23] concluded that the properties of the adhesive show a high influence on the bond behaviour. The response of the joint was improved in terms of load capacity and ductility when using a more ductile adhesive, allowing a better redistribution of stresses along the bond length. *Rizzo and De Lorenzis* [24] also noted that stiffer and stronger groove-filling epoxy led to a reduction in FRP contribution to the shear capacity. The stiffer bond-slip behaviour caused higher peak bond stresses and faster debonding crack formation. In these research studies it was observed that the stiffness of the adhesive affected the bond behaviour. The needed flexibility however was not quantified.

This quantification was done in other research studies covering Externally Bonded (EB) FRP reinforcement. *Derkowski et al.* [25] conducted research on EB CFRP strengthening of bent Reinforced Concrete (RC) beams using stiff and flexible adhesives. The researchers observed in the case of a stiff adhesive that many wide cracks with high stress concentration appear, because the sum of the CFRP local deformations was higher than in the case of a flexible adhesive. Additionally it was observed that with a flexible adhesive, cracks did not go through the ductile adhesive but were stopped in it. Additionally, stress redistribution occurring in the adhesive layer allowed for a more equal distribution of load to the CFRP laminate. *Dai et al.* [26] performed pullout tests of FRP sheets and concrete. The researchers concluded that the application of a flexible adhesive bonding system instead of a normal adhesive bonding system increased the pullout capacity (with a sufficient long anchorage length) and improved the ultimate capacity of

FRP strengthened RC beams. Additionally the flexible adhesive led to equal or better fatigue performance and contributed to a more ductile failure. The added value of flexible adhesives for EB FRP reinforcement was also confirmed by *Kwiecien* [27] for masonry units. The tests demonstrated that the shear stress was reduced by the adhesive flexibility in the bond layer. Flexible polymers protected the brittle substrate against the locally acting peak stress, significantly increased the ultimate load of the tested strengthening system and expanded the CFRP end slip. The last phenomena is especially of added value in seismic areas, as the higher slip generates a significantly higher value of dissipated energy.

From the 733 pull-out experiments on CFRP-to-masonry bond strength tests found in open literature, spread over 27 separate research studies [13, 21, 28–53], only two experimental campaigns included flexible mounting adhesives with a Young's Modulus of ≤ 100 N/mm^2 [45,53]. All other researchers used mounting adhesives with Young's Moduli in the range 1,230-12,840 N/mm^2. An overview of all Near Surface Mounted (NSM) / Externally Bonded (EB) CFRP-to-masonry bond strength tests, obtained from *Vaculik et al.* [54], is presented in Table A.1. The predominant failure mechanism in the 27 aforementioned research studies was substrate debonding, leading to a general under-utilization of the added CFRP reinforcement.

No records in open literature were found for the bond behaviour of NSM FRP strips in a flexible adhesive for both masonry and concrete substrates. Combing the NSM technique with a flexible adhesive would be a very logical step in this research field considering the several advantages the NSM strip technique provides over the EB technique. Based on the findings summarized in this section the implementation of a flexible adhesive could additionally make center-depth installation of FRP components possible, leading to cost effective retrofitting efforts.

1.4 Out-of-plane retrofitting with Flexible Deep Mounted CFRP strips

Türkmen et al. [55] conducted an extensive experimental program on the -out-of-plane behaviour of various strengthened masonry wallettes. The standard added retrofit for all the specimens consisted of two CFRP strips, which were installed using a flexible adhesive in separate pre-cut deep grooves underneath the surface of the masonry. The CFRP strips were positioned at the centre-depth of the wallettes. The observed deformation capacities and maximum withstandable loads showed that deep mounted CFRP reinforcement using a flexible adhesive was a promising solution to improve the out-of-plane seismic performance of clay brick masonry walls. The predominant failure mechanism was found to be masonry crushing and debonding of the CFRP strip. Substrate debonding, i.e. damage within the masonry material surrounding the embedded CFRP strips, was not observed. From these findings the retrofitting concept using Flexible Deep Mounted (FDM) CFRP strips was further developed. An illustration of the retrofitting process with FDM CFRP strips is provided in Fig.1.3.

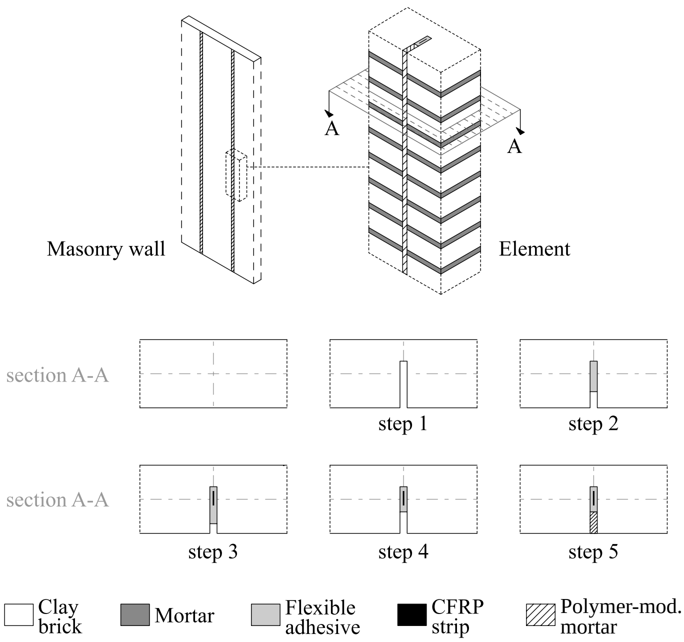

Figure 1.3: Schematization of the reinforcement process with FDM CFRP strips.

The installation of the CFRP strip in the FDM configuration starts with milling vertical grooves (first step in Fig.1.3) by using a portable groove cutter. The dust in the groove is removed with compressed air. After cutting the CFRP strips to a specified length, the CFRP strips are cleaned with acetone. A layer of primer is then applied to the groove to improve the bond between the adhesive and the masonry. After partially filling the groove with the flexible adhesive (step 2 in Fig.1.3), the CFRP strip is inserted into the groove using a positioning fork (step 3 in Fig.1.3). Excess adhesive in the grooves is removed using a scraper (step 4 in Fig.1.3). After the placement of the strip, the adhesive is left to cure for one day in an unheated but dry environment. The remaining unfilled part of the groove is filled with a polymer modified mortar (final step in Fig.1.3) after wetting the masonry surface to improve bond. The addition of the polymer modified mortar is done with the purpose of partially restoring the compressive and shear capacity in the groove in order to prevent possible vertical shear failure.

1.5 In-plane retrofitting with FRCM overlay

For walls subjected to critical in-plane loading, the application of solely the FDM CFRP strips retrofit was expected to be not sufficient. The embedded CFRP strips would have an insufficient effect on the in-plane shear strength of the masonry [56], mainly due to the flexibility of the used adhesive. An additional strengthening system was needed, that could be combined with the FDM CFRP strip retrofit in order to enhance the strength and pseudo-ductility of masonry for in-plane loading conditions. Due to the drawbacks of externally-bonded FRP using organic resins, as was presented in section 1.2, one solution was the replacement of the organic resin with a cementitious matrix, i.e. an inorganic binder [57]. Moreover, textiles (FRP meshes) were selected over continuous fibre sheets in order to achieve mechanical interlock between the textile and the cement-based mortar, because these inorganic binders lack the ability to penetrate and wet individual fibres [17]. This system of cement-based mortar matrix reinforced by continuous dry-fiber textiles is proposed for retrofitting masonry walls and it is becoming progressively in use for both in-plane strengthening and masonry related research [57–67]. The FRCM strengthening system is also known under different appellations: Fabric-Reinforced Cementitious Matrix (FRCM), Textile Reinforced Mortar (TRM), Textile-Reinforced Concrete (TRC) and Fiber Reinforced Cement (FRC) [68].

The FRCM system was selected to form a hybrid retrofit system with the FDM CFRP strips: if a FDM CFRP strip retrofitted wall also needed in-plane strengthening, an additional single-sided FRCM overlay was installed. A schematic overview of the retro-fitting process with an additional FRCM overlay is provided in Fig.1.4. It should be noted that the FRCM overlay in Fig.1.4, that normally covers the entire face of the wall, is only partly shown.

Directly after filling the remaining part of the groove with the polymer-modified (final step in Fig.1.3), a first layer of the polymer-modified mortar (approximately 5 mm in thickness) is applied by hand (step 6 in Fig. 1.4). Again, the masonry surface is wetted prior to the mortar application to improve bonding conditions. After pressing the CFRP mesh into position (step 7 in Fig. 1.4), a final layer of polymer-modified mortar is applied to embed the CFRP mesh, resulting generally in a nominal FRCM layer thickness of 10 mm (last step in Fig. 1.4). The FRCM layer needs to cure for 28 days.

1.6 Problem definition

Due to the novelty of the proposed retrofitting technique, the mechanical properties of the system with CFRP strips embedded in the flexible adhesive are only roughly understood. The effectiveness of any FRP retrofit system largely depends on the ability to develop shear transfer across the FRP-to-masonry bond [69]. No validated models are available to predict the bond behaviour of CFRP strips embedded with a flexible adhesive to unreinforced clay brick masonry. This significant knowledge gap can also be extended to the out-of-plane behaviour of FDM CFRP strip retrofitted masonry walls. Even though extensive research has been done on both the in-plane and out-of-plane behaviour of FRCM retrofitted masonry, the behaviour of the hybrid retrofit with the FDM CFRP strips and single sided FRCM overlay on masonry when subjected to either in-plane or out-of-plane loading conditions remain unknown.

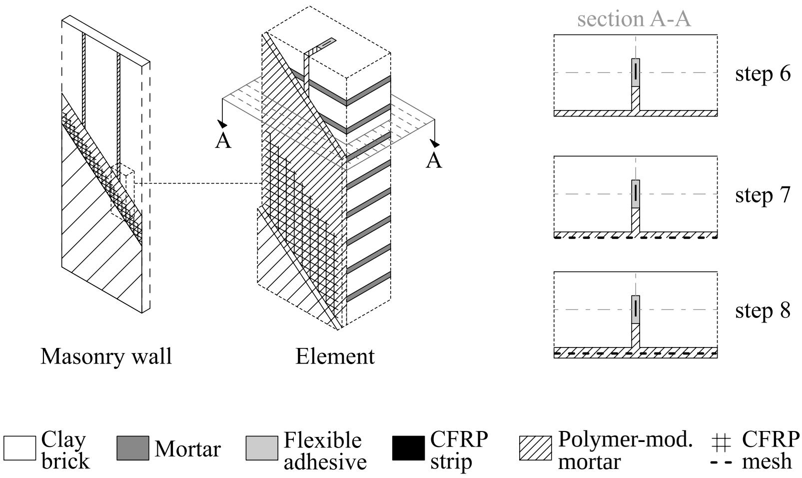

Figure 1.4: Schematization of the (continued) reinforcement process with FRCM.

1.7 Objectives and scope

This research is a part of a collaborative project between Eindhoven University of Technology, Royal Oosterhof Holman, SealteQ and QuakeShield to develop an innovative, minimally invasive and cost effective retrofit system suitable for unreinforced clay brick masonry buildings with a high seismic-vulnerability. The objective of this PhD study is to propose well founded and validated calculation guidelines to be used for the seismic upgrading of earthquake-prone masonry buildings, involving Flexible Deep Mounted (FDM) Carbon Fibre Reinforced Polymer (CFRP) strip retrofitting, optionally combined with a Fabric Reinforced Cementitious Matrix (FRCM) overlay. The scope of this research is limited to clay brick walls and one-way out-of-plane loading. The primary objectives of this thesis are formulated as follows:

1. To define and model the bond behaviour between CFRP strips and masonry when the flexible adhesive is used;

2. To define and model the out-of-plane behaviour of FDM CFRP strip retrofitted masonry walls, either with or without a single-sided FRCM overlay; and

3. To define and model the in-plane behaviour of FDM CFRP strip retrofitted masonry walls with a single-sided FRCM overlay.

1.8 Methodology

The conceptual framework that was used through this research is given in Fig. 1.5. Firstly, the relevant retrofitting and building materials were characterized through an extensive experimental campaign at material-level following various standards, as the relevant properties would be used throughout the entire doctoral study. This campaign not only included the standalone materials such as bricks, mortar, flexible adhesive, CFRP strip, polymer-modified mortar and CFRP mesh, but also covered the composite materials masonry and FRCM overlay. The FRCM was characterized through an extensive, component-level experimental program, following the relevant standards for the evaluation and characterization of FRCM systems [70,71].

As no records could be found in open literature regarding the bond behaviour of CFRP strips bonded with a flexible adhesive to masonry underneath the surface, this research started with an extensive experimental campaign in order to gain more insight on this bond behaviour. The most common experimental technique for studying the bond, being the shear pull-test, was used to construct generalized bond laws for modelling purposes and to gain insights into the governing failure mechanisms.

Using the generalized bond laws, an engineering model for the calculation of FDM CFRP strip retrofitted masonry walls was developed. This engineering model was in turn improved and validated through an out-of-plane experimental campaign on full-scale retrofitted FDM CFRP strip masonry walls. Material models were proposed and validated by cross-section analyses of the wall specimens from both the small-scale and full-scale out-of-plane experimental campaigns.

The in-plane performance of full-scale masonry walls retrofitted with both FDM CFRP strips and a single sided FRCM overlay was obtained using existing loading protocols for determining the seismic performance characteristics of structural and nonstructural components [72]. Additionally, the shear strength of the strengthened masonry elements was obtained following a broadly applied testing procedure [73]. Analytical models were proposed and compared with Eurocode 8 [5] design provisions.

The findings of this research were put into practice by sharing the outcomes on a continuous base. The developed engineering models were validated and the proposed experimental campaigns were discussed with consultants, the former Centrum Veilig Wonen (CVW) and Dutch engineering firms involved in the Groningen retrofitting project. CVW was the Dutch advisory and executive organization for inspecting and repairing damage caused by the induced earthquakes.

The engineering models that have been developed to predict both the out-of-plane (stand-alone FDM CFRP strips retrofit; combined FDM CFRP strips + FRCM retrofit) and in-plane (combined FDM CFRP strips + FRCM retrofit) behaviour of retrofitted masonry walls have been applied in various seismic retrofitting processes throughout the course of this doctoral research.

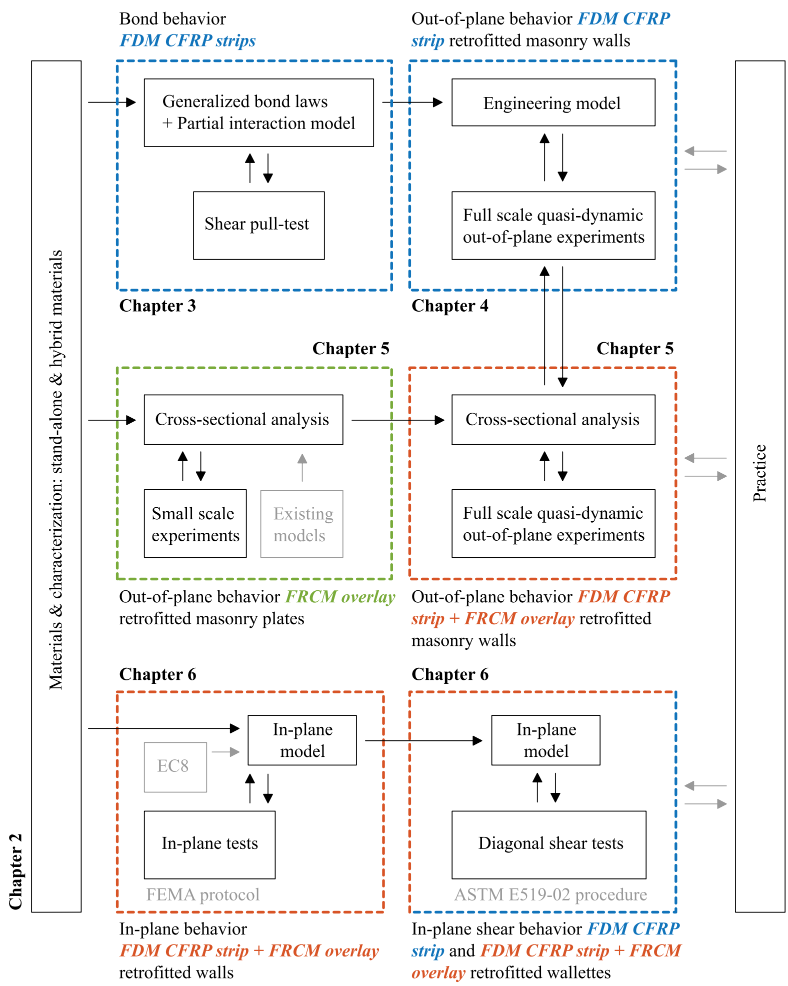

Figure 1.5: Theoretical framework.

1.9 Thesis outline

This thesis consists of 8 chapters. Each chapter, which consists of an introduction, the main content and a summary of the main conclusions, can be read separately. In the current chapter, the context of the flexible deep mounted (FDM) CFRP retrofitting technique is discussed (optionally in combination with the single-sided FRCM overlay), along with the system explanation, problem definition, research objectives and corresponding methodology of the doctoral research.

Chapter 2 presents an overview of the characteristics of the several (composite) materials used in this research for building and retrofitting the various test specimens. Chapter 2 is partially based on [74].

The following four chapters cover the proposed (hybrid) retrofitting technique. Whereas Chapters 3 and 4 only cover the FDM CFRP strip retrofit configuration, Chapters 5 and 6 cover the hybrid retrofit configuration with an additional single-sided FRCM overlay.

Chapter 3 covers the extensive experimental program on the bond behaviour of FDM CFRP strips. The proposed model is validated with the experimental findings. Finally, a comparison is made with the bond-behaviour of stiff adhesive systems. Chapter 3 is based on [75, 76]

Chapter 4 discusses the out-of-plane (OOP) behaviour of vertically spanning masonry walls retrofitted with FDM CFRP strips. The experimental program on (retrofitted) full-scale masonry walls is presented and the results are discussed. Two modelling approaches are discussed in detail and compared with the experimental findings. Finally, the out-of-plane behaviour of CFRP retrofitted masonry walls is compared for both the stiff and the flexible adhesive system. Chapter 4 is based on [77].

Chapter 5 outlines the OOP behaviour of masonry walls retrofitted with FDM CFRP strips and a single-sided FRCM overlay. The chapter starts with a discussion of the experimental campaign on the OOP behaviour of masonry panels retrofitted with solely a single sided FRCM overlay. The discussion of a second experimental campaign focuses on the OOP behaviour of full-scale masonry walls retrofitted with both CFRP strips and a single-sided FRCM overlay. The proposed modelling approach is validated for both experimental campaigns. Chapter 5 is based on [74, 78].

Chapter 6 offers insight into the in-plane (shear) behaviour of FDM CFRP strip and single sided FRCM overlay retrofitted masonry. Two different experimental campaigns are presented and the results are discussed. An existing analytical model as well as various design provisions are compared to the found failure mechanisms and failure loads. Chapter 6 is based on [79, 80].

Chapter 7 presents various FDM CFRP retrofit case studies in the Dutch province of Groningen carried out during the course of this doctoral research. Furthermore, preliminary finite strategies for the modelling of the bond-slip and pull-out behaviour of FDM CFRP strips are provided. The challenges and opportunities of the proposed novel retrofitting technique are illustrated. Moreover, the simplified analysis procedures are presented, used to estimate the force-displacement response of vertically spanning (strengthened) masonry walls subjected to out-of-plane loading, which is required for the he implementation of the FDM CFRP strip retrofit system into structural engineering practice. Finally, the dynamic out-of-plane response of FDM CFRP strip retrofitted and vertically spanning masonry walls for different scenarios was determined by performing a series of Nonlinear Time History (NLTH) analyses on single degree of freedom (SDOF) systems.

Chapter 8 provides conclusions, recommendations and an outlook to the future of FDM CFRP retrofitting.

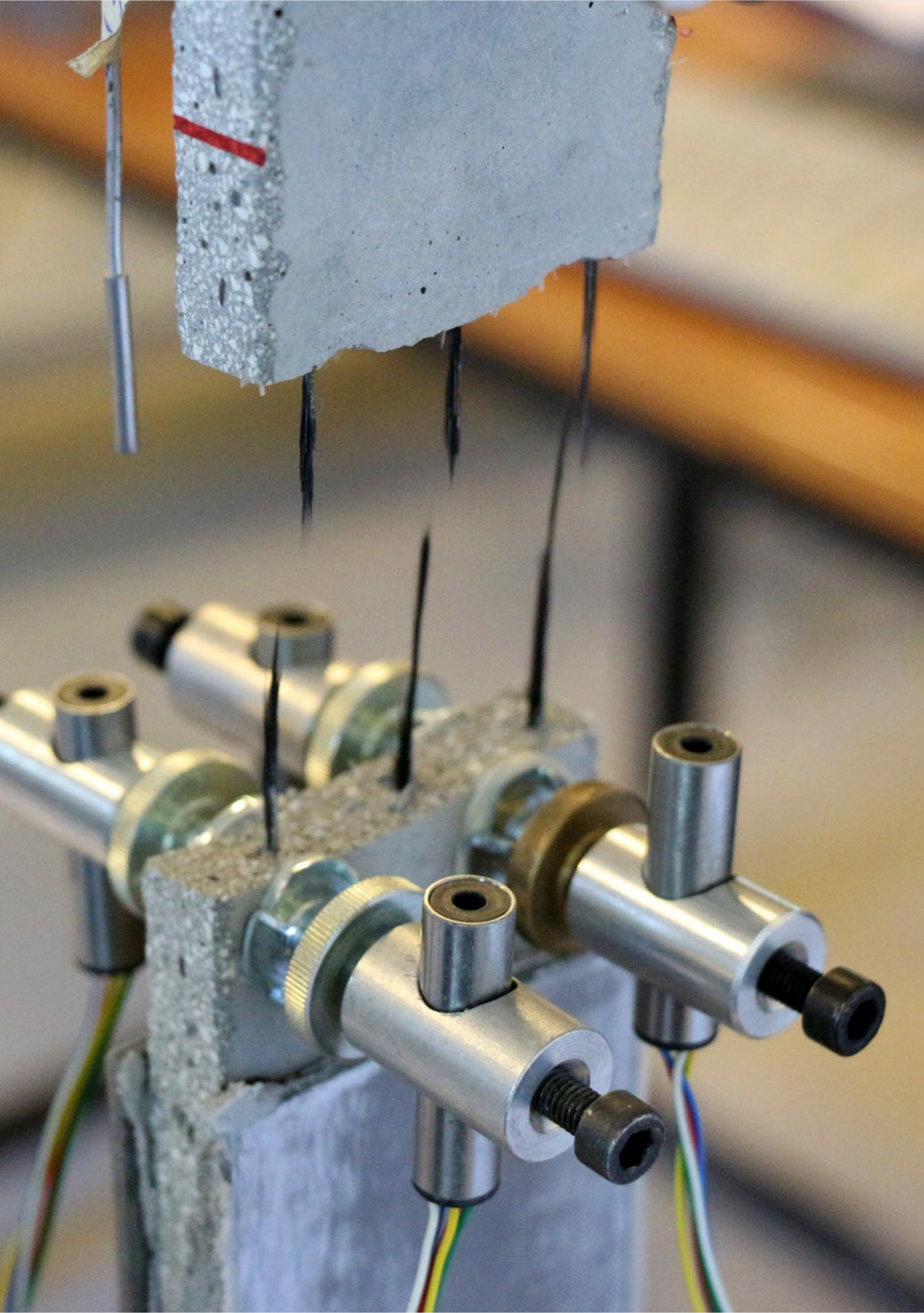

Chapter 2

Material characterization

In this chapter the relevant retrofitting and building materials used through this research are characterized through an extensive material-level experimental campaign following various standards. Chapter 2 is partially based on [74].

2.1 Masonry

The mechanical properties of the constituent materials of the masonry are summarized in Table 2.1. The test methods used to obtain these values are discussed in the following paragraphs.

2.1.1 Bricks

The tunnel kiln fired, soft mud molded clay bricks used in this research had dimensions of $205(\pm 4) \times 95(\pm 2) \times 50(\pm 2)$ mm^3 $(l_b \times w_b \times h_b)$. Mechanical characteristics of the clay bricks were determined according to the relevant standards. The bricks had a mean compressive strength of 31.7 N/mm^2, determined in accordance with EN 772-1 [83]. The mean splitting tensile strength (3.3 N/mm^2) and mean flexural tensile strength (5.89 N/mm^2) of the bricks were obtained following ASTM C1006-07 [82] and ASTM C67-03 [81] respectively.

2.1.2 Mortar

A ready to use factory-made dry mortar mix with strength class M15 was used for the experimental campaigns presented in Chapters 3 and 6 and section 5.1. The mean flexural tensile strength and the mean compressive strength of the M15 mortar specimens were 3.6 N/mm^2 and 10.6 N/mm^2 respectively, both determined according to EN 1015-11 [84].

Table 2.1: Mechanical properties of the masonry materials used. (Number of tested specimens; Coefficient of Variation)

Parameter	Symbol	Unit	Clay brick	Building mortar	Masonry
Mass density	ρ	kg/m^3	1738 (12; 3.6%)	1745 (8; 1.9%)	-
Young's Modulus	E	N/mm^2	-	-	3,100$^{(e)(2)}$ 3,373$^{(e)(1)}$ (6; 10.6%)
Flexural strength	f_{fl}	N/mm^2	5.89$^{(a)}$ (9; 7.4%)	3.6$^{(d)(2)}$ (8; 16.5%) 2.4$^{(d)(1)}$ (3)	0.38$^{(f)(2)}$ (4; 22.9%)
Splitting strength	f_{st}	N/mm^2	3.34$^{(b)}$ (12; 8.7%)	-	-
Compressive strength	f_c	N/mm^2	31.7$^{(c)}$ (12; 7.4%)	10.6$^{(d)(2)}$ (16; 20.7%) 9.3$^{(d)(1)}$ (6; 3.2%)	14.8$^{(2)}$ 8.0$^{(1)}$ (6; 3.4%)
Initial shear strength	$f_{v,0}$	N/mm^2	-	-	0.38 $^{(g)(I)(2)}$
Coefficient of friction	μ_{ma}	-	-	-	0.75 $^{(g)(I)(2)}$
Residual shear strength	$f_{v0,res}$	N/mm^2	-	-	0.02 $^{(g)(II)(2)}$
Residual coefficient of friction	$\mu_{ma,res}$	-	-	-	0.81 $^{(g)(II)(2)}$

(I) Obtained with linear regression ($R^2 = 0.77$); (II) Obtained with linear regression ($R^2 = 0.96$).
(1) Applicable to chapter 4 and section 5.2; (2) Applicable to chapters 3 and 6 and section 5.1.
(a) ASTM C67-03 [81]; (b) ASTM C1006-07 [82]; (c) EN 772-1 [83]; (d) EN 1015-11 [84];
(e) EN 1052-1 [85]; (f) EN 1052-2 [86]; (g) EN 1052-3 [87]

M10 masonry mortar, also a ready to use factory-made dry mortar mix, was used for the experimental campaigns presented in Chapter 4 and section 5.2. The mean flexural tensile strength and the mean compressive strength of the M10 mortar specimens were 2.4 N/mm^2 and 9.3 N/mm^2 respectively. For both the M10 and M15 test batches, the moulds used to prepare the mortar specimens were not placed in a humidity chamber, nor sealed polyethylene bags were used, as suggested by EN 1015-11 [84].

2.1.3 Compression

Compression tests were performed on masonry specimens consisting of 6 brick high (360 mm) stack bonded masonry prisms with an average mortar joint thickness of 12.5 mm. The tests were conducted under displacement control with a loading speed of 0.20 mm/min.

The mean compressive strength of the masonry built using the M15 and M10 mortar was 14.8 N/mm^2 and 8.0 N/mm^2 respectively. Softboard was used as capping material during the compression experiments for fast preparation. It should be noted that "soft capping" materials such as fiberboard reduce the observed compressive strength of masonry units [88] where Maurenbrecher [89] quantified this decrease with 4% compared to dental plaster capping. This reduction is caused by the lateral deformation of the non-confined fiberboard, imparting lateral forces on the specimen and effectively lowering the measured compressive strength. It should be noted that the influence of the head joints on the compression behaviour is not taken into accounts when using bond stacked prisms for compression tests. Thamboo and Dhanasekarm [90] reported that bond stacked prism tests (6 layers high) consistently provide higher compressive strength (25%) than that of the corresponding wallettes specimens (6 layers high, 2 bricks in width with running bond).

The Young's modulus was determined as a secant modulus at 33% of the compressive strength in accordance with EN 1052-1 [85]. The mean Young's modulus of the masonry prims built with M15 mortar and M10 mortar was 3,100 N/mm^2 and 3,373 N/mm^2 respectively. The mean axial strain at peak stress was found to be 0.52% and 0.43% for the masonry specimens built with M15 and M10 mortar respectively. The axial stress-strain diagrams in compression for both masonry types is shown in Fig. 2.1a.

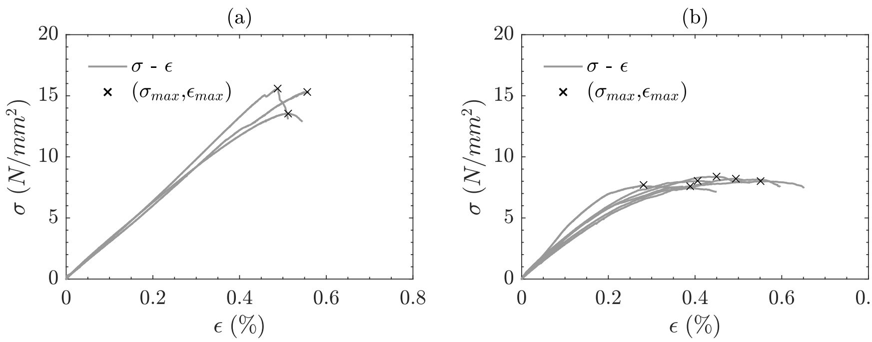

Figure 2.1: Uniaxial stress-strain relation of masonry in compression: (a) M15 mortar; (b) M10 mortar, where the maximum stress and corresponding strain are marked with an *x*.

2.1.4 Shear

In order to determine the mechanical properties of the M15 masonry in shear in accordance with EN 1052-3 [87], a total of 9 triplet shear tests was performed at three different normal stress levels: 0.2, 0.6 and 1.0 N/mm^2. For each group of specimens the ratio between the applied normal stress and the corresponding shear strength was established using linear regression. The parameters for the Coulomb's friction criterion follow from Eq. 2.1, with $f_{v,0}$, μ_{ma} and σ_n being the initial shear strength, friction coefficient and normal stress respectively. The residual shear strength ($f_{v0,res}$) and residual coefficient of friction ($\mu_{ma,res}$) were determined by applying the same linear regression analysis when a plateau was reached in the post-peak phase.

$$f_v = f_{v,0} + \mu_{ma}\sigma_n \tag{2.1}$$

The obtained values regarding the mechanical properties of the masonry in shear were compared with the results of an experimental study on the material properties characterization of Dutch URM [91] and the values proposed in the Dutch Practical Guideline for the seismic assessment of local buildings in Groningen [92]. From the comparison it was concluded that the shear properties of masonry used in this study showed an acceptable agreement with the other reported shear properties.

2.2 Stand-alone retrofit components

The mechanical properties of the materials used for reinforcement are summarized in Table 2.2. The test methods used to obtain these values are discussed in the following paragraphs.

Table 2.2: Mechanical properties of the reinforcement materials used.

Parameter	Unit	Flexible adhesive	CFRP strip	Polymer-modified mortar	CFRP mesh
Mass density	kg/m^3	1,550	1,700	2,138 (6; 1.7%)	1,790
Young's Modulus	N/mm^2	16.0$^{(a)}$ 33.9$^{(b)}$	215,000$^{(d)}$ (5; 1.0%)	25,000	230
Tensile strength	N/mm^2	4.3$^{(a)}$ 5.5$^{(b)}$	2,876$^{(d)}$ (5; 3.4%)	-	1,700
Flexural strength	N/mm^2	-	-	7.58$^{(e)}$ (9; 11.7%)	-
Ultimate strain	%	72.2$^{(b)}$ 88.6$^{(b)}$	1.59$^{(d)}$ (5; 14.7%)	-	-
Shear modulus	N/mm^2	20.2$^{(c)}$	-	-	-
Shear strength	N/mm^2	5.4$^{(c)}$	-	-	-
Ultimate shear strain	%	125.5$^{(c)}$	-	-	-
Poisson ratio	-	0.48	-	-	-
Compressive strength	N/mm^2	-	-	62.55$^{(e)}$ (12; 1.6%)	-

(a) ISO 527-1 $\dot{\epsilon} = 0.46\%/s$; (b) ISO 527-1 $\dot{\epsilon} = 10.33\%/s$ (c) ISO 11003-2;
(d) ISO 527-1 $\dot{\epsilon} = 0.45\%/min$; (e) EN 1015-11

2.2.1 CFRP strip

The prefabricated (pultruded) carbon fibre reinforced polymer (CFRP) strip was 20 mm in width and 1.4 mm in thickness, with a fibre volume content >68%. The Young's modulus, tensile strength and elongation at rupture of the CFRP strip as provided by the supplier were 215 kN/mm^2, 2,876 N/mm^2 and 1.59% respectively.

2.2.2 Flexible adhesive

The material properties of the flexible adhesive were provided by the supplier. The mechanical properties in tension (mode I loading) were obtained following ISO 527-1 [93] using three specimens at a loading rate of 10 mm/min (mean strain rate 0.46%/s). The Young's modulus was determined as the secant modulus between 0.5% and 5% of the tensile strength, and was found to be 16.0 N/mm^2. The tensile strength and elongation at rupture were determined as 4.3 N/mm^2 and 72.1%, respectively. With a loading rate of 200 mm/min (mean strain rate 10.33 %/s), the values for the Young's modulus, tensile strength and elongation at rupture were determined to be 33.9 N/mm^2, 5.5 N/mm^2 and 88.6% respectively. The significant increase in these values, especially for the Young's modulus, shows that strain-rate dependency plays an important role in the mechanical behaviour of the visco-elasto-plastic adhesive. The stress-strain relations of the flexible adhesive are provided in Fig. 2.2.

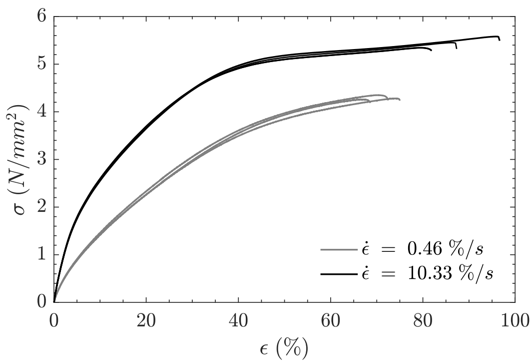

Figure 2.2: Tensile stress-strain relations (Mode I) of the visco-elasto-plastic adhesive, obtained for two loading rates: $\dot{\epsilon} = 0.46\%/s$ (grey lines) and $\dot{\epsilon} = 10.33\%/s$ (black lines).

The material properties for the flexible adhesive in shear (mode II loading) were quantified using thick adherend shear tests (TAST), partly following ISO 11003-2:1999 (1993). Aluminum substrates were used, with dimensions of 70 mm x 25 mm x 12 mm, as illustrated in Fig. 2.3. The nominal bondline thickness was 1.75 mm. The test was performed with a constant crosshead rate of 10 mm/min. The shear stress-strain curves are shown in Fig. 2.4. The shear modulus, shear strength and ultimate shear strain were found to be 20.2 N/mm^2, 5.4 N/mm^2 and 125.5 % respectively.

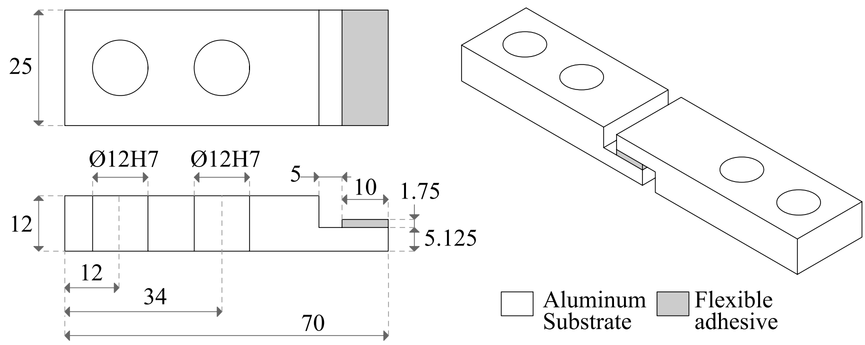

Figure 2.3: Aluminum substrates used for thick adherend shear test (TAST).

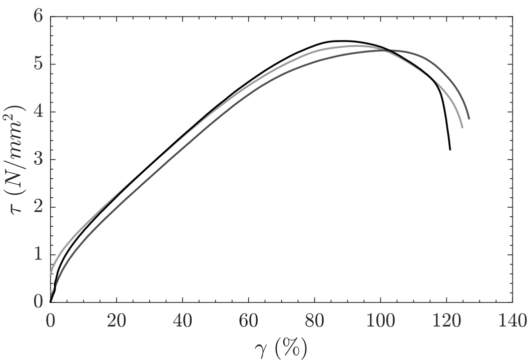

Figure 2.4: Shear stress-strain relations of the visco-elasto-plastic adhesive.

Durability

Adhesive strength is affected by many common environments, including temperature, moisture, chemical fluids, and outdoor weathering [94]. Water can permeate the adhesive and displace the adhesive at the bond interface. This mechanism is the most common cause of adhesive-strength reduction in moist environments [94]. Primers and surface treatments tend to hinder adhesive strength degradation in moist environments [95]. A fluid primer that easily wets the interface presumably tends to fill in minor discontinuities on the surface [94]. The flexible adhesive supplier reported limited water-uptake when immersed directly into water, and expected limited effects to the adhesive being present inside the wall. Moreover, while the CFRP strips are installed on the load-bearing inner leaf of the cavity wall, significant water permeation is not present.

The service temperature window of the flexible adhesive as reported by supplier was -40°C to +30°C. The maximum internal air temperature for a cavity brick construction was reported at 29.7°C by Sugo, Page and Moghtaderi [96], during heat wave conditions in Newcastle (Australia) with a maximum recorded air temperature of 43°C. The cavity brick construction consisted of two 110 mm thick masonry skins separated by a 28 mm air cavity (no insulation), similar to the historic building typologies in Groningen.

2.2.3 Polymer-modified mortar

The mortar used for the fabric reinforced cementitious matrix (FRCM) overlay was a polymer-modified mortar containing organic binders, polymer fibres and selected aggregates with a maximum grain size of 1.8 mm. The selected mortar is generally used in renovation and strengthening of existing buildings, underground structures and tunnels. For the preparation of the polymer-modified mortar, a plastic bonding agent was used in order to improve the adhesion to the masonry, by mixing 110 g of the plastic bonding agent per 10 kg of prepared mortar. The polymer-modified mortar was prepared following the manufacturer's instructions by adding 2.6 L of water to a bag of 25 kg dry mortar. Both the flexural tensile strength and the compressive strength of the mortar specimens were determined according to EN 1015-11 [84]. The mean flexural tensile strength of the mortar specimens was 7.58 N/mm^2. The compressive strength of the mortar was 62.6 N/mm^2. The weight density was 2,138 kg/m^3 .

2.2.4 CFRP mesh

The orthogonal CFRP mesh with about 3 mm width per thread and a fibre weight density of 1,790 kg/m^3, had a square aperture dimension of approximately 20 x 20 mm^2. The theoretical cross sectional area of the CFRP mesh for design was 44 mm^2/m. The Young's modulus and roving strength for the CFRP mesh were reported as 230 kN/mm^2 and 1,700 N/mm^2 respectively [97]. The theoretical tensile strength of CFRP mesh (50 continuous strands) is 74.8 kN/m.

Figure 2.5: Dry polymer-modified mortar used for FRCM overlay.

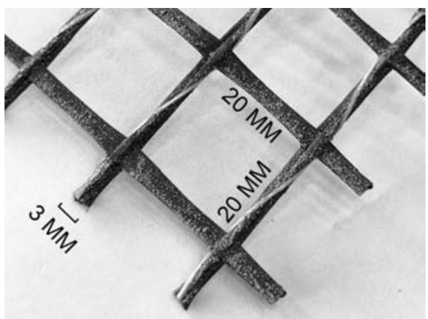

Figure 2.6: Orthogonal CFRP mesh.

2.3 Fabric Reinforced Cementitious Matrix

This section provides an overview on the mechanical characterization of the proposed CFRP FRCM composite system by means of double shear bond of tensile experiments.

2.3.1 Bond behaviour with masonry

In order to investigate the bond between the Fabric Reinforced Cementitious Matrix *(FRCM)* system and masonry substrate, double shear bond *(DSB)* tests were conducted, where the bond length between the FRCM layer and the masonry was varied. The double shear bond tests were performed following the guidelines provided by RILEM TC 250-CSM [70].

Preparing the test specimens

A total of n=25 small clay brick masonry prisms, consisting of 5 stacked bricks, were built by an experienced mason. The masonry specimens were constructed against a vertical sideboard to ensure minimum horizontal deviation and were left to cure for 28 days in the unheated laboratory (10-25°C) before applying the FRCM layer. On both sides of the *DSB* specimens a stroke of polymer-modified mortar was applied. The stroke length (l_{FRCM}) was 55, 100, 150, 200 or 250 mm, and the stroke width was kept constant at 60 mm. Each configuration was applied on three *DSB* specimens. In order to prevent stress concentrations at the edge, the polymer-modified mortar stroke had a distance of 30 mm from the top of the wallette. The first layer of polymer-modified mortar had a thickness of approximately 5 mm. CFRP mesh strokes, consisting of 3 continuous CFRP strands in the longitudinal direction, were cut to a length equal to approximately the sum of two times the stroke length and an additional 800 mm. Both ends of the CFRP mesh were then applied on the mortar surface on both sides, and were pressed into the polymer-modified mortar. After placing the CFRP mesh, a new thin layer of polymer-modified mortar was applied to embed the CFRP mesh, resulting in a nominal FRCM layer thickness of 10 mm. After wrapping the specimens in damp proof membrane sheets, the wallettes were cured at laboratory ambient conditions at a temperature of 20°C for 28 days. A schematic overview of the DSB specimen is shown in Fig. 2.7.

Double shear bond test setup

The DSB tests were conducted on an Instron universal testing machine. The process started by carefully positioning the specimen under the loading grips of the setup, with the specimen resting on the machine‘s basement. Softboard was put on the top and bottom of the prism to prevent stress concentrations due to the non-flat surface of the brick. Subsequently, a 20 mm

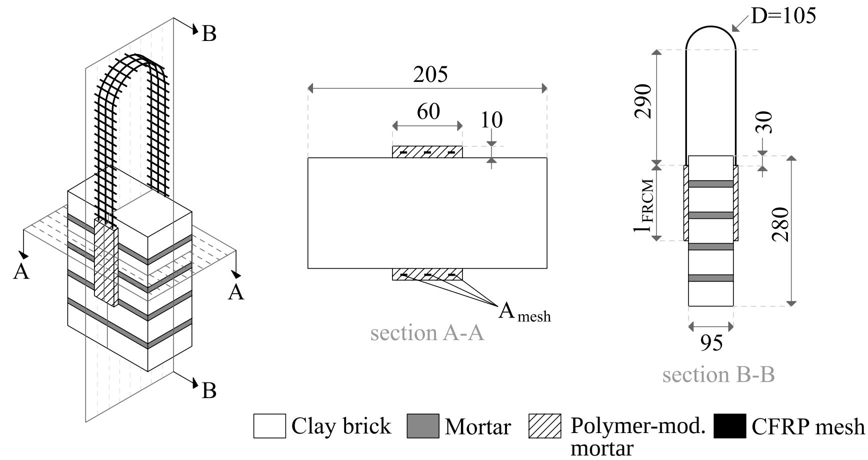

Figure 2.7: Double shear bond *(DSB)* specimen.

thick steel restraint plate was placed on top of the prism. Using threaded rods, the steel restraint plate was bolted tightly to the base of the installation. The CFRP mesh was placed around a wooden wheel with a 105 mm diameter, equal to the thickness of the wall and one FRCM layer. In order to reduce eccentricity, a hinge was used to mount the wooden wheel to the loading grips of the machine. After setting the pre-tension force in the mesh to 0.1 kN, the experiment started at a displacement controlled pull-out speed of 0.5 mm/min. Slip of the mesh was reported as the distance covered by the loading grips ($\delta_{machine}$). A schematic overview and photo of the test setup is shown in Fig. 2.8.

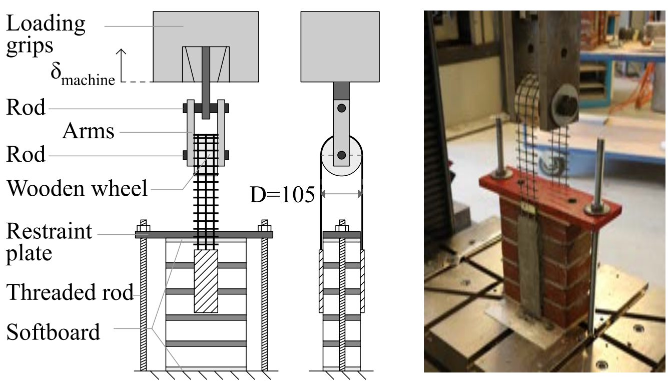

Figure 2.8: Double lap shear test setup: schematic overview (left) and photo (right).

Results

The overall results of the double lap shear tests are shown in Fig. 2.9a. The peak stress ($\sigma_{mesh,u}$) in the strands of the CFRP mesh was determined by dividing the peak load by the cross-section area of the three strands of the CFRP mesh (2.64 mm²). The failure mechanism for all the specimens was slippage of the CFRP mesh. In order to filter out start-up effects, such as settling of the CFRP mesh, the stress-displacement relation below σ_{mesh} = 200 N/mm² was replaced by a linear extrapolation using the slope in the range σ_{mesh} = [200-250] N/mm² in the load-displacement graph. It should be noted that the linear extrapolation was solely done with the purpose of making the data in Fig. 2.9a more presentable.

The mean peak stress per FRCM stroke length was found to be $\sigma_{mesh,u}$ = 368, 472, 871, 955 and 1,339 N/mm² for l_{FRCM} = 55, 100, 150, 200, 250 mm respectively. The peak stress per FRCM stroke length is provided in Fig. 2.9b. A strong linear correlation (R^2 = 0.93) was found between the bond length and peak stress in the mesh. The peak stress in the mesh was found to be approximately 500 N/mm² per 100 mm bond length. Based on these findings and the roving strength of the mesh of 1,700 N/mm², the mesh will rupture with an anchorage length ≥ 340 mm.

The residual stress $\sigma_{mesh,res}$ represents the plateau caused by friction at the end of the test. Fig. 2.9b also provides the residual stress as a function of the FRCM stroke length. The mean residual stress per FRCM stroke length was found to be $\sigma_{mesh,res}$ 130, 175, 317, 372 and 453 N/mm² for l_{FRCM} = 55, 100, 150, 200, 250 mm respectively.

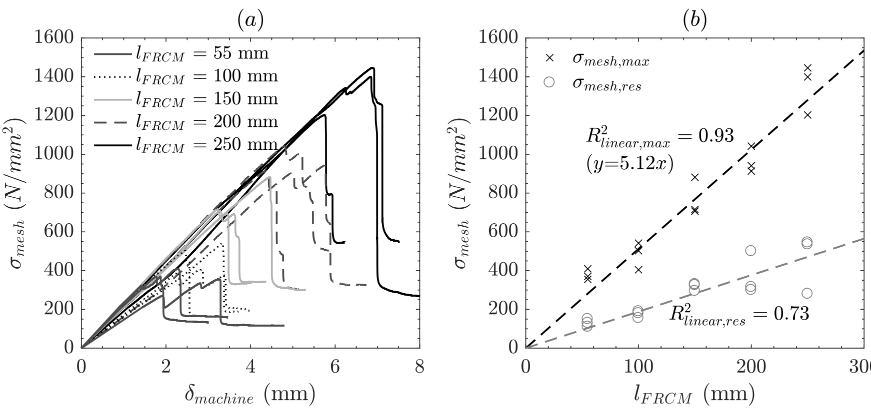

Figure 2.9: Results from double shear bond tests: σ_{mesh} versus $\delta_{machine}$ (a); $\sigma_{mesh,max}$ and $\sigma_{mesh,res}$ versus l_{FRCM} (b).

2.3.2 Tensile behaviour

In order to characterize the tensile behaviour between the CFRP mesh and the polymer-modified mortar, tensile tests were performed using clevis type grips, following Annex A of AC434.13 [71].

Preparing the test specimens

Prior to preparing the tensile test specimens, two moulds were built with an inner length and width of 600 and 400 mm respectively. The height of the moulds was 10 mm (mould 1) and 15 mm (mould 2). The inside of the moulds were covered with a non-stick (bond free) layer. The first layer of polymer-modified mortar was applied to the flat surface with a trowel with an overall mortar thickness of 5 mm and 7-8 mm for mould 1 and mould 2 respectively. After applying the CFRP mesh on the mortar surface, the remaining part of polymer-modified mortar was applied up to the top surface of the mould. Finally, the mould was placed on a vibrating table for compaction of the prepared FRCM panels. After wrapping the boxes in damp proof membrane sheets, the panels were cured at laboratory ambient conditions at a temperature of 20°C for 28 days. The FRCM panels were cut in prismatic coupons with 400 mm length and width (w_c) of approximately 60 mm, using a water cooled circular saw. The cuts were positioned in such a way that the coupons had 3 continuous CFRP strands centered in the length direction. Steel tabs, 3 mm thick and with the same width as the coupons, were attached at the ends of the FRCM coupons over a contact length of 150 mm with a fast-curing two component epoxy and were cured for at least 24 hours. With this type of configuration, the tensile load is transferred from the testing machine to the specimen only through adhesive shear tensions, without applying normal forces to the specimen ends by clamping grips [98]. Further, a tab contact length of 150 mm was reported as the most suitable length, able to fully characterize the behaviour of all the tested FRCM specimens. A schematic overview of the FRCM coupon is presented in Figure 5. The coupons for the tensile tests are denoted as TT-10 and TT-15 for the 10 mm and 15 mm thick (t_c) specimens respectively. From each group 6 specimens were made.

Tensile test setup

Using a clevis-type gripping mechanism, following AC434.13 [71], the steel tabbed FRCM coupons were installed in an Instron universal testing machine. The deformation was measured with two LVDT sensors on each side, covering a length of 60 mm. After resetting the sensors and setting the pre-tension force in the coupon to 0.1 kN, the experiment started at a displacement controlled loading speed of 0.3 mm/min. A schematic overview and a photo of the test setup are shown in Fig. 2.11.

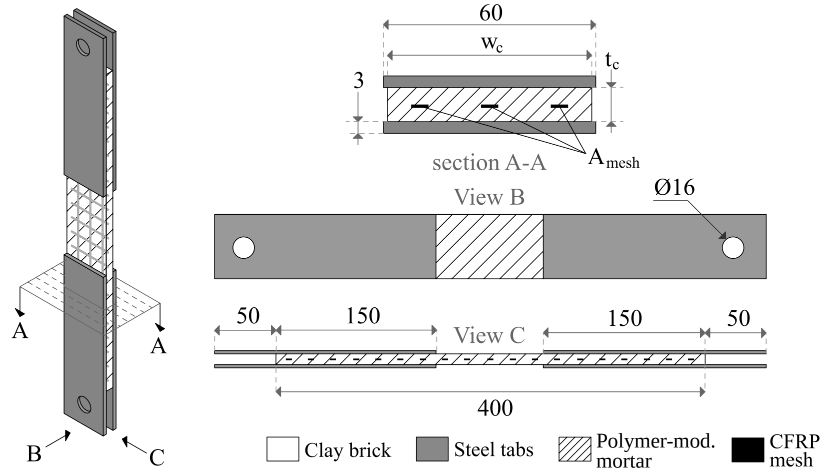

Figure 2.10: FRCM coupon for tensile test purposes.

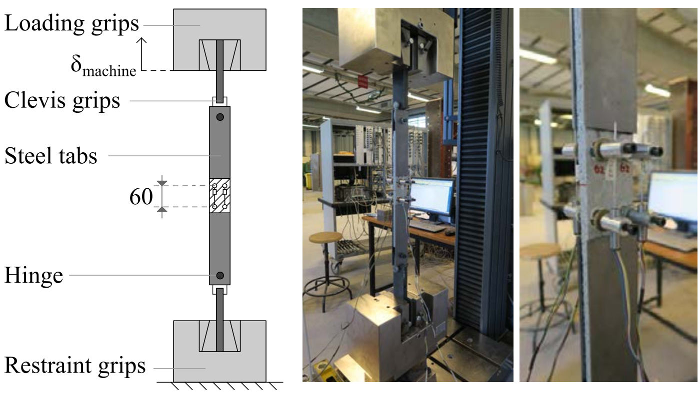

Figure 2.11: Tensile coupon test FRCM: schematic overview (left) and photo (right).

Results

The results of the tensile tests on the FRCM coupons are summarized in Table 2.3. The load versus machine displacement diagram is shown in Fig. 2.13a and Fig. 2.14a for the *TT-10* (n=5) and *TT-15* (n=4) specimens respectively. The behaviour of the tensile coupon specimens during the tensile loading process can be divided in three stages:

- Stage I - uncracked: The cementitious matrix layer cracks when the tensile stress limit of the polymer-modified mortar is exceeded.

- Stage II – crack formation: Crack formation (Fig. 2.12) causes a softening behaviour in the cementitious matrix layer. As cracking progresses, the mortar matrix loses its stiffness at a relatively high rate. However, this softening behaviour is counteracted by the embedded CFRP mesh.

- Stage III – stabilized cracking: At this stage no further cracking occurs until the failure load. The predominant failure mode was slippage of the CFRP mesh within the specimen (Fig. 2.12).

Table 2.3: Results of tensile tests (stages I and II) on the FRCM coupons.

	w_c mm	t_c mm	$f_{CM,I}$ N/mm²	ϵ_{CM} %	E_{CM} kN/mm²	$f_{CM,II}$ N/mm²	$\epsilon_{mesh,em}$ %	$f_{mesh,em,u}$ N/mm²	$E_{mesh,em}$ kN/mm²
TT-10-1	57.7	9.8	4.72	0.016	30.2	3.77	1.66	1761	78.06
TT-10-2	57.6	9.9	4.13	-	-	-	1.71	1392	75.22
TT-10-3	58.0	10.3	4.99	0.018	27.9	5.25	-	1571	-
TT-10-4	58.2	10.4	5.24	0.019	28.2	4.50	-	1564	-
TT-10-5	58.0	10.4	3.65	0.013	28.5	2.92	1.74	1891	86.90
Mean	58.0	10.2	4.55	0.016	28.71	4.11	1.70	1636	80.06
COV	0.3%	2.3%	12.8%	14.0%	3.2%	21.1%	1.9%	10.6%	6.2%
TT-15-1	54.7	14.0	3.87	0.014	28.5	3.83	1.61	1518	71.14
TT-15-2	57.5	13.7	3.60	0.018	20.0	-	2.67	1884	55.96
TT-15-3	58.1	13.6	4.99	0.018	28.2	-	-	1496	-
TT-15-4	55.2	13.4	3.56	0.013	26.7	4.39	2.08	1572	58.26
Mean	56.4	13.7	4.00	0.015	25.07	4.11	2.12	1617	61.79
COV	2.2%	0.9%	14.5%	14.4%	14.3%	-	20.5%	9.7%	10.8%

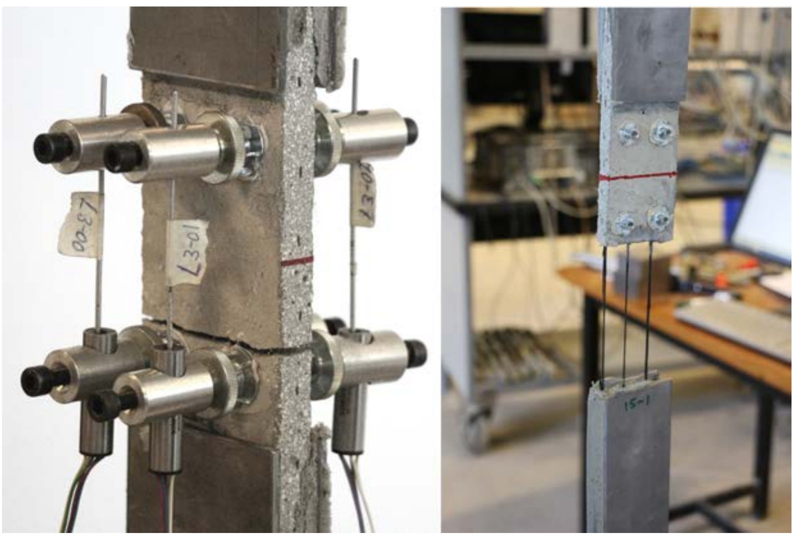

Figure 2.12: Damage on a FRCM coupon specimen during the tensile test: Crack formation (left) CFRP mesh slippage (right).

The results related to stage I (uncracked) of the *TT-10* and *TT-15* specimens are shown in Fig. 2.13b and 2.14b respectively. The mean tensile strength (f_{CM}), Young's modulus (E_{CM}) and cracking strain (ϵ_{CM}) for the (uncracked) *TT-10* specimens were found to be 4.55 N/mm^2, 28.71 kN/mm^2 and 0.016% respectively. The Young's modulus of the uncracked specimen, was determined in accordance with Eq. 2.2. With a mean tensile strength, Young's modulus and cracking strain for the (uncracked) *TT-15* specimens of 4.0 N/mm^2, 25.07 kN/mm^2 and 0.015% respectively, no significant differences were found with the results of the *TT-10* specimens.

$$E_{CM} = \frac{f_{CM,I}}{\epsilon_{CM}} \tag{2.2}$$

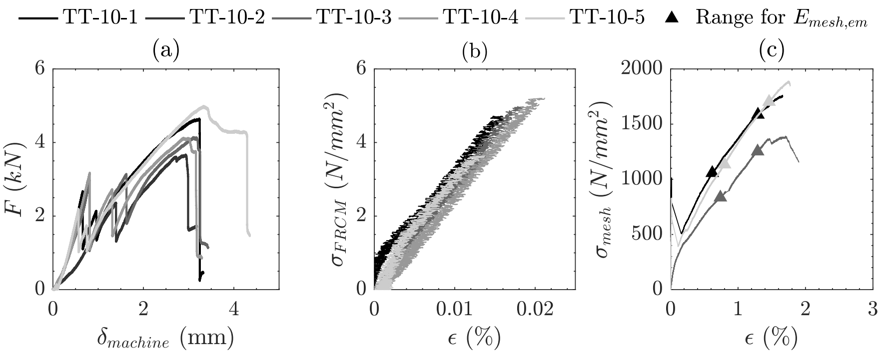

Figure 2.13: Results of the tensile tests for the *TT-10* specimens: force-machine displacement (a), stress-strain diagrams of stage I (b) and stage III (c).

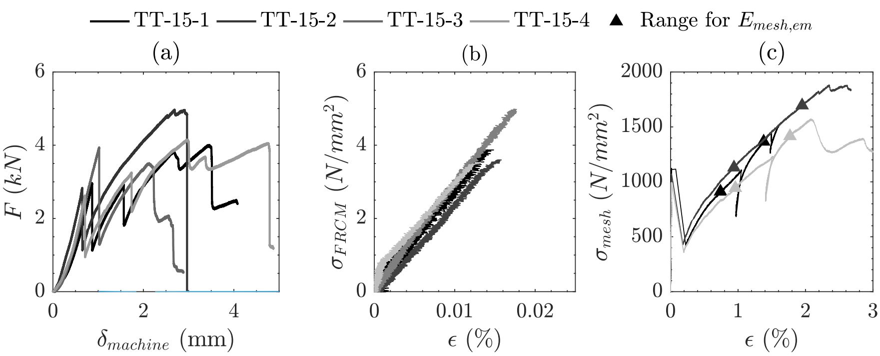

Figure 2.14: Results of the tensile tests for the *TT-15* specimens: force-machine displacement (a), stress-strain diagrams of stage I (b) and stage III (c).

During the second stage (crack formation), the second crack occurred at a mean load ($\sigma_{CM,II}$) of 4.11 N/mm^2 for both the *TT-10* and *TT-15* specimens, which was similar to the load needed to initiate the first crack. The overall mean tensile strength of the cementitious matrix was found to be 4.23 N/mm^2.

The results related to stage III (stabilized cracking) of the *TT-10* and *TT-15* specimens are shown Fig. 2.13c and 2.14c respectively. The mean failure load ($f_{mesh,em,u}$) and ultimate strain ($\epsilon_{mesh,em,u}$) were 1636 N/mm^2 and 1.7% respectively. The failure load in the CFRP mesh was determined by dividing the peak load by the cross-sectional area of the CFRP mesh of 2.64 mm^2. The mean Young's modulus was found to be 80.1 kN/mm^2. As indicated in the AC434.13 [71], the modulus of the cracked specimens ($E_{mesh,em}$), caused by the slipping of the CFRP mesh, was calculated as the slope of the segment of the response curve between the points $0.6f_{mesh,em,u}$ and $0.9f_{mesh,em,u}$, indicated with triangles in Fig. 2.13c. Similar values were found for the failure of the *TT-15* specimens, with 1617 N/mm^2 (Table 2.3, Fig. 2.14c). The ultimate strain (2.12%) and Young's modulus (61.79 kN/mm^2) showed some deviation with the *TT-10* specimens. This discrepancy can be attributed to the difference in strengthening ratio.

It should be noted that in order to obtain the modulus of the cracked specimen, the cracks in the specimen need to form in the area measured by the LVDT's. If the cracks occurred outside the measuring area, as was the case for *TT-10-3*, *TT-10-4* and *TT-15-3* specimens, the slip of the CFRP mesh could not be measured.

2.3.3 Durability

At the time of writing this thesis, limited studies were available in literature regarding the long-term behaviour of FRCM composites with respect to different environmental conditions [99]. Arboleda, Babaeidarabad, Hays and Nanni [100] studied the durability characteristics of the carbon fibre FRCM composite system. Environmental stresses such as frost and chemical attack were addressed with exposure environments such as freeze/thaw cycles, high temperature water vapor and immersion in seawater. The authors concluded that no significant loss of residual tensile strength and bond strength were observed under the aforementioned conditions. The results gathered by Al-Lami, D'antino and Colombi [99] showed that the exposure of the FRCM to some harsh environmental conditions may lead to the formation of microcracks, which in turn affect the cracking strength and stiffness of the composite. The carbon fibre itself was reported to have enhanced durability [101, 102].

Chapter 3

Flexible deep mounted CFRP strips: bond-slip behaviour

Due to the novelty of the proposed retrofitting technique with flexible deep mounted (FDM) CFRP strips, the mechanical properties of the CFRP strips embedded in the flexible adhesive are only roughly understood. The effectiveness of any FRP retrofit system largely depends on the ability to develop shear transfer across the FRP-to-masonry bond [69]. As no records could be found in open literature regarding the bond behaviour of CFRP strips bonded with a flexible adhesive to masonry underneath the surface, an extensive experimental campaign was essential in order to gain more insight on this bond-behaviour. In this chapter, the experimental program on the bond behaviour of FDM CFRP strips is presented and the results are discussed. The proposed model is validated with the experimental findings. Finally, a comparison is made with the bond-behaviour of stiff adhesive systems. The content of this chapter is primarily based on [75, 76].

3.1 Extraction of bond-slip behaviour

The most common experimental technique for studying the bond, the shear pull-test (or simply "pull-out test"), was used to construct generalized bond laws for modelling purposes and to gain more insights on the governing failure mechanisms. Despite the substantial pull-out testing undertaken to date, no standardised guidelines for performing pull-out tests exist. The pull-out test involves adhesively bonding the FRP plate/strip to the masonry and applying an increasing slip until the CFRP plate/strip eventually debonds [69], all while restraining the masonry. The pull-out test is shown diagrammatically in Fig. 3.1 for masonry with a single flexible deep mounted (FDM) CFRP strip.

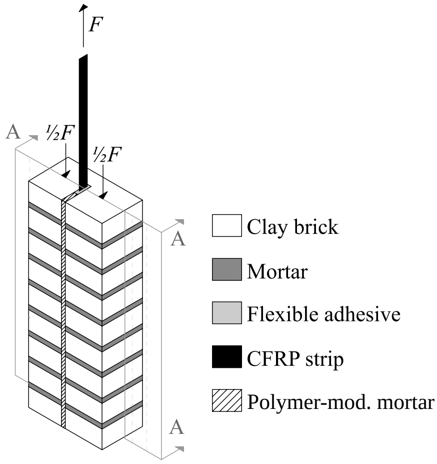

Figure 3.1: Diagrammatic representation of the pull-out test.

Pull-out tests can provide insight into the local behaviour of the bond between the CFRP strip and the flexible adhesive under shear deformation, which is typically characterised in terms of a bond-slip ($\tau - \delta$) model relating shear stress to slip. In order to establish the bond versus slip behaviour using the experimentally determined strain profile of the CFRP strip over the embedded length, a one-dimensional partial-interaction (PI) model was used as illustrated in Fig. 3.2. It should be noted that due to symmetry of the pull-out test diagram, only half of the cross-section A-A (as illustrated in Fig. 3.1) is depicted. As the masonry is assumed as a homogeneous material for this model, the clay bricks and mortar were not included separately. The influence of the polymer-modified mortar and the bonded areas perpendicular to the CFRP strip thickness direction were neglected. Additionally, only the shear component was included in the partial-interaction model. It was assumed that no significant equivalent tensile stresses would develop at the interface between CFRP strip and adhesive with the considered loading scheme. It should be noted that when a one-way spanning retrofitted wall is subjected to out-of-plane loading, equivalent tensile stresses at the interface between the CFRP and the adhesive can conceivably develop.

The specimen was modeled using elements with small length Δx. For each element the decrease in tensile force in the CFRP strip was approximated using the constructed polynomial and Eq. 3.1, where $\epsilon_{p,i}$ is the strain of the CFRP strip at position i and E_p is the Young's modulus of the CFRP strip.

$$\Delta F_i = (\epsilon_{p,i} - \epsilon_{p,i-1}) \cdot E_p \cdot b_p \cdot t_p \tag{3.1}$$

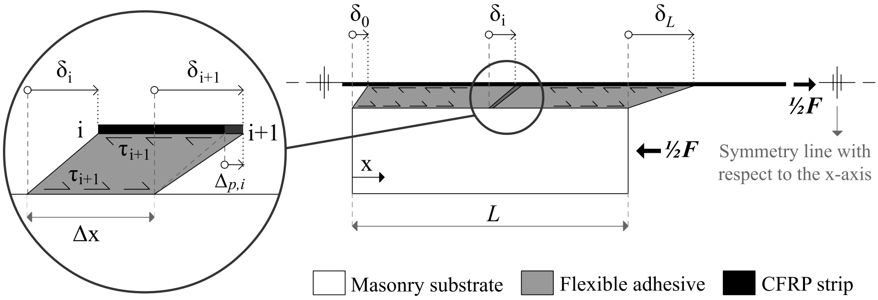

Figure 3.2: One-dimensional partial- interaction (PI) model.

The decrease in tensile force is in equilibrium with the sum of the bond stress over the length Δx and perimeter of the element, as provided in Eq. 3.2

$$\Delta F_i = \tau_i \cdot \Delta x \cdot (2b_p + 2t_p) \tag{3.2}$$

Combining Eqs. 3.1 and 3.2, and making the assumption that the CFRP thickness is negligible compared to the width ($b_p + t_p \approx b_p$), the bond stress for element i was obtained using Eq. 3.3

$$\tau_i = \frac{(\epsilon_{p,i} - \epsilon_{p,i-1}) \cdot E_p \cdot t_p}{2 \cdot \Delta x} \tag{3.3}$$

The pull-out load can be obtained by summing the local bond stresses over the length and multiplying with the CFRP strip width, taking into account both bonded area's of the CFRP strip.

$$F = 2b_p \sum_{i=1}^{L} \tau_i \tag{3.4}$$

Contrary to previous experimental campaigns [13, 40], the calculation of the loaded end slip was based on the assumption that the axial strain in the masonry and the slip at the unloaded end could not be neglected. Because of the significantly higher embedment length used in this research, the influence of the axial strain of the masonry was taken into account. The tensile force in the strip is in equilibrium with the compression force in the masonry. When a uniform compression stress over the complete cross section of the specimen was assumed, the axial stress in the masonry at position i was obtained following Eq. 3.5

$$\sigma_{m,i} = \sum_{k=1}^{i} \frac{\Delta F_k}{A_m} \tag{3.5}$$

The axial deformation of the composite masonry for element i was determined using Eq. 3.6, whereas the mean axial deformation of the CFRP strip for element i, using the constructed quadratic polynomial, was determined using Eq. 3.7

$$\Delta_{m,i} = \frac{\sigma_{m,i}}{E_m} \Delta x \tag{3.6}$$

$$\Delta_{p,i} = \frac{1}{2} (\epsilon_{p,i} + \epsilon_{p,i-1}) \Delta x \tag{3.7}$$

Within this research, the CFRP slip was defined as the displacement of the CFRP strip relative to a fixed point in the intial state of the masonry. For each element in the CFRP strip, the corresponding slip was the sum of the free end slip, the summation of the CFRP deformation between the free end and the considered element, and the summation of the axial masonry deformation between the free end and the considered element, as per Eq. 3.8

$$\delta_i = \delta_0 + \sum_{k=1}^{i} \Delta_{p,k} + \sum_{k=1}^{i} \Delta_{m,k} \tag{3.8}$$

The predictive capability of the bond-slip model covers various aspects of retrofit behaviour: the debonding load, required anchorage length, axial strain profile, as well as the global load-slip behaviour of the system [69]. For the calculations, a length of 1 mm was selected for Δx.

3.2 Quasi-static pull-out experiments

One of the recommendations following the preliminary research projects [22] was the necessity of more knowledge regarding the bond-slip behaviour of the CFRP strips in the masonry, where the bond is created by embedding the strips in a flexible adhesive which is used as a groove filler. It is essential to quantify the interfacial bond-slip relation to allow for accurate modelling and understanding of debonding failures in FRP strengthened structures, and to be able to model the behaviour of a wall strengthened with FDM CFRP strips. There are several parameters that can influence this relation, such as the groove and the strip dimensions, the tensile and shear strength of the groove filler, and the position of the CFRP strip within the member being strengthened. The challenge is to find a suitable configuration at which the bond-slip behaviour provides sufficient flexibility to prevent masonry from premature cracking and results in high pull-out capacities in order to realise effective strengthening.

The bond behaviour of CFRP systems can be experimentally studied with direct pull-out tests (DPT) and beam pull-out tests (BPT). Because the DPT method is less time consuming and easier to prepare and to undertake compared to the BPT test, this method was the starting point to find a configuration that led to the previously stated and desired bond slip behaviour.

3.2.1 Building the specimens

A summary and schematic overview of the specimens are provided in Table 3.1 and Fig. 3.3 respectively. A total of 16 masonry prisms were constructed against a vertical sideboard to ensure minimum vertical deviation and were left to cure for 28 days in an unheated environment. Each masonry prism consisted of 16 bond stacked bricks in height and had typical mortar joint thicknesses of 13 mm, resulting in a total prism height of approximately 1,000 mm.

Table 3.1: Overview specimens for quasi-static pull-out experimental campaign

Specimen	Adhesive	Groove width	Surface treatment CFRP	Strain gauges
Std-U-10	Standard	10	Untreated	1
Std-U-10-SG	Standard	10	Untreated	9 (8 embedded)
Std-U-15	Standard	15	Untreated	1
Std-U-15-SG	Standard	15	Untreated	9 (8 embedded)
Mod-U-10	Modified	10	Untreated	1
Mod-U-10-SG	Modified	10	Untreated	9 (8 embedded)
Mod-U-15	Modified	15	Untreated	1
Mod-U-15-SG	Modified	15	Untreated	9 (8 embedded)
Std-RP-10	Standard	10	Roughened and primer	1
Std-RP-10-SG	Standard	10	Roughened and primer	9 (8 embedded)
Std-SB-10	Standard	10	Sandblasted	1
Std-SB-10-SG	Standard	10	Sandblasted	9 (8 embedded)

Six pairs of CFRP strips were cut in lengths of 1,480 mm. Two pairs of CFRP strips were subjected to additional surface treatment methods prior to the installation of strain gauges: one pair (coded *RP*) of CFRP strips was roughened with sandpaper prior to the application of a primer, whereas the other pair (coded *SB*) was sand-blasted.

One CFRP strip of each pair was instrumented with nine strain gauges, whereas the other strip of the pair was equipped with only one strain gauge.

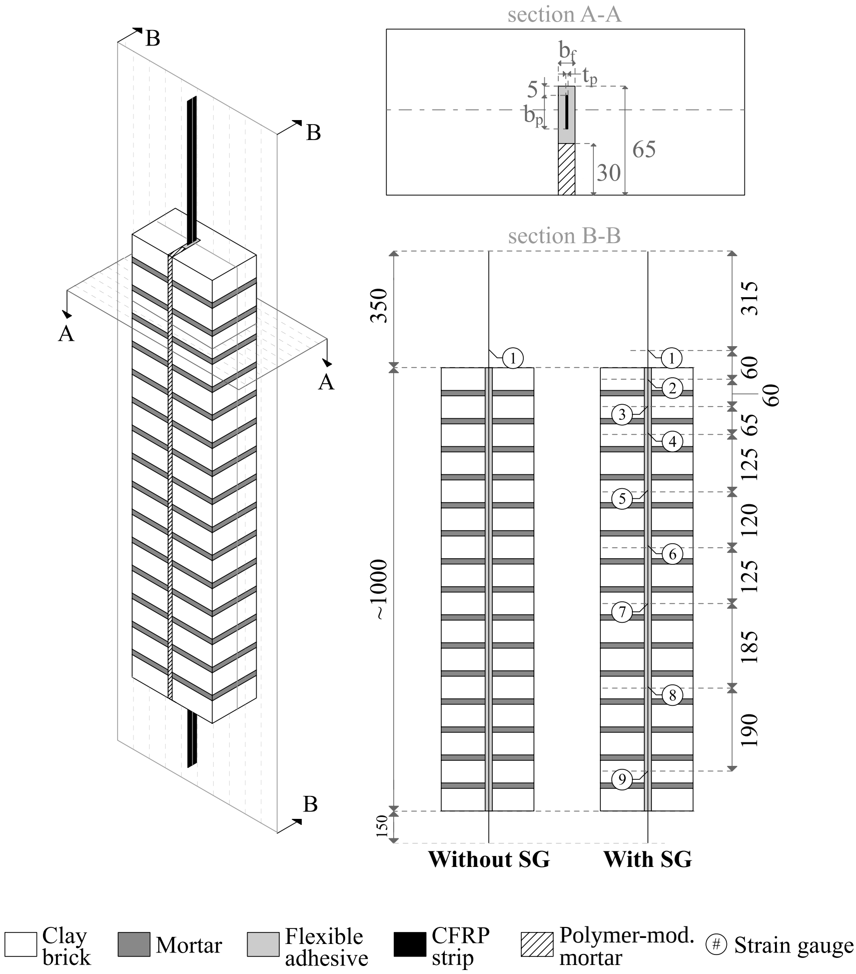

Figure 3.3: Schematic overview specimens quasi-static pull-out campaign.

The CFRP strips that were instrumented with nine strain gauges were coded *SG*. Type *PFL-10-11* foil strain gauges with polyester resin backing were used. For the *SG* coded specimens, the embedded strain gauges were both positioned with a varying inter distance to alternating sides (as illustrated in Fig. 3.3) in order to minimize asymmetry effects, and were covered with wax to reduce the influence of the flexible adhesive on the measurements. The strain gauges that were not embedded were placed on the loaded end of the CFRP strip (strain gauge 1 in Fig. 3.3).

One CFRP strip was installed in the centre of each masonry prism following the installation procedure mentioned in section 1.4. Two pairs of the non-surface treated CFRP strips were mounted using a modified flexible adhesive. The inclusion of the modified adhesive was done with the purpose of determining whether replacing the standard adhesive with an even more flexible alternative would lead to an increase of system performance in terms of pull-out strength and stress distribution. This modified flexible adhesive had a Young's modulus, tensile strength and elongation at break of 16.6 N/mm^2, 2.95 N/mm^2 and 98 % respectively. The tensile stress-strain relations of both the standard and modified adhesive are shown in Fig. 3.4 for a loading rate of 200 mm/min (mean strain rate 10.3 %/s). The standard flexible adhesive and modified flexible adhesive were coded *Std* and *Mod* respectively.

For the non-surface treated CFRP strips, there also was a variation in the groove width b_f: being either 10 or 15 mm. The effects of an even smaller groove width than 10 mm were not investigated due to expected difficulties of milling such a small groove in practice. All of the surface treated CFRP pairs were inserted in a groove with a width of 10 mm.

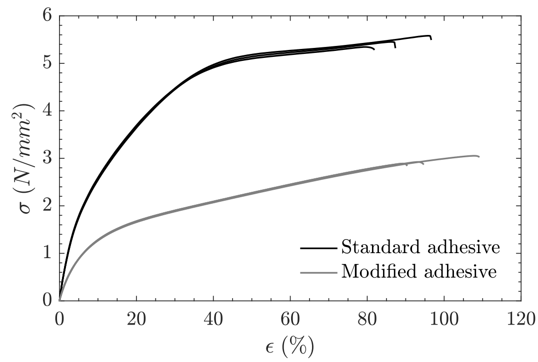

Figure 3.4: Tensile stress-strain relations (Mode I) of the standard (black lines) and modified (grey lines) visco-elasto-plastic adhesive ($\dot{\epsilon} = 10.3\%/s$).

3.2.2 Test setup and procedure

The direct pull-out tests were conducted on an Instron universal testing machine, as shown in Fig.3.5. An illustration of the setup is provided in Fig.3.6.

Before the experiment, 2 mm thick aluminum plates were cut in strips of 200 mm in length and 20 mm in width. After the tabs were roughened with sandpaper and thoroughly cleaned with acetone, the tabs were glued to both sides of the CFRP strip at the loaded end using high strength and fast-curing epoxy. These tabs were used to facilitate load introduction into the specimen without producing premature failure due to an undesired failure mode such as brooming or crushing of the CFRP between the grips of the testing machine [103].

Figure 3.5: Test setup of the quasi-static DPT experimental campaign.

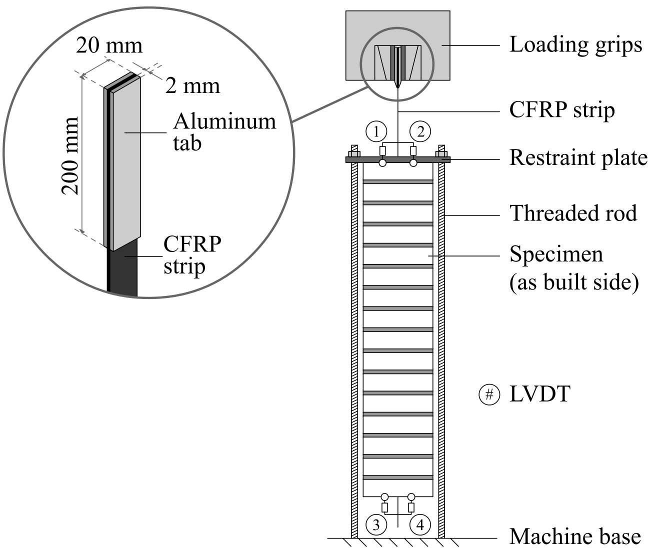

Figure 3.6: Schematic overview test setup quasi-static pull-out tests.

The process continued by carefully positioning the prism under the loading grips of the testing equipment, with the specimen resting on two support blocks. Hard cardboard was put on the top of the prism to prevent stress concentrations due to the non-smooth surface of the brick. A steel restraint plate was placed on top of the prism at the loaded end, as shown in Fig.3.7. To prevent undesirable wedge type failure modes, the plate was 25 mm thick and provided full bearing against the specimen, with the exception of three small openings: one for the CFRP strip and two for LVDTs. The specimen was then lifted up via the aluminum grip plates. This procedure made it possible for the prism to settle into a balanced condition and thus minimize the eccentricity caused by possible imperfect installation of the CFRP strips. Using M12 threaded steel rods, the steel restraint plate was bolted tight to the base of the installation until a pre-tension force of 1.6 kN in the CFRP strip was monitored. The weight of the specimen (~0.36 kN) was neglected.

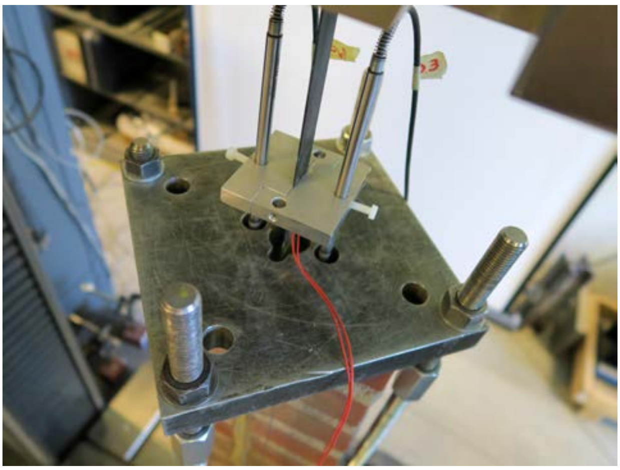

Figure 3.7: Restraint plate and loaded-end instrumentation.

Prior to the load application process, four LVDT sensors were installed. The upper two 20 mm range sensors measured the loaded-end slip (sensors 1 and 2 in Fig. 3.6) and the bottom two 20 mm range sensors measured the free-end slip (sensors 3 and 4 in Fig. 3.6) . The mean of the LVDT pairs was used to establish the corresponding slip. Prior to the analysis, the loaded-end slip was corrected for the elongation of 70 mm of CFRP strip outside the specimen. The 70 mm was the distance between the masonry and the clamp on the CFRP strip which was used to mount the LVDT pair measuring the loaded end slip. After resetting the sensors, the experiment was started with the pre-determined pull-out speed of 0.5 mm/min. The data was logged with a frequency of 2 Hz.

3.2.3 Processing the strain-gauge readings

Based on the active strain gauges, a second-order polynomial was constructed for the strain distribution over the entire embedded length of the CFRP strip at each instant of measurement, using the boundary condition of zero strain in the CFRP strip at the free end $\epsilon_0 = 0$. This polynomial is presented in Eq. 3.9. Using the polynomial for the CFRP strain, the bond, slip and pull-out load were determined using the partial-interaction model presented in 3.1.

$$\epsilon_{p,qp,x} = p_1 x^2 + p_2 x + p_3; \tag{3.9}$$

The coefficients of the polynomial are determined using least-squares fitting on the measured strain data. The process of generating the polynomials using the strain data is demonstrated in the paragraph *Local bond-slip behaviour* of subsection 3.2.4.

3.2.4 Results and discussion

The test results are summarized in Table 3.2. A generalized representation of the force-slip behaviour is shown in Fig. 3.8, along with five derived parameters: the initial stiffness (k_{ini}), pull-out strength (P_{max}), the corresponding slip at the loaded end ($\delta_{L,max}$), the pull-out force at the end of the test (F_{end}), and the corresponding slip at the loaded end at the end of the test ($\delta_{L,end}$). The initial loaded-end slip rate of the CFRP strip ($\dot{\delta}_{L,ini}$), the derived Young's modulus of the CFRP strip (E_p), the governing failure mechanism and the damage to the masonry substrate are also provided in Table 3.2. All mentioned parameters will be covered in the following sections.

Table 3.2: Overview results quasi-static DPT experimental campaign.

	$\dot{\delta}_{L,ini}$ mm/s	E_p kN/mm²	k_{ini} kN/mm	P_{max} kN	$\delta_{L,max}$ mm	F_{end} kN	$\delta_{L,end}$ mm	Failure mode*	Damage to masonry
Std-U-10	0.24	196	13.0	60.2	11.7	17.5	21.9	IF/CF	Yes
Std-U-10-SG	0.25	200	10.9	56.0	9.9	15.6	30.1	IF/CF	No
Std-U-15	0.27	196	10.1	49.0	7.5	13.8	14.3	IF/CF	No
Std-U-15-SG	0.28	194	10.2	45.4	7.9	14.9	10.9	IF/CF	No
Mod-U-10	0.32	191	8.5	28.8	5.4	11.7	10.1	IF/CF	No
Mod-U-10-SG	0.28	191	9.1	27.6	5.3	15.8	8.2	IF/CF	No
Mod-U-15	0.29	193	8.9	30.3	5.9	15.2	9.5	IF/CF	No
Mod-U-15-SG	0.26	193	10.3	31.3	5.8	13.7	10.9	IF/CF	No
Std-RP-10	0.22	199	13.6	66.7	11.3	18.9	32.4	IF/CF	No
Std-RP-10-SG	0.24	198	14.8	64.5	7.6	15.1	40.2	IF/CF	No
Std-SB-10	0.25	197	12.2	51.6	5.3	5.4	46.0	IF/CF	No
Std-SB-10-SG	0.23	198	15.2	62.3	9.4	17.8	20.6	IFS	No

* IF = Interfacial failure CFRP/adhesive; CF = Cohesive failure;
* IFS = Interfacial failure sand-layer/adhesive

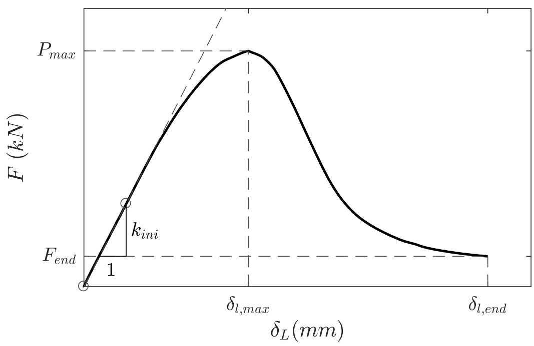

Figure 3.8: Global force - (loaded-end) slip behaviour

Failure mechanisms and damage to masonry

For all the specimens of the quasi-static pull-out experimental campaign, a combined CFRP/adhesive interface failure and cohesive failure of the adhesive occurred. Fig. 3.9 shows the typical detachment of the CFRP strips from the adhesive as was observed during this experimental campaign.

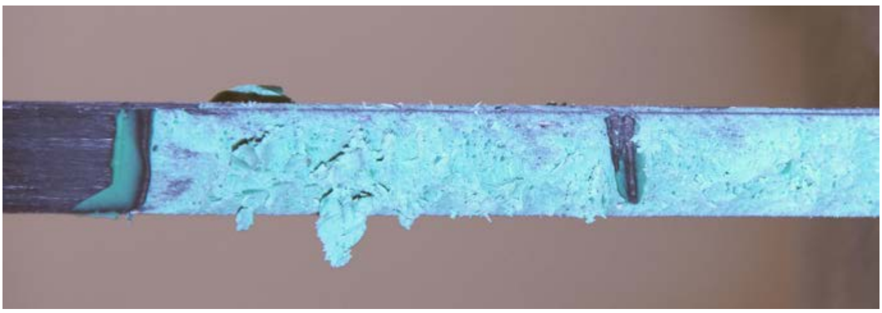

Figure 3.9: Close-up of an embedded CFRP strip after testing, showing the predominant cohesive failure of specimens in the quasi-static pull-out experimental campaign.

Despite a groove depth of 65 mm for all the specimens, premature brick splitting was not observed. Only specimen *Std-U-10* developed some hairline cracks during the post-peak process over the length of the specimen near the groove (Fig. 3.10). These cracks started developing after a 30% decline from the peak pull-out force, at a loaded end slip of 15 mm. For the remaining specimens no hairline crack development was observed. This observation was contradictory to the findings of *Dizhur* [13], where pre-mature brick splitting was observed during the direct pull tests for specimens with a groove depth of only 30 mm with the conventional stiff adhesive.

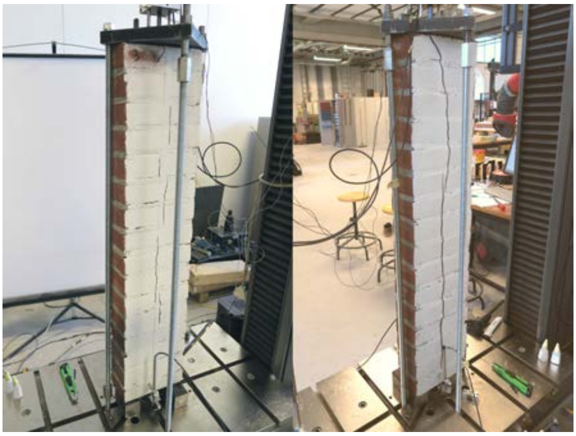

Figure 3.10: Marked hairline cracks of the front (left) and back side (right) of specimen Std-U-10, formed in the post-peak loading phase.

Due to gripping problems, specimen *Std-SB-10* slipped from the grips during the experiment at the aluminum plate and CFRP strip interface. As the embedded region near the loaded end had most likely entered the post-peak region of the local bond-slip behaviour, the specimen was not tested again. For specimens *Std-SB-10-(SG)* the detachment was observed at the sand-layer/adhesive interface.

Global force-slip behaviour

The initial stiffness (k_{ini}) was determined as the secant modulus at 35% of the pull-out strength (P_{max}). The force F_{end} represents the (residual) force at the end of the test, which was marked as the final moment where all LVDTs measuring the slip were in range. The corresponding slips at P_{max} and F_{end} are denoted by $\delta_{L,max}$ and $\delta_{L,end}$ respectively. The global force-slip diagrams for the tested specimens, taking into account both the free end (dashed lines) and the loaded end (solid lines), are shown Fig.3.11. It should be noted that for clarity the loaded-end slip is presented with an initial offset of 10 mm.

Based on the load slip diagrams, the standard ahdesive (higher tensile strength and Young's modulus) showed both a significantly higher displacement and pull-out capacity when compared to the modified adhesive. Additionally, a significant improvement of the pull-out capacity was realized when decreasing the groove width from 15 to 10 mm for standard adhesive. This difference was not observed for the modified adhesive. Additional practical advantages of the smaller groove of 10 mm width are increased time-efficiency during installation and 33% less material usage compared to the wider groove width of 15 mm.

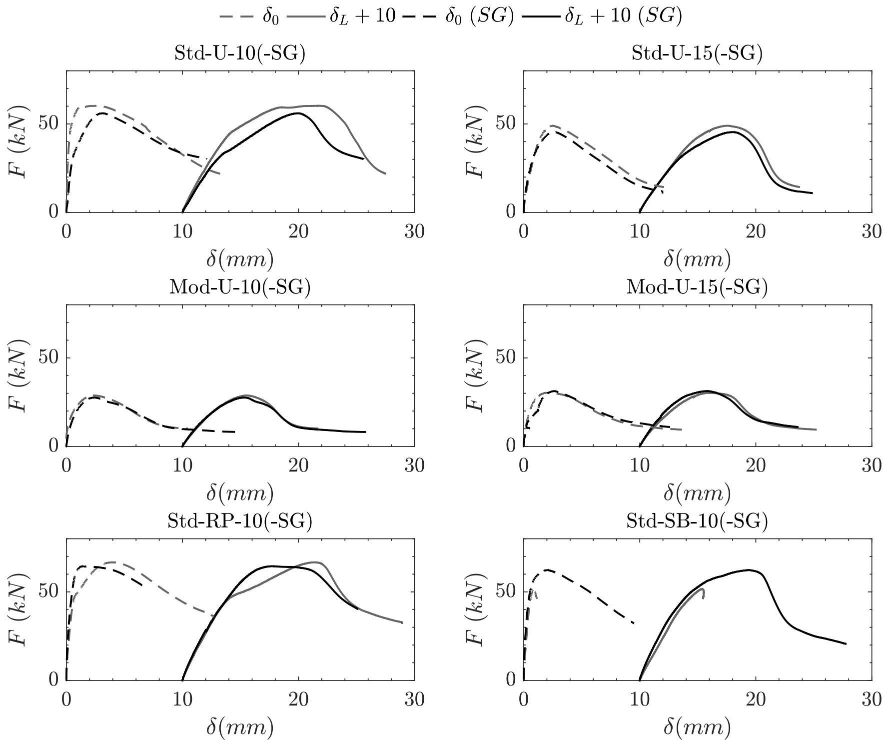

Figure 3.11: Global force - (loaded-end) slip behaviour for the specimens in the quasi-static DPT experimental campaign.

Comparing the load-slip diagrams of the specimens with additional surface treatment with the load slip diagram of specimen *A-S10(-SG)*, an increase in pull-out capacity of >10% was found. This finding indicated that both surface treatment methods provided a higher strength in terms of pull-out capacity to the smooth CFRP strip surface.

Local bond-slip behaviour

The process of obtaining the local bond-slip behaviour using the embedded strain gauge readings is demonstrated using specimes *STD-U-10-SG*. Based on the active strain gauges and the boundary condition at the free end ($\epsilon_{p,0}$=0), a quadratic polynomial was constructed for the strain value over the entire embedded length for each instant of measurement (Eq. 3.9). These polynomials for different pull-out loads are shown in Fig.3.12 for both the pre-peak and post-peak phase. The determined polynomial was rejected if the number of active and embedded strain gauges reduced to two.

The obtained local bond-slip relations for all the specimens with embedded strain gauges are provided in Fig.3.13. In this figure the bold black lines, the thin grey lines and the bold grey lines represent the obtained local-bond slip behaviour at the loaded end, the position of the embedded strain gauges, and the free end respectively. One reoccurring phenomena for all tested specimens was the difference between the the obtained loaded-end bond-slip relation and free-end bond-slip relation, the latter relation generally resulting in stiffer and stronger bonds. This deviation was linked to an error in the loading protocol and test setup, as explained in section 3.3.3. Due to the limited number of tested specimens per configuration in the quasi-static DPT experimental campaign, no general local bond-slip relation was determined for modelling purposes.

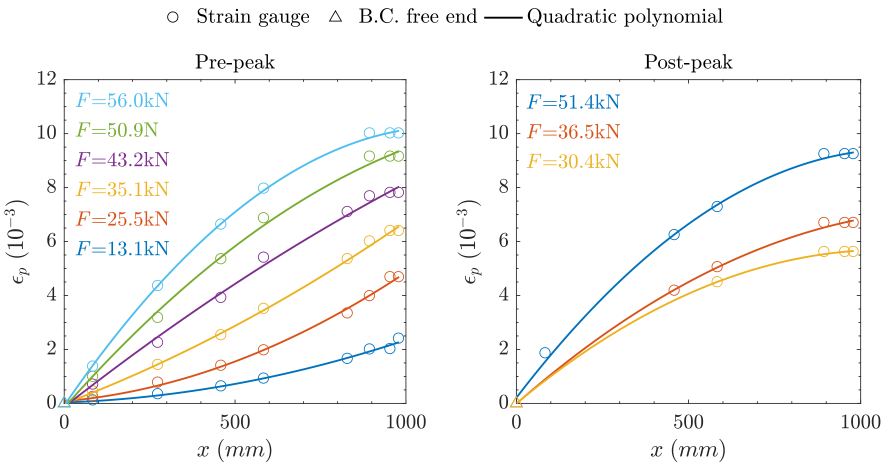

Figure 3.12: Obtained quadratic polynomials of the strain distribution along the embedded length, using the strain gauge readings of *Std-U-10-SG*.

The validity of the obtained bond-slip relations and the partial interaction model was checked by comparing the pull-out load and loaded end slip relationship determined using the obtained strain distributions and procedure described in section 3.1 (bold black line, Fig. 3.14), with the measured pull-out load versus loaded end slip relationships (bold grey line, Fig. 3.14). With the exception of specimen *Mod-U-10-SG*, the partial interaction model provided a good approximation of the experimentally obtained pull-out load and loaded end slip relation.The relatively high error for specimen *Mod-U-10-SG* was most likely caused by malfunctioning strain gauges, as the obtained local bond-slip relations for specimen *Mod-U-10-SG* were limited in range when compared to the other specimens in the quasi-static DPT experimental campaign, as provided in Fig.3.13. Leaving out the deformation of the masonry in the partial interaction model ($\Delta_{mas} = 0$) did not significantly affect the fit of the model with the experiments, as shown with the dashed black lines in Fig. 3.14.

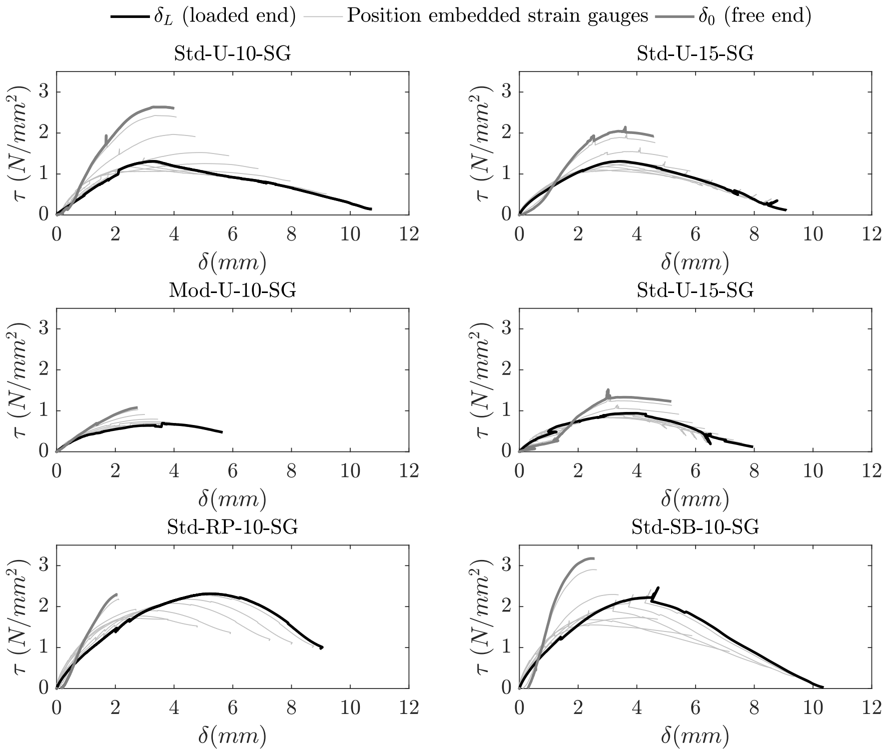

Figure 3.13: Local bond-slip behaviour obtained for the specimens with embedded strain gauges in the quasi-static DPT experimental campaign.

3.3 Quasi-dynamic pull-out experiments

The experimental campaign in the previous section stimulated the need for further research on the governing pull-out mechanics deep-mounted CFRP strips bonded with a flexible adhesive to clay brick masonry. A follow-up experimental campaign was conducted, consisting of 14 direct pull-out tests on masonry prisms with an FDM CFRP strip. In order to investigate the influence of the embedded length of the FRP strip on the pull-out strength and the initial stiffness, four different specimen lengths were tested. To utilize the strain-dependent properties of the system, the vast majority of the specimens were tested under a high loading speed, generally reaching the pull-out strength within 10 seconds. The effect of loading speed on the bond strength and the occurring failure mechanism is also studied. Moreover, an analytical model is elaborated to describe the force-slip behaviour of the retrofit system. Finally, the test results are compared to previous tests on masonry specimens retrofitted with NSM FRP strips embedded in stiff epoxy.

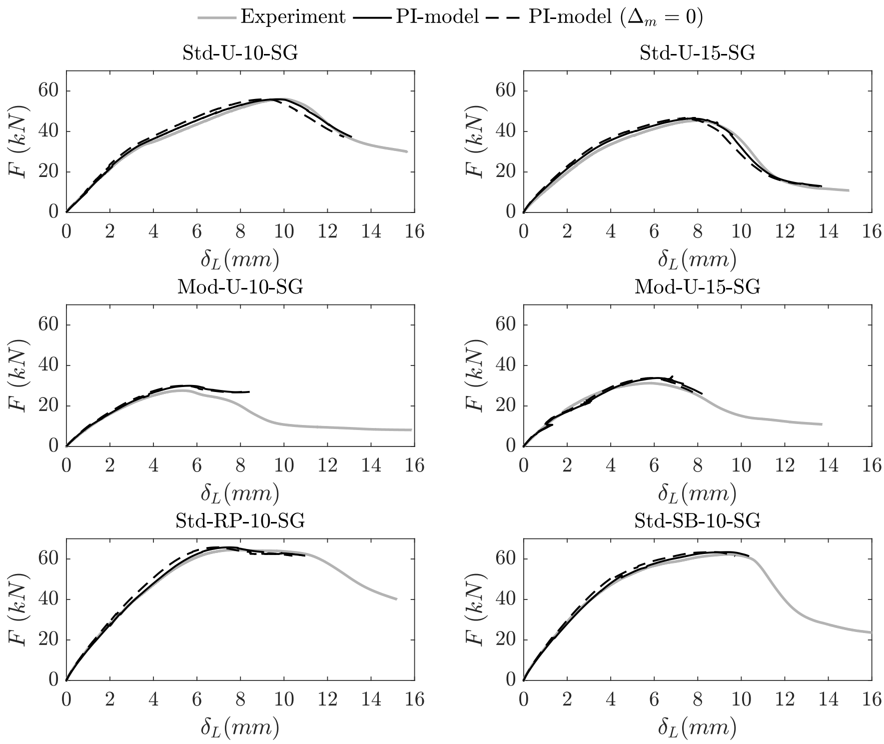

Figure 3.14: Comparison of the pull-out load versus loaded end slip diagram following from the partial-interaction model (bold black line), with the measured pull-out load versus loaded end slip relations (bold grey line).

3.3.1 Building the specimens

Again the prisms were constructed against a vertical sideboard to ensure minimum vertical deviation and were left to cure for 28 days in an unheated environment. The masonry prisms consisted of 6, 9, 12 or 16 bond stacked bricks in height (n_b) and had typical mortar joint thicknesses of 13 mm. Per height three specimens were made except for the specimen with (n_b)=16, for which 5 specimens were made in total. Each prism was denoted with the following notation:

[*PO* - n_b - $v_{machine}$ - *prism number in group*]

For example, PO-6-100-2 denotes the second prism in the group of 6 stacked bricks that was tested with a machine displacement speed ($v_{machine}$) of 100 mm/min.

One CFRP strip was installed in the centre of each masonry prism following the installation procedure mentioned in sections 1.4 and 3.2. The groove had a width of 10 mm, and was placed in the centre of the prisms. Due to a communication error the strips were not cleaned with acetone as was specified by the supplier, but were only wiped with a cloth. Strain gauges (type PFL-10-11, foil strain gauges having polyester resin backing) were attached to alternating sides (to minimize asymmetry effects) of the strip with a constant inter distance of approximately 275 mm for the imbedded strain gauges *(SG-1 – SG-5)*, starting from the center of the second brick from the loaded end. The strain gauges that were not imbedded *(SG-0)* were placed on the loaded end of the CFRP strip, with a distance of 30 mm from the masonry. The embedded strain gauges were covered with wax to reduce the influence of the adhesive on the measurements. A schematic overview of the specimens and the locations of all strain gauges are provided in Fig. 3.15.

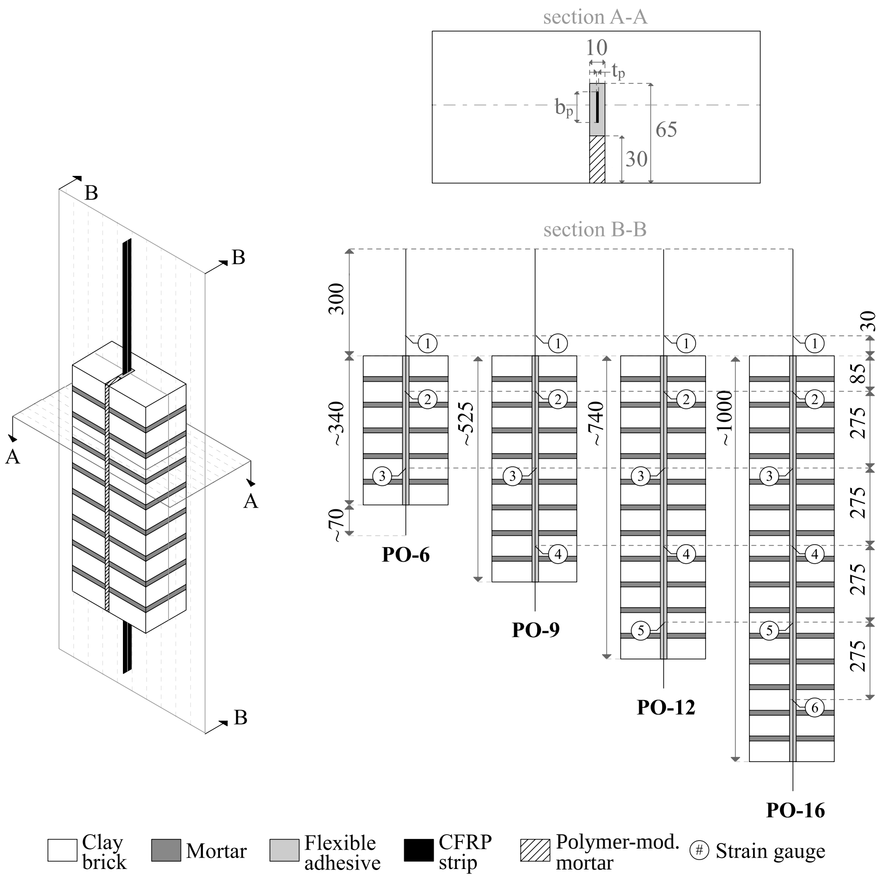

Figure 3.15: Schematic overview specimens quasi-dynamic pull-out campaign.

3.3.2 Test setup and procedure

The test setup and positioning procedure for this experimental campaign was similar to the setup and procedure covered in section 3.2.2. An illustration of the updated setup is provided in Fig.3.6.

Before the experiment, aluminum plates of 110 mm in length, 20 mm in width and 2 mm in thickness were tapered at an angle of 12 degrees, following the guidelines for selecting suitable tabbing configurations for composite material test specimens provided by *Adams & Adams* [103]. The tabbing guide was followed in order to prevent detachment of the aluminum plates from the CFRP strip during the loading process. After the tabs were roughened with sandpaper and thoroughly cleaned with acetone, the tabs were glued to both sides of the CFRP strip at the loaded end using high strength and fast-curing epoxy.

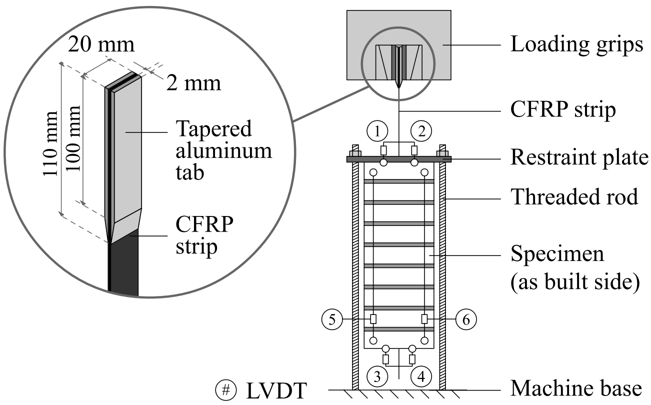

Figure 3.16: Schematic overview test setup quasi-dynamic pull-out tests.

Prior to the load application process, eight LVDT sensors were installed (6 for the PO-6 and PO-9 specimens). The upper two 20 mm range sensors measured the loaded-end slip (sensors 1 and 2 in Fig. 3.16) and the bottom two 20 mm range sensors measured the free-end slip (sensors 3 and 4 in Fig. 3.16). The mean of the LVDT pairs was used to establish the corresponding slip. Prior to the analysis the loaded-end slip was corrected for the elongation of 70 mm of CFRP strip outside the specimen, 70 mm being the distance between the top surface of the masonry and the clamp on the CFRP strip which was used to mount the two LVDTs measuring the loaded end slip. In order to measure the axial deformation within the masonry, additional short range LVDT sensors were applied: four to the PO-16-5, PO-16-25, PO-16-100 and PO-12-100 specimens, and two to the PO-9-100 and PO-6-100 specimens (sensors 5 and 6 in Fig. 3.16).

Similar to the quasi-static pull-out experimental setup, the steel restraint plate was bolted tight to the base of the installation using M12 threaded steel rods until a pre-tension force of 1.6 kN in the CFRP strip was monitored. The weight of the specimens (up to 0.36 kN) was neglected. After resetting the sensors, the experiment was started with the pre-determined pull-out speed. Due to errors, the data from specimens *PO-16-100-5* and *PO-16-100-25* was logged with only 2.5 Hz, giving limited data-points. For the remaining part of the experiments the logging frequency was increased to 20 Hz.

3.3.3 Results and discussion

The test results are summarized in Table 3.3. The generalized representation of the force-slip behaviour along with relevant parameters was presented in Fig. 3.8. Next to the initial loaded-end slip rate of the CFRP strip ($\dot{\delta}_{L,ini}$), the Young's modulus of the CFRP strip (E_p), the governing failure mechanism and the damage to the masonry substrate, the maximum deformation of the masonry over the length (Δ_{mas}) is also included in Table 3.3. The important parameters will be covered in the following sections.

Table 3.3: Overview results for quasi-dynamic pull-out experimental campaign

Specimen	L mm	$\dot{\delta}_{ini}$ mm/s	E_p $\frac{kN}{mm^2}$	k_{ini} $\frac{kN}{mm}$	P_{max} kN	$\delta_{L,max}$ mm	F_{end} kN	$\delta_{L,end}$ mm	Δ_{mas} mm	Failure mode*	Dam. mas.**
PO-6-100-1	340	0.92	197	10.4	38.7	5.9	6.9	18.3	0.05	IF/CF	SP
PO-6-100-2	342	1.12	201	8.8	33.1	4.3	6.4	18.6	0.05	IF/CF	SP
PO-6-100-3	347	1.03	194	10.0	33.5	4.1	5.7	18.9	0.08	IF/CF	SP
PO-9-100-1	524	1.09	200	9.1	42.6	6.0	8.2	18.1	0.28	IF/CF	SP
PO-9-100-2	525	1.01	204	11.0	53.3	6.9	6.6	18.6	0.12	IF/CF	SP
PO-9-100-3	529	1.03	200	11.2	39.5	5.5	8.7	17.0	0.07	IF/CF	SP
PO-12-100-1	729	1.07	204	11.8	63.6	7.4	8.2	18.1	0.15	IF/CF	SP
PO-12-100-2	735	1.04	203	10.9	54.3	7.6	19.4	13.3	0.23	IF/CF	SP
PO-12-100-3	732	1.10	202	10.4	52.8	6.1	6.5	16.9	0.17	IF/CF	SP
PO-16-5	1001	0.04	199	13.3	68.0	8.6	13.7	18.2	0.66	IF/CF	SP
PO-16-25	998	0.22	204	11.5	81.0	9.7	81.0	9.7	0.44	CR	HC
PO-16-100-1	996	0.93	203	14.6	87.8	7.9	87.8	7.9	0.19	CR	HC
PO-16-100-2	995	1.04	220	12.2	83.2	8.6	83.2	8.6	0.25	CR	HC
PO-16-100-3	992	1.00	214	13.8	80.1	12.0	22.3	19.0	0.46	IF/CF	SP

* IF = Interfacial failure CFRP/adhesive; CF = Cohesive failure; CR = CFRP rupture
** SP = Masonry splitting over entire length; HC = Hairline cracks over limited length

Failure mechanisms and damage to masonry

In all specimens, except *PO-16-25*, *PO-16-100-1* and *PO-16-100-2*, splitting of the masonry prism was observed. A typical crack is shown in Fig. 3.17. The general observation was that the crack initiation occurred near the loaded end when the pull-out strength was reached, and propagated over the entire bonded length during the post-peak phase. Despite splitting, specimens did not fall apart due to small regions of intact adhesion. The splitting was an unavoidable aspect of the selected test method. The pull-out experiments were conducted in the absence of lateral confinement pressure, which may exist in the practical situations.

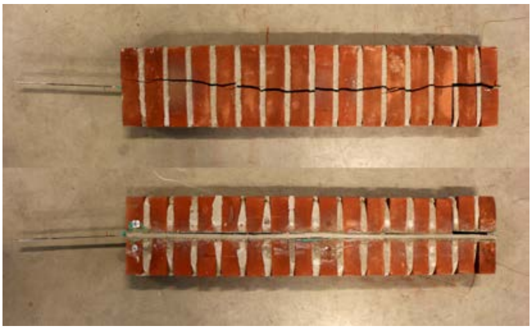

Figure 3.17: Post-experiment photos of the as-built side (top) and treated side (bottom) of specimen *PO-16-100-6*.

Based on observation of the loaded end, the predominant failure mechanism was determined as cohesive failure in the adhesive. After breaking the specimens in two using a chisel and a hammer, the previously observed cohesive failure mechanism was confirmed with the exposed embedded CFRP strip. Traces of interfacial failure were also found. A typical photo of an embedded CFRP strip after breaking the specimen is shown in Fig. 3.18.

Figure 3.18: Close-up of specimen *PO-12-100-2* after breaking the specimen apart post-experiment, showing the predominant cohesive failure.

For specimens *PO-16-25*, *PO-16-100-1* and *PO-16-100-2*, which failed due to CFRP rupture, no splitting of the masonry was observed. Fig. 3.19 (top) shows the undamaged treated side of the considered specimens. On the as-built side, hairline cracks were observed along the 6 bricks at the loaded end (bottom image Fig. 3.19). Local crushing failure at the loaded end was also observed, as shown in Fig. 3.20.

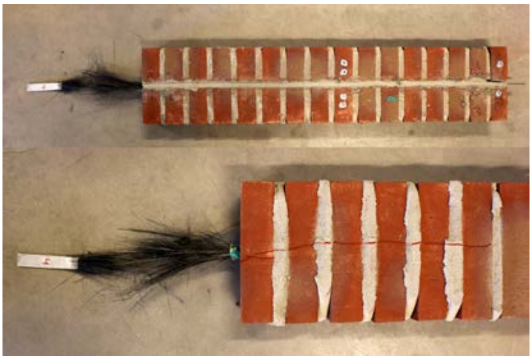

Figure 3.19: Post-experiment photos of the treated side (top) and cracked (top 6 bricks) as-built side (bottom) of specimen *PO-16-100-4*.

Figure 3.20: Post-experiment close-up of the loaded end of specimen *PO-16-100-4*, showing the governing failure mechanism: CFRP rupture.

Global force-slip behaviour

The global force-slip diagrams for the tested specimens, taking into account both the free end (dashed lines) and the loaded end (solid lines), are shown in Fig. 3.21. It should be noted that for clarity the loaded-end slip is presented with an initial offset of 10 mm. CFRP rupture in Fig. 3.21 is marked with an *x*. An overarching observation is that the global force-slip relations remain consistent within the same specimen group. The highest deviation is observed in the specimen pull-out strength, which can be attributed to the imperfect placement of the CFRP strips. Looking at the initial stiffness, an increasing trend is observed with longer embedment lengths, as shown in Fig. 3.22a. The initial stiffness ranged from 8.8 kN/mm *(PO-6-100-1)* to 14.6 kN/mm *(PO-16-100-1)*. A linear correlation ($R^2 = 0.70$) was found between the initial stiffness and the embedment length.

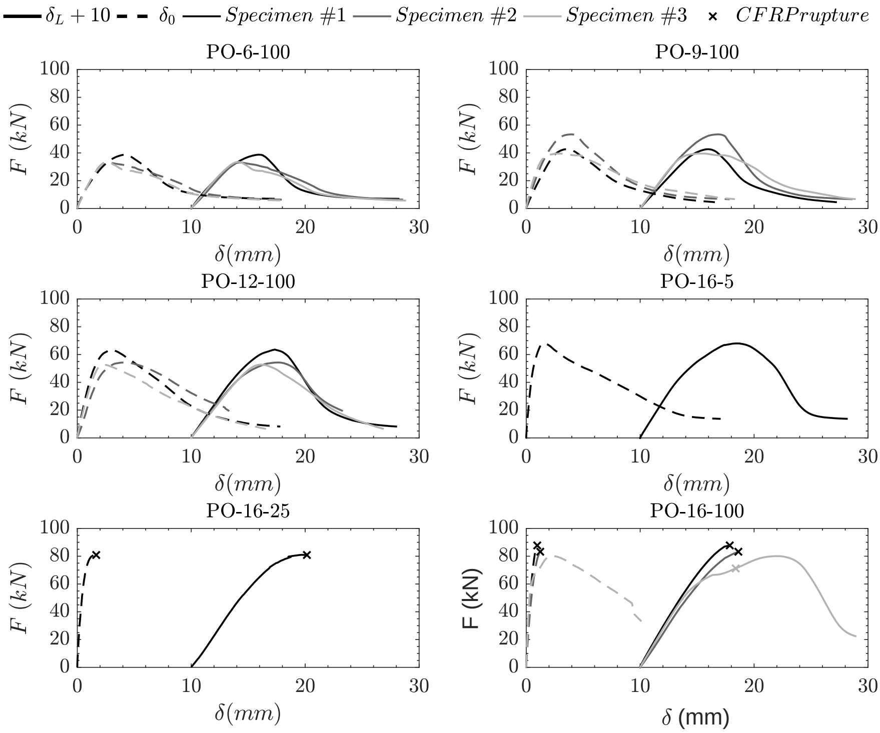

Figure 3.21: Global force - (loaded-end) slip behaviour for the specimens in the quasi-dynamic pull-out campaign.

A very strong linear correlation was found between pull-out strength and the embedment length range of the performed tests, as shown in Fig. 3.22b. This linear dependency was also observed for similar test configurations with short bonded lengths [54, 104]. The linear relation between pull-out strength and the embedment length within the current experimental campaign was found to be applicable until the load capacity became sufficiently large that rupture of the CFRP started to govern. An embedment length of 1.0 m was sufficient to initiate CFRP rupture ($T_P = 80.5\ kN$) governed failure mechanism instead of cohesive failure. It should be noted that in the context of partial-interaction mechanics, a linear dependency between P_{max} and L occurs only for short bond lengths while the shear stress distribution along the bonded length remains near-uniform.

Looking at the effect of the initial loaded-end slip rate ($\dot{\delta}_{L,ini}$) on the pull-out strength, a strong logarithmic correlation was found, as shown in Fig. 3.22c. The initial loaded-end slip rate was determined as the mean loaded-end slip rate from the start of the pull-out experiment up to and including the moment where 35% of the pull-out strength was reached. The pull-out strength corresponding to $\dot{\delta}_{L,ini} \approx 0.004$ mm/s ($v_{machine} = 0.5$ mm/min) was taken from the quasi-static experimental campaign as was presented in section 3.2 (specimen *Std-U-10-SG*). It was observed that while keeping the embedment length constant at ≈ 1.0 m, increasing the machine speed from 0.5 mm/min to 100 mm/min ($\dot{\delta}_{L,ini} \approx 1.0$ mm/s) led to a 67% increase in failure load, with the governing failure mechanism shifting from cohesive failure to CFRP rupture. Looking at the *PO-16-5*, *PO-16-25* and *PO-16-100* specimens, the pull-out speed had no significant effect on the initial stiffness.

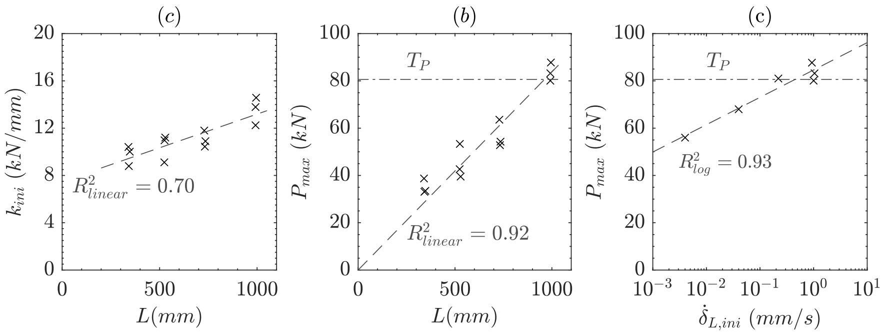

Figure 3.22: Obtained linear and logarithmic relations in the quasi-dynamic DPT experimental campaign: The initial stiffness k_{ini} as a function of the embedded length L for specimens tested at $v_{machine} = 100 mm/min$ (a); The pull-out strength P_{max} as a function of the embedded length L for specimens tested at $v_{machine} = 100 mm/min$ (b); The pull-out strength P_{max} as a function of the initial loaded-end slip rate ($\dot{\delta}_{L,ini}$ for specimens with an embedment length of 1m (c).

Local bond-slip behaviour

The process of obtaining the local bond-slip behaviour using the embedded strain gauge readings is demonstrated using specimen PO-12-100-1. Based on the active strain gauges and the boundary condition at the free end ($\epsilon_{p,0}$=0), a second-order polynomial was constructed for the strain value over the entire embedded length for each instant of measurement. These polynomials for different pull-out loads are shown in Fig. 3.23 for the pre-peak and post-peak phase.

The determined polynomial was rejected if either the number of active and embedded strain gauges reduced to one, or the polynomial showed an upward slope at the free end. The latter rejection case is shown with a bold black line in Fig. 3.23. Using the PI model the local bonds-slip relations were determined from the constructed polynomials for the loaded end, the position of the embedded strain gauges and the free end. An overview of the determined local bond-slip relations for the PO-100 specimens is provided in Fig. 3.24. The local bond-slip correlation at the loaded end and the free end are provided with solid black and grey lines respectively. For specimens *PO-6-100*, *PO-9-100* and *PO-12-100*, a limited difference was found between the

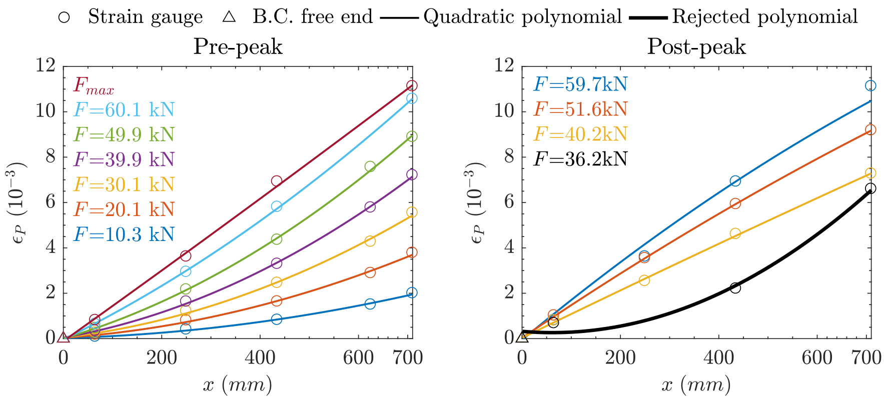

Figure 3.23: Obtained (rejected) quadratic polynomials of the strain distribution along the embedded length, using the strain gauge readings for specimen *PO-100-12-1*: pre-peak and post-peak.

loaded end and the free end in terms of local-bond slip relation. The average bond strength was 2.45 N/mm². Looking at the *PO-16-100* specimens, it was observed that the free-end bond-slip behaviour showed a steep increase. This phenomenon of a stiffer local bond-slip response was also observed with the *PO-16-0.5* (=*Std-U-10-SG* from the quasi-static experimental campaign), *PO-16-5* and *PO-16-25* specimens, as shown in Fig. 3.25. Due to damaged sensors and/or failure of the specimen, the full local bond-slip behaviour near the free end could not be determined.

For specimen *PO-16-0.5* (*Std-U-10-SG*) the steeper increase in local bond-slip behaviour at the free end continued until a significantly higher local bond strength (with respect to the loaded end) was reached. This phenomenon of a stiffer and stronger local bond-slip response can be attributed to the viscous properties of the adhesive and the non-uniform pull-out speed.

Fig. 3.26 provides the maximum shear stress (τ_{max}) and corresponding slip rate at the loaded end ($\dot{\delta}_L$), free end, and embedded strain gauge locations for the *PO-6-100*, *PO-9-100* and *PO-12-100* specimens. For the *PO-6-100-1* and *PO-6-100-3* specimens, the local bond strength seems to remain constant over the embedment length. With the *PO-9-100* and *PO-12-100* specimens, the local bond strength reduces from the loaded end towards the mid-embedment length. This finding agrees with fracture mechanics theory, stating that the propagation of cracks occur at stresses lower than the critical stress required for fracture. However, somewhat unexpectedly, the local bond strength increased from the mid embedment length towards the free end for the *PO-9-100* and *PO-12-100* specimens, as illustrated in Fig. 3.26. This increase is linked to the increase of the corresponding slip rate. Despite the machine displacement rate being constant, the finite stiffness of the machine, the threaded rods (used to connect the restraint plate to the

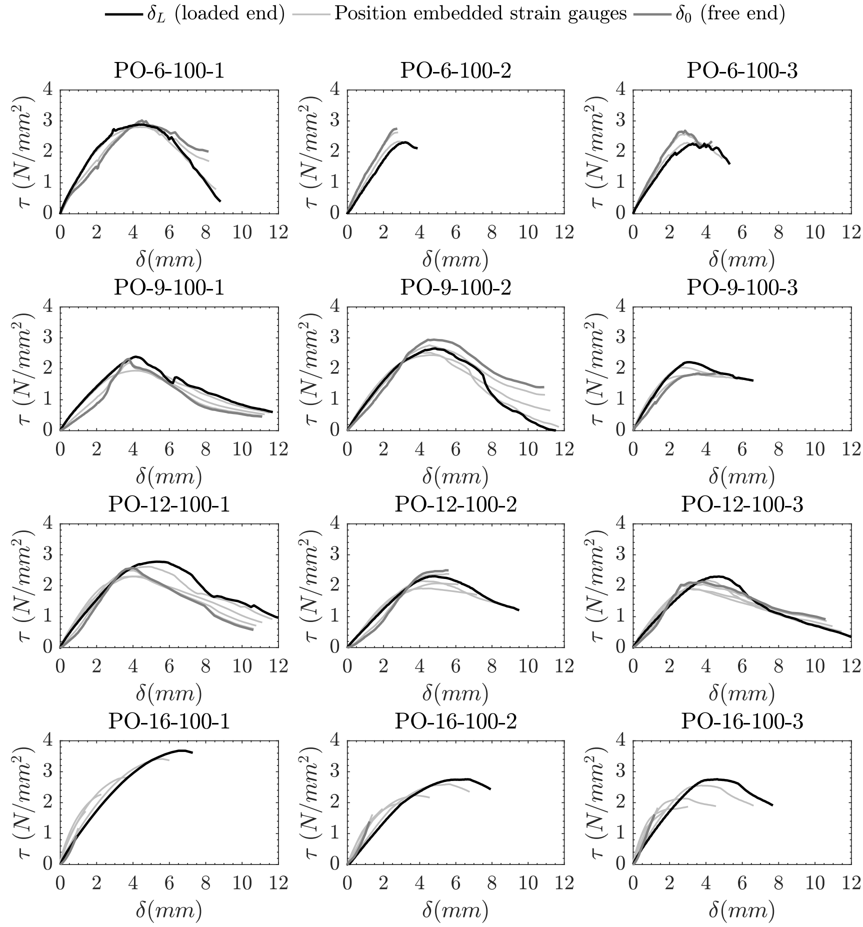

Figure 3.24: Local bond-slip behaviour obtained for the specimens tested with $v_{machine} = 100mm/min$ in the quasi-static pull-out campaign.

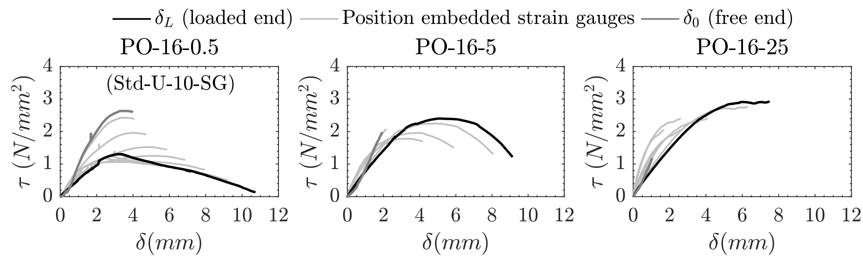

Figure 3.25: Local bond-slip behaviour obtained for the specimen tested with $v_{machine}$=0.5mm/min, 5mm/min and 25mm/min.

base of the machine) and the CFRP strip between the masonry and the grips of the machine disrupted the loaded-end slip rate. The elongation rate of the machine, the threaded rods and the free CFRP strip at the loaded end resulted in a decrease of the actual slip rate at the loaded end. The mean slip-rate at the loaded end was ~70% of the machine displacement speed for all the specimens. This was applicable as long as there was an increase in exerted pull-out force. During the post-peak phase, where the applied pull-out force started to decrease, the relaxation rate of the aforementioned (finite stiffness) components resulted in an increase of the actual slip rates. This increase in local slip rate, being more significant for longer specimens, resulted in higher local bond strength due to the strain-rate dependent properties of the visco-elasto-plastic adhesive.

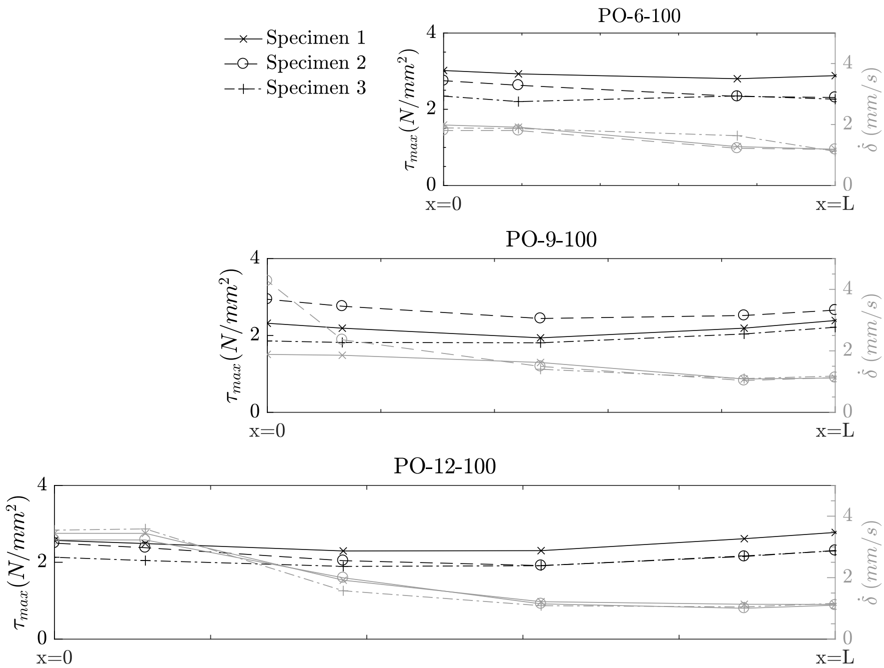

Figure 3.26: Local bond strength (τ_{max}) and corresponding slip rate ($\dot{\delta}$) at the loaded end, free end and strain gauge locations for specimen groups *PO-6-100*, *PO-9-100* and *PO-12-100*.

The contour plots of the local bond development over the embedded length, as a function of the loaded-end slip, is provided in Fig. 3.27, where the load is represented with a solid black curve (secondary y-axis). It should be noted that the full range of the contour plots could not be given due to the limited strain gauge readings. In all cases, the maximum pull-out load was reached in the phase where the maximum local bond stresses shifted from the loaded end *(x=L)* towards the free end *(x=0)*. Specifically, when the local bond-slip ($\tau - \delta$) relation at the loaded end entered the post-peak stage and the local $\tau - \delta$ relation at the free end neared its peak, the specimen reached full strength. It should be noted that this shift of stresses happened rapidly. With increasing bond length, there was a clear distinction between the level of bond stresses near both the loaded end and free-end, and the level of bond stresses at mid-embedment length.

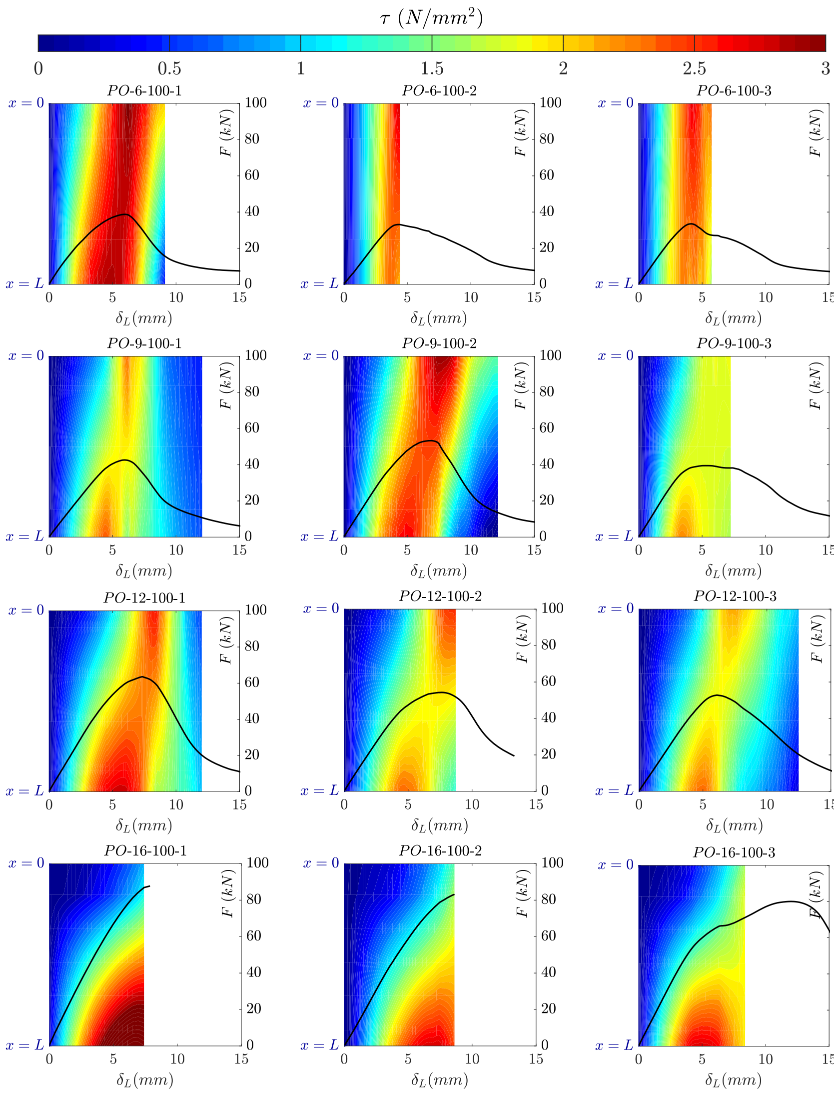

Figure 3.27: Contour plots of the local bond development over the embedded length, as a function of the loaded-end slip for specimens tested at $v_{machine} = 100 mm/min$. Black curves show the pull-out load.

3.4 General bond-slip law

With the obtained local bond-slip correlations as shown in Fig. 3.24 a general local bond-slip relation was determined for modelling purposes. The first step to reach a general local bond-slip correlation is to construct an averaged local bond-slip relation for the PO-6-100, PO-9-100 and PO-12-100 (quasi-dynamic) specimens. The PO-16-100 specimens were not considered due to the incomplete bond-slip relations. The averaged curve is shown with a solid grey line in Fig. 3.28 for specimen PO-6-100-1. This averaging process, based on slip increments of 0.4 mm, continued while three or more local bond-slip relations were present. The end point of the averaged curve is denoted with δ_a and τ_a. The bond energy is determined using Eq. 3.10:

$$G_f = \int_{\delta=0}^{\delta_a} \tau_{averaged}(\delta) d\delta \tag{3.10}$$

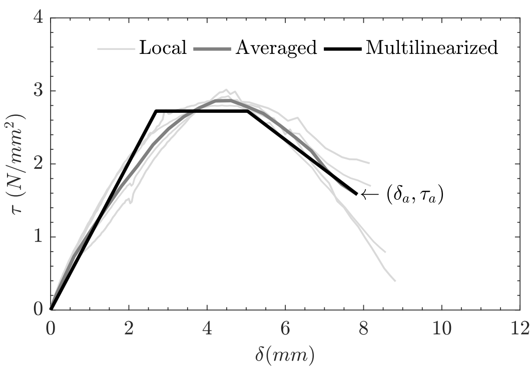

Figure 3.28: Generalization and multi-linearization of the obtained local bond-slip relations of *PO-6-100-1*.

The second step to reach an averaged local bond-slip correlation is to multi-linearize the averaged local bond-slip curve of the considered specimens. The multi-linearized local $\tau-\delta$ behaviour at the CFRP-adhesive interface consists of four zones: *elastic* (I), *damage initiation* (II), *damage development* (III), and *residual* (IV), as shown in Fig. 3.29. This is a modification of the bi-linear frictional rule as reported by Vaculik et al. [105]. The local $\tau-\delta$ relationship at the interface can be expressed with the set of conditional equations as provided in Eq. 3.11, where the slope parameters k_1 and k_2 were determined in accordance with Eq. 3.12 and Eq. 3.13 respectively.

$$\tau_{ml}(\delta) = \begin{cases} k_1\delta & \delta \leq \delta_1, \\ \tau_f & \delta_1 < \delta \leq \delta_2, \\ \tau_f - k_2(\delta - \delta_2) & \delta_2 < \delta \leq \delta_3, \\ \tau_r & \delta > \delta_3, \end{cases} \tag{3.11}$$

$$k_1 = \frac{\tau_f}{\delta_1} \tag{3.12}$$

$$k_2 = \frac{\tau_f - \tau_r}{\delta_3 - \delta_2} \tag{3.13}$$

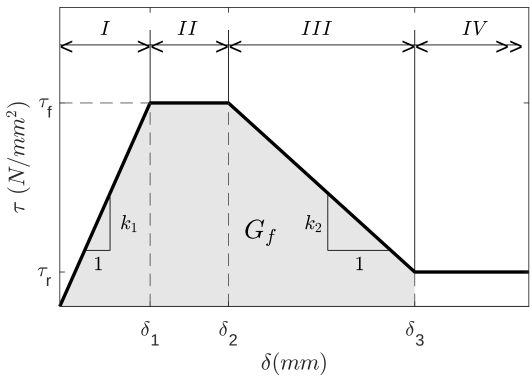

Figure 3.29: Local $\tau - \delta$ relation to represent the bond behaviour along the bond interface (CFRP strip - flexible adhesive).

The value for the damage initiation plateau, τ_f, was determined in accordance with Eq. 3.14.

$$\tau_f = 0.95\tau_{max} \tag{3.14}$$

The initial stiffness is determined as a secant modulus at 35% of the bond strength. Using the initial stiffness and the value for the damage initiation plateau τ_f, the value for δ_1 can be determined using Eq. 3.12. As the bond energy for the multi-linearized and averaged bond-slip relation until slip δ_a are assumed equal, the value for δ_2 can be determined following Eq. 3.15. This way the bond energy is determinative of the final shape of the multi-linearized bond-slip relation.

$$\delta_2 = \frac{2G_f - (\tau_f + \tau_a)\delta_a + \tau_f\delta_1}{\tau_f - \tau_a} \tag{3.15}$$

Using δ_a, τ_a, δ_2, τ_f and the residual bond stress τ_r (estimated at 0.4 N/mm^2 based on the measured forces at the end of the tests), the value for δ_3 can be determined by means of linear extrapolation.

The multi-linearized $\tau - \delta$ relations for the *PO-6-100*, *PO-9-100* and *PO-12-100* specimens are shown in Fig. 3.30. By averaging these, a global-average multi-linear $\tau - \delta$ correlation was determined. It should be noted that the post-peak part of the multi-linearized bond-slip curve could not be determined for specimens *PO-6-100-2* and *PO-6-100-3* due to incomplete data, so these specimens were excluded from the averaging process. The averaged multi-linear $\tau - \delta$ relation was found to be a good representation of all the obtained $\tau - \delta$ relations for the *PO-6-100*, *PO-9-100* and *PO-12-100* specimens, as shown in Fig. 3.31. The parameters defining the averaged multi-linear $\tau - \delta$ relation are provided in Table 3.4. In general, the interfacial fracture energy G_f is defined as the area under the $\tau - \delta$ curve. *Vaculik et al.* [105] considered this integral only up to the slip at debonding (δ_3) as the integral becomes unbounded for $\tau_r > 0$. Using this definition, the interfacial fracture energy was determined as 16.9 Nmm/mm².

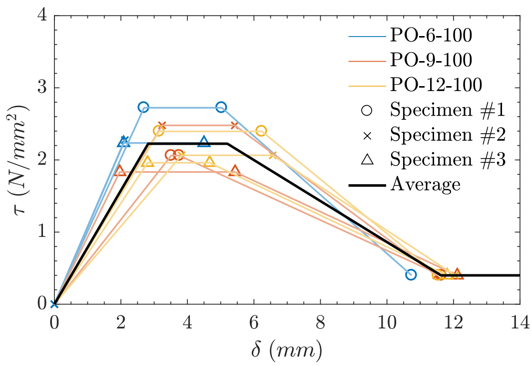

Figure 3.30: Multi-linearized $\tau - \delta$ relations (individual tests and averaged) for the *PO-6-100*, *PO-9-100* and *PO-12-100* specimens.

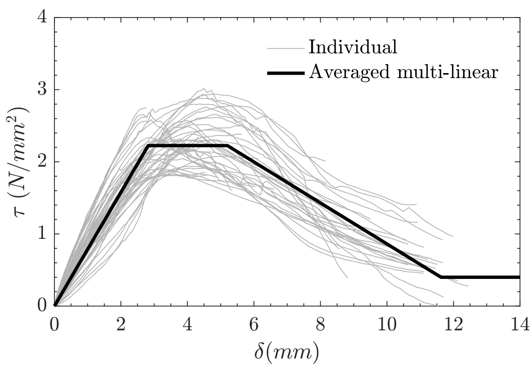

Figure 3.31: Averaged and multi-linearized $\tau - \delta$ relation and all the obtained $\tau - \delta$ relations for the *PO-6-100*, *PO-9-100* and *PO-12-100* specimens.

Table 3.4: Parameters averaged multi-linear local bond-slip behaviour (Fig. 3.29).

Parameter	Value	Unit
τ_f	2.22	N/mm^2
τ_r	0.40	N/mm^2
δ_1	2.82	mm
δ_2	5.20	mm
δ_3	11.62	mm
G_f	16.87	Nmm/mm^2

Using the one-dimensional partial-interaction (PI) model as presented in Section 3.1 and the obtained averaged multi-linear $\tau - \delta$ relation, the pull-out load versus loaded end slip ($F - \delta$ relation was calculated. By rewriting 3.3 into Eq. 3.16, the strain per element, as was illustrated in Fig. 3.2 can be determined with the averaged multi-linear $\tau - \delta$ relation. The free-end slip δ_0 was used as an input for the analysis. The strain in the CFRP strip was zero at the free end ($\epsilon_{p,0} = 0$). The local slip for each element in the PI-model was determined using Eq. 3.17.

$$\epsilon_{p,i} = \epsilon_{p,i-1} + \frac{2\delta x \cdot \tau_{ml}(\delta_{i-1})}{E_p \cdot t_p} \tag{3.16}$$

$$\delta_i = \delta_0 + \frac{1}{2}\sum_{k=1}^{i}(\epsilon_{p,k} + \epsilon_{p,k-1}) \tag{3.17}$$

The F-δ relation was determined for different anchorage lengths, as shown in Fig. 3.32. The end of the elastic (δ_1), damage initiation (δ_2) and damage development (δ_3) zones from the interfacial constitutive law are highlighted with circles, squares and diamonds respectively.

The results following from the proposed model showed good agreement with the experimental outcomes. The only exception is for an anchorage length of 1000 mm, where the model seems to result in a significant steeper decrease in the post-peak region (marked with a light grey area). This difference can be attributed to the non-uniform local slipping speeds and the strain-rate dependent properties of the visco-elasto-plastic adhesive.

The contour plots of both the modelled and experimentally determined local bond development over the embedded length, as a function of the loaded-end slip, is provided in Fig. 3.33. From each specimen group, the specimen with the broadest measured range is selected for the comparison. Comparing the modelled and experimentally determined local bond development over the embedded length, the model provides a good approximation, especially when looking at the shape of the contour plots.

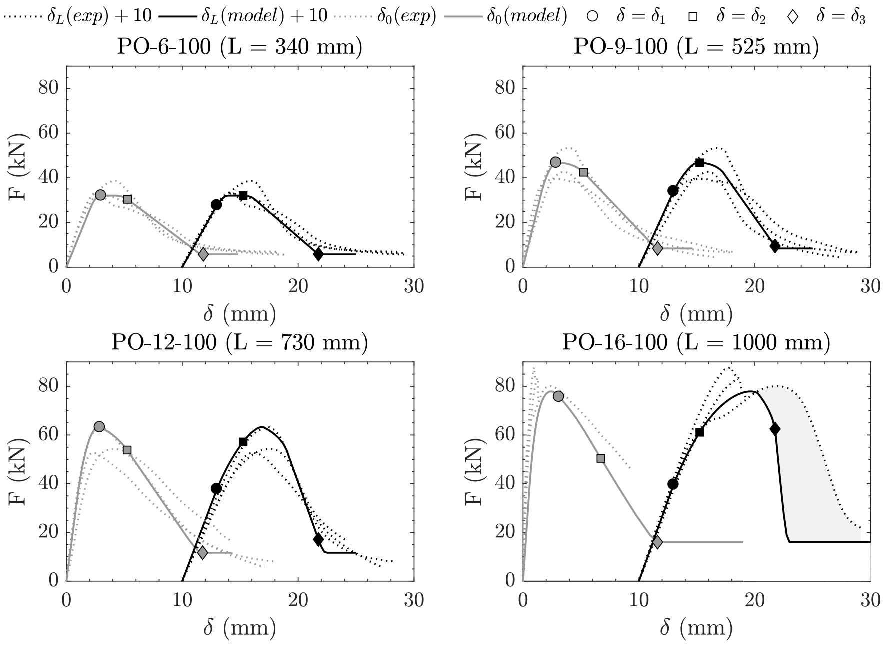

Figure 3.32: Comparison results model with experimental outcomes. For clarity the loaded-end slip is presented with an initial offset of 10mm. The end of the elastic (δ_1), damage initiation (δ_2) and damage development (δ_3) zones from the interfacial constitutive law are highlighted with circles, squares and diamonds respectively.

With the partial-interaction model and the input parameters as provided in Table 3.4, F-δ relations were determined for various anchorage lengths, ranging from 400 mm to 1800 mm in increments of 100 mm, as shown in Fig. 3.34. The shear stress distribution over the bonded length L at the instance of peak pull-out load are shown in Fig. 3.35.

Up to and including an anchorage length of 550 mm, the pull-out strength is reached when the free-end slip is equal to δ_1 (2.82mm). Over this bonded length range, the peak strength coincides with a near-uniform stress distribution where the entire bonded interface is in the damage initiation phase, and each additional 100 mm of bonded length increases the pull-out strength by around 8.9 kN. Increasing the bonded length from 550 to 1300 mm, it can be observed that each additional unit of bonded length results in a less effective increase of the pull-out strength, assuming the tensile strength of the CFRP strip is no limiting factor. The loaded-end slip shifts towards 12mm (damage development zone) whereas the free-end slip shifts towards 1.7 mm (elastic zone) at the instance when the pull-out strength is reached. The plateau of damage initiation shifts from the free end towards the loaded end, covering a bonded length of 550 mm. For bonded lengths of 1300 mm or longer,

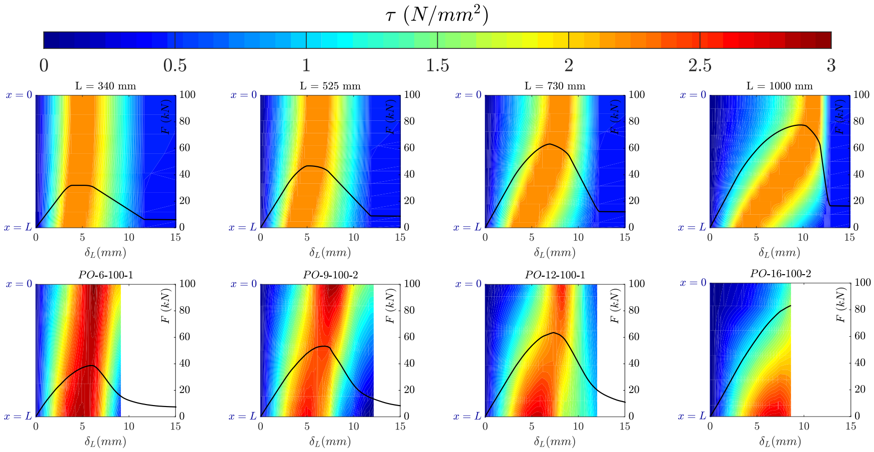

Figure 3.33: Modelled (top row) and experimentally obtained (bottom row) contour plots of the local bond development over the embedded length, as a function of the loaded-end slip. Black curves shows the pull-out load.

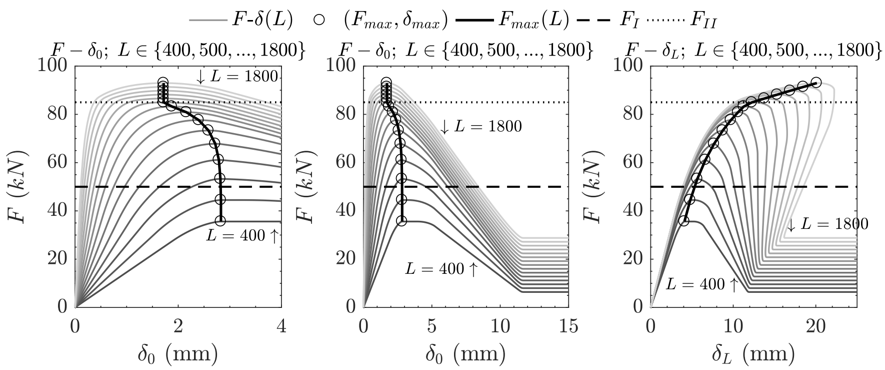

Figure 3.34: F-δ relations for various anchorage lengths.

the pull-out strength is reached when the free-end slip equals 1.7mm. The bonded interface remains in the elastic zone between $x = 0$ (free end) and $x = 120$ mm. Between $x = 1100$ mm and $x = 1300$ mm, the adhesive interface is in the residual zone, where the shear stress is solely caused by friction. Increasing the bonded length above the critical value (1300 mm) has limited effect on the pull-out strength, because any incremental increase is only due to residual stress, so that every 100 mm of bonded length only increases the pull-out strength by an additional 1.6 kN.

The force versus loaded-end slip relation of the flexible adhesive mounted CFRP strip, following from the partial-interaction analysis, is provided in Fig. 3.36 for various anchorage lengths. When the loaded end enters the dam-

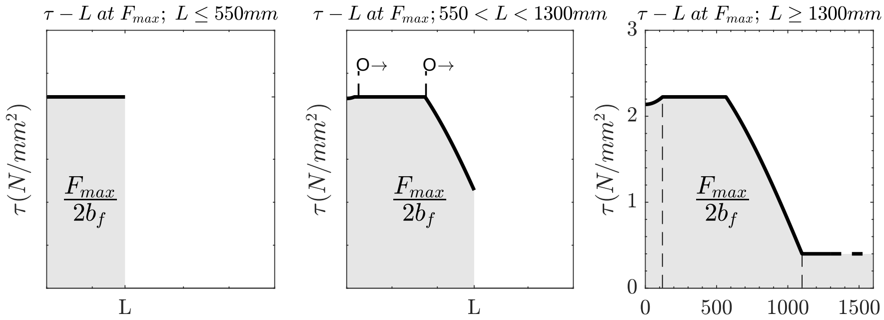

Figure 3.35: Shear stress distribution over the bonded length L at the instance of peak pull-out load.

age development zone ($\delta_L \geq \delta_2$), especially for bonded lengths over 200mm, the load can still increase. This increase becomes more significant for higher bonded lengths. Entering the damage development zone at the loaded end, the shear stresses for the remaining part of the bonded length can further increase the load since the bond law is still either in the linear elastic zone (towards the free end) or the damage initiation zone. For bonded lengths of 500mm or less, the load is either in, or very close to the residual phase. This would mean that at the moment the loaded end region enters the residual zone of the local bond law, the pull-out load will enter the residual phase either instantly or very soon. Considering the tensile limit of the CFRP strip, Fig. 32 shows that for bonded lengths of ≥1250 mm, CFRP rupture (marked with *x*) starts to govern, according to the partial-interaction analysis.

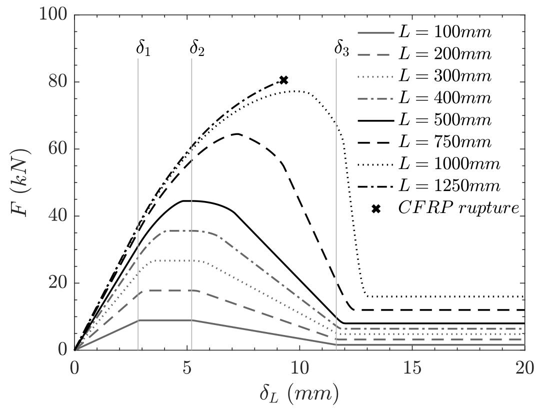

Figure 3.36: Force versus loaded-end slip relation following from the partial-interaction analysis, for various anchorage lengths. CFRP strip rupture is marked with an *x*. The end of the elastic (δ_1), damage initiation (δ_2)and damage development (δ_3) zones from the interfacial constitutive law are highlighted.

The pull-out strength versus the bonded length, predicted using the partial-interaction analysis, is provided in Fig. 3.37. Over the experimentally tested bonded lengths (L = 300 to 1,000 mm), the analysis demonstrates the relationship between P_{max} and L to be almost linear ($R^2 = 0.97$), in agreement with the experiments. It should be noted that this linear trend is only apparent because of the lengths considered and the fact that the rupture of CFRP caps off the strength at a bonded length of 1000 mm.

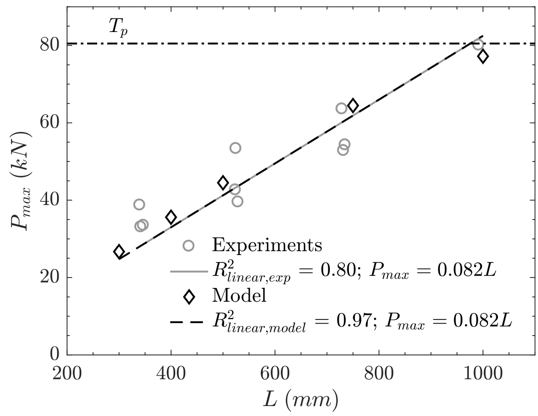

Figure 3.37: Tested and predicted pull-out strength versus the bonded length.

It should be noted that during a seismic event, the CFRP strips of a wall retrofitted with FDM CFRP strips are most likely subjected to higher loading rates than maintained in the quasi-dynamic campaign (100 mm/min). However, even for higher loading rates, no significant difference is expected for the force-loaded end slip relationship determined using the proposed averaged and multilinearized bond-slip law for anchorage lengths of over 1.0 m. This is due to both the limited effect of the loading rate on the initial stiffness for embedment lengths of 1.0 m (as shown in Tables and 3.2 and 3.3), and the pull-out force limit due to the tensile strength of CFRP strip.

3.5 Quasi-dynamic pull-out experiments with active speed control

In order to investigate the effect of the increased slip rate on the quasi-dynamic pull-out test results, an additional experimental campaign was initiated. Four additional specimens were made following the same procedure as was maintained for the PO-12 specimens in the quasi-dynamic pull-out campaign (Fig. 3.15), the only difference being the additional cleaning of the CFRP strips with acetone before installation. The test setup and procedure remained unchanged, except for the loading protocol, which was software enhanced in order to maintain a steady loaded-end slip rate of 1 mm/s. Three of the specimens (coded PO2-12-SC) were tested with the active speed control, whereas the remaining specimen (coded PO2-12) was tested without active speed control.

3.5.1 Results and discussion

The test results are summarized in Table 3.5. The generalized representation of the force-slip behaviour was presented in Fig. 3.8.

Table 3.5: Overview results for the active speed controlled quasi-dynamic pull-out experimental campaign.

Specimen	L mm	$\dot{\delta}_{ini}$ mm/s	E_p kN/mm²	k_{ini} kN/mm	P_{max} kN	$\delta_{L,max}$ mm	F_{end} kN	$\delta_{L,end}$ mm	Failure mode*	Dam. mas.**
PO2-12-SC-1	690	0.99	-	14.7	75.8	7.6	19.7	13.6	CF	SP
PO2-12-SC-2	694	1.00	-	13.8	71.8	7.7	17.1	13.5	CF	SP
PO2-12-SC-3	693	1.03	212.5	12.6	68.5	6.7	21.8	13.6	CF	SP
PO2-12	689	0.90	-	16.6	79.1	7.5	14.4	17.9	CF	SP

* IF = Interfacial failure CFRP/adhesive; CF = Cohesive failure
** SP = Masonry splitting over entire length

The failure mechanism observed in the current experimental campaign was cohesive failure, as limited to none adhesive failure was observed on the CFRP strip. In all specimens splitting of the masonry prism was observed.

The global force-slip diagrams for the tested specimens, taking into account both the free end (dashed lines) and the loaded end (solid lines), are shown Fig. 3.38. It should be noted that for clarity the loaded-end slip is presented with an initial offset of 10 mm.

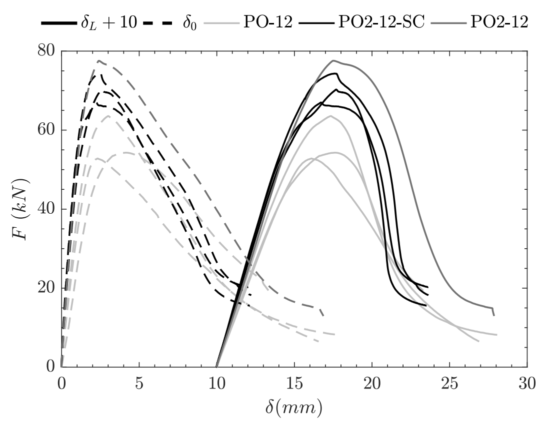

Figure 3.38: Global force - (loaded-end) slip behaviour for the specimens in the current experimental campaign and the *PO-12* specimens from the quasi-dynamic pull-out experimental campaign.

The observed difference between the PO-12 specimens and the PO2-12 specimen, all tested following the same loading protocol, was mainly attributed to the difference in CFRP strip preparation. Cleaning the CFRP strip with acetone prior to installation, which wasn't applicable for the PO-12 specimens, resulted in a higher pull-out strength (+30%). As the average curing temperature in the unheated environment, estimated using the the daily mean ambient temperatures, was around 12 $°C$ for the specimens of both quasi-dynamic experimental campaigns, no significant influences were expected due to possible curing condition differences for the adhesive.

From Fig. 3.38 it was also observed that the specimens with active speed control (PO2-12-SC) showed a significant steeper decrease of the pull-out load in the post peak region, with respect to the specimen with no active speed control (PO2-12). A similar phenomena was also observed from Fig. 3.32, where the predicted F-δ relations using the model also showed a steeper decrease in the post-peak region when compared to the experimental outcome for the PO-16 specimens. In section 3.3 this difference was attributed to the non-uniform local slipping speeds and the strain-rate dependent properties of the flexible, visco elasto-plastic adhesive.

The loaded end slip rate $\dot{\delta_L}$ versus the loaded end slip δ_L is shown in Fig. 3.39 for the case with active speed control (PO2-12-SC-1) and without active speed control (PO2-12). A significant difference in the reached maximum loaded end slip rates were observed with $\dot{\delta_{L,max}}$ = 2.6 and 12.8 mm/s for the specimens with and without active speed control respectively.

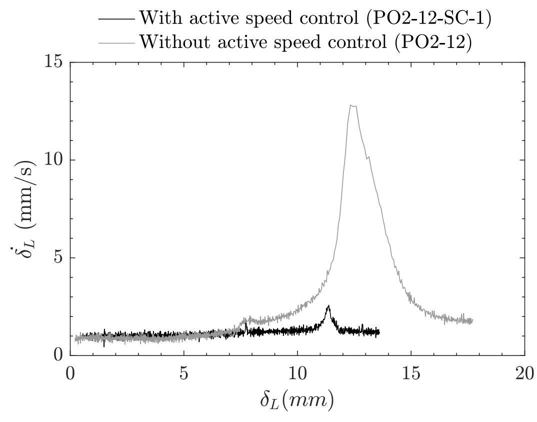

Figure 3.39: Loaded end slip rate $\dot{\delta_L}$ versus the loaded end slip δ_L with (PO2-12-SC-1) and without active speed control (PO2-12).

Both the lower-magnitude and narrower region disruption of the loaded end slip when using active speed control, result in a lower pull-out strength, lower slip levels and a steeper decrease of the F-δ behaviour in the post-peak region. This effect of the active speed control is visualized in Fig. 3.40 using the averaged F-δ relation of the active speed control tested specimens.

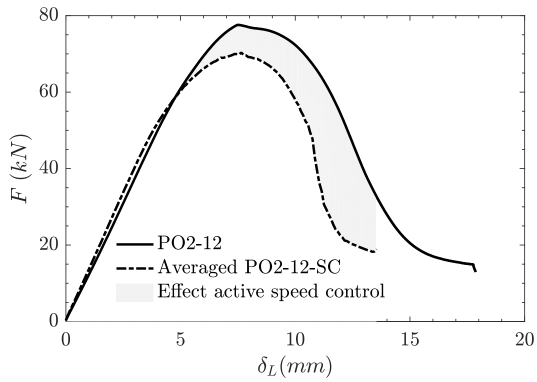

Figure 3.40: Global force - (loaded-end) slip behaviour for the specimens in the current experimental campaign and the *PO-12* specimens from the quasi-dynamic pull-out experimental campaign.

3.5.2 Bond-slip law

The local bond-slip relations and averaged multi-linear $\tau - \delta$ relation were obtained using the same procedure as followed in section 3.4. Due to damaged non-embedded strain gauges for specimens PO2-12-SC-1, PO2-12-SC-2 and PO2-12, a Young's modulus of 200,000 N/mm^2 was assumed for the CFRP strips. The averaged and multi-linearized $\tau - \delta$ relation (bold solid line), together with all the obtained $\tau - \delta$ relations for the *PO2-12-SC* specimens (grey lines), are provided in Fig. 3.41. Comparing the new averaged and multi-linearized $\tau - \delta$ relation for the *PO2-12-SC* specimens with the original averaged and multi-linearized $\tau - \delta$ relation for specimens *PO-6-100*, *PO-9-100* and *PO-12-100* (bold dotted line), it was observed that the most significant difference between the two averaged and multi-linearized $\tau - \delta$ relations is the value for the damage initiation plateau, τ_f. As stated earlier, this difference was attributed to the correct preparation of CFRP strips prior to installation.

With the partial-interaction model and the new $\tau - \delta$ relation, *F*-*δ* relations were determined for an anchorage length of 690 mm. The results following from the proposed model showed reasonable agreement with the experimental outcomes regarding the steep decline in the post-peak phase (Fig. 3.42). The pull-out strength and residual strength were respectively over- and underestimated. Reducing the bond strength for the damage initiation plateau to $\tau_f = 2.7N/mm^2$ and increasing the residual bond stress to $\tau_r = 0.65N/mm^2$, resulted in an improved fit with the experimental outcomes, as shown with the dot-dashed line in Fig. 3.42. Due to the limited sample size in the current experimental campaign to construct the $\tau - \delta$ relation, the original bond-slip law developed in the previous section will be used for modelling purposes in the remaining part of this doctoral research.

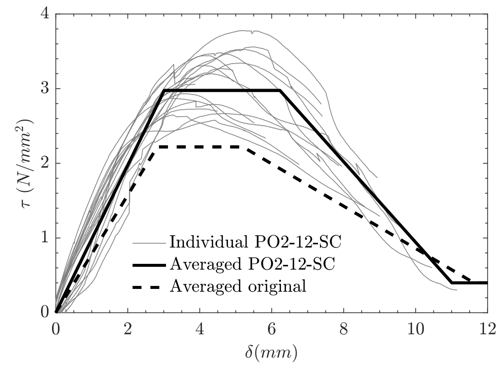

Figure 3.41: Averaged and multi-linearized $\tau - \delta$ relation (bold solid line) and all the obtained $\tau - \delta$ relations for the *PO2-12-SC* specimens (grey lines), together with the original averaged and multi-linearized $\tau - \delta$ relation for specimens *PO-6-100*, *PO-9-100* and *PO-12-100* (bold dotted line).

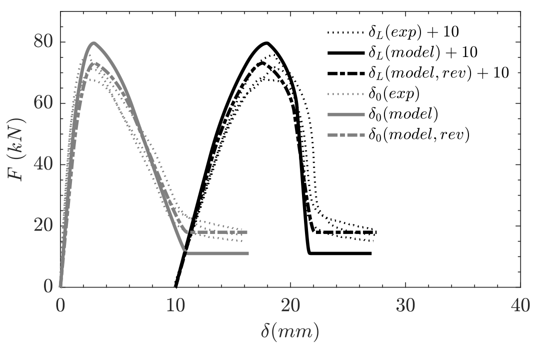

Figure 3.42: Comparison results model with experimental outcomes. For clarity the loaded-end slip is presented with an initial offset of 10 mm. The results using the revised $\tau - \delta$ relationship are provided with dot-dashed lines.

3.6 Stiff versus flexible adhesive systems: bond behaviour

Past experimental research into the bond between FRP retrofit of masonry has focused predominantly on externally bonded strips and to a lesser degree near surface mounted (NSM) strips [54,69]. To the authors' knowledge, no tests have been previously undertaken using the deep-mounted arrangement. The NSM arrangement, in which the FRP strip is embedded just below the surface of the masonry, provides the closest basis for comparisons to the deep-mounted FRP configuration adopted in the current work.

From the database reported in *Vaculik et al.* [54] and supplemented with recent work [106], a total of 124 tests on the NSM retrofit of clay brick substrates were compiled across six separate studies [13,21,32,33,40, 106].These tests share the following features:

- All used conventional, stiff adhesives (two-part epoxy);
- All used rectangular CFRP strips;
- Only the tests by Maljaee et al [106] used individual-brick prisms; the others all used masonry prisms comprising bricks and mortar joints, same as the present study.

In contrast to the present study where failure occurred mainly by cohesive failure of the adhesive, the predominant mode of failure observed in the NSM stiff-adhesive tests was cohesive debonding in the masonry substrate (Fig. 3.43), occurring in over 80% of the tests. In the remaining tests, failure occurred either by sliding at the FRP-to-adhesive interface or rupture of the FRP. A comparison of the maximum force achieved in the respective studies is shown in Fig. 3.44. As the dimensions of the CFRP strip varied among the different studies (A_p = 12–72 mm^2), Fig. 3.45 demonstrates the retrofit efficiency in terms of the ultimate force per unit area of the strip (i.e. strip stress). It is seen that at the longest bonded length of 1,000 mm, the flexible-adhesive system achieves both the largest load and stress among the tests considered.

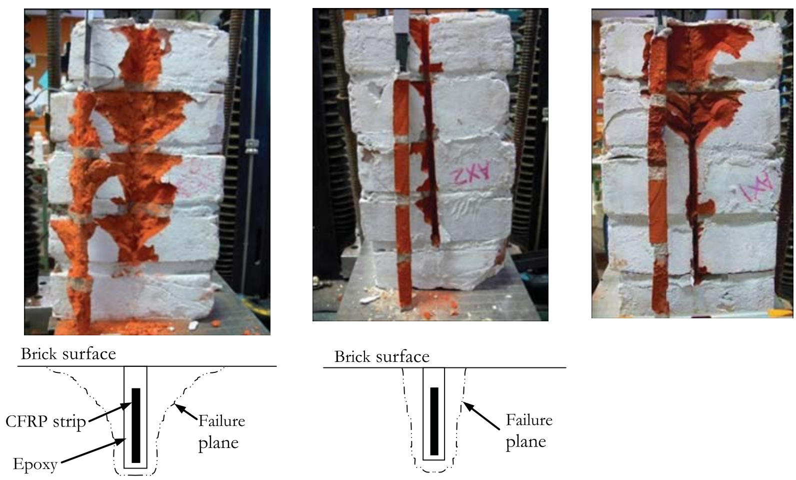

Figure 3.43: Cohesion debonding forms in the masonry substrate, where the NSM CFRP strip is installed using a conventional, stiff adhesive [13].

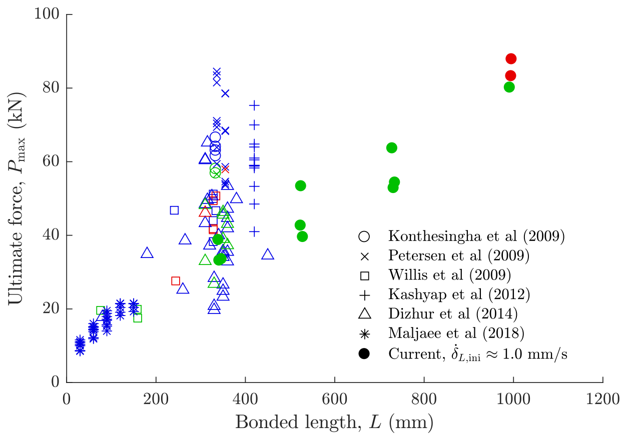

Figure 3.44: Comparison of stiff-adhesive NSM tests to the present study in terms of the ultimate force versus the bonded length. Color denotes mode of failure: blue = cohesive debonding in the brick substrate, green = adhesive failure, red = FRP rupture.

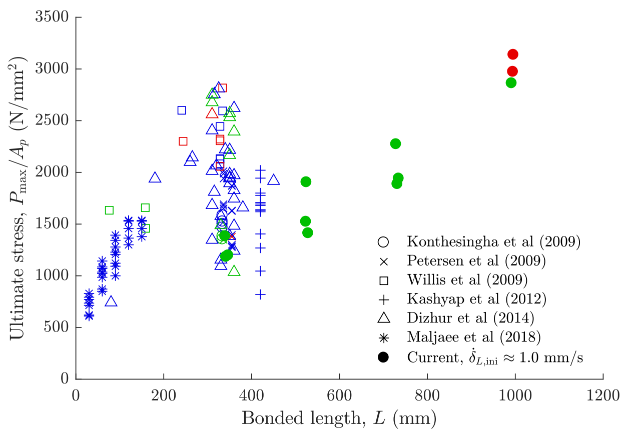

Figure 3.45: Comparison of stiff-adhesive NSM tests to the present study in terms of the ultimate strip stress versus the bonded length. Color denotes mode of failure: blue = cohesive debonding in the brick substrate, green = adhesive failure, red = FRP rupture.

3.6.1 Bond-slip behaviour

Each of the NSM/stiff-adhesive studies that used masonry prisms [13, 21, 32, 33, 40] extracted the local bond-slip properties using the strain gauge approach. In each case, the bond-slip behaviour was idealized as bilinear and ignored any residual friction (τ_r) that may have been present. The range of reported bond-slip properties is summarized in Table 3.6.

Table 3.6: Bond-slip properties for NSM retrofits of clay brick masonry prisms strengthened with CFRP strips by means of stiff adhesives (see Fig. 3.29). Properties τ_f, δ_1 and δ_3 were obtained from the respective sources, and from these, the fracture energy (G_f) and initial slope (k_1) were calculated. Uniaxial compressive strength ($f_{c,b}$) and flexural tensile strength ($f_{fl,b}$) of the brick units are also provided for comparison.

	τ_f N/mm²	δ_1 $(=\delta_2)$ mm	δ_3 mm	G_f Nmm/mm²	k_1 N/mm³	$f_{c,b}$ N/mm²	$f_{fl,b}$ N/mm²
[32]	12.5	0.25	1.75	10.9	50	-	3.57
[21]	8.2–13.1	0.2–0.4	1.22–1.77	5.3–11.6	33–41	-	3.57
[33]	12.1–14.4	0.30–0.49	1.12–1.30	7.3–9.0	25–41	-	4.74
[40]	13.8–15.2	0.32–0.55	1.42–1.97	10.5–15.0	26–46	-	3.41
[13]	16.5	0.37	0.68	5.6	45	17.1	2.60

In Fig. 3.46, the bilinear bond-slip relationships reported for stiff-adhesive retrofits are compared graphically to the flexible-adhesive system in the present study. The latter is represented using both a trilinear and bilinear ($\delta_1 = \delta_2$ in Fig. 3.29) idealization. To benchmark the stiff-adhesive system behaviour against the masonry mechanical properties in the current study, the expected bond-slip behaviour was predicted using the model by Kashyap et al. [40], and is plotted in Fig. 3.46 as a dashed line. These predictions are based on Eq. 3.18 and Eq. 3.19, where φ_f is the depth-to-width aspect ratio of the failure plane, $f_{fl,b}$ is the flexural tensile strength of the substrate (modulus of rupture), and c is a correction factor taken as 0.84 to provide better fit between the model and the current experimental database [54]. The correction factor c was tuned by re-calibrating the model proposed by *Kashyap et al.* [40] using the more recent and extensive experimental database of NSM tests reported in Vaculik et al [54] to provide better agreement between the measured and predicted P_{max} values. This re-calibration was simplified in that only the factor c as presented in Eqs. 3.18 and 3.19 was calibrated, and the other factors and exponents in these equations were kept as per *Kashyap et al.* [40] original values. This is tantamount to re-calibrating the fracture energy (product of τ_f and δ_f), while keeping the critical length (resulting from the quotient τ_f/δ_f) as per the original calibration.

$$\tau_f = c \cdot 8.83\varphi_f^{0.15}\, f_{fl,b}^{0.2} \tag{3.18}$$

$$\delta_f = c \cdot 0.45\varphi_f^{0.23} f_{fl,b}^{0.74} \tag{3.19}$$

In the predictions, $f_{fl,b}$ was calculated using the formula $f_{fl,b} = 0.53\sqrt{f_c}$ as used in *Kashyap et al.* [40]. The predicted bond-slip behaviour is comparable to that reported in the individual test studies as seen in Fig. 3.46. The main observation are:

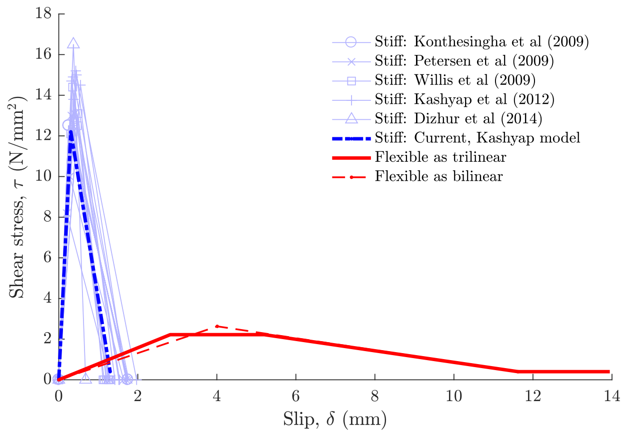

Figure 3.46: Comparison of the local bond-slip behaviour of the stiff-adhesive NSM systems to the flexible-adhesive system in the current study.

- The stiff-adhesive systems achieved considerably higher peak shear stress, τ_f, (8.2–16.5 MPa) than the flexible-adhesive system in the present study (2.2 N/mm^2). This can be explained by the fact that in the flexible-adhesive tests, the mechanism of local bond stress transfer was limited by the cohesive strength of the adhesive, whereas in the stiff-adhesive tests the adhesive was sufficiently strong so that failure was governed by the cohesive strength of the brick units. This is consistent with the mode of failure generally observed in the respective tests.

- Conversely, the flexible-adhesive system achieved a much larger ultimate debonding slip of 11.6 mm compared to 0.68–2.0 mm for the stiff-adhesive systems.

- Despite having a lower τ_f, the flexible-adhesive system was still able to achieve an overall higher fracture energy, G_f, (16.9 Nmm/mm^2) than the stiff-adhesive systems. For the latter, the reported fracture energy ranges from 5.3 to 15 Nmm/mm^2 with a mean value of 9.7 Nmm/mm^2. Importantly, the debonding force that can be developed over a sufficiently long bonded length is controlled by the G_f term rather than the peak stress τ_f, through the Eq. 3.20, which is based on partial-interaction theory (e.g. [107]), where L_{per} is the perimeter of the failure plane and the other variables are as defined previously.

$$F_u^{\infty} = \sqrt{2G_f E_p A_p L_{per}} \tag{3.20}$$

The contrasting local behaviour of the flexible-adhesive system in the present study (low τ_f, high $\delta 3$) versus stiff-adhesive systems (high τ_f, low $\delta 3$), means that the critical bonded length (L_{crit}) needed to achieve the full debonding force is much longer for a flexible system. This is evident from the closed-form solution for L_{crit} given by Eq. 3.21, which is 'exact' for an idealized linear-descending ($\delta_1 = \delta_2 = 0$) bond-slip with zero residual stress (e.g. [107]), where it is seen that the ratio δ_3/τ_f is the controlling parameter.

$$L_{crit} = \frac{\pi}{2}\sqrt{\frac{\delta_3}{\tau_f} \cdot \frac{E_p A_p}{L_{per}}} \tag{3.21}$$

3.6.2 Force-slip behaviour

The predicted global force-slip behaviour of the flexible-adhesive and stiff-adhesive systems are provided in Fig. 3.47 and Fig. 3.48 respectively. Both sets of predictions assume the use of a retrofit configuration identical to the current study in terms of strip arrangement and bonded lengths, but differ in their local bond-slip properties. In each case, the τ-δ relationship is modelled as bilinear with a residual friction component: the flexible-adhesive system was modelled with τ_f = 2.63 N/mm², δ_3 = 11.6 mm, δ_1 = 4.0 mm, and τ_r = 0.4 N/mm² as a bilinear representation of the multi-linear rule fitted in Fig. 3.46; and the stiff-adhesive system with τ_f = 12.20 N/mm², δ_3 = 1.30 mm, δ_1 = 0.31 mm, and τ_r = 0.4 N/mm², where τ_f and δ_f were obtained using the Kashyap model (Eqs. 3.18 and 3.19), and δ_1 was obtained by taking the initial slope $k_1 = 40\ N/mm^3$ (Table 3.6). The force-slip solutions plotted in Figs. 3.47 and 3.48 were computed using the method described in Vaculik et al. [105].

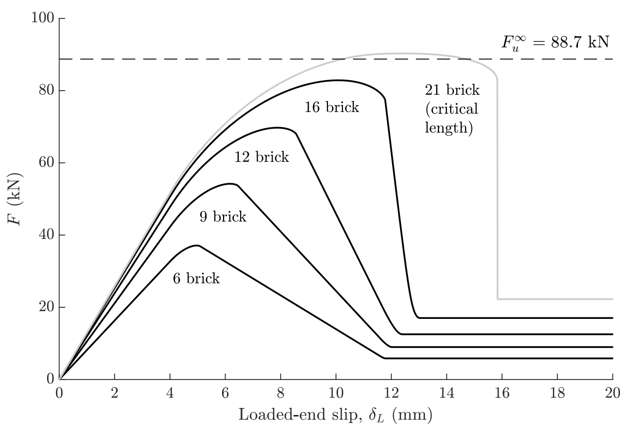

Figure 3.47: Theoretical force-slip behaviour of the flexible-adhesive system.

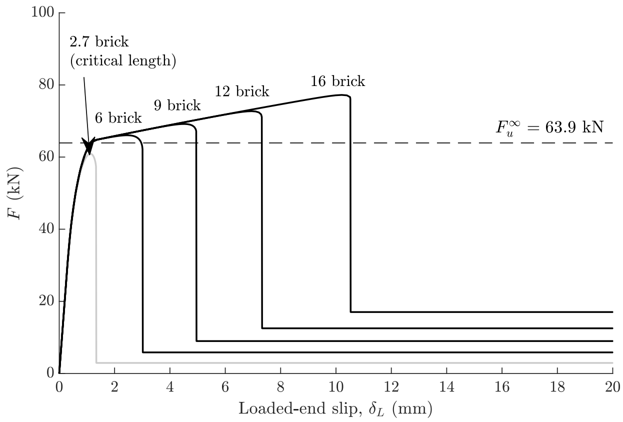

Figure 3.48: Theoretical force-slip behaviour of stiff-adhesive systems.

The full debonding force F_u^∞ calculated using Eq. 3.20 is 63.9 kN for the stiff system and 88.7 kN for the flexible system. Additionally, the critical bond length, L_{crit}, for a bilinear-frictional system was calculated in accordance with the definition and method provided in Vaculik et al. [105] as 171 mm (equivalent to a 2.7 brick-tall prism) and 1200 mm (21 brick prism) for stiff and flexible adhesive systems, respectively. These comparisons demonstrate that flexible adhesives are a viable alternative to conventional stiff adhesives for FRP strengthening of masonry. Among the indicated advantages of using a flexible-adhesive system with respect to out-of-plane wall strengthening are:

- Higher interfacial fracture energy G_f leading to increased wall strength capacity;
- Increased wall displacement capacity arising from higher local slip capacity δ_3; and
- Larger slip capacity at damage initiation, δ_1, leading to increased wall displacement capacity at the onset of irreversible damage to the retrofit.

3.6.3 Shear stress distribution

The shear stress distribution over the critical embedded length is provided in Fig. 3.49 for both the stiff adhesive system (dashed line) and a flexible adhesive system (solid line). For this comparison the tensile strength of the CFRP strip was neglected, and the possible under-utilisation of the stiff adhesive material and the initiation of premature brick splitting due to a deep groove depth [13] was excluded. Where a the stiff adhesive system shows shear stress concentrations over a limited embedded length

($\tau = 2.4 - 12.2\ N/mm^2$), the flexible adhesive shows a nearly uniform distribution ($\tau = 0.4 - 2.3\ N/mm^2$). The nearly uniform distributed low-magnitude bond stresses over the embedded length achieved when using a flexible adhesive prove to be crucial in preventing cohesive debonding in the masonry substrate, and thus ruling-out under-utilization of the CFRP.

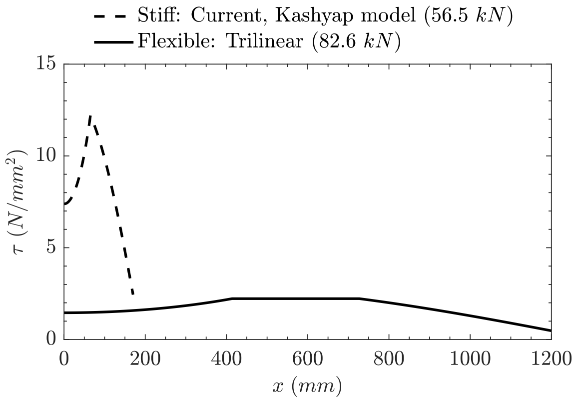

Figure 3.49: Shear stress τ over the critical embedded length (x) at maximum pull-out force for a stiff adhesive system (dashed line) and a flexible adhesive system (solid line).

3.7 Conclusions

An experimental program was undertaken to assess the pull-out behaviour of deep-mounted CFRP strips bonded with a flexible, visco-elasto-plastic adhesive to clay brick masonry. The direct pull-out test was used for the evaluation of the bond-slip behaviour of the embedded CFRP strips.

Multiple bond stacked masonry prisms with an FDM CFRP strip and anchorage length of 1.0 m were tested. With this quasi-dynamic experimental campaign, using a machine displacement rate of 0.5 mm/min for loading the specimens, the following conclusions were drawn:

1. For all the quasi-static loaded specimens, a combined CFRP/adhesive interface failure and cohesive failure of the adhesive was the predominant failure mechanism.

2. Despite a groove depth of 65 mm, premature brick splitting was not observed. This observation was contradictory to the findings of a similar research [13], where pre-mature brick splitting was observed during the pull-out tests using a conventional stiff adhesive with a groove depth of only 30 mm. The prevention of the premature failure mechanism was linked to the application of a more flexible adhesive.

3. Both considered surface treatment methods, sand-blasting of the CFRP strip and combined roughening of and adding a primer layer to the CFRP strip, provided a higher strength in terms of pull-out resistance with respect to the smooth CFRP strip surface. Despite the slight increase in pull-out resistance, this advantage does not outweigh the costs and time needed for both surface treatment methods.

4. Widening the groove width from 10 mm to 15 mm did not result in a higher pull-out resistance and corresponding loaded end slip.

5. Replacing the standard adhesive with an even more flexible alternative did not lead to an increase of system performance in terms of both pull-out resistance and stress distribution.

From the quasi-dynamic experimental campaign, where FDM CFRP strips with anchorage lengths of 0.34 m, 0.53 m, 0.73 m and 1.0 m were tested with loading rates varying from 5 mm/min to 100 mm/min, the following conclusions were drawn:

6. Increasing the machine displacement rate from 0.5 mm/min ($\dot{\delta}_{L,ini} \approx$ 0.004 mm/s as maintained in the quasi-static experimental campaign) to 100 mm/min ($\dot{\delta}_{L,ini} \approx$ 1.0 mm/s) led to an increase of 67% in pull-out strength for an embedment length of 1.0 m. A strong logarithmic correlation (R^2 = 0.93) was found for the relation between strength and displacement rate. Additionally the governing failure mechanism shifted from cohesive failure to CFRP strip rupture. The latter was applicable to two of the three specimens with an embedment length of ~ 1.0 m.

7. Testing the pull-out behaviour of systems that include visco-elasto-plastic components should be conducted at a loading rate that is representative for the practical application of the system.

8. Keeping the machine displacement rate constant at 100 mm/min ($\dot{\delta}_{L,ini}$ $\approx$ 1.0 mm/s) and varying the embedment length, shifted the governing failure mechanism from CFRP strip rupture ($L \approx =$ 1.0 m) to cohesive failure in the adhesive ($L <$ 1.0 m). A very strong linear correlation (R^2=0.92) was found for the relation between embedment length and pull-out strength, up to the critical embedment length of approximately 1.0 m.

9. Brick splitting was observed when the CFRP/adhesive interface entered the damage initiation phase. For specimens that were governed by cohesive failure, the complete specimen showed splitting. For the specimens with CFRP rupture, the splitting was limited to the bonded length where the CFRP/adhesive interface entered the damage initiation phase.

10. The increase in local bond strength towards the free end of the specimen was attributed to the non-uniform slip rate throughout the experiment. The slip-rate was disrupted by the finite stiffness of the machine, the threaded rods (used to connect the restraint plate to the base of the machine) and the CFRP strip between the masonry and the grips of the machine. The relaxation of the aforementioned elements during the post-peak region caused a significant noise in the slip rate over the entire embedment length, particularly at the free-end side.

11. Based on the readings of the strain gauges on the embedded CFRP strip, multiple tri-linear local bond-slip relations were obtained for specimens that were subjected to a 100 mm/min machine displacement rate. The separate bond-slip relations were averaged to obtain a universal local bond-slip law. For the averaged tri-linear local bond-slip behaviour the interfacial fracture energy was determined at 16.9 Nmm/mm^2.

12. Using the averaged multi-linear local bond-slip model as a part of a partial-interaction analysis led to a good agreement with experimental results for embedment lengths of 0.34 m, 0.53 m and 0.73 m. For an embedment length of $\sim$ 1.0 m, the agreement was good for the pre-peak phase. In the post-peak phase, the proposed model showed a reduced post-peak behaviour and stronger decline when compared to the experimental results. This deviation was attributed to the non-uniform slip rate during the experiment and the visco-elasto-plastic properties of the adhesive.

13. During a seismic event higher loading rates of an FDM CFRP strip could occur than maintained in the presented experimental campaign. Even for higher loading rates the validity of the proposed averaged multi-linear local bond-slip law for determining the force and loaded end slip relationship is expected to remain unaffected.

Additionally, a comparison was made between the system tested in this part of the research and a database consisting of 124 tests on near-surface-mounted (NSM) retrofits of clay brick substrates using a conventional stiff adhesive. From this comparison, considering both bond-slip and force-slip behaviour, the following conclusions can be drawn:

13. Stiff-adhesive systems were able to achieve considerably higher peak shear stresses (8.2–16.5 N/mm^2) than the flexible-adhesive system used in the present study (2.2N/mm^2). Conversely, the flexible-adhesive system achieved a much larger ultimate debonding slip of 11.6 mm compared to between 0.68–2.0 mm for the stiff-adhesive systems. Despite having a lower peak bond stress, the flexible-adhesive system was still able to achieve an overall higher fracture energy (16.9 Nmm/mm^2) than the stiff-adhesive systems (mean 9.7 Nmm/mm^2).

14. The debonding force that can be developed over a sufficiently long bonded length is controlled by the fracture energy (flexible adhesive) rather than the peak stress (stiff adhesive). The estimated critical bond length is 1200 mm (equivalent to a 21 brick prism) for the flexible-adhesive system tested, and 171 mm (equivalent to roughly a three bricks long prism) for an equivalent retrofit with stiff adhesive.

15. The nearly uniform distributed low-magnitude bond stresses over the embedded length achieved when using a flexible adhesive prove to be crucial in preventing cohesive debonding in the masonry substrate, and thus ruling-out under-utilization of the CFRP.

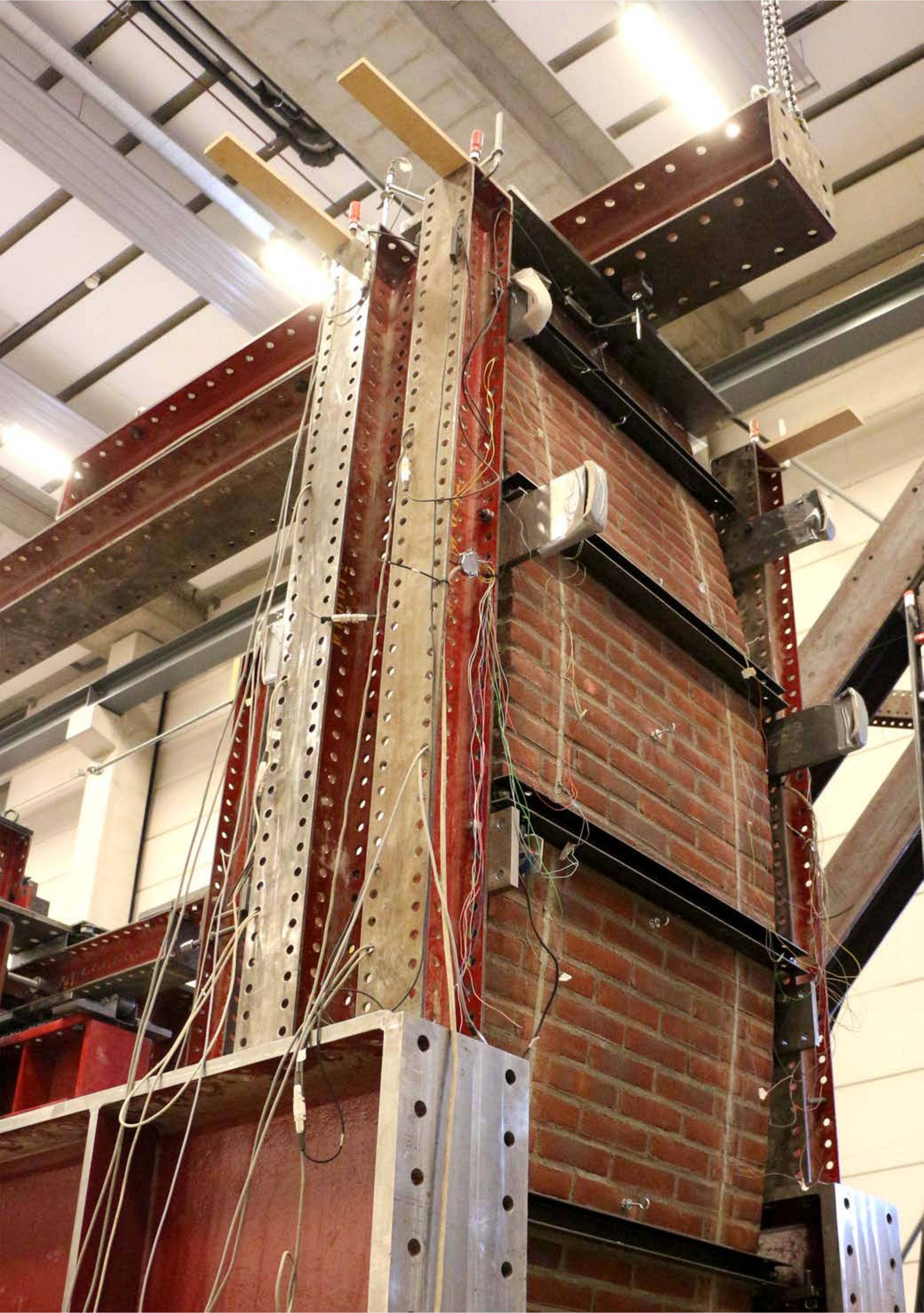

Chapter 4

Flexible deep mounted CFRP strips: out-of-plane behaviour

This chapter discusses the cyclic out-of-plane *(OOP)* behaviour of vertically (one-way) spanning masonry walls retrofitted with flexible deep mounted (FDM) CFRP strips by means of an extensive experimental program. An overarching objective of this study was to verify the effectiveness of the proposed retrofit system. An additional objective of this research was to validate the engineering model proposed for FDM CFRP retrofitted walls. Furthermore, the validity of the proposed bond-slip laws for FDM CFRP strips were assessed for flexural, rather than uni-axial tensile, loading conditions. Finally, the OOP behaviour of CFRP strip retrofitted masonry walls are compared for both the stiff and the flexible adhesive system. This chapter is mainly based on [77].

4.1 Full-scale experimental program

4.1.1 Building the specimens

The wall specimens for the full-scale out-of-plane experimental program were built and tested in the Structures Laboratory of Eindhoven University of Technology. A total of nine specimens were constructed of which three specimens remained unreinforced and functioned as control specimens while six specimens were reinforced with FDM CFRP strips. The specimens were each constructed on a steel plate by an experienced mason to ensure compliance to good construction practices. The steel plate functioned as a base for the specimens and allowed for a connection between the test setup and the specimen. On top of the steel plate a first layer of bricks was glued with a high performance epoxy on which the actual masonry specimen was constructed. The glued layer of bricks functioned as a foundation for the wall.

The masonry walls were nominally 2750 mm high, 965 mm long and had a thickness of 95 mm (t_w). Based on the observed level of bed-joint coverage, the effective wall thickness ($t_{w,eff}$) was estimated at 90 mm. The mortar for the wall specimens was prepared in the laboratory and the walls were built in running bond. Both the bed and head joints had a nominal thickness of 12 mm. All walls cured in laboratory environment (17-20 °C) for at least 28 days prior to strengthening.

A total of six walls were reinforced with two FDM CFRP strips each, following the installation procedure mentioned in 1.4. A schematic overview of the reinforced specimens is provided in Fig. 4.1. The CFRP strips were prepared prior to the installation process. Strain gauges (type *PFL-10-11*, foil strain gauges having polyester resin backing) were attached to alternating sides (to minimize asymmetry effects) of the CFRP strips with a constant inter distance of approximately 310 mm, starting 95 mm from the top side of the specimen. The locations of the strain gauges are provided in Fig 4.1.

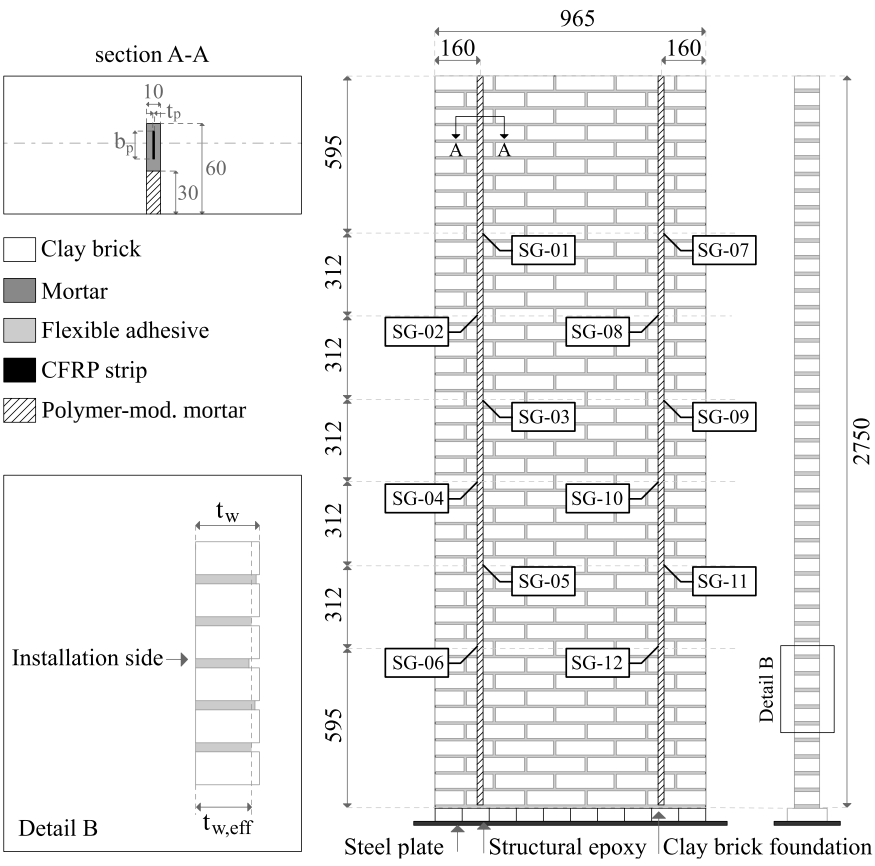

Figure 4.1: Schematic overview of a FDM CFRP strip retrofitted specimen.

4.1.2 Test setup

When characterizing the out-of-plane seismic behaviour of walls through a quasi-static bending test, researchers generally endeavor to apply (as close to) uniformly distributed loads on the wall surfaces, trying to simulate inertia forces developed under seismic actions [108]. The testing technique that is applied for this kind of tests generally consists of air-bags for applying the face load in addition to load cells to monitor the applied forces. Previous experiments by researchers have proven the successfulness of this testing technique for both monotonic [109, 110], one-directional cyclic [111] and reversed-cyclic loading [112–114]. This test methodology allows for a closer approximation to the distribution of seismic loads, which are mass proportional, compared to a test method which uses multiple line loads. However, a disadvantage of using air-bags for reversed-cyclic bending tests is the difficulty of visual inspection of damage evaluation in specimens during tests, because both wall surfaces are covered with air-bags. Moreover, careful in and deflating of air-bags during reversed-cyclic bending tests makes this testing method only suitable for low speeds. In the testing program reported in this study it was considered important that the test setup was able to load the specimens with higher rates, such that similar CFRP strip loading rates were obtained as maintained in the previous experimental campaigns on the high-speed pull-out behaviour of FDM CFRP strips (Chapter 3). Because a traditional air-bag setup for cyclic out-of-plane bending tests can only be performed at low loading rates, the air-bag setup was not suitable for this research. Despite being one of the most widely used techniques to assess the seismic performance of (sub)structures, the shaking table was also not considered. The main objective of shaking table tests is to understand the dynamic (damage) characteristics of a (sub)structure. As limited knowledge is available regarding the behaviour of FDM CFRP retrofitted masonry walls, conducting a dynamic test would result in too many parameters and too many unknowns.

Due to the limitations of both afore-mentioned out-of-plane testing methods within the scope of this research, a new four or six point-bending test setup using line-loads was adopted for cyclic quasi-dynamic testing with loading rates up to 30 mm/s. Even though line loads can be an adequate loading system, they have their limitations such as affecting the localization of the cracks: different results can be obtained based on a different position and/or number of applied line loads. These possible limitations were closely monitored during the experimental campaign presented in this chapter. The quasi-dynamic out-of-plane experiments were an intermediate step towards shaking table tests.

The test setup used in this experimental campaign is depicted in Fig. 4.2. Details of the loading beams and the boundary conditions at the top and bottom of the wall are provided in Fig. 4.3.

Figure 4.2: Test setup for the full-scale out-of-plane experimental campaign.

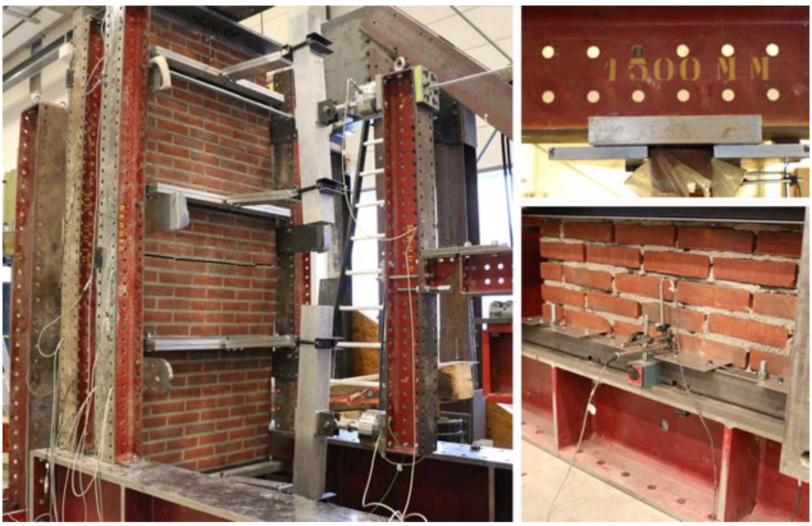

Figure 4.3: Detail photos of the setup: Loading beam for the 6-point bending configuration (left), top boundary condition of the wall (upper left), bottom boundary condition of the wall (bottom left).

After having cured for a sufficient time, the wall was positioned in the test setup. A schematic overview of the test setup is provided in Fig. 4.4. The bottom steel plate on which the specimen was built, was bolted to the base of the test setup. Subsequently, the wall was provided with a gypsum layer at the top to prevent peak stress concentrations, after which the vertical load was applied on top of the specimen using dead weight in the form of a steel beam, which simulated a stiff slab boundary condition. When the wall would start to displace in the opposite directions, the position of the load transfer point between the vertical load and the wall specimen therefore would shift due to the rotation of the top of the wall. This way, the axial load was always positioned at the upward-displaced point of the top of the wall specimen, as illustrated in Fig. 4.5. Steel blocks on both faces of the wall, restrained the top side of the wall over the entire length against sliding. At the bottom-side thin steel plates were positioned at the first course from below, again over the entire length of the wall (Fig. 4.3), to prevent sliding of the wall.

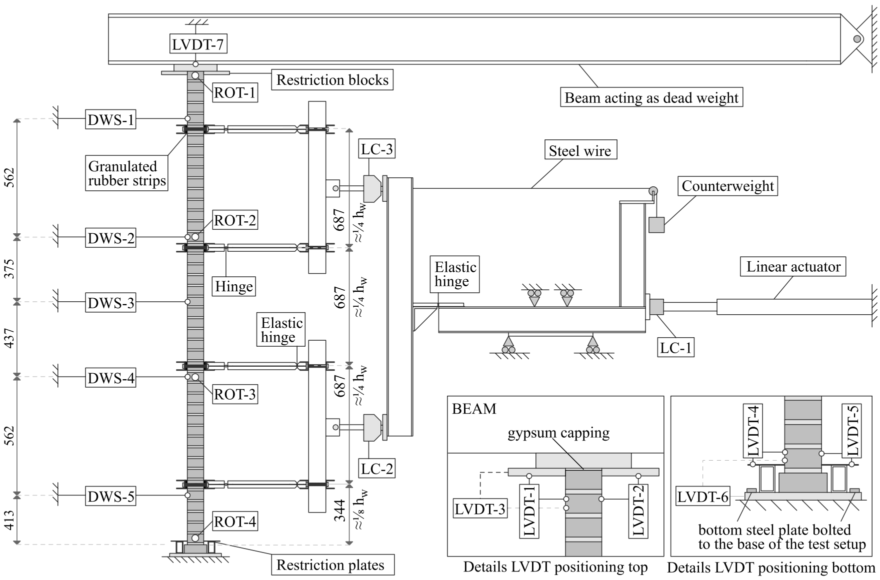

Figure 4.4: Schematic overview test setup for full-scale out-of-plane experimental campaign: four line-load configuration

Hereafter the horizontal loading equipment was attached to the specimens. All URM-specimens as well as three strengthened specimens were tested using four line loads (Fig. 4.4). Three of the remaining strengthened specimens was tested with the two line load configuration, for which the partial schematic overview is provided in Fig. 4.6. The horizontal force was generated by an electric actuator with a maximum capacity of 15.6 kN and maximum speed of 250 mm/s. The horizontal force generated by the actu-

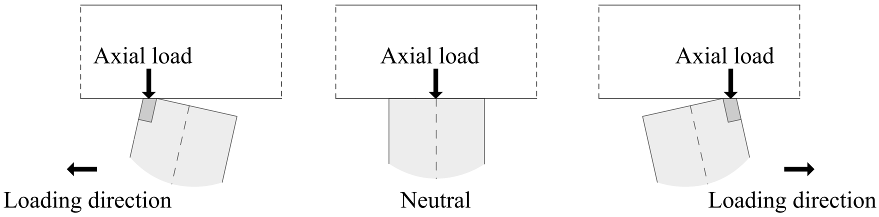

Figure 4.5: Position axial load on top of the wall specimen.

ator was transferred through a horizontal beam, which had roller supports on the top and bottom surface. This was done with the purpose of allowing lateral movement with low friction, and restraining the horizontal beam against rotation. The end of the horizontal beam was connected to a primary spreader beam (steel) using an elastic hinge. In case of the 6-point bending configuration a counterweight was used to balance the primary spreader beam and to ensure that minimal vertical load was applied on the specimens due the self-weight of the force distribution mechanism. At both ends of the primary spreader beam a load cell was installed, LC-2 (bottom) and LC-3 (top) to measure the exerted lateral force. Both the LC-2 and LC-3 load cells were in turn connected to a secondary spreader beam (aluminum) using a hinge. This spreader beam was used to divide the load generated by the actuator into two equal loads. At both ends of the spreader beam, solid aluminum plates were attached using an elastic hinge. The end of the solid aluminum plates was hingedly connected with steel u-profiles, which were used to transfer the lateral forces in the form of line loads onto the specimen via a single row of bricks. These steel profiles were in turn clamped onto the specimen, in order to be able to subject the specimens to reversed-cyclic loading. A layer of granulated rubber was applied in between these steel profiles and the specimen to prevent peak stresses at these points.

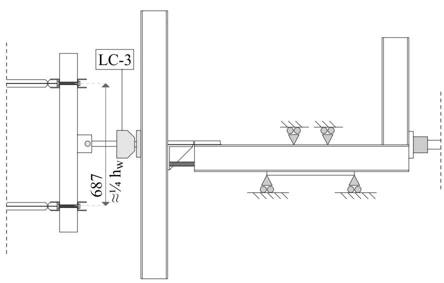

Figure 4.6: Partial schematic overview two line-load configuration.

A total of seven LVDT's were used, of which two were used to measure the uplift at the topside (LVDT-1 and LVDT-2), two were used to measure the uplift at the bottom side (LVDT-4 and LVDT-5), two were used to measure the horizontal displacement at the top and bottom (respectively LVDT-3 and LVDT-6) and one was used to measure the vertical uplift of the vertical loading beam (LVDT-7). Five draw wire sensors (DWS) with a measurement range of 500 mm measured the out-of-plane deformations at different locations over the height of the specimens. The mid-span displacement of the specimens was obtained using draw wire sensor DWS-3. Four rotation sensors were applied to measure rotations at different locations over the height of the specimens. Data was collected at a frequency of 20 Hz using a computerized data acquisition system.

4.1.3 Loading procedure

Eight of the nine specimens were burdened with a vertical compressive force of 4.8 kN (i.e. a compressive stress of approximately 0.05 N/mm^2). To investigate the influence of the level of vertical stress, additional steel beams were stacked on top of the beam acting as dead weight to increase the vertical compressive force to 20 kN (i.e. a compressive stress of approximately 0.22 N/mm^2). This increased axial load was only applicable to one strengthened wall specimen.

Each wall was tested in displacement control, with cycles of increasing amplitude. Each cycle was composed by two runs, a run being the time needed to apply the maximum positive and negative target displacement starting and ending at zero displacement [115], as illustrated in Fig. 4.7.

For the URM walls, the loading procedure consisted of a single stage. The target displacement (actuator stroke) was increased with increments of 2.5 mm after completing a single cycle, with an actuator speed of 2.0 mm/s. This continued until a ultimate target displacement of 95 mm.

For the STRIP specimens, the loading procedure consisted of two stages, as illustrated in Fig. 4.7. Similar to the URM loading procedure, the target displacement initially increased with increments of 2.5 mm after each completed cycle, with an actuator speed of 2.0 mm/s. This protocol (*Stage I*) continued until a target displacement of 27.5 mm. Starting from a target displacement of 30 mm (*Stage II*), the target displacement increment was increased to 5 mm. The loading procedure ended when the target displacement reached 210 mm or when the lateral load resistance of the specimen decreased to nearly 0 kN. The loading rate for *stage II* was selected such that the strain rate of the embedded CFRP strips were magnitude-wise similar to the strain rate used in the quasi-dynamic pull-out campaign presented in Chapter 3. The actuator speed during *Stage II* was initially set to 40 mm/s. However, due to the limitation of the electric actuator the test malfunctioned multiple times during the testing of specimen STRIP-1. Therefore all other STRIP specimens were tested using an actuator speed of 20 mm/s.

The main reason why a loading phase with a lower loading speed (*Stage I*) was implemented for the strengthened specimens, was to prevent the initiation of dynamic effects for the smaller displacement amplitudes. Since the URM walls were expected to have limited to viscous materials properties, the loading rate will have no significant influence on the URM specimens.

The loading speed for all specimens, during both test stages is provided in Table 4.1. The draw-wire sensor located at mid-height of the specimens (DWS,3) was used to determine the loading speed at mid-height of the specimens.

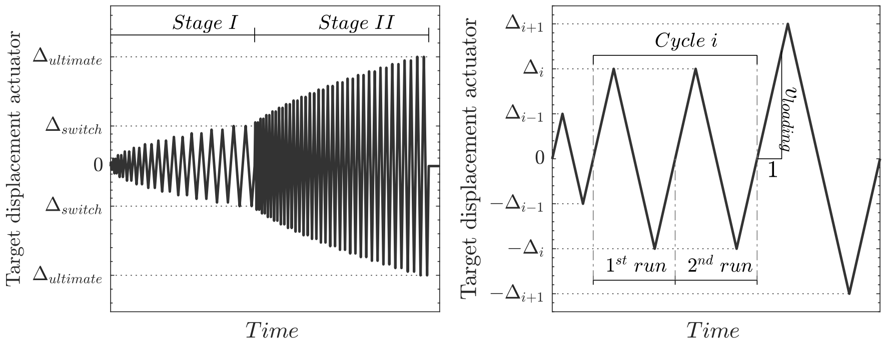

Figure 4.7: Loading protocol.

Table 4.1: Loading speed: actuator and specimen at mid-height.

Specimen	Stage I		Stage II	
	Actuator (mm/s)	Specimen* (mm/s)	Actuator (mm/s)	Specimen* (mm/s)
URM-1	2	1.87	-	-
URM-2	2	1.49	-	-
URM-3	2	1.78	-	-
STRIP-1	2	1.45	40	30.84
STRIP-2	2	1.41	20	15.23
STRIP-3	2	1.47	20	15.51
STRIP-4	2	1.04	20	15.98
STRIP-5	2	1.03	20	16.05
STRIP-6	2	1.01	20	16.67

* Specimen displacement at mid height.

4.1.4 Processing the measurements

The processing of the gathered data was done by using a simplified mechanical representation of the wall, as provided in Fig. 4.8. Using the measurements of the five draw wire sensors and the displacement boundary conditions at the top and bottom of the wall ($\delta(0) = \delta(h_w) = 0$), a quartic ($4^{th}$

order) polynomial was constructed for the out-of-plane displacement of the wall as a function of the height. This polynomial is shown in Eq. 4.1, where x is height position with respect to the top of the wall, as shown in Fig. 4.8.

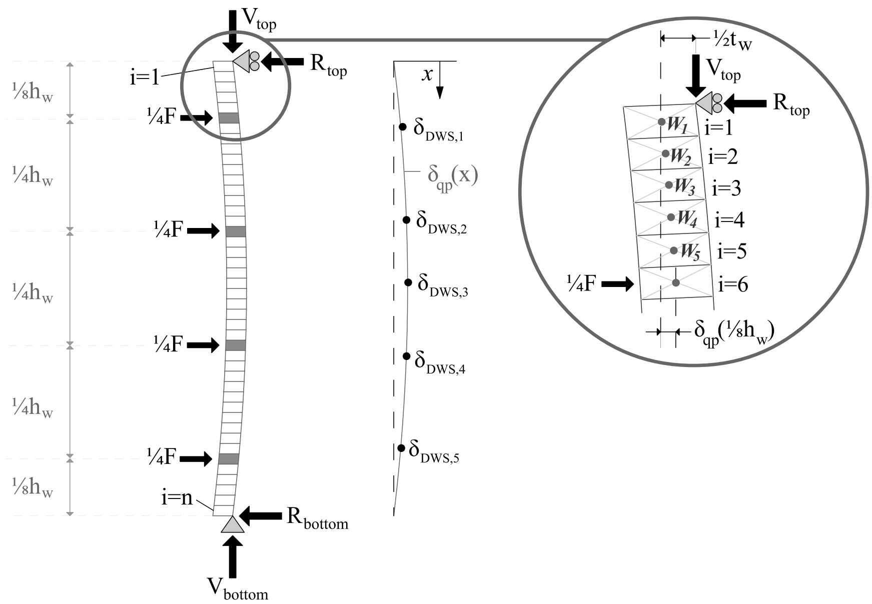

Figure 4.8: Mechanical model for processing the measurements.

Using the polynomial from Eq. 4.1, the curvature over the height of the wall was determined using Eq. 4.2. The moment around the bottom hinge, assumed at the edge of the footing of the wall, is provided with Eq. 4.3.

$$\delta_{qp}(x) = p_1 x^4 + p_2 x^3 + p_3 x^2 + p_4 x + p_5 \tag{4.1}$$

$$\kappa_{qp}(x) = \frac{\frac{d^2\delta_{qp}}{dx^2}}{\left(1 + \left(\frac{d\delta_{qp}}{dx}\right)^2\right)^{\frac{3}{2}}} \tag{4.2}$$

$$\frac{1}{2}F \cdot\ h_w\ = R_{top} \cdot\ h_w + \sum_{i=1}^{n} W_i \left(\frac{t_w}{2} - \delta_{qp,i}\right) \tag{4.3}$$

Rewriting Eq. 4.3 results in the lateral reaction force at the top (R_{top}) as shown in Eq. 4.4. The lateral moment in element k follows from Eq. 4.5 in case of four line load. With two line loads, the lateral moment for element k is obtained using with Eq. 4.6.

$$R_{top} = \frac{1}{2}F + \frac{1}{h_w}\sum_{i=1}^{n} W_i\left(\delta_{qp,i} - \frac{t_w}{2}\right) \tag{4.4}$$

$$M_{lateral,k} = \begin{cases} x \cdot R_{top} & if\ x \leq \frac{1}{8}h_w \\ x \cdot R_{top} - \frac{1}{4}F\left(x - \frac{1}{8}h_w\right) & if \frac{1}{8}h_w < x \leq \frac{3}{8}h_w \\ x \cdot R_{top} - \frac{1}{4}F\left(2x - \frac{1}{2}h_w\right) & if\ \frac{3}{8}h_w < x \leq \frac{5}{8}h_w \\ x \cdot R_{top} - \frac{1}{4}F\left(3x - \frac{9}{8}h_w\right) & if \frac{5}{8}h_w < x \leq \frac{7}{8}h_w \\ x \cdot R_{top} - \frac{1}{4}F\left(4x - 2h_w\right) & if\ x > \frac{7}{8}h_w \end{cases} \tag{4.5}$$

$$M_{lateral,k} = \begin{cases} x \cdot R_{top} & if\ x \leq \frac{3}{8}h_w \\ x \cdot R_{top} - \frac{1}{2}F\left(x - \frac{3}{8}h_w\right) & if\ \frac{3}{8}h_w < x \leq \frac{5}{8}h_w \\ x \cdot R_{top} - \frac{1}{2}F\left(2x - h_w\right) & if\ x > \frac{5}{8}h_w \end{cases} \tag{4.6}$$

The moment due to the second order effects for element k, described from the mid-axis, was obtained using Eq. 4.7, where W_i is the weight of a single row of masonry.

$$M_{2^{nd}\ order,k} = V_{top}\left(\delta_{qp,k} - \frac{t_w}{2}\right) + \sum_{i=1}^{k-1} W_i\left(\delta_{qp,k} - \delta_{qp,i}\right) \tag{4.7}$$

The total internal moment around the mid-axis of the wall, in the deformed state follows from

$$M_{internal,k} = M_{lateral,k} + M_{2^{nd}\ order,k} \tag{4.8}$$

Using the measurements of the strain gauges on the CFRP strips, another quartic polynomial was constructed for the strain distribution over the length of the CFRP strip. This polynomial is shown in Eq. 4.9, where x is again the height position with respect to the top of the wall.

$$\varepsilon_{qp} = p_1x^4 + p_2x^3 + p_3x^2 + p_4x + p_5 \tag{4.9}$$

The stress in the CFRP strip follows from Eq. 4.10, where E_p is the Young's modulus of the CFRP strip.

$$\sigma_p(x) = E_p \cdot \varepsilon_{qp}(x) \tag{4.10}$$

Hysteretic damping

Hysteretic damping (ξ_{hyst}) represents a measure of the dissipative capacity of structures in the inelastic range. Energy dissipation through hysteretic damping is of crucial importance in the analysis of the seismic performance of structures during a seismic event. The equivalent hysteretic damping values for the specimens tested within this experimental campaign were calculated using the area-based method, typically attributed to the work of Jacobsen (1930), following Eq. 4.11, where U_{run} is the area enclosed within the hysteresis loop and U_{box} is the area inside the loop's bounding box as shown in Fig. 4.9. The other parameters presented in Fig. 4.9 are the lateral resistance (P_{max}), the corresponding moment (M_{max}) and mid-span displacement $(\delta_{DWS,3,max})$, the lateral load at the end of the test (F_u), the corresponding moment (M_u) and mid-span displacement $(\delta_{DWS,3,u})$.

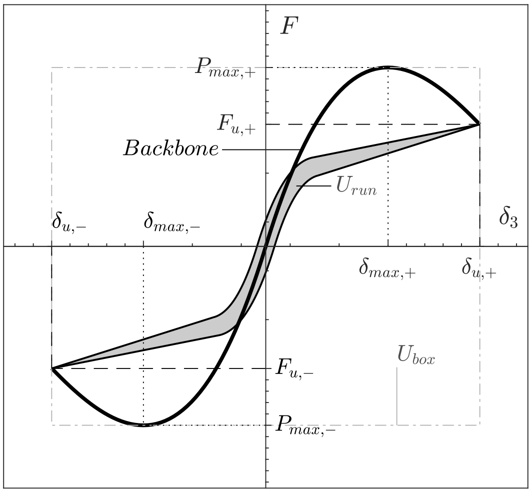

Figure 4.9: Global force – mid-span displacement behaviour. The backbone curve and one complete run are provided by solid and slim black lines respectively. U_{run} is the area enclosed within the hysteresis loop and U_{box} is the area inside the loop's bounding box

The energy U_{run} dissipated during a cycle is evaluated by the integral provided in Eq. 4.12, where t_1 is the time at start of the cycle and t_2 the time at the end of the cycle. The area U_{box} inside the loop's bounding box is determined in accordance with Eq. 4.13. It should be noted that in the calculation of ξ_{hyst}, the energies U_{run} and U_{loop} were determined based on the wall's mid-span displacement $\delta_{DWS,3}$.

$$\xi_{hyst} = \frac{2}{\pi} \frac{U_{run}}{U_{box}} \tag{4.11}$$

$$U_{run} = \int_{t=t_1}^{t_2} F\delta_{DWS,3} \tag{4.12}$$

$$U_{box} = \left[max\left(\delta_{DWS,3}(t_1:t_2)\right) - min\left(\delta_{DWS,3}(t_1:t_2)\right)\right] \times \left[max(F(t_1:t_2)) - min(F(t_1:t_2))\right] \tag{4.13}$$

Initial and effective stiffness

From the force displacement relationship per half run, both the initial stiffness (k_{ini}) and effective stiffness $\left(k_{eff}\right)$ of the tested walls were determined. A half run was defined as the loading and unloading path in either the push or pull direction, as represented by the grey shaded area in Fig 4.10. Both the initial and effective stiffness were determined for both the push and pull direction per run.

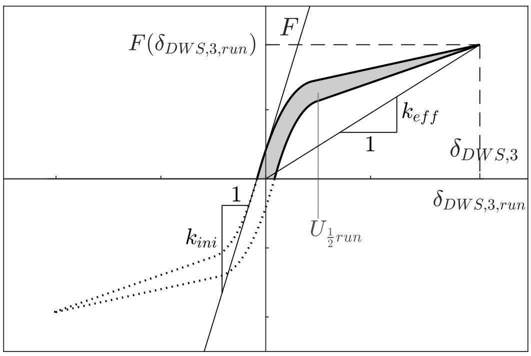

Figure 4.10: Initial and effective stiffness per half run.

The initial stiffness of the wall, k_{ini}, was taken as the slope of the F-δ loading branch within the displacement range $\delta_{DWS,3}$=[-2.5mm,2.5mm]. The value of the slope was calculated by fitting a linear regression through the data points. The effective secant stiffness of a half run was determined in accordance with Eq. 4.14 obtained from [113], using the target isplacement $\delta_{DWS,3,run}$ and corresponding lateral force $F\left(\delta_{DWS,3,run}\right)$.

$$k_{eff} = \frac{F\left(\delta_{DWS,3,run}\right)}{\delta_{DWS,3,run}} \tag{4.14}$$

Load transferred from CFRP to masonry

The load $F_{p,m,i}$ is transferred from the CFRP strip into the masonry (for a specific region) by the interface shear stresses that develop due to bond between the CFRP strip and the masonry, as illustrated in Fig. 4.11. This load $F_{p,m}$ is determined using the absolute difference in strain between two sequential strain gauges positions, per Eq. 4.15. The load $\bar{F}_{p,m}$, being the average load per unit length between two sequential strain gauges positions, is determined using Eq. 4.16.

$$F_{p,m,i}[x_{SG,i}, x_{SG,i+1}] = b_p t_p E_p \left|\varepsilon_{SG,i+1} - \varepsilon_{SG,i}\right| \tag{4.15}$$

$$\bar{F}_{p,m,i}[x_{SG,i}, x_{SG,i+1}] = \frac{F_{p,m,i}}{x_{SG,i+1} - x_{SG,i}} \tag{4.16}$$

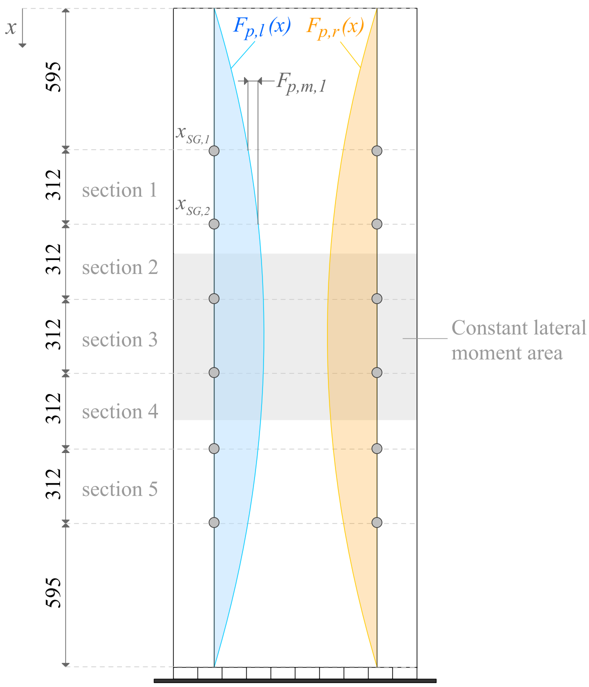

Figure 4.11: Illustration of the CFRP strip force $F_p(x)$ over the height, and the force $F_{p,m}$ transferred from the CFRP strip to the masonry.

4.2 Test results and discussion

The test results of the experimental campaign on the OOP behaviour of (FDM CFRP strip retrofitted) vertically spanning masonry walls are summarized in Table 4.2, with the following nine measured or derived parameters:

- Lateral resistance (P_{max}), the corresponding moment (M_{max}) and mid-span displacement $(\delta_{3,max})$;
- Lateral load at the end of the test (F_u), the corresponding moment (M_u) and mid-span displacement $(\delta_{3,u})$;
- Maximum stresses in both the left $(\sigma_{max,L})$ and right $(\sigma_{max,R})$ CFRP strip; and
- Tensile utilization (Φ_{CFRP}) for the CFRP strip, with respect to the tensile strength of 2880 N/mm².

All the parameters are presented as absolute values for both the positive and negative displacement direction. A generalized representation of the backbone and envelope curves are shown in Fig. 4.9. All mentioned parameters will be covered in the following sections.

4.2.1 Moment-displacement behaviour

The global mid-height lateral moment-displacement diagrams for the tested specimens, are shown Fig. 4.12 *(URM)*, Fig. 4.13 *(STRIP-1-2-3)* and Fig. 4.14 *(STRIP-4-5-6)*. Per graph, the grey line represents the individual cycles, whereas the bold black lines highlight the backbone curve. The bold grey lines represent the first cycles with 50 mm and 100 mm target displacement for the URM and STRIP specimens respectively. The final cycles are highlighted by the dotted bold grey lines.

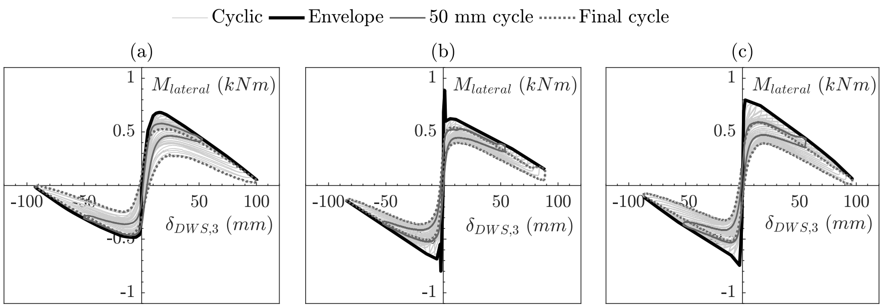

Figure 4.12: Moment – mid span displacement plots of specimens *URM-1* (a), *URM-2* (b) and *URM-3* (c).

Table 4.2: Global force - mid-span displacement behaviour.

	Parameter	Unit	Direction	URM1	URM2	URM3	STRIP1	STRIP2	STRIP3	STRIP4	STRIP5	STRIP6
	V	kN		4.8	4.8	4.8	4.8	4.8	4.8	4.8	4.8	20
	Line loads			4	4	4	4	4	4	2	2	2
Maximum	P_{max}	kN	+	1.99	2.60	2.34	8.12	4.41	6.36	3.32	3.31	3.78
			-	1.40	2.34	2.16	4.15	5.05	6.16	3.80	3.22	3.78
	M_{max}	kNm	+	0.68	0.89	0.80	2.78	1.51	2.18	1.7	1.7	1.94
			-	0.48	0.80	0.74	1.42	1.73	2.1	1.95	1.71	1.94
	$\delta_{3,max}$	mm	+	15.7	1.3	2.4	216	211.4	209.2	202.6	199.9	9.4
			-	7.2	2.2	2.6	166.6	129.6	177.6	195.6	160.4	9.7
Ultimate	F_u	kN	+	0.15	0.44	0.18	8.12	4.41	6.31	3.31	3.25	0.78
			-	0.03	0.41	0.26	3.82	4.91	6.1	3.80	3.06	1.45
	M_u	kNm	+	0.05	0.15	0.06	2.78	1.51	2.16	1.7	1.67	0.4
			-	0.01	0.14	0.09	1.31	1.69	2.09	1.95	1.57	0.75
	$\delta_{3,u}$	mm	+	100.3	88.6	96.5	216	211.4	217.9	202.6	216.1	179.3
			-	92.8	84.2	87.3	193.1	189.8	183.9	195.6	213.1	179.5
CFRP	$\sigma_{L,max}$	N/mm^2	+	-	-	-	1300	1004	1137	1188	1083	1032
			-	-	-	-	962	1181	1329	1072	943	1350
	$\sigma_{R,max}$	N/mm^2	+	-	-	-	1107	951	1202	1095	1110	1092
			-	-	-	-	938	926	1062	1371	1254	1031
	Φ	%		-	-	-	45	41	46	48	44	47

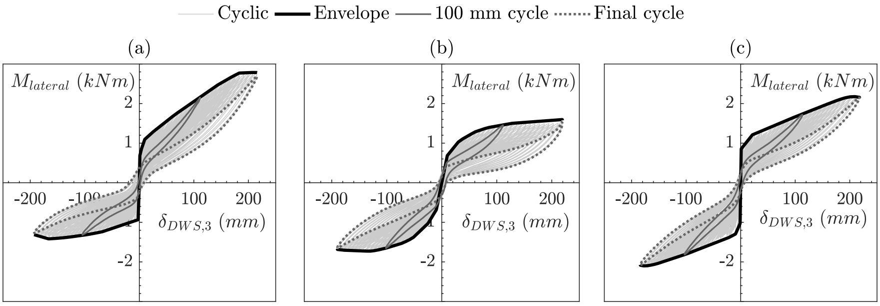

Figure 4.13: Moment – mid span displacement plots of specimens *STRIP-1* (a), *STRIP-2* (b) and *STRIP-3* (c).

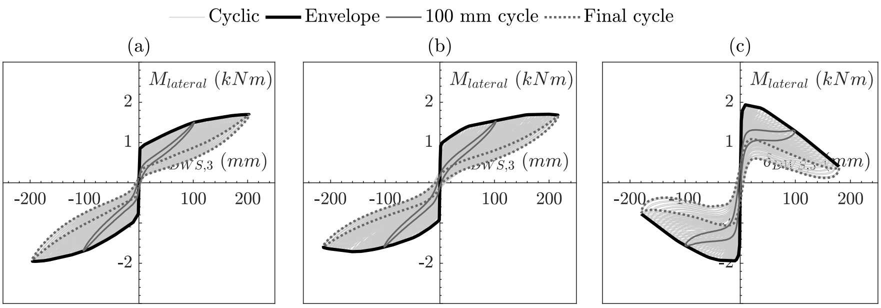

Figure 4.14: Moment – mid span displacement plots of *STRIP-4* (a), *STRIP-5* (b) and the wall tested with a higher axial load $V = 20$ kN: *STRIP-6* (c).

The backbone curves of the lateral moment - mid span displacement for all the *URM* specimens, and the *STRIP-2*, *STRIP-3*, *STRIP-4* and *STRIP-5* specimens are shown together in Fig. 4.15. Due to the strong asymmetric behaviour of *STRIP-1*, caused by erroneous CFRP positioning (explained in section 4.2.3, the corresponding envelope curve was not included.

The average moment capacity of the *URM* specimens, leaving out the push side of *URM-1*, was 0.78 kNm. The push-side of *URM-1* was not included due to the incorrect application of the gypsum layer on top of the specimen, leading to a non-uniform compression zone, and thus causing a difference in eccentricity of the axial load during hinge formation at the top of the specimen. The resistance reached nearly zero when the mid span displacement ($\delta_{DWS,3}$) reached the nominal wall thickness. Unanticipated hick-ups were observed towards the end of the pull cycles for specimens *STRIP-2* and *STRIP-3* (Fig. 4.13). These were attributed to the unexpected scraping of the profile that was clamped on the specimen (2^{nd} from top) to the steel frame at the right side of the wall. Traces of scraping on the steel frame were observed after the experiment.

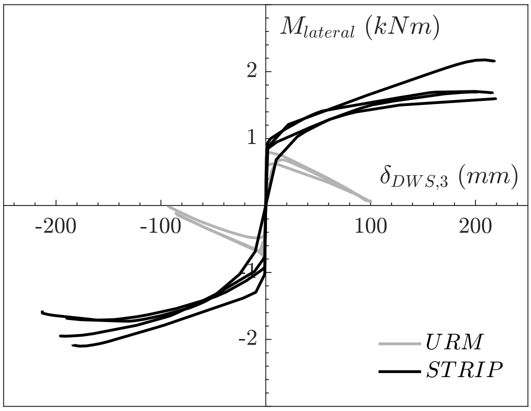

Figure 4.15: Backbone lateral moment – mid span displacement plots of all *URM* and *STRIP-2-3-4-5* specimens.

The average moment capacity of the STRIP specimens with an axial load of 4.8 kN, leaving out STRIP-1 due to the asymmetric behaviour, was found to be 1.82 kNm. The moment capacity of the URM wall (with 4.8 kN axial load) is increased with 133% with the installation of the flexible deep mounted CFRP strips. The mean displacement $(\delta_{3,max})$ corresponding to the maximum lateral resistance increased roughly with a factor 90 from 2.1 mm *(URM-2 and URM-3)* to 186.7 mm *(STRIP-1 until STRIP-5)*. Due to the limitations of the actuator stroke, the instability displacement of the retrofitted specimens with low axial load could not be determined. For *STRIP-6*, the specimen with an axial load of $V = 20$ kN, the instability displacement was estimated at roughly 200 mm by extrapolating the backbone curve. Due to the high axial load on specimen STRIP-6, the tensile forces from the CFRP strips were predominately countering the second order effects rather than increasing the lateral moment resistance.

4.2.2 Failure mechanisms and damage to masonry

The crack patterns that occurred in the *URM* and *STRIP* specimens are provided in Figs. 4.16 and 4.17 respectively. In fixed-fixed cases, the rocking mechanism develops after cracking at the wall top, usually the weakest section due to the lower axial load, followed by cracking at the bottom and finally at the wall mid-height [116]. Since there was no bond present between the (gypsum capped) top of the specimens and the beam exerting the vertical load, the first full crack developed at at the bottommost mortar bed joint for all specimens except *STRIP-3*. The second and final bed joint crack occurred at mid-height of the URM specimens, above the 23^{rd}, 28^{th} and 24^{th} layer for the *URM-1*, *URM-2* and *URM-3* specimens respectively. A two-block rigid body behaviour was initiated after the mid-height crack.

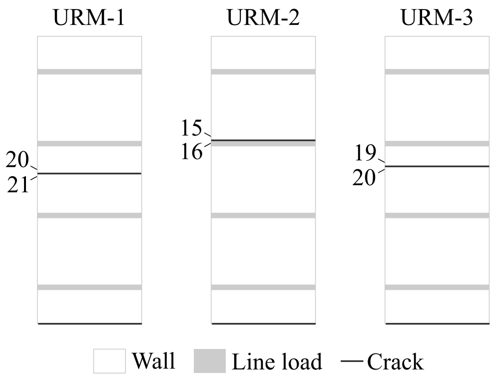

Figure 4.16: Schematic overview of the crack pattern of the URM specimens in the full-scale out-of-plane experimental campaign.

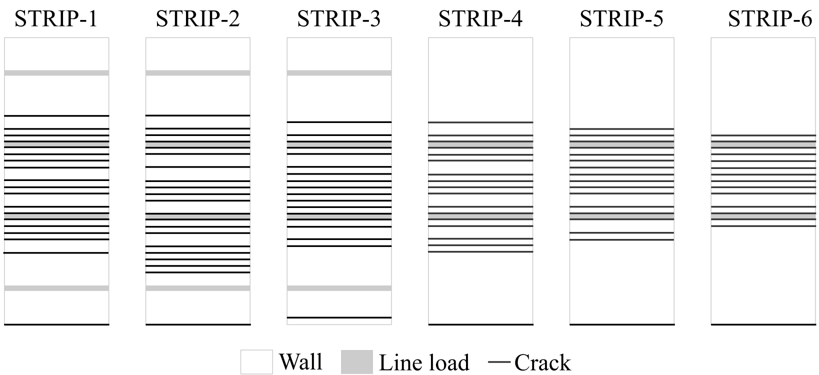

Figure 4.17: Schematic overview of the crack pattern of the STRIP specimen in the full-scale out-of-plane experimental campaign.

Multiple bed joint cracks over the height of STRIP specimens were formed, ranging from 14 to 20 in total. The distance between the bed joint cracks was predominantly a single brick layer. The cracks were more concentrated around the part with the maximum, constant moment. The fully developed crack pattern of *STRIP-3* is shown in Fig. 4.18a.

Looking at the similarities between the *STRIP-1-2-3* (four line load) and *STRIP-4-5* (two line load) specimens in terms of envelope shape, individual cyclic shapes, lateral resistance and the number of observed bed-joint cracks over the height, the different position and/or number of applied line loads did not have a significant influence on the crack pattern and response of the STRIP specimens with a low axial load. Due to the relatively high loading rates, the exact determination of the first mid-height crack and the evolution of the fracture path during the experiments was difficult to determine.

(a)

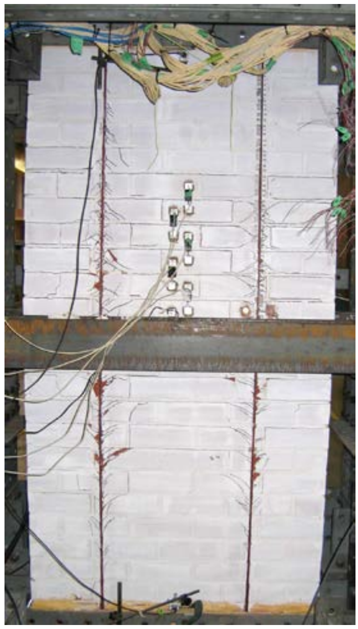

(b)

Figure 4.18: Comparison damage on out-of-plane loaded CFRP retrofitted masonry. Specimen STRIP-3 at the maximum target displacement (a). Intermediate cracking failure mechanism of an NSM CFRP retrofitted masonry wall (b), using a conventional stiff adhesive for CFRP mounting. [117]

With increasing target displacement, more crushing of the mortar layers was observed. In contrast to the quasi-dynamic experimental pull-out campaign, no splitting behaviour or intermediate cracking of the masonry was observed due to the deep mounted CFRP reinforcement. This can either be attributed to the improved confinement, or to the lower stress levels of the CFRP strips in the current experimental campaign with respect to the direct pull-out experiments performed (1,400 N/mm^2 versus 2,800 N/mm^2).

An experimental study on the out-of-plane behaviour of NSM CFRP retrofitted and one-way spanning masonry walls was conducted by *Kashyap* [117]. This experimental campaign included masonry walls which had similar dimensions. Regarding the failure mechanisms of these walls intermediate crack debonding and vertical in-plane shear failure were reported, as shown in Fig. 4.18b. With the exception of one wall specimen, herringbone cracking predominantly occurred in the brick units in the vicinity of the CFRP strip, indicating formation of the Intermediate Crack (IC) debonding failure mechanism. With out-of-plane airbag experiments on NSM CFRP retrofitted, one-way spanning masonry walls, *Dizhur* [118] also reported the intermediate crack debonding failure mechanism. Except for the formation of multiple bed joint cracks and crushing of the masonry for higher mid-span displacements, the application of a flexible adhesive instead of a conventional stiff adhesive seems to protect the masonry substrate from the intermediate cracking and vertical in-plane shear failure, likely due to a more evenly spread of the stresses over the masonry.

4.2.3 Stresses in the CFRP strip

Using the equations presented in paragraph 4.1.4, the tensile stress distribution of the CFRP strips was determined. The stress distribution in both the left and right CFRP strip are shown in Fig. 16 for all the STRIP specimens, at four different target displacements. The pull direction (positive force and displacement) is represented by solid lines, whereas a dashed line represents the push-direction. Some lines were incomplete due to failing strain gauges during the tests.

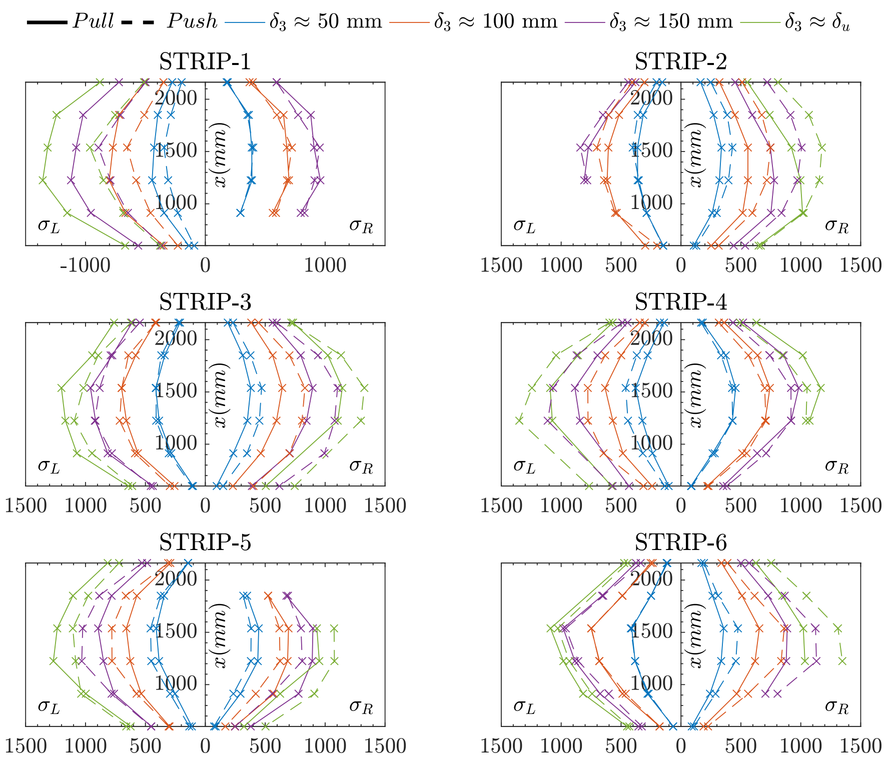

Figure 4.19: Stresses in left (σ_L) and right (σ_R) CFRP strips in N/mm² over the height for all the STRIP specimens.

The maximum stress in the CFRP strips at the ultimate displacement was in the range 926-1371 N/mm², with a mean value of 1115 N/mm². The maximum utilization of the tensile capacities of the used CFRP strips was 48% within this experimental campaign. In overall, the reached stress levels in the CFRP strip did not differ for the push and pull cycles. The left strip of specimen STRIP-1 and right strip of specimen STRIP-6 showed noticeable difference. Following the strain gauge readings, the left CFRP strip reached a peak stress of approximately 1,300 N/mm² during a pull cycle, whereas this value was around 950 N/mm² during a push cycle for STRIP-1. This significant difference was attributed to the position of the CFRP strips within the groove. In order to validate the correlation between the CFRP stress and strip positioning, specimen STRIP-1 was cut in multiple prisms after the out-of-plane experiment. The cuts, parallel to the bed joints, were made above brick layers 14, 18, 22 (mid-height of the specimen), 26 and 30. A photo of the CFRP strip positioning at these cross-sections are provided in Fig. 4.20.

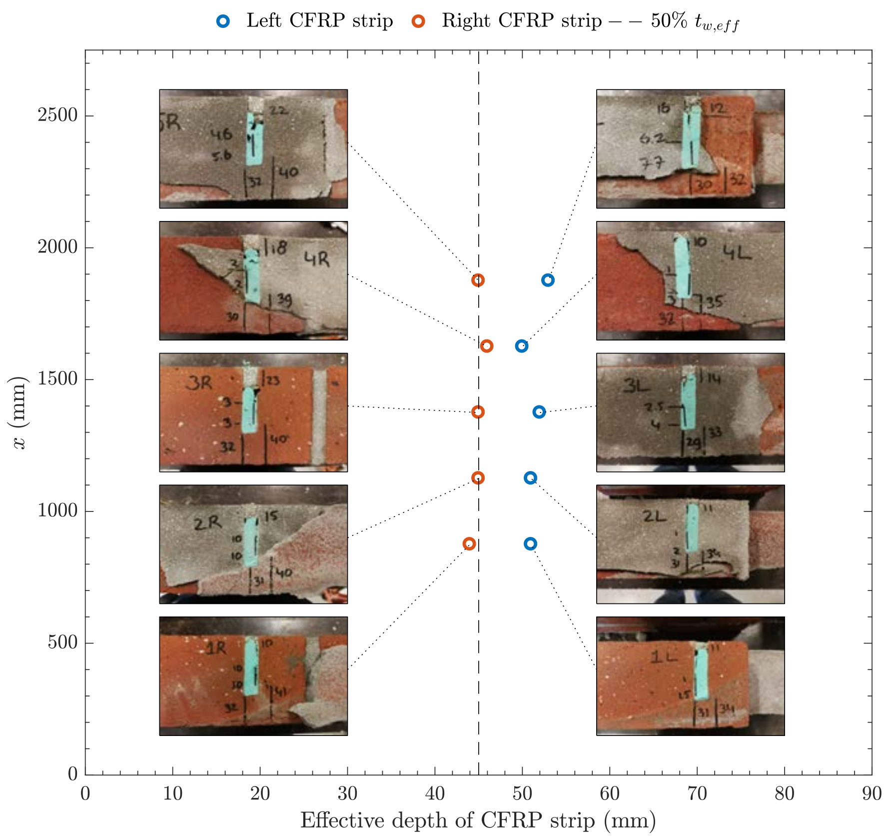

Figure 4.20: Effective depth of both CFRP strips of specimen *STRIP-1*.

The mean depth of the CFRP strip with respect to the retrofitted surface was 51.4 mm and 45.0 mm for the left and right CFRP strip respectively. Looking at the stresses of the right CFRP strip for *STRIP-1*, as shown in Fig. 4.19, it was observed that the stress levels over the height of the CFRP strip for both the pull and push direction showed no significant difference. This is conform the expectations, as the mentioned CFRP strip is positioned centrally with respect to the effective thickness (90 mm) of the wall. Looking at the cross-section of the wall, shown in Fig. 4.21 for a centrally placed CFRP strip, the strain levels of the CFRP strip are the same for both the pull and push direction for a given displacement of the wall. For this illustration the actual stress block was replaced by a fictitious rectangular block. When the CFRP strip has an offset of 6.4 mm with respect to the center position, as was the case for the left CFRP strip of specimen *STRIP-1*, there is a significant difference of strain in the CFRP strip for both the push and pull direction. As the slender walls have a limited thickness, this difference in CFRP strain between the push and pull direction can lead to a significant deviation in CFRP stress levels. The influence of the inaccurate placement of the CFRP strips had a significant impact on the lateral moment resistance, as the lever arm, i.e. the distance between the compressed zone of the masonry and the CFRP strip, also was affected.

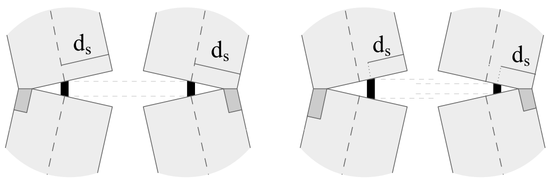

Figure 4.21: Effect offset retrofit on the CFRP strip strain for a given displacement.

Fig. 4.20 also shows that at certain locations the CFRP strip is placed too close to the side of the grooves, leading to insufficient adhesive coverage between the masonry and the CFRP strip. This could have affected the bond of the CFRP strips, resulting in (local) underutilization of the FDM CFRP retrofit.

4.2.4 CFRP force transferred to masonry

Fig. 4.19 shows that the difference between the strain gauge readings decreased towards mid-height of the specimen. This difference was quantified in Fig. 4.22, where the mean difference in force ΔF_p in a single CFRP strip per unit length is plotted against the measured displacement $\delta_{DWS,3}$. ΔF_p follows from Eq. 4.15

Fig. 4.22 shows five sections, as was illustrated in Fig. 4.11. For all the *STRIP* specimens, it was observed that the mean difference in tensile force is the lowest for section 3, at the mid-height of the specimens. The mean difference in tensile force in a single CFRP strip per unit length ΔF_p, i.e. the mean force per unit length transferred from a single CFRP strip to the masonry, was in the range of 1-10 N/mm for section 3. This means that under cyclic out-of-plane loading, limited force is transferred from the CFRP strip to the masonry around mid-height for a region of ~ 300 mm in length.

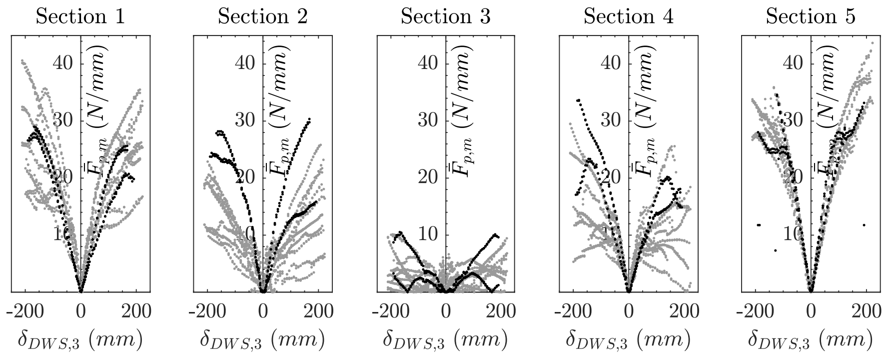

Figure 4.22: Mean difference in force ΔF_p in a single CFRP strip per unit length, plotted against $\delta_{DWS,3}$ for specimens *STRIP1-5* (grey dots) and specimen *STRIP-6* (black dots).

For all *STRIP* specimens with a low axial load, ΔF_p was predominately in the range 10-20 N/mm and 20-35 N/mm at $|\delta_{DWS,3}| \approx 200$ mm for sections 2/4, and sections 1/5 respectively. This means that the stress transferred from the CFRP strip to the masonry decrease towards mid-height of the wall. For the *STRIP-6* specimen, ΔF_p was predominately in the range 15-30 N/mm at $|\delta_{DWS,3}| \approx 200$ mm for sections 1/2/4/5. The stresses transferred from the CFRP strip to the masonry remain approximately the same outside the mid-height region of approximately 300 mm.

4.2.5 Moment - CFRP stress - curvature relationships

The internal moment and CFRP stress relationships for the cross-sections at height $\frac{3}{8}h_w \leq x < \frac{5}{8}h_w$ of the *STRIP1-5* specimens and *STRIP-6* specimen, are provided in Figs. 4.23a and 4.23b respectively. A strong linear correlation was found between stress in the CFRP strips and the internal moment: $R^2 = 0.93$ for *STRIP-1-2-3-4-5* and $R^2 = 0.94$ for *STRIP-6*. Even though a strong linear correlation was found between stress in the CFRP strips and the internal moment (Fig. 4.23), the lateral moment resistance tends to flatten out towards a mid-span displacement of 200 mm (Figs. 4.13-4.14). This was especially the case for *STRIP-2*, *STRIP-4* and *STRIP-5*. In the course of the experiment an increasing part of the tensile force in the CFRP strips were likely used to counter the increasing second order effects rather than increasing the lateral resistance of the retrofitted wall.

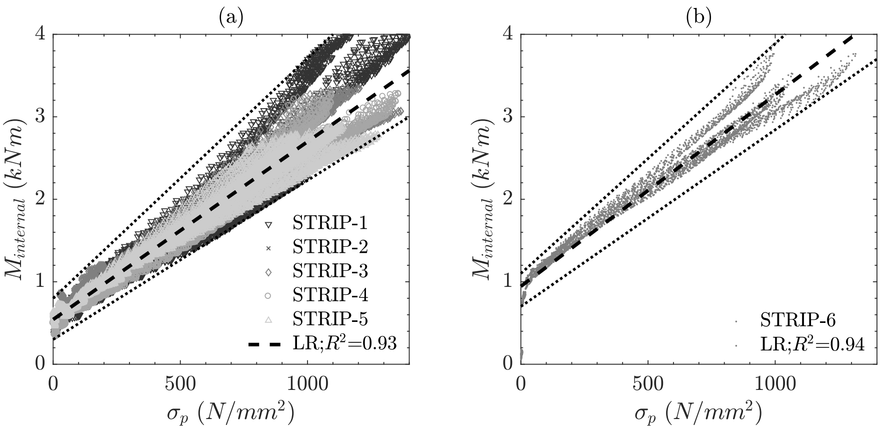

Figure 4.23: Internal moment and CFRP stress (σ_p) relation for $\frac{3}{8}h_w \leq x \leq \frac{5}{8}h_w$ for: *STRIP1-5* (a) and *STRIP-6* (b). Dashed lines show the linear regression.

The moment curvature correlations for the STRIP specimens were determined using the data processing steps as mentioned in section 4.1.4. The internal moment and curvature relationships for the specimen cross-sections at height $\frac{3}{8}h_w \leq x < \frac{5}{8}h_w$ of the *STRIP1-5* specimens and *STRIP-6* specimen, are provided in Figs. 4.24a and 4.24b respectively. The relationships presented in this subsection were used for modelling purposes in the sections 4.3, 4.4 and 4.5.

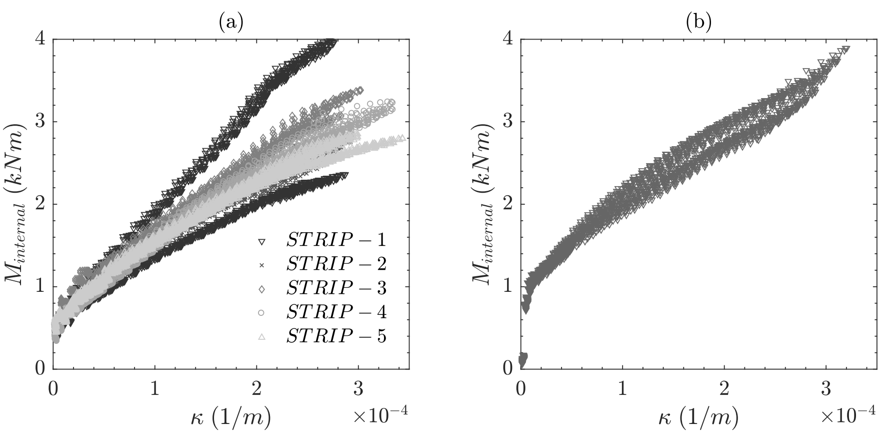

Figure 4.24: Internal moment and curvature (κ) relation for $\frac{3}{8}h_w \leq x \leq \frac{5}{8}h_w$ for: *STRIP1-5* (a) and *STRIP-6* (b).

4.2.6 Equivalent viscous damping

The equivalent hysteretic damping values as a function of the target displacement for each cycle $\delta_{DWS,3,target}$ is provided in Fig. 4.25a and Fig. 4.25b for all specimens tested four and two line loads respectively. For both the *URM* and *STRIP* groups, the hysteretic damping values increased with increasing values for the cycle displacement target. The increase in damping was likely linked to the accumulation of damage during test repetitions, such as the mortar deterioration in the cracked bed joints. Both the *URM* and *STRIP-6* (high axial load) specimens showed significantly higher hysteretic damping values with respect to the other *STRIP* specimens. Additionally, where the hysteretic damping values remained constant in order of magnitude for increasing target displacements for the *STRIP-1-2-3-4-5* specimens, both the URM and *STRIP-6* (high axial load) specimens roughly showed a linear increase of hysteretic damping values for increasing target displacements until $\xi_{hyst} \approx 0.10$ and 0.13 respectively at ultimate target displacements.

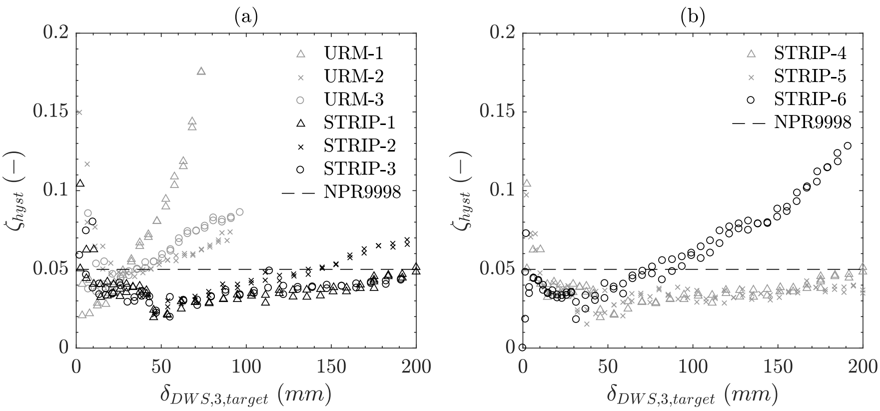

Figure 4.25: The equivalent hysteretic damping values versus the target displacement $\delta_{DWS,3,target}$ for each run for all specimens tested with: the four line load configuration: *URM* and *STRIP-1-2-3* (a) and tested with the two line load configuration: *STRIP-4-5-6* (b). The dashed line represents the standard damping value $\xi_{hyst} = 0.05$ for out-of-plane loaded URM walls as provided in *NPR9998*.

The mean value for hysteretic damping for the *STRIP-1-3-4-5* specimens was determined at 0.036. Specimen *STRIP-2* $\left(\xi_{hyst,mean} = 0.048\right)$ was not included in the determination of the overall mean hysteretic damping value due to the significant overshoot for hysteretic damping values, especially for target displacements of 130 mm or more, with respect to the other STRIP specimens tested at a low axial load. The standard damping value $\xi_{hyst} = 0.05$ for out-of-plane loaded URM walls as provided in NPR9998 [92], results in an overestimation for the *STRIP-1-2-3-4-5* specimens, and a conservative assumption for the URM and *STRIP-6* specimens.

4.2.7 Initial and effective stiffness

The initial stiffness k_{ini} as a function of the target displacement $\delta_{DWS,3,run}$ for each run for all specimens tested with the four line load configuration *(URM, STRIP-1-2-3)* is shown in Fig. 4.26a. The same relation is shown in Fig. 4.26b for the specimens tested with the two line load configuration *(STRIP-4-5-6)*.

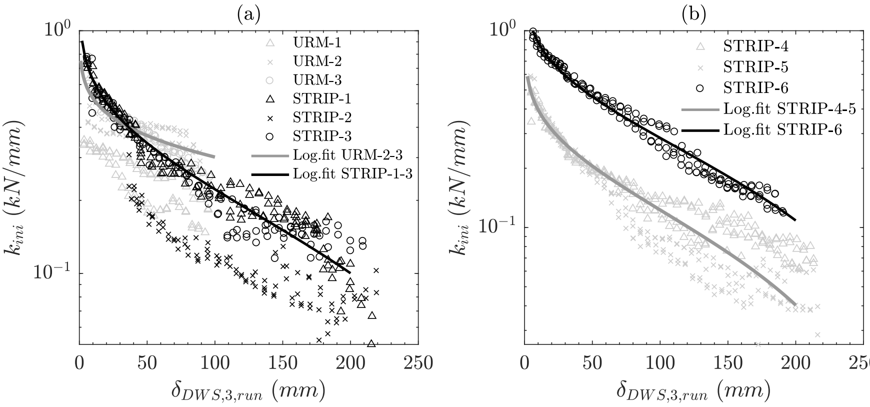

Figure 4.26: The initial stiffness k_{ini} versus the target displacement $\delta_{DWS,3,target}$ for each run for all specimens tested with: the four line load configuration: *URM* and *STRIP-1-2-3* (a) and tested with the two line load configuration: *STRIP-4-5-6* (b). Grey and black solid lines represent the logarithmic regression for specimens: URM-2-3 (R_2 = 0.68) and STRIP-1-3 (R_2=0.95) respectively (a); STRIP-4-5 (R_2 = 0.95) and STRIP-6 (R_2=0.99) with the higher axial load respectively (b).

Looking at target displacements up to ~ 40 mm in Fig. 4.26a, the decrease in initial stiffness with increasing target displacement is approximately the same for the URM and STRIP-1-2-3 specimens. For target displacements in the range 40 mm to ~ 100 mm, the initial stiffness of the STRIP specimens showed a stronger decrease with respect to the URM specimens. This stronger decrease in initial stiffness was linked to the accumulation of more damage during test repetition. Due to the activation of the FDM CFRP strips, the compression forces in the masonry are increased, leading to more mortar deterioration in the cracked bed joints. The slope of decrease of the initial stiffness with increasing target displacement was comparable for the STRIP-4-5 and STRIP-6 (higher axial load) specimens, as shown in Fig. 4.26b with the logarithmic fitting curves.

The effective stiffness k_{eff} as a function of the target displacement for each run ($\delta_{DWS,3,target}$) for all specimens tested with the four line load configuration *(URM, STRIP-1-2-3)* is shown in Fig. 4.27a, and in in Fig. 4.27b for the specimens tested with the two line load configuration *(STRIP-4-5-6)*.

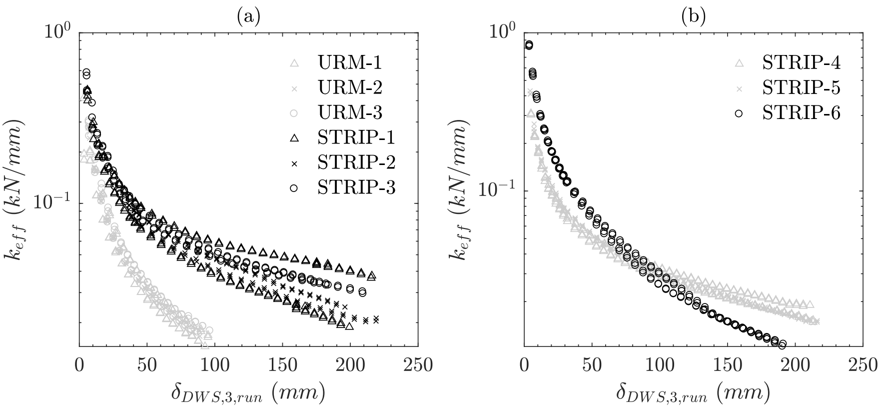

Figure 4.27: The effective stiffness k_{eff} versus the target displacement $\delta_{DWS,3,target}$ for each run for all specimens tested with : the four line load configuration: *URM* and *STRIP-1-2-3* (a) and tested with the two line load configuration: *STRIP-4-5-6* (b).

4.3 Initial engineering model

The out-of-plane experiment results described in the previous chapter have demonstrated the effectiveness of the proposed retrofit scheme within the current study. With the initial engineering model proposed by Wijte et al. (2017), the out-of-plane capacity of a FDM CFRP retrofitted wall was derived from the CFRP strips. The mechanical model consisted of two rigid masonry blocks and a discrete joint at mid-height of the wall, as shown in Fig. 4.28. The relation between the internal moment and the rotation in the joint is based on the bond behaviour of the CFRP-strips.

The relation between the rotation in the joint and the displacement at mid-height, follows from Eq. D.7. The rotation in the joint results in a displacement difference between the CFRP strip and the masonry (Δ_s), which is obtained in accordance with Eq. 4.18, where here d_s is the effective depth of the CFRP strip and x_u is the ultimate depth of the compression zone. This displacement will be denoted as slip.

$$\varphi(\delta) = \frac{\delta}{\frac{1}{2}h_w} \tag{4.17}$$

$$\Delta_s(\delta) = \varphi(\delta)\left(d_s - xu\right) \tag{4.18}$$

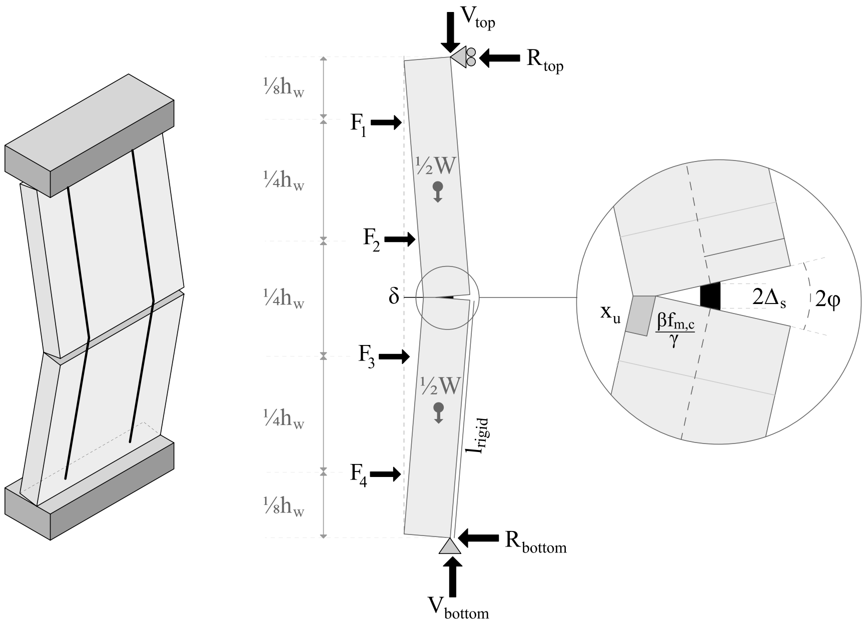

Figure 4.28: Original engineering model for out-of-plane behaviour of the tested one-way spanning FDM CFRP retrofitted masonry.

The force-slip relation for the CFRP strip in the rigid block was determined using the averaged multi-linear local bond-slip relation as a part of a partial-interaction model, as proposed in section 3.5. This averaged multi-linear local bond-slip relation was determined at a loading rate that had a similar order of magnitude as the loading rate of the CFRP strips within the current experimental campaign. The force-slip relationship of the FDM CFRP strip for various rigid block heights is provided in Fig. 4.29.

Since the maximum stress in a single CFRP strip was determined as 1350 N/mm² during the experimental campaign, a linear relation was assumed between the loaded-end slip and the stress in stress in the CFRP strip up to this limit (Eq. 4.19). The force in a single CFRP strip was determined using Eq. 4.20, where b_p and t_p are the width and thickness of the CFRP strip respectively.

$$\sigma_p(\delta) = \frac{\Delta_s(\delta)}{2.9mm} 1{,}350 \frac{N}{mm^2} \tag{4.19}$$

$$F_s(\delta) = \sigma_p(\delta)\, b_p t_p \tag{4.20}$$

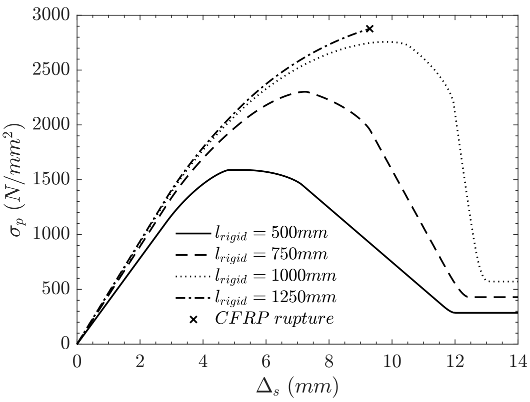

Figure 4.29: Original engineering model for out-of-plane behaviour of the tested one-way spanning FDM CFRP retrofitted masonry.

The depth of the compression zone was determined using Eq. 4.21, where the actual stress block was replaced by a fictitious rectangular block of intensity β times the masonry compressive strength (f_m). The degradation in masonry is covered by factor γ.

$$x_u(\delta) = \frac{n_s F_s(\delta) + F_M}{\frac{\beta f_m}{\gamma} l_w} \tag{4.21}$$

The number of CFRP strips and the length of the wall is represented by n_s and l_w respectively. F_M is the axial compressive force in the joint without the CFRP strip contribution, determined with Eq. 4.22, where W is the weight of the wall and V is the axial force on the wall.

$$F_M = V + \frac{1}{2} W \tag{4.22}$$

The internal moment was obtained using Eq. 4.23

$$M_{int}(\delta) = 2F_M z_N(\delta) + n_s F_s(\delta)\left(d_s - \frac{x_u}{2}\right) \tag{4.23}$$

where z_N is the distance between the centre of the cross section and the point of gravity of the compression force in the masonry, determined using Eq. 4.24.

$$z_N = \frac{t_w - x_u}{2} \tag{4.24}$$

The sum of the external moment follows from Eq. 4.25.

$$M_{lat}(\delta) = M_{int}(\delta) - V\delta \tag{4.25}$$

The lateral moment - displacement relationship determined using the original rigid block model was compared with the experiments in Fig. 4.30, using the input parameters as provided in Table 4.3. The original engineering model significantly overestimated the lateral-moment and displacement relation. Even with the instruction of a degradation factor in masonry of $\gamma = 1.6$ the overestimation of the model remained.

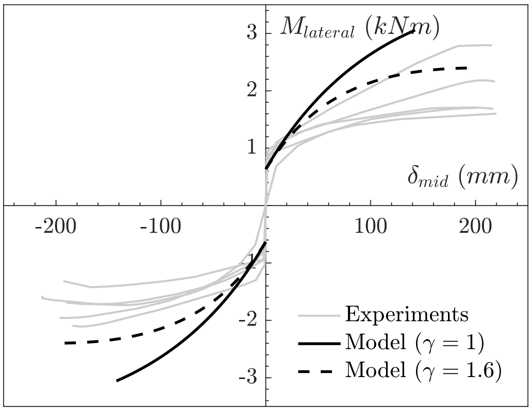

Figure 4.30: Lateral moment-displacement: relations determined with the original engineering model and relations obtained from the experiments with specimens *STRIP-1-2-3-4-5*.

Table 4.3: Input parameters for engineering model.

Parameter	Description	Value	Unit
b_p	Width of a CFRP strip	20	mm
d_s	Effective depth of CFRP strip	45	mm
f_m	Compressive strength masonry	8	N/mm²
h_w	Height wall	2,750	mm
l_w	Length wall	965	mm
n_s	Number of CFRP strips	2	-
t_p	Thickness of a CFRP strip	1.4	mm
t_w	Effective thickness of the wall	90	mm
V	Axial load on wall	4.8	kN
W	Mass of the wall	4.7	kN
β	Rectangular block parameter	0.85	-
γ	Masonry degradation factor	1-1.6	-

The CFRP stress - internal moment relation determined with the model and obtained via experiments of the *STRIP1-2-3-4-5* specimens are presented in Fig. 4.31. The CFRP stress - internal moment relation following from the initial engineering model showed good correspondence with the experimentally obtained values. The inclusion of the masonry degradation factor had limited influence on the internal moment and CFRP stress relation following from the original engineering model.

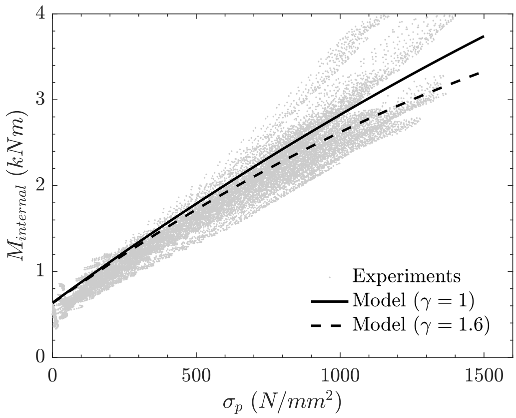

Figure 4.31: Internal moment - CFRP stress: relations determined with the original engineering model and relations obtained from the experiments with specimens *STRIP-1-2-3-4-5*.

The original engineering model failed to provide a good approximation of the experimentally obtained lateral moment – mid span displacement relations. The main limitation of this model was the assumption of a single crack at mid-height of the wall, whereas multiple bed joint cracks over the height of the wall, ranging from 14 to 20 in total, were observed during the experimental campaign.

4.4 Non-linear model

4.4.1 Material model

FOr the cross-section analysis, the masonry and the CFRP strip were considered as separate interacting components with an own stress-strain relation. The stress-strain relations are summarized in Fig. 4.32. It should be stated that the tensile and compression side of the masonry as shown in Fig. 4.32 are disproportionate for illustrative purposes. An overview of the material parameters is provided in Table 4.4.

The idealized stress-strain curve for masonry under compression and tension is determined using Eq. 4.26, where:

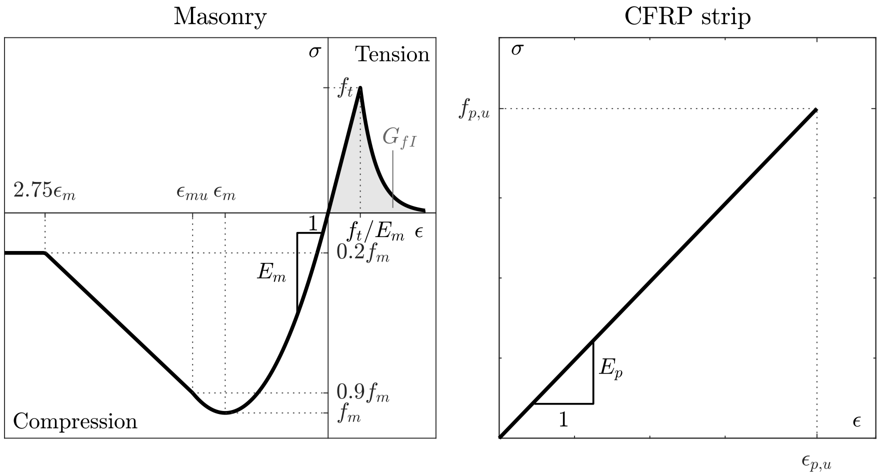

Figure 4.32: Idealized stress-strain relations for masonry under compression and tension, and CFRP under tension.

Table 4.4: Material parameters for the non-linear model.

Parameter	Symbol	Value	Unit
Young's modulus masonry	E_m	3,350	N/mm²
Young's modulus CFRP strip	E_p	198,000	N/mm²
Compressive strength masonry	$f_{m,c}$	8	N/mm²
Tensile strength masonry	$f_{m,t}$	0.25	N/mm²
Tensile strength CFRP	$f_{p,t}$	2,880	N/mm²
Mode I fracture energy	G_{fI}	4.2-11.5	N/m

- E_m is the Young's modulus of masonry;
- $f_{m,c}$ is the compressive strength of masonry, $\varepsilon_{m,c}$ the corresponding strain determined with Eq. 4.27;
- $\varepsilon_{m,cp}$ is the strain corresponding to $0.9f_{m,c}$ in the descending part. At this point the stress-strain curve shifts from parabolic to linear descending relation;
- $0.2f_{m,c}$ is the maximum residual compressive stress and corresponding failure strain $(\varepsilon_{m,cu})$. The failure strain determined as $\varepsilon_{m,cu} = 2.75\varepsilon_{m,cm}$ for mortar with lime content [119];
- $f_{m,t}$ is the tensile strength of the masonry;
- G_{fI} is the mode I fracture energy of the masonry;
- w is the crack width. The relation between the crack width and the strain is determined with the sum of the height of a single bed joint and the height of a single brick, as presented in Eq. 4.28;

- $e^{-\frac{f_{m,t}}{G_{fI}}w}$ is the factor representing tension softening.

$$\sigma_m(\varepsilon) = \begin{cases} f_{m,t}e^{-\frac{f_{m,t}}{G_{fI}}w} & \text{if } \varepsilon > \frac{f_{m,t}}{E_m}; \\ E_m\varepsilon & \text{if } 0 > \varepsilon \leq \frac{f_{m,t}}{E_m}; \\ f_{m,c}\left(2\frac{\varepsilon}{\varepsilon_{m,cm}} - \left(\frac{\varepsilon}{\varepsilon_{m,cm}}\right)^2\right) & \text{if } \varepsilon_{m,cp} < \ \varepsilon \leq 0; \\ f_{m,c}\left(0.9 - 0.7\frac{\varepsilon-\varepsilon_{m,cp}}{\varepsilon_{m,cu}-\varepsilon_{m,cp}}\right) & \text{if } \varepsilon_{m,cu} < \ \varepsilon \leq \varepsilon_{m,cp},; \\ 0.2f_{m,c} & \text{otherwise} \end{cases} \tag{4.26}$$

$$\varepsilon_{m,cm} = \frac{2f_{m,c}}{E_m} \tag{4.27}$$

$$w = \varepsilon\left(h_{brick} + h_{bedjoint}\right) \tag{4.28}$$

The Young's modulus and the compressive strength of the masonry were determined as 3,350 N/mm² and 8.0 N/mm² respectively with the companion tests. The flexural strength of masonry obtained was 0.375 N/mm². Generally a factor 1.5 is assumed between the average tensile bond strength and the flexural strength [120]. The tensile strength of the masonry was thus assumed at 0.25 N/mm². For the fracture energy, values in the range 4.2-11.5 N/m were reported by Vermeltfoort & van der Pluijm [121] for masonry typologies that are similar to the masonry used in this research. Comparing the compression stress-strain relation of the material model with the measurements obtained from the compression tests on masonry prisms, both shown in Fig. 4.33, it was observed that the proposed material model and parameters provide a good approximation of the experimentally determined compression behaviour until the peak strength. Due to lack of experimental data for the post-peak region within the current study, a comparison was made with the results of another experimental study on the characterization of different types of Groningen masonry. From the comparison of the normalized (towards the peak) stress-strain curve of the proposed material model (dotted line in Fig. A.3) with the stress-strain curve domain (grey area in Fig. A.3) of masonry in vertical compression as reported by Jafari, Rots, Esposito and Messali [91], it was observed that the post-peak stress-strain relationship following from the proposed material model was within the boundaries of the obtained stress-strain curves for masonry by [91].

The stress-strain relationship of the embedded CFRP strips are provided in Eq. 4.10. The Young's modulus and tensile strength of the CFRP strip, as reported in section 2.2, was 198,000 N/mm² and 2,880 N/mm².

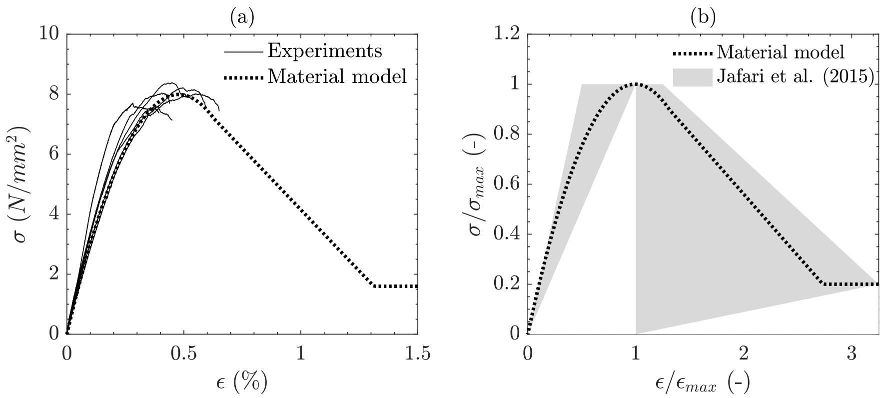

Figure 4.33: (a) Comparison of the compression stress-strain relationship of the material model (dotted line) with the measurements obtained from the compressions tests on masonry prisms (black lines). (b) Comparison of the normalized (towards their peak) compression stress-strain relationship of the material model (dotted line) with the normalized stress-strain curve domain reported by [91] (grey area).

4.4.2 Cross section analysis

The simplified rectangular cross section of the FDM CFRP strip retrofitted specimens is provided in Fig. 4.34. The lined area represents the compressed zone of the cross section. Two CFRP strips are present at position z=0, which result in a combined tensile force of F_p. The net force in the masonry is the sum of the masonry tensile force $(F_{m,t})$ and the masonry compression force $(F_{m,c})$. It is assumed that the strain profile is linear, and the CFRP strips are perfectly bonded without any slip. The strain distribution over height z is obtained using Eq. 4.29, where ε_A and ε_B are the maximum compressive and tensile strain respectively for the masonry.

$$\varepsilon(z) = \frac{1}{2}(\varepsilon_A + \varepsilon_B) + (\varepsilon_B - \varepsilon_A)\frac{z}{t_w} \tag{4.29}$$

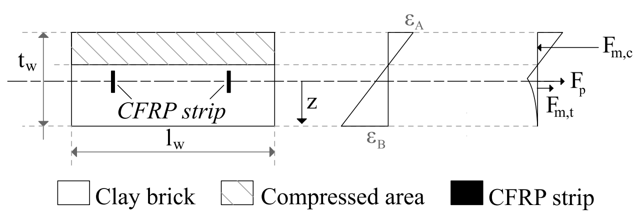

Figure 4.34: Cross section analysis of the FDM CFRP retrofitted specimens.

For the maximum strain on compressed side (A), a corresponding maximum tensile strain of the masonry (B) was determined where the condition as provided in Eq. 4.30 was met. This was the condition in which the tensile forces (CFRP strip, masonry) and compressive forces in the masonry were in balance. The moment curvature relation at mid-height is assumed to be representative for the full wall. The axial load (V) on a specimens and the weight (W) of a specimens were 4.8 kN and 4.7 kN respectively. The net force in the masonry, and the tensile forces in the CFRP strips were derived from Eqs. 4.31 and 4.32 respectively. The moment and curvature were determined with Eq. 4.33 and 4.34 respectively.

$$F_m + F_p + V + \frac{W}{2} = 0 \tag{4.30}$$

$$F_m = \int_{-\frac{t_m}{2}}^{\frac{t_m}{2}} \sigma_m(\varepsilon(z))\, l_w dz \tag{4.31}$$

$$F_p = E_p \cdot \varepsilon(z=0) \cdot b_p \cdot t_p \cdot n_s \tag{4.32}$$

$$M = \int_{-\frac{t_m}{2}}^{\frac{t_m}{2}} \sigma_m(\varepsilon(z))\, l_w z dz \tag{4.33}$$

$$\kappa = \frac{\varepsilon_B - \varepsilon_A}{t_w} \tag{4.34}$$

With the material parameters as provided in Table 4.4, the moment-curvature relation following from the model was obtained for $V = 4.8$ kN. This is shown with a black dotted line in Fig. 4.35a and compared to the moment-curvature relations of the constant moment zone $\left(\frac{3}{8}h_w \leq x \leq \frac{5}{8}h_w\right)$ for FDM CFRP retrofitted specimens (grey dots). After the first crack occurred in the model, there was a slight decline in the moment resistance, which was not consistent with the experimental findings. Furthermore, for curvatures higher than $1.5 \times 10^{-4} \frac{1}{m}$, the moment resistance following from the model was overestimated. This overestimation became stronger for higher curvatures. The moment – CFRP stress relation following from the model, as shown in Fig. 4.35b, provided a good approximation of the experimental results.

Using the non-linear material models and the cross section analysis, the moment-displacement relation was determined and compared with the experiments. This was done in Fig. 4.36 for both the 4 line loads and 2

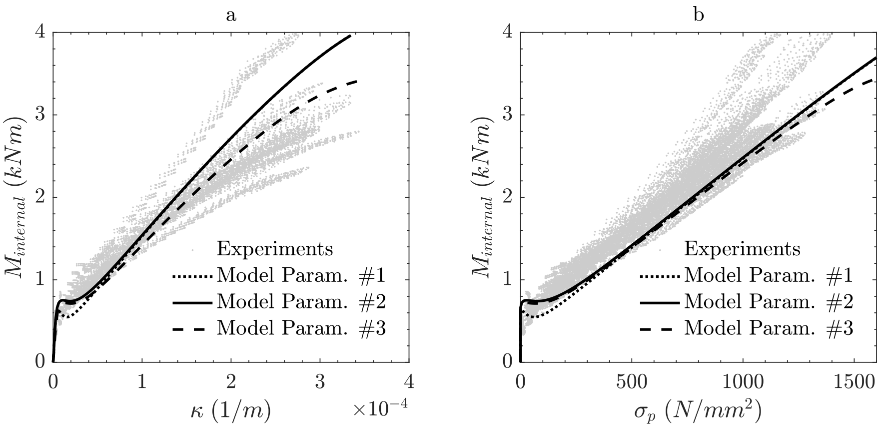

Figure 4.35: Internal moment-curvature relation (a) and Internal moment-CFRP stress relation (b) following from the cross-section analysis with the moment-curvature relations for the constant lateral moment zone for the FDM CFRP retrofitted specimens (V=4.8 kN).

line loads configuration when testing FDM CFRP retrofitted walls. With the initial set of parameters (set 1, as shown in Table 4.5), the first major difference with the non-linear model and the experiments was observed for the moment resistance at the end of the elastic branch of the envelope. This kink in the moment-displacement curve following the model, the kink being the first significant difference in stiffness of the envelope curve, was initiated at a moment resistance that was lower than found with the experiments. Increasing the fracture energy G_{fI} to 11.5 N/m (parameter set 2), the moment-displacement following the model fitted better with the experimentally obtained moment-displacement correlations for low displacement values ($\delta_{mid} \leq 5mm$). This improved fit was also observed for the moment-curvature relation and moment CFRP stress relation as shown in Fig. 4.35a and Fig. 4.35b respectively. Looking at the moment versus mid span displacement plots, it was observed that the model provides an underestimation of the moment resistance for $\delta_{mid} \leq 120mm$. For higher values for mid span displacement, the moment resistance following from the beam model proved an overestimation. Reducing the compressive strength and Young's modulus of masonry to 6 N/mm² and 2500 N/mm² respectively (keeping $\varepsilon_{m,cm}$ constant), which represents parameter set 3, did not result in an improved fit.

The model was also run with an axial load of 20 kN, and compared with the experimental results of specimen *STRIP-6*. No significant difference was observed between the outcomes following the three different parameter sets (Fig. 4.37). It should be noted that the calculations for the model were force based, so no results were obtained after the maximum moment was reached.

Table 4.5: Parameter set for the cross section analysis of the FDM CFRP retrofitted specimens (V=4.8 kN)

	E_m (N/mm^2)	f_m (N/mm^2)	G_{fI} (N/m)
Parameter set 1	3350	8	4.2
Parameter set 2	3350	8	11.5
Parameter set 3	2500	6	11.5

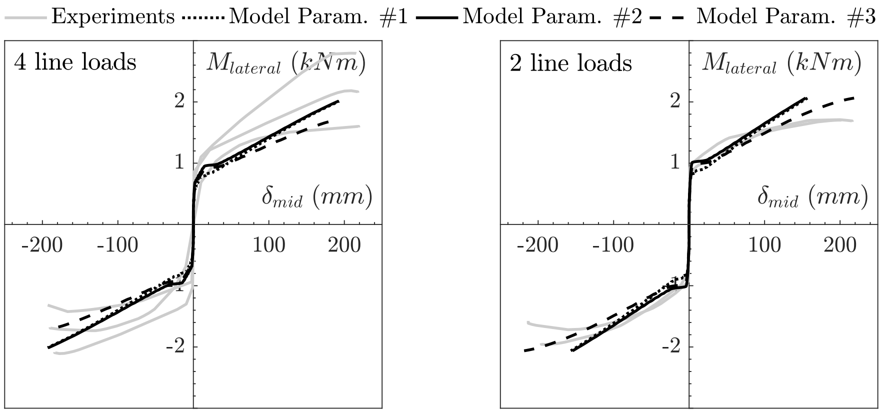

Figure 4.36: Lateral moment-displacement relation following from the cross section analysis for the FDM CFRP retrofitted specimens (V=4.8 kN), tested with four line loads (left) and two line loads (right).

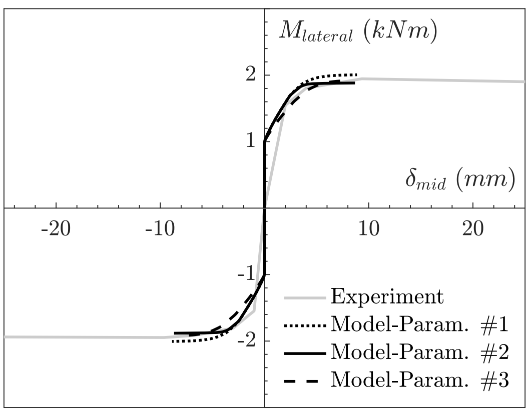

Figure 4.37: Lateral moment-displacement relation following from the non-linear model for an axial load of V =20 kN.

For low axial loads it was concluded that the cross-section analysis provided a decent estimation of the moment resistance until $\delta_{mid} \leq 120mm$. The over estimation of the model after $\delta_{mid} \approx 120mm$ was pre-dominantly attributed to the assumption of the slip of the CFRP strip being negligible. By means of the direct pull-out experimental campaign presented in section 3.3, free end slips around 2 mm for anchorage lengths of 1 m were obtained. For higher mid-span displacements, the slip of the CFRP laminates could become significant with respect to the elongation of the CFRP.

4.5 Revised engineering model

Due to the limitation of the original engineering model (section 4.3) and the non-linear model (section 4.4) for the out-of-plane assessment of vertically (one-way) spanning FDM CFRP retrofitted masonry walls, a revised engineering model was proposed. In addition to the original engineering model, the revised engineering model allowed for the introduction of additional cracks over the height of the wall. The revised engineering model is shown in Fig. 4.38.

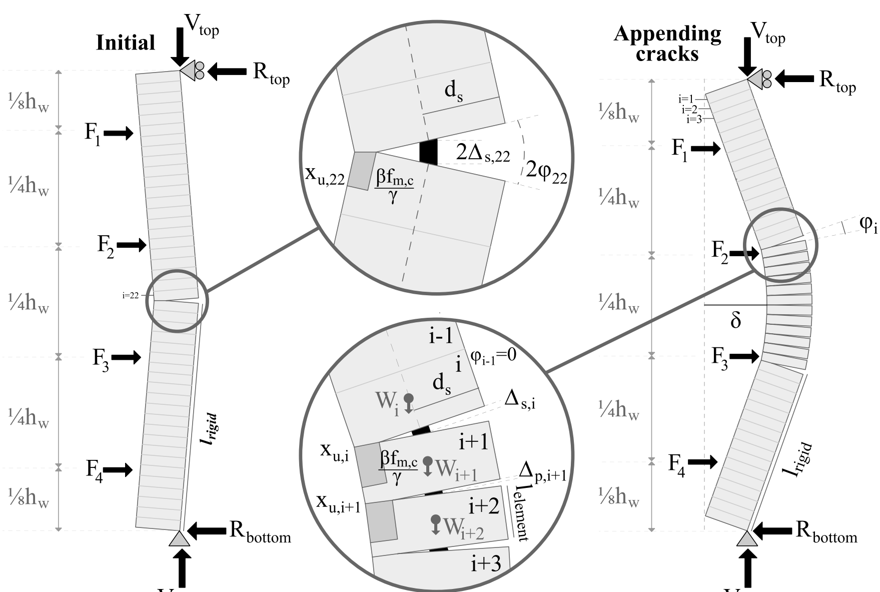

Figure 4.38: Revised engineering model for the out-of-plane behaviour of the tested vertically (one-way) spanning FDM CFRP retrofitted masonry.

4.5.1 Initial state: single crack

A single crack at mid-height is assumed as the initial state of the model, similar to the original model. The CFRP stress at mid-height was set as an input for the proposed rigid block model.

With the CFRP stress (σ_p), the axial load was determined as a function of the position using Eq. 4.35:

$$F_{axial,k} = \sigma_p \cdot b_p \cdot t_p \cdot n_s + V + \sum_{i=1}^{k} W_i \tag{4.35}$$

The depth of the compression zone $x_{u,k}$ was obtained using Eq. 4.36.

$$x_{u,k} = \frac{F_{axial,k}}{\frac{\alpha}{\gamma} f_{m,c} \cdot l_w} \tag{4.36}$$

Similar to the original engineering model, the actual stress block was replaced by a fictitious rectangular block of intensity β times the masonry compressive strength. The masonry degradation due to cyclic loading is covered by factor γ. It was assumed that the lever arm (z_s) equals the effective depth minus one-half of the assumed depth of the compression zone, as provided in Eq.4.37:

$$z_{s,k} = d_s - \frac{x_{u,k}}{2} \tag{4.37}$$

The internal moment is the result of the product of the total axial load at the considered height and the lever arm, following Eq. 4.38:

$$M_{int,k} = F_{axial,k} \cdot z_{s,k} \tag{4.38}$$

The rotation in the joint (Φ) connected to an uncracked rigid block (l_{rigid}) was obtained using Eq. 4.39, where δs_k is the loaded end slip at joint k.

$$\Phi_k = \frac{\delta s_k}{d_s - x_{u,k}} \tag{4.39}$$

The slip for the uncracked rigid block (l_{rigid}) was determined using the averaged multi-linear local bond-slip relation with the partial-interaction model, as was proposed in section 3.5. The force-slip relation of the deep and flexible mounted CFRP strip for various rigid block heights was provided in Fig. 4.29.

4.5.2 Crack initiation

The initial state as was shown in Fig. 36 was used to determine the relation between the CFRP stress and the internal moment. For a given stress in the CFRP strip, the axial load on the joint on mid-height $\left(F_{axial,22}\right)$ was determined using Eq. 4.35. The depth of the compression zone was obtained using Eq. 4.36, where degradation in masonry was neglected $\left(\gamma = 1\right)$. The internal moment followed from Eq. 4.38.

Given the axial load on the joint at mid height, the cracking moment for the adjoining bed joints was determined using a cross section analysis of the masonry (Fig. 4.39). The CFRP strips were excluded from this analysis. The strain distribution over height z is obtained using Eq. 4.40:

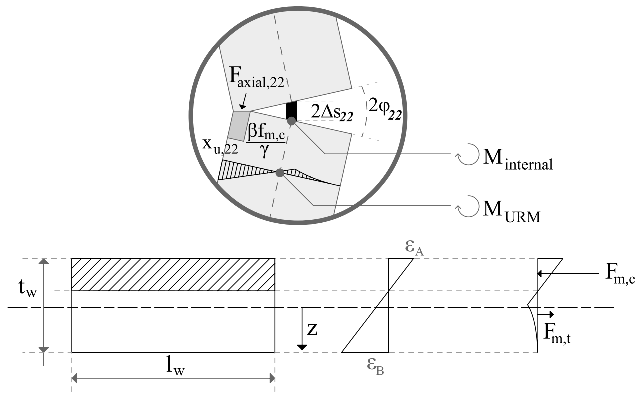

Figure 4.39: Cross section analysis rigid block.

$$\varepsilon\left(z\right) = \frac{1}{2}\left(\varepsilon_A + \varepsilon_B\right) + \left(\varepsilon_B - \varepsilon_A\right)\frac{z}{t_w} \tag{4.40}$$

For the strain on side A, a corresponding strain of the masonry on side B is determined where the condition as provided in Eq. 4.41 is met. This is the condition in which the tensile and compressive forces in the cross-section are in balance.

$$F_m = F_{axial,22} \tag{4.41}$$

The net force and moment in the rigid block cross section was derived from Eq. 4.42 and Eq. 4.43 respectively.

$$F_m = \int_{-\frac{t_m}{2}}^{\frac{t_m}{2}} \sigma_m\left(\varepsilon\left(z\right)\right) l_w dz \tag{4.42}$$

$$M_{URM} = \int_{-\frac{t_m}{2}}^{\frac{t_m}{2}} \sigma_m(\varepsilon(z))\, l_w z\, dz \tag{4.43}$$

Given the total axial load $(F_{axial,22})$ on the considered cross section, the maximum moment resistance of the rigid block can be determined. This moment resistance was compared with the internal moment to determine crack introduction in the rigid block. The URM moment resistance was exceeded when the stress in a single CFRP strips exceeds 470 N/mm^2 and 190 N/mm^2 for an axial load on top of the wall of 4.8 kN and 20 kN respectively.

4.5.3 Crack propagation

Once the CFRP stress level exceeded the limit determind in the previous section, an additional crack was initiated on the first uncracked bed joint of the rigid block, starting from the loaded end. The rotation in the newly cracked joint was obtained by using Eq. 4.39. The rotation in the joint not connected to the rigid block was determined by the elongation $\delta_{p,k}$ of the CFRP within that row with length $l_{element}$, according to Eq. 4.44, where $\delta_{p,k}$ follows from Eq. 4.45.

$$\varphi_k = \frac{\delta_{p,k}}{d_s - x_{u,k}} \tag{4.44}$$

$$\delta_{p,k} = \sigma_p E_p l_{element} \tag{4.45}$$

It should be noted that as long as the cracking stress is not reached, the rotation in a joint is equal to zero. Additionally, with every appending bed joint crack, the length of the rigid block reduces. The force-slip relation of the deep and flexible mounted CFRP strip therefore needs correction for shorter rigid block lengths.

Following the afore-mentioned calculations step by step, the lateral moment - displacement relation of the original rigid block model was determined and compared with the experiments in Fig. 4.40 for both the 4 line loads *(STRIP-1-2-3)* and 2 line loads configuration *(STRIP-4-5)*.

When using no degradation factor for the masonry due to cyclic loading $(\gamma = 1)$ and two line loads, the model (indicated with a solid black line) resulted in a significant overestimation of the moment resistance for $\delta_{mid} > 80$ mm. Implementing a degradation factor for the masonry due to cyclic loading of $\gamma = 1.6$ (dashed black lines in Fig. 4.40) resulted in a significantly improved overall fit. The same conclusions were drawn for a higher axial

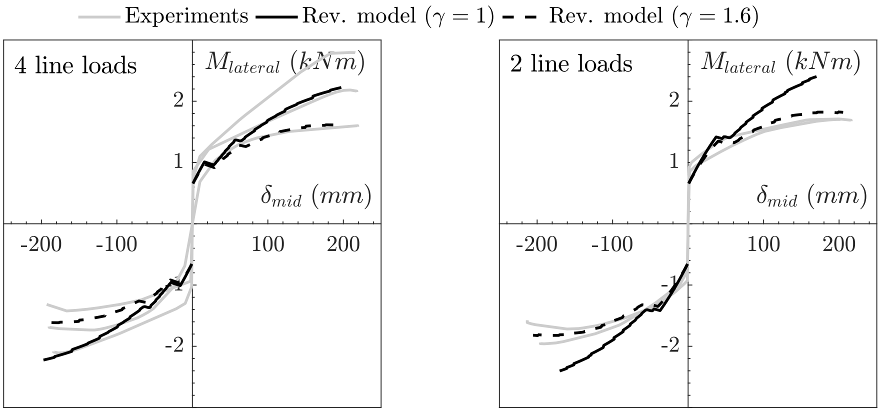

Figure 4.40: Lateral moment-displacement relation following from the revised engineering model for 4 line loads (left, specimens *STRIP-1-2-3*) and for 2 line loads (right, specimens *STRIP-4-5*).

load, as shown in Fig. 4.41, meaning the revised engineering model provides a good approximation of the experimental outcome for different axial loads when a cyclic degradation factor of $\gamma = 1.6$ is implemented. No significant difference was found between the obtained moment-displacement relationship using $\gamma = 1$ and $\gamma = 1.6$ until a mid-span displacement of 80 mm of the wall. The additional force of the FDM CFRP strips resulted in increased compressive stresses in the compression zone, which combined with high levels of deflection (up to 210% of the wall thickness) most probably resulted in excessive damage accumulation in the bed-joints. In this context, the factor of 1.6 to account for masonry degradation seems acceptable. It should be noted that the degradation factor of 1.6 was calibrated on this specific study and may not be extrapolated to a general conclusion.

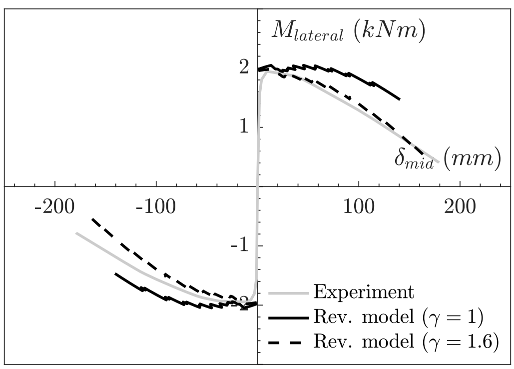

Figure 4.41: Lateral moment-displacement relation following from the revised engineering model for axial load $V = 20$ kN (specimen *STRIP-6*).

Comparing for the internal moment and CFRP stress relation, as shown in Fig. 4.42a and Fig. 4.42b for the low *V=4.8 kN)* and high axial load case *V=20 kN)* respectively, no significant deviation between the outcome of the revised engineering model and the experimental results were found. It should be noted that with the inclusion of cyclic degradation of the masonry (dashed black line), the internal moment and CFRP stress relation bends further away from the linear regression on the experimental results, nevertheless remaining within an acceptable range.

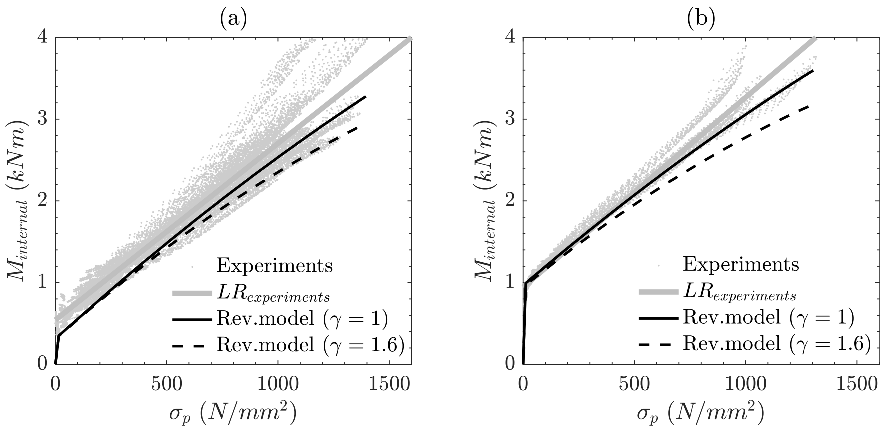

Figure 4.42: Moment-CFRP stress relation following from the revised engineering model (i = 22) with the moment- CFRP stress relations of the constant moment zone for axials loads: *V=4.8 kN* (a, *specimens STRIP-1-2-3-4-5*); *V=20 kN* (b, *specimen STRIP-6*).

4.6 Stiff vs. flexible adhesive systems: OOP behaviour in the NSM configuration

The vertical bending behaviour of CFRP retrofitted masonry walls was modelwise compared for both the stiff and the flexible adhesive system. For this analysis, the same wall dimensions and retrofitting configuration (2 CFRP strips) as the test specimens in this chapter are used. For the comparative study only the Near Surface Mounted (NSM) configuration was considered, as the effect of the deeper groove depth on the initiation of premature brick splitting when using a stiff adhesive couldn't be quantified. The CFRP strips were assumed to be placed right underneath the surface, resulting in an effective depth of 10 mm, instead of the regular $\frac{1}{2}t_w$ (center-depth of the wall) for the deep mounted configuration.

For the calculation of the lateral moment - displacement relation of the NSM CFRP retrofitted wall using a stiff adhesive, the cross-section analysis using the (non-) linear material models was used, following the design methodology provided by [117, 122]. Parameter set 3 was selected (Table 4.5) and the slip of the CFRP strip was neglected. The full debonding force F_u^∞ was determined at 63.9 kN for the stiff system in section 3.6.2. When the force in a single CFRP strip reached this value, intermediate cracking debonding occurred and the wall was considered as failed. As for the calculation of the lateral moment - displacement relation of the NSM CFRP retrofitted wall using a flexible adhesive, the revised engineering model was used with a degradation factor for the masonry of γ = 1.6. The wall was considered failed when the force in a single CFRP strip reached the rupture strength.

The lateral moment - displacement relation of NSM CFRP retrofitted walls using a stiff adhesive and a flexible adhesive are provided in Fig. 4.43. For both adhesive types, the lateral moment - displacement relation was determined at three levels of axial loads (V = 0; 10 and 20 kN).

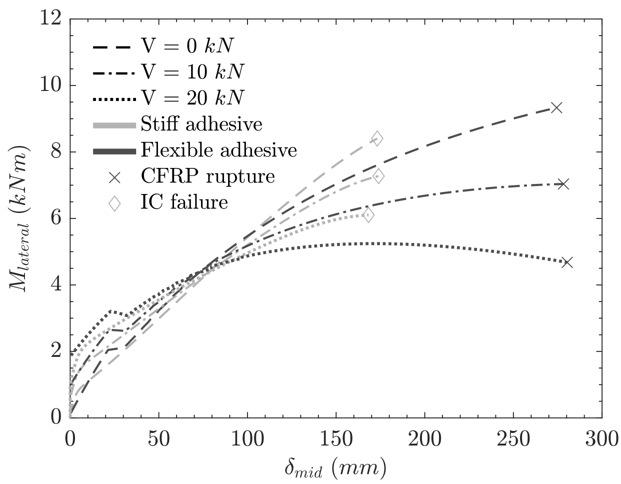

Figure 4.43: The lateral moment - displacement relation of NSM CFRP retrofitted walls using a stiff adhesive (light grey)and a flexible adhesive (dark grey). Three levels of axial load (V = 0; 10 and 20 kN) are considered. The failure mechanisms are intermediate crack debonding (diamond) and CFRP rupture (cross).

The stiff adhesive system eventually fails due to intermediate crack debonding (diamond in Fig. 4.43), whereas the flexible system adhesive system fails due to CFRP rupture (cross in Fig. 4.43). Up to an including an axial load of V =20 kN, the mean ultimate displacement (277 mm) of the flexible adhesive system was 62% higher than the mean ultimate displacement (171 mm) of the stiff adhesive system. With no axial load (V= 0 kN) the maximum lateral moment resistance was 8.4 kNm and 9.3 kNm respectively for the the stiff adhesive system and flexible adhesive system. Increasing the axial load to 10 kN, the maximum lateral moment resistance decreases for both the stiff (7.3 kNm) and flexible adhesive system (7.0 kNm). Further increasing the axial load, leads to a further decline of the maximum lateral moment resistance: (6.1 kNm) and (4.7 kNm) for the stiff and flexible system respectively. Due to the non-negligble slip and higher second order effects, the ultimate lateral moment resistance of the flexible adhesive system decreases more rapidly with increasing axial load.

4.7 Conclusions

An experimental program was undertaken to assess the out-of-plane behaviour of vertically (one-way) spanning full scale clay brick masonry walls retrofitted with flexible deep mounted (FDM) carbon fiber reinforced polymer (CFRP) strips. In the experimental testing program nine full-scale masonry walls were tested, from which six were retrofitted using the FDM CFRP technique. A new four or six point-bending test setup was proposed and used for cyclic out-of-plane testing of masonry walls, due to the limitations of both the air-bag setup and shaking table test within the scope of this research. The loading rate was selected at a level where the visco-elastoplastic effects of the used flexible adhesive were activated. An overarching objective of this study was to verify the effectiveness of the FDM CFRP strip strengthening system for the out-of-plane behaviour of one-way vertically spanning full-scale masonry walls. An additional objective of this research was to validate the engineering model for FDM CFRP retrofitted walls. Furthermore, the validity of the proposed bond slip laws for FDM CFRP strips (Chapter 3) was assessed for flexural loading conditions rather than uni-axial tensile loading conditions. From the experimental campaign the following conclusions were drawn:

1. Except for the formation of multiple bed joint cracks (ranging from 14 to 20 in total) and crushing of the masonry for higher mid-span displacements, the application of a flexible adhesive instead of a conventional stiff adhesive seems to protect the masonry substrate from intermediate cracking and vertical in-plane shear failure.

2. The maximum stress in the CFRP strips at the ultimate displacement was in the range 926-1371 N/mm^2, with a mean value of 1115 N/mm^2. The maximum utilization of the tensile capacities of the used CFRP strips was 48% within this experimental campaign.

3. For the specimens tested with an axial load of (V=4.8 kN), the average resistance of the unreinforced masonry (URM) specimens (n=3) was 0.78 kNm, whereas the average resistance of the FDM CFRP retrofitted specimens (n=5) was found to be 1.82 kNm. The moment capacity of the URM wall is increased with 133% with the installation of the FDM CFRP strips.

4. For the FDM CFRP retrofitted specimen with high axial load (V=20 kN), the tensile forces from the CFRP strips were predominately countering the second order effects rather than increasing the lateral moment resistance.

5. For the mean mid-span displacement corresponding to the lateral resistance, an increase of roughly a factor 90, from 2.1 mm (URM) to 186.7 mm (V = 4.8 kN), was determined. The instability displacement was approximately equal to the wall thickness for the URM specimens. For the FDM CFRP retrofitted specimen with high axial load, the instability displacement was estimated at 200 mm. For the FDM CFRP retrofitted specimens loaded with a low axial load, the instability displacement was not obtained due to the stroke limits of the used actuator.

6. Even though a strong linear correlation was found between stress in the CFRP strips and the internal moment, the lateral moment resistance tends to flatten out towards a mid-span displacement of 200 mm. This was linked to the increasing second order effects and damage accumulation at the masonry joints.

7. The mean value for hysteretic damping For the FDM CFRP retrofitted specimens with low axial load was determined at 0.036. Both the URM specimens and high axial load FDM CFRP retrofitted specimen showed a linear increase of hysteretic damping values for increasing target displacements with 0.1 and 0.15 respectively at ultimate target displacements.

The out-of-plane experimental campaign demonstrated the effectiveness of the proposed retrofit scheme within the current study. Another goal of this study on the out-of-plane behaviour was the development of a simple and practical applicable out-of-plane engineering model for FDM CFRP retrofitted masonry walls. From the modelling efforts the following conclusions were drawn:

8. The initial engineering model consisted of two rigid masonry blocks and a discrete joint at mid-height of the wall. The relation between the internal moment and the rotation in the joint was based on the bond behaviour of the CFRP-strips within the rigid blocks. This engineering model failed to provide a good approximation of the experimentally obtained lateral moment – mid span displacement relations, the main limitation being the presence of only one crack in the wall, whereas multiple bed joint cracks over the height of the wall were observed during the experimental campaign.

9. Performing a cross-section analysis using non-linear material models, it was found that the lateral moment capacity was overestimated after a mid-span displacement of 120 mm. The model assumed that the strain profile was linear, and the CFRP strips perfectly bonded without any slip. From the direct pull-out experimental campaign however, it was found that the slip of FDM CFRP strips was not negligible, especially for higher CFRP stresses.

10. A revised engineering model was proposed, where multiple cracks over the height of the wall were introduced. Using a factor of 1.6 to cover for bed joint degradation of the masonry due to cyclic loading, the model provided good agreement with the experimentally obtained lateral moment – mid-span displacement relationships for both the low axial load and the high axial load cases. Despite the slightly lower CFRP stress and internal moment relationship compared to the experimentally obtained values, the CFRP stress following from the revised engineering model provided a decent fit. It should be noted that the degradation factor of 1.6 was calibrated on this specific study and may not be extrapolated to a general conclusion.

11. The bond slip laws for FDM CFRP strips as determined in Chapter 3 using uni-axial tensile tests were successfully implemented in the engineering models.

12. The vertical bending behaviour of CFRP retrofitted masonry walls was model-wise compared for both the stiff and the system with flexible adhesive. For the comparative study only the Near Surface Mounted (NSM) configuration was considered, as the effect of the deeper groove depth on the initiation of premature brick splitting when using a stiff adhesive couldn't be quantified. The mean ultimate displacement (277 mm) of the flexible adhesive system was 62% higher than the mean ultimate displacement ($171mm$) of the stiff adhesive system. Due to the non-negligble slip and higher second order effects, the ultimate lateral moment resistance of the flexible adhesive system decreases more rapidly with increasing axial load when compared to the ultimate lateral moment resistance of the stiff adhesive system.

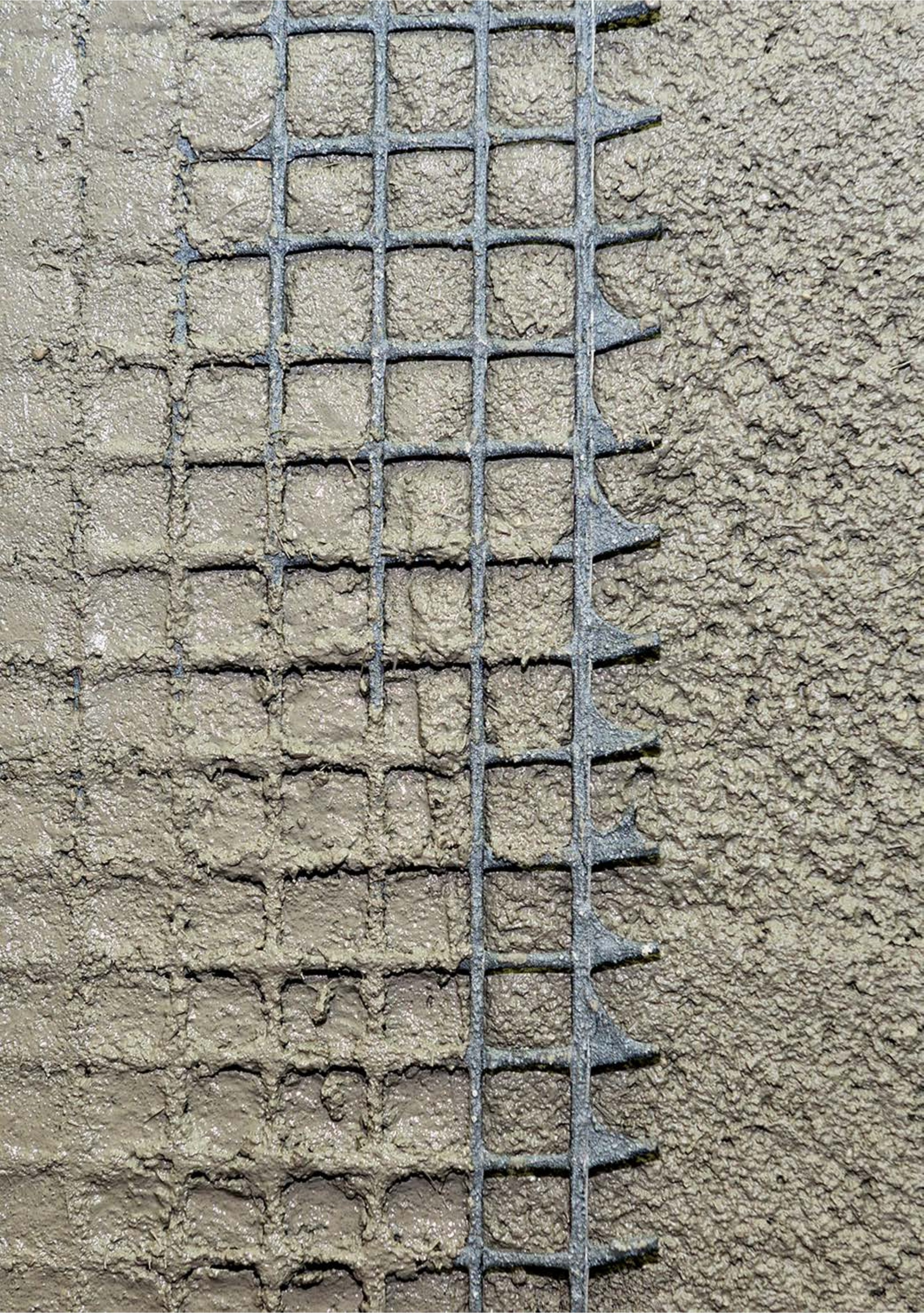

Chapter 5

Hybrid retrofit with FDM CFRP and FRCM: out-of-plane behaviour

For walls subjected to critical in-plane loading, the application of solely the flexible deep mounted (FDM) CFRP strips retrofit was expected to be insufficient. In Chapter 1 the addition of a one-sided fabric reinforced cementitious matrix (FRCM) overlay was proposed to form a hybrid retrofit with the FDM CFRP strips, in order to enhance the strength and pseudo-ductility of masonry for in-plane loading conditions. The addition of a single-sided FRCM overlay however, will also have a significant influence on the out-of-plane behaviour of the wall.

This chapter, based on [74, 78], outlines the out-of-plane (OOP) behaviour of masonry walls retrofitted with FDM CFRP strips and a single-sided FRCM overlay. The chapter starts with the discussion of an experimental campaign on the OOP behaviour of masonry panels retrofitted with solely a single sided FRCM overlay. The discussion of a second experimental campaign focuses on the OOP behaviour of full-scale masonry walls, retrofitted with both FDM CFRP strips and a single-sided FRCM overlay. The proposed modelling approach is validated for both experimental campaigns.

5.1 Small scale experiments

5.1.1 Building the specimens

A total of n=7 clay brick masonry panels, each panel consisting of 20 bond stacked bricks, were built by an experienced mason. The masonry specimens were constructed vertically, like a column, against a vertical sideboard to ensure minimum horizontal deviation and were left to cure for 28 days in the unheated laboratory (10-25 °C) before applying the FRCM layer.

The FRCM layer was installed only on one side of the masonry panels. After applying the first layer of polymer-modified mortar (5 mm in thickness), the CFRP mesh was pressed into position. This only applied to 4 of the 7 specimens (coded *OOP-FRCM*). The mesh, consisting of 10 continuous CFRP strands in the longitudinal direction, did not cover the outer two bricks at both sides. This was done to prevent clamping forces acting on the mesh near the supports during the out-of-plane experiments. Finally, a new layer of polymer-modified mortar was applied to embed the CFRP mesh, resulting in a nominal FRCM layer thickness of 20 mm. The OOP specimens were left to cure for 28 days in the unheated workshop (10-25 °C). An illustration of an OOP-FRCM specimen with a mesh is shown in Figure 5.1. No mesh was applied on three specimens (coded *OOP-CM*).

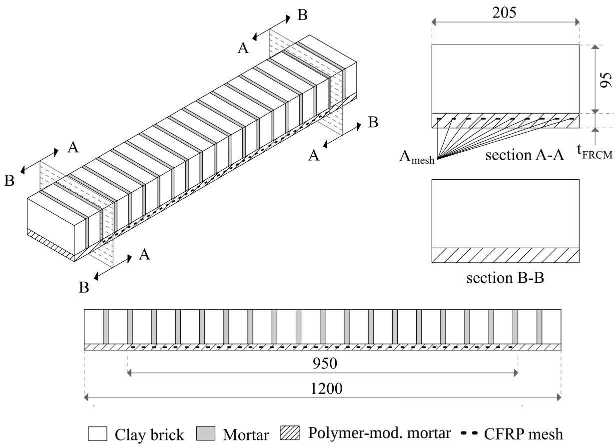

Figure 5.1: Schematic overview of an FRCM retrofitted masonry panel.

5.1.2 Test setup

A four-point flexural test was selected to test the out-of-plane response of the reinforced masonry panels. A schematic overview and a photo of the test setup are shown in Figs. 5.2 and 5.3 respectively. Two loading noses with an inter-distance of 340 mm applied load on the top of the masonry panel with a span of 1000 mm. One of the loading noses and one of the lower roller supports were able to rotate on their axes, parallel to the span direction. The others remained fixed. Softboard was placed between the masonry panel and the noses/rollers. To measure the curvature of the constant moment region of the masonry panel, two yoke deflectometers (one at each side) were used. A lightweight yoke was suspended between two bolts (spaced with distance $L_k = 280$ mm from each other) attached to the neutral axis of the masonry (within the constant moment region). LVDT's were attached to the centre of the yokes. The tip of the LVDT's rested on an L-shaped plate, measuring the deflection $(\delta_{\kappa_1}, \delta_{\kappa_2})$ during the experiment. On the opposite side of these L-shaped plates, two additional LVDT's measured the mid-span deflection $(\delta_{m1}, \delta_{m2})$. The results of these LVDT's were also averaged. Another two LVDT's measured the displacement with respect to the ground of the masonry panel right above the roller supports $(\delta_{s1}, \delta_{s2})$.

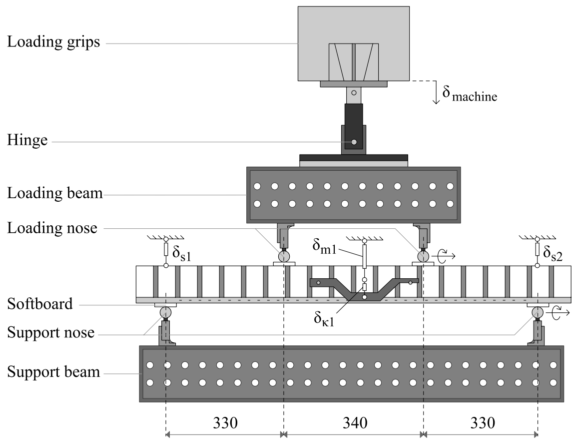

Figure 5.2: Schematic overview test setup for out-of-plane experimental campaign on FRCM reinforced masonry panels.

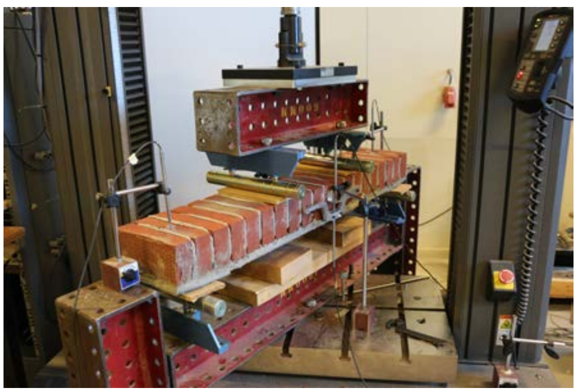

Figure 5.3: Photo test setup for out-of-plane experimental campaign on FRCM reinforced masonry panels.

5.1.3 Processing the measurements

Based on the sensor readings, several parameters were determined. The mean mid-span deflection was obtained in accordance with Eq. 5.1. The bending moment and curvature were obtained using Eqs. 5.2 and 5.3 respectively.

$$\delta_m = \frac{\delta_{m1} + \delta_{m2}}{2} - \frac{\delta_{s1} + \delta_{s2}}{2} \tag{5.1}$$

$$M = \frac{1}{2} F \left(\frac{1000 - 340}{2} \right) \tag{5.2}$$

$$\kappa = 4 \left[\frac{\delta_{\kappa 1}}{L_k^2 + 4\delta_{\kappa 1}^2} + \frac{\delta_{\kappa 2}}{L_k^2 + 4\delta_{\kappa 2}^2} \right] \tag{5.3}$$

After an initial load of 0.1 kN was applied, the experiment started at a deflection controlled loading speed of 1 mm/min. For the *OOP-FRCM* specimen that was tested unidirectional cyclic (coded *OOP-FRCM-C*), the initial mid-span deflection step was 1 mm. Each deflection step was applied two times in the single loading direction forming one load cycle, before increasing the mid-span target deflection with 1 mm. The moment of switching the loading direction, from unloading to loading, occurred force-controlled at a measured force of $F = 0.2\ kN$.

5.1.4 Results and discussion

An overview of the results of the four-point bending tests is provided in Table 5.1. It should be noted that the mid-span deflection results for specimen *OOP-FRCM-1* were not included due to errors with the LVDT's.

Failure mechanisms

The *OOP-CM* specimens that were reinforced with solely a polymer-modified mortar layer, failed suddenly with the formation of a single crack. It should be noted that one of the three *OOP-CM* specimen was damaged during transport, and therefore could not be tested. For the *OOP-FRCM* specimens, a total of five to seven cracks per specimen formed. The distance between the cracks ranged from 47 to 159 mm, and had a mean value of 98 mm. For the OOP-FRCM-C specimen a total of 11 cracks were formed, with a mean interdistance of 82 mm. The higher number of cracks was attributed to the cyclic loading. The crack patterns for the *OOP-FRCM(-C)* specimens are provided in Fig. 5.4. The pre-dominant failure mechanism for all *OOP-FRCM(-C)* was CFRP rupture, Fig. 5.5 shows an example.

Table 5.1: Results out-of-plane tests on FRCM reinforced masonry panels.

Parameter	Unit	OOP-CM-1	OOP-CM-2	OOP-FRCM-1	OOP-FRCM-2	OOP-FRCM-3	OOP-FRCM-C
$F_{max,uncr}$	kN	3.74	3.61	2.73-4.12	2.70-3.49	2.50-3.71	3.03-3.64
$\delta_{max,uncr}$	mm	0.35	0.41	-	0.27-0.56	0.21-0.71	0.29-0.83
$M_{max,uncr}$	kNm	0.60	0.58	0.45-0.68	0.44-0.56	0.42-0.60	0.49-0.60
$\kappa_{max,uncr}$	$10^{-3}/m$	2.5	3.1	2.4-4.2	0.8-4.3	1.6-3.9	2.4-6.7
$F_{max,cr}$	kN	-	-	8.06	7.35	5.25	8.55
$\delta_{max,cr}$	mm	-	-	-	6.99	5.49	8.77
$\delta_{u,cr}$	mm	-	-	-	7.04	5.68	8.80
$M_{max,cr}$	kNm	-	-	1.33	1.20	0.85	1.39
$\kappa_{max,cr}$	$10^{-3}/m$	-	-	85.8	80.3	44.2	87.4
$\kappa_{u,cr}$	$10^{-3}/m$	-	-	87.2	81.6	44.2	87.8

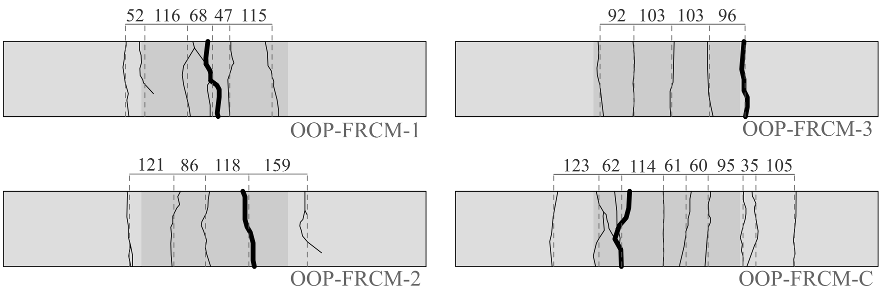

Figure 5.4: Crack patterns of the FRCM retrofitted masonry panels.

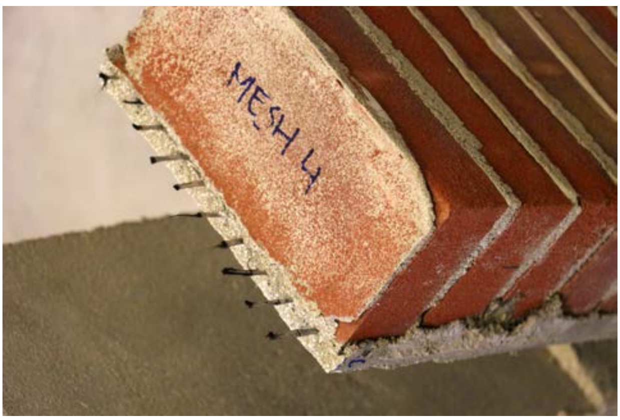

Figure 5.5: CFRP mesh rupture.

Moment, displacement and deflection

The *OOP-CM* specimens failed at a mean load and mid-span deflection of 3.64 kN and 0.38 mm respectively. The corresponding mean moment and curvature were 0.60 kNm and $2.9{\cdot}10^{-3}/m$. The cracking moment for the *OOP-FRCM* specimens was difficult to determine as no exact moment of cracking could be assigned in the graphs. With a mean moment of 0.53 kNm (range 0.42-0.68 kNm) to initiate the first crack, the cracking load for the *OOP-FRCM* showed a slight discrepancy with the results of the *OOP-CM* specimens. This was also applicable to the curvature, with a mean value and range of $3.2{\cdot}10^{-3}/m$ and $0.8\text{-}6.7{\cdot}10^{-3}/m$ respectively. When the upper bound was considered, the overall mean cracking moment and corresponding curvature for the specimens were 0.60 kNm and $4.1{\cdot}10^{-3}/m$ respectively.

Looking at the mean values for moment capacity (1.3 kNm), ultimate deflection (7.92 mm) and ultimate curvature ($85.5{\cdot}10^{-3}/m$) for the *OOP-FRCM* specimens (*OOP-FRCM-3* excluded), the added value of the CFRP mesh is quantified. The implementation of a CFRP mesh in the cementitous matrix leads to a significant improvement in deformation capacity.

Specimen *OOP-FRCM-3* was excluded from the determination of the mentioned mean values due to a different failure mechanism. This specimen failed due to a combination of moment and shear (brick splitting), outside of the constant moment regime.

Loading cyclically *(OOP-FRCM-C)* did not affect the strength, ultimate deflection or ultimate curvature when compared to the statically loaded specimens. Additionally, looking at the M-κ diagram presented in Fig. 5.6, it can be observed that there is no significant difference between the envelope of the cyclically tested specimen and the statically loaded specimens. With cyclic loading, during the unloading process towards the near initial state, an increasing permanent deflection was observed. This was attributed to the permanent slip of the CFRP mesh within the cementitous matrix.

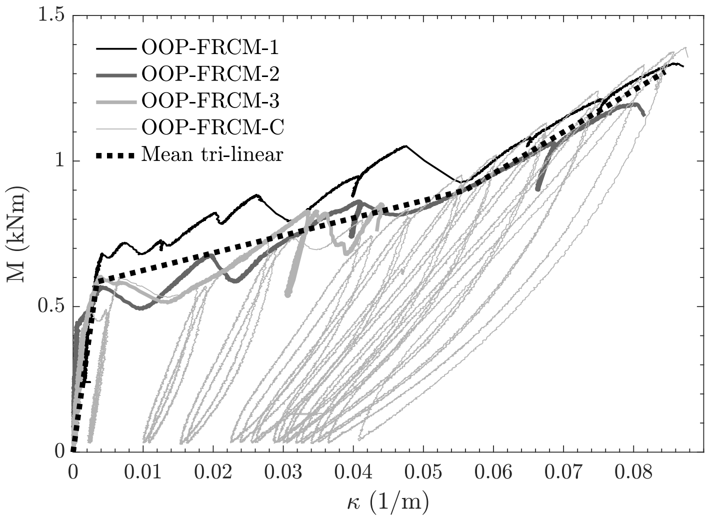

Figure 5.6: Moment curvature diagrams of the tested FRCM retrofitted panels.

5.1.5 Non-linear model

For the purpose of modelling the out-of-plane behaviour of FRCM retrofitted masonry panels, the masonry, the cementitous matrix and the CFRP mesh were considered as separate interacting components with an own stress-strain relation. After the formation of separate (non-) linear material models for the cementitous matrix and the embedded CFRP mesh, the cross sectional analysis was performed.

Material model

An overview of the material properties is provided in Table 5.2. The idealized stress-strain relation of the cementitous matrix and the embedded CFRP mesh are summarized in Fig. 5.7. The stress-strain curves for the cementitous matrix and the embedded CFRP mesh were determined using Eqs. 5.4 and 5.5 respectively, where E_{CM}, and $E_{mesh,em}$ are the Young's moduli of the cementitous matrix and the embedded CFRP mesh respectively.

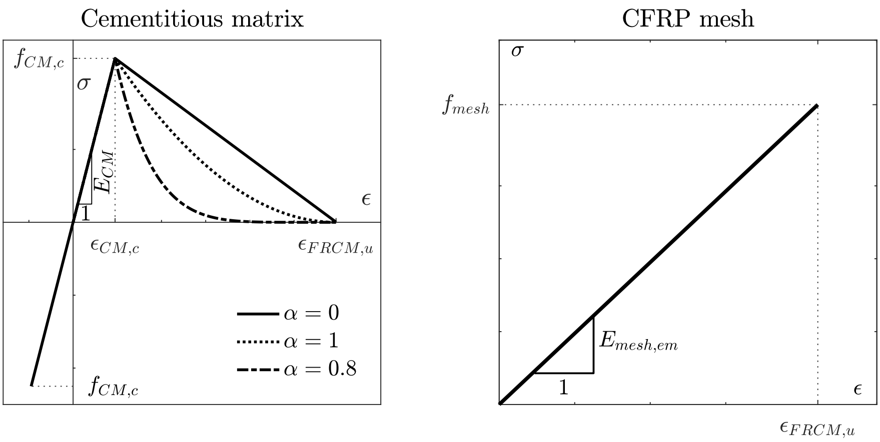

Figure 5.7: Idealized stress-strain relations for the cementitous matrix under compression and tension, and the embedded CFRP mesh under tension.

Table 5.2: Material parameters cementitous matrix and embedded CFRP mesh.

Parameter	Symbol	Value	Unit
Young's modulus of the cementitous matrix	E_{CM}	27,680	N/mm²
Tensile strength of the uncracked FRCM	$f_{CM,t}$	4.23	N/mm²
Tensile strength of the embedded CFRP mesh	$f_{mesh,em}$	1,700	N/mm²
Ultimate tensile strain of the CFRP mesh	$\varepsilon_{FRCM,u}$	1.9	%

$$\sigma_{CM}(\varepsilon) = \begin{cases} 0 & \varepsilon < 0, \\ \varepsilon \cdot E_{CM} & 0 < \varepsilon \leq \varepsilon_{CM}, \\ \varphi(\varepsilon) \cdot E_{CM} & \varepsilon_{CM} < \varepsilon \leq \varepsilon_{FRCM,u}, \\ 0 & \varepsilon > \varepsilon_{FRCM,u}, \end{cases} \tag{5.4}$$

$$\sigma_{mesh}(\varepsilon) = \begin{cases} 0 & \varepsilon < 0, \\ \varepsilon \cdot E_{FRCM,u} & 0 < \varepsilon \leq \varepsilon_{FRCM,u}, \\ 0 & \varepsilon > \varepsilon_{FRCM,u}, \end{cases} \tag{5.5}$$

The factor φ, used to describe the post-peak behaviour of the cementitous matrix using tension softening, is determined using Eq. 5.6, where the factor α defines the shape of the tension softening curve, where $\alpha = 0$ represents a linear declining tension softening curve.

The Young's moduli for the cementitous matrix and the embedded CFRP mesh are obtained following Eqs. 5.7 and 5.8 respectively, where $f_{mesh,em,u}$ is the roving strength of the CFRP mesh (1,700 N/mm^2) and f_{CM} is the tensile strength of the cementitous matrix (4.23 N/mm^2, section 2.3).

$$\varphi = \left(\frac{\varepsilon_{FRCM,u} - \varepsilon}{\varepsilon_{FRCM,u} - \varepsilon_{CM,c}} \right)^{1+\alpha} \tag{5.6}$$

$$E_{CM} = \frac{f_{CM}}{\varepsilon_{CM}} \tag{5.7}$$

$$E_{mesh,em} = \frac{f_{mesh,em,u}}{\varepsilon_{FRCM,u}} \tag{5.8}$$

The parameters $\varepsilon_{m,u}$, ε_{CM} and $\varepsilon_{FRCM,u}$ are the cracking strain of the masonry, cracking strain of the cementitous matrix and the ultimate strain of the FRCM respectively. Following the tensile test results presented in section 2.3, the value for $\varepsilon_{FRCM,u}$ was selected as 1.9% (overall mean value).

Cross-sectional analysis

The simplified rectangular cross section of the FRCM retrofitted masonry panel is provided in Fig. 5.8. The lined area represents the compressed zone of the cross section. The FRCM layer was modelled using two components, the embedded CFRP mesh (dotted line) and the reinforced mortar (dense lined area). It was assumed that the strain profile was linear, and the CFRP mesh and reinforced mortar were perfectly bonded without any slip until CFRP mesh rupture occurs.

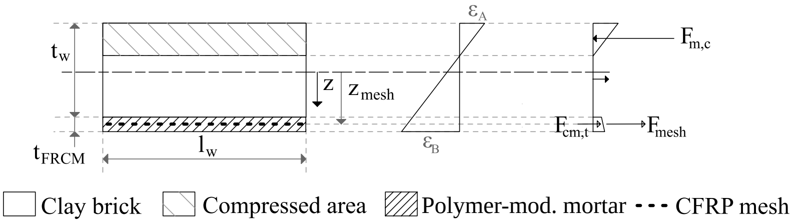

Figure 5.8: Cross section analysis of FRCM retrofitted specimens.

The strain distribution over height z was obtained using Eq. 4.29. For the maximum strain on the compressed side (ε_A), a corresponding maximum tensile strain of the masonry (ε_B) was determined where the condition as provided in Eq. 5.9 was met. This was the condition in which the tensile forces (CFRP mesh and cementitous matrix) and compressive force in the masonry were in balance. The net force in the masonry was obtained using Eq. 4.31. It should be noted that for the analysis in this section, the masonry was selected as a material with a bilinear compressive behaviour with a compressive strength, yield strain and ultimate strain of 14.8 kN, 0.25% and 0.35% respectively. The tensile strength of the mortar joints was neglected. The tensile forces in the embedded CFRP mesh and the cementitous matrix were determined in accordance with Eqs. 5.10 and 5.11 respectively.

Both the moment and curvature were determined with Eqs. 5.12 and 4.34 respectively. The thickness of the unreinforced masonry and the FRCM layer were represented by t_m and t_{FRCM} respectively. The distance between the centre of the URM panel (z=0 mm) and the CFRP mesh (z=50 mm) is represented by z_{mesh}. The cross-sectional area of the CFRP mesh (A_{mesh}) was 8.8 mm^2 for 10 continuous CFRP strands.

$$F_m + F_{CM} + F_{mesh} = 0 \tag{5.9}$$

$$F_{CM} = \int_{\frac{t_m}{2}}^{\frac{t_m}{2}+t_{FRCM}} \sigma_{CM}(\varepsilon(z))\, l_w dz \tag{5.10}$$

$$F_{mesh} = \varepsilon(z)\, E_{mesh,em} A_{mesh} \tag{5.11}$$

$$\begin{aligned} M = {} & \int_{-\frac{t_m}{2}}^{\frac{t_m}{2}} \sigma_m(\varepsilon(z))\, l_w z\, dz + \int_{\frac{t_m}{2}}^{\frac{t_m}{2}+t_{FRCM}} \sigma_{CM}(\varepsilon(z))\, l_w z dz \\ & + \varepsilon(z_{mesh})\, E_{mesh,em} A_{mesh} z_{mesh} \end{aligned} \tag{5.12}$$

Results

Using the input parameters as provided in Table 5.2, a moment-curvature curve is obtained using the proposed model and compared with the mean (tri-linear) experimental outcome, as shown in Fig. 5.9. With the given set of input parameters, (f_{CM}= 4.23 N/mm² and $\varepsilon_{FRCM,u}$ = 1.91%) the moment at ultimate curvature following the model was obtained as 1.39 kNm, which corresponds well with the mean experimental result. The value for the ultimate curvature following from the model however significantly overestimated the curvature found in the experiments. This is mainly attributed to the difference in the governing failure mechanism between the tensile tests and the out-of-plane experiments. In contrast to the tensile tests that failed predominantly due to CFRP mesh slippage, the *OOP-FRCM* specimens all failed due to CFRP mesh rupture. The measurements of the (ultimate) strain in the tensile tests included the slip of the CFRP mesh, whereas in the out-of-plane experiments only limited slippage of the CFRP mesh occurred, which resulted in a lower value for the (ultimate) strain. By changing the ultimate strain $\varepsilon_{FRCM,u}$ to 0.64%, as shown with the dashed line in Fig. 5.9, both the ultimate curvature and moment capacity following from the model correspond well with the mean experimental results.

A significant deviation was observed for both the cracking moment and corresponding curvature when comparing the model outcome with the experiments. This difference was attributed to the formation of shrinkage cracks during the curing process and transport, leading to a decrease in cracking strength. When the tensile strength of the uncracked FRCM is reduced from 4.23 N/mm² to 1.73 N/mm², a better fit is obtained between the model and mean experimental outcome for stage I (dash-dotted line in Fig. 5.9). Additionally changing the value from α=0 to α=0.8 (to account for non-linear tension-softening behaviour) improves the fit of the slope of stage II and stage III between the model outcome and the mean experimental results (solid black line Fig. 5.9).

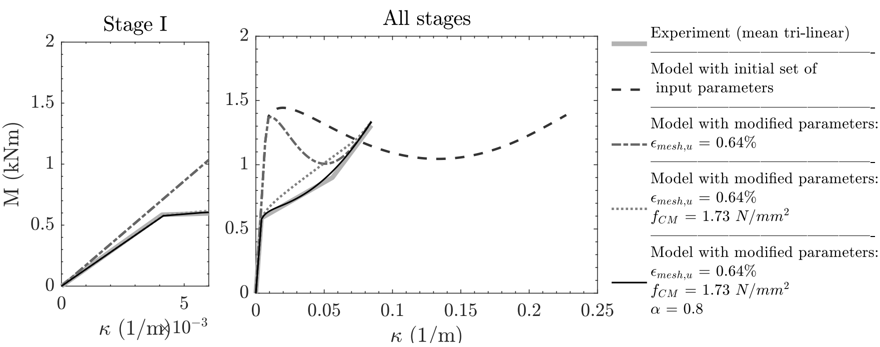

Figure 5.9: Moment-curvature comparison between proposed model and mean tri-linear experimental outcome.

5.2 Full scale experimental program

The wall specimens for the full-scale out-of-plane experimental program were built in the testing laboratory, using M10 mortar (see section 2.1 for more information). These specimens were built and tested in the same batch as the experimental program covered in Chapter 4 and the construction of the masonry walls followed the same procedure as presented in section 4.1. A total of 3 walls were constructed and reinforced with two FDM CFRP strips each and a single-sided FRCM overlay, following the installation procedure mentioned in section 1.4 and 1.5. The CFRP mesh had 44 continuous strands in the vertical direction. A schematic overview of the reinforced walls is provided in Fig. 5.10. Similar to the *STRIP* walls in Chapter 4, strain gauges were attached to the CFRP strips.

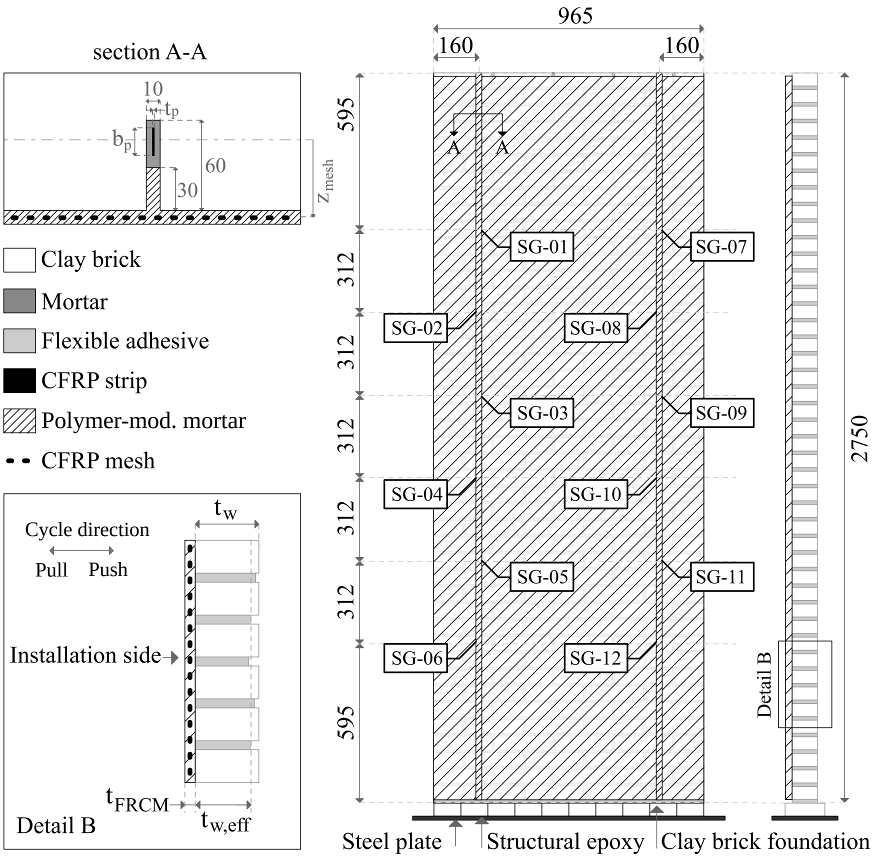

Figure 5.10: Schematic overview of a FDM CFRP and single-sided FRCM overlay retrofitted specimen and location of the strain gauges.

The tests were conducted on the test setup provided in Fig. 4.4, with the two line-load configuration as presented in Fig. 4.6. As for the loading procedure, the cyclic loading protocol presented in section 4.1.3 was followed, consisting of a low loading speed phase *Stage I; 1 mm/s* and a higher speed loading phase *Stage II; 5 mm/s*. It should be noted that due to control difficulties of the electric actuator at higher loads, a lower loading rate was maintained compared to the STRIP specimens covered in 4. The loading speed for the FRCM specimens, during both test stages is provided in Table 5.3. The measurements during the experiments were processed following the steps covered in section 4.1.4.

Table 5.3: Loading rates: target values and realized values at mid-height.

Specimen	Stage I		Stage II	
	Target (mm/s)	Mid-height (mm/s)	Target (mm/s)	Mid-height (mm/s)
FRCM-1	2	1.35	5	4.13
FRCM-2	2	0.98	5	4.05
FRCM-3	2	1.00	5	4.10

5.3 Full scale test results and discussion

The results of the full scale tests are summarized in Table 5.4 and the parameters were explained and illustrated in section 4.1 and Fig. 4.9 respectively.

Table 5.4: Global force - mid-span displacement behaviour.

	Parameter	Unit	Direction	FRCM-1	FRCM-1	FRCM-3
	V	kN		4.8	4.8	4.8
	Line loads			2	2	2
Maximum	P_{max}	kN	+	15.25	15.03	14.50
			-	7.94	8.00	7.16
	M_{max}	kNm	+	7.83	7.72	7.45
			-	4.08	4.11	3.68
	$\delta_{3,max}$	mm	+	145.4	91.7	97.4
			-	117.4	93.1	94.5
Ultimate	F_u	kN	+	2.63	1.10	1.21
			-	4.09	7.37	7.86
	M_u	kNm	+	1.35	0.56	0.62
			-	2.10	3.79	4.04
	$\delta_{3,u}$	mm	+	184.2	175.1	130.1
			-	122.1	141.1	135.4
CFRP	$\sigma_{L,max}$	N/mm²	+	336	284	288
			-	1045	1126	1068
	$\sigma_{R,max}$	N/mm²	+	312	288	367
			-	1031	1092	1057
	Φ	%		36	39	37

5.3.1 Moment-displacement behaviour

The global mid-span lateral moment-displacement diagrams for the tested specimens are shown Fig. 5.11. The light grey lines represent the individual cycles, whereas the thick black lines highlight the backbone curve. The solid dark grey lines represent the first cycle with 50 mm target displacement. The cycle in which FRCM failure occurred is highlighted by the dotted thick grey lines. The top graphs in Fig. 5.11 represent the pre-failure cycles, whereas the graphs at the bottom graphs represent the post-failure cycles. The backbone curve covers the envelope curves up to and including the failure cycle. The post-failure behaviour has no relevance for the practical applicability of the seismic retrofit system because CFRP mesh rupture was considered as wall failure.

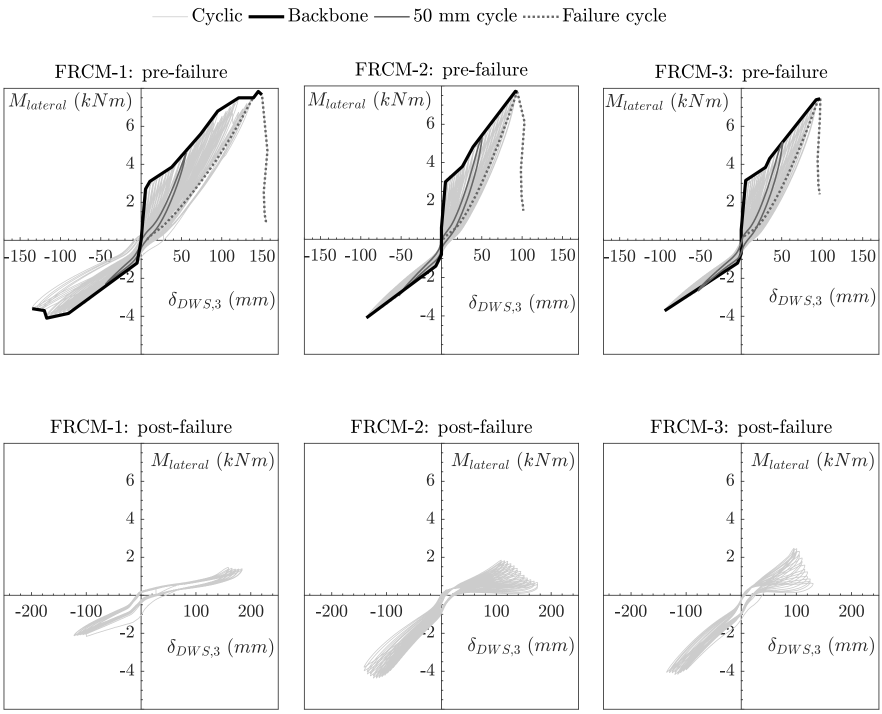

Figure 5.11: Moment – mid span displacement plots of specimens *FRCM-1*, *FRCM-2* and *FRCM-3*: pre-failure (top row) and post-failure (bottom row).

The backbone curves of the lateral moment - mid span displacement for all *FRCM* specimens are shown together in Fig. 5.12, together with the backbone cures for *URM* walls and walls retrofitted solely with FDM CFRP strips (coded *STRIP*) obtained from the experimental campaign presented in Chapter 4. From Fig. 5.12 the difference was observed between the mid-span displacements ($\delta_{DWS,3}$) corresponding to the maximum lateral moment resistance. Even though no significant differences were found in the maximum lateral moment resistances between the FRCM specimens for both the push (mean 3.96 kNm) and pull side (mean 7.67 kNm), the corresponding mid-span displacements for *FRCM-1* was significantly greater when compared to specimens *FRCM-2-3*. This difference was predominantly caused by the debonding failure mechanism of *FRCM-1*, as no significant difference was observed for the push direction of the *FRCM* specimens until $\delta_{DWS,3} \approx 100mm$.

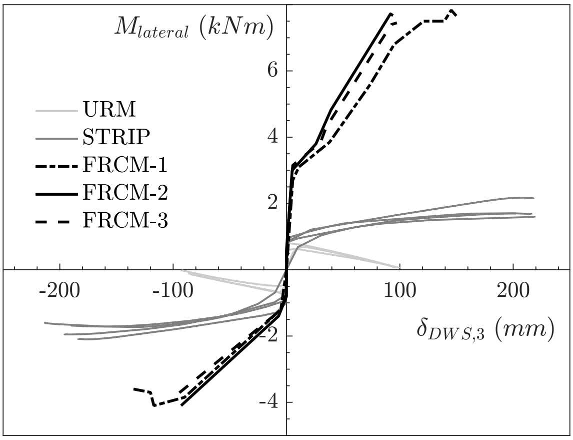

Figure 5.12: Backbone lateral moment – mid span displacement plots of all *FRCM* specimens. The *URM* and *STRIP-2-3-4-5* specimens were obtained from Chapter 4.

Compared to the *URM* and *STRIP* specimens, the single-sided *FRCM* overlay not only provided significant added value in terms of lateral moment – mid span displacement capacity on the pull side, but also for the push side as shown in Fig. 5.12. The mean lateral moment resistance of the *URM* specimens was 0.78 kNm. With the specimens in the current experimental campaign, the mean lateral moment resistance was increased by 408% and 883% for the FRCM side in compression and tension respectively. For the mean displacement $(\delta_{3,max})$ corresponding to the lateral moment resistance, an increase from 2.1 mm *(URM)* to 94.2 mm *(FRCM-2-3)* was realised.

The mean lateral resistance of the *STRIP* specimens corresponding to a mid-span displacement target of 100 mm was 1.6 kNm. The presence of the 15 mm thick FRCM layer in the compressed area of the cross-section during push cycles resulted in a 148% increase in lateral moment resistance of FDM CFRP retrofitted walls for similar mid-span displacement target values and same axial load on top of the wall. The average lateral moment resistance of FDM CFRP retrofitted walls was found to be 1.82 kNm, meaning that the addition of a single sided FRCM overlay to form a combination of retrofit measures provided a significant increase in lateral moment resistance.

5.3.2 Failure mechanisms and damage to masonry

The hairline cracks (grey lines) and full crack patterns (bold black lines) for the FRCM side of the tested specimens are illustrated in Fig. 5.13. At the start of the loading process the lateral load was primarily resisted by the cementitious matrix until cracking. Afterwards the matrix underwent a multi-cracking process with some debonding at the mesh–matrix interface similar to findings reported in [123]. Eventually, all specimens failed due to CFRP mesh rupture (Fig. 5.14. The location of these ruptures was approximately at the bed joints between the 26^{th}-27^{th} , 18^{th}-19^{th} and 30^{th}-31^{st} brick layers (counted from the top) for *FRCM-1*, *FRCM-2* and *FRCM-3* respectively.

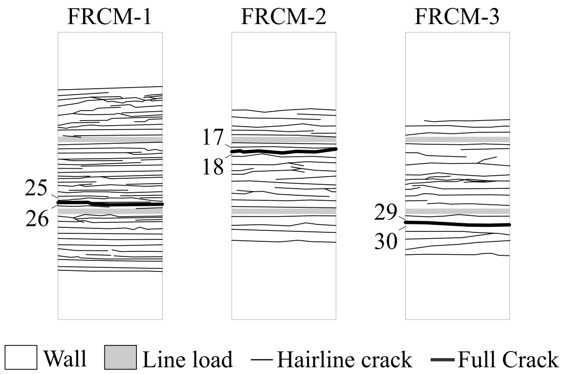

Figure 5.13: Schematic overview of the crack pattern of the FRCM specimens in the full-scale out-of-plane experimental campaign.

Specimen FRCM-1 showed approximately twice the hair-line cracks over the height of specimens compared to *FRCM-2-3*. Additionally, the hairline cracks of *FRCM-1* also reached towards the top and bottom of the specimen. These differences were attributed to the FRCM debonding failure mechanism which was observed for the *FRCM-1* specimen, as shown in Fig. 5.15. This failure mechanism was caused by the faulty installation of the CFRP mesh within the cementitious matrix for specimen *FRCM-1*.

Looking at the damage to the masonry on the as-built side of the specimens, multiple bed joint cracks over the height of the wall were observed, ranging from 14 to 17 cracks in total and mainly concentrated at the constant lateral moment region. This observation was in line with the damage observed for walls retrofitted with solely FDM CFRP, as was illustrated in 4.17. Some local crushing of the mortar was also observed on the as-built side of the specimens. After the CFRP mesh rupture, increased crushing of the cementitious matrix was observed for the post-failure push cycles.

Figure 5.14: Close-up of the CFRP mesh rupture failure of *FRCM-3*.

Figure 5.15: FRCM debonding failure of *FRCM-1*.

5.3.3 Stresses in the CFRP strip

Using the equations presented in section 4.1.4 the tensile stress distribution of the CFRP strips were determined. The stress distribution in both the left (dashed lines) and right (solid lines) CFRP strips are shown in Fig. 5.16 for all the FRCM specimens, at various target displacements during the pull (+) cycles (FRCM in tension). The same stress distributions are shown in Fig. 5.17 for the push (-) cycles (FRCM in compression).

Overall the stress levels of the CFRP strip that were attained in the push and pull cycles differed significantly for both the pre-failure and post-failure stages. The stress in the CFRP strips at 50 mm mid-span displacement (diamond marked lines) was significantly lower for the pull cycles than for the push cycles. The overall mean stress values following from the middle two strain gauges at approximately 50 mm mid-span displacement was 161 N/mm² and 642 N/mm² respectively. For the displacement corresponding to the pre-failure cycle, the difference of the CFRP strip stresses remained significant between the pull (336 N/mm²) and push cycles (1107 N/mm²). A difference in CFRP strip stresses was also observed between *FRCM-1* and *FRMC-2-3* on the pull side for the pre-failure cycle. The overall mean stress value from the middle two strain gauges were 434 N/mm² and 287 N/mm² respectively when the target displacement was reached. This difference in CFRP stress was attributed to the difference between the mid-span displacement levels corresponding to the pre-failure cycles, which were 130 mm for *FRCM-1* and 93 mm for *FRCM-2-3*.

Looking at the post-failure cycles the tensile stress distribution of the CFRP strips for the *FRCM-1* specimen was similar for the push and pull-cycles. The CFRP strip stress difference between the push and pull cycles for the *FRCM-2-3* specimens contrarily, showed a significant difference in stress distribution. Whereas the push cycles continued to show a parabolic stress distribution over the height, the pull cycles had a more bilinear shape, with lower peak values near the height position of the full FCRM crack. Comparing the push cycle of *FRCM-1* with *FRCM-2-3*, the CFRP strip stresses were significantly lower for the *FRCM-1* specimen. This was attributed to the debonding failure mechanism of specimen *FRCM-1*, where due to the local detachment of the FRCM layer the effective lever arm (and thus the CFRP stresses) between the compressed zone and the CFRP strips decreased.

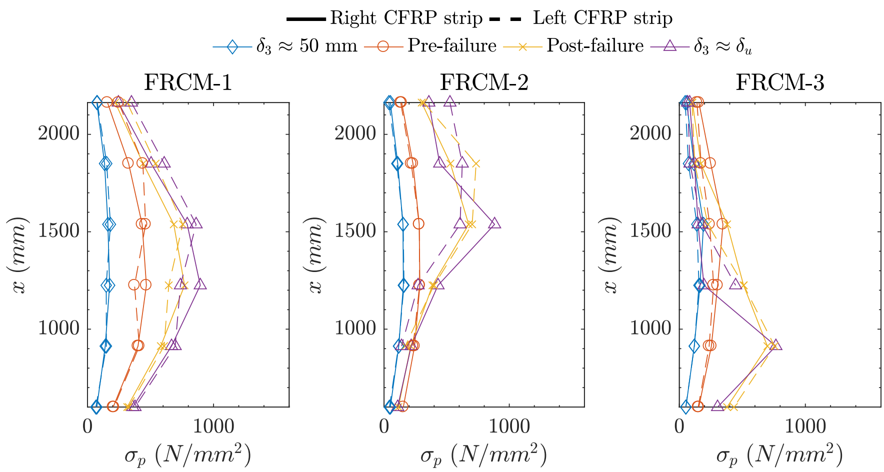

Figure 5.16: Stresses in left (dashed line) and right (solid line) CFRP strips in N/mm² over the height for all the FRCM specimens during a pull cycle (FRCM in tension).

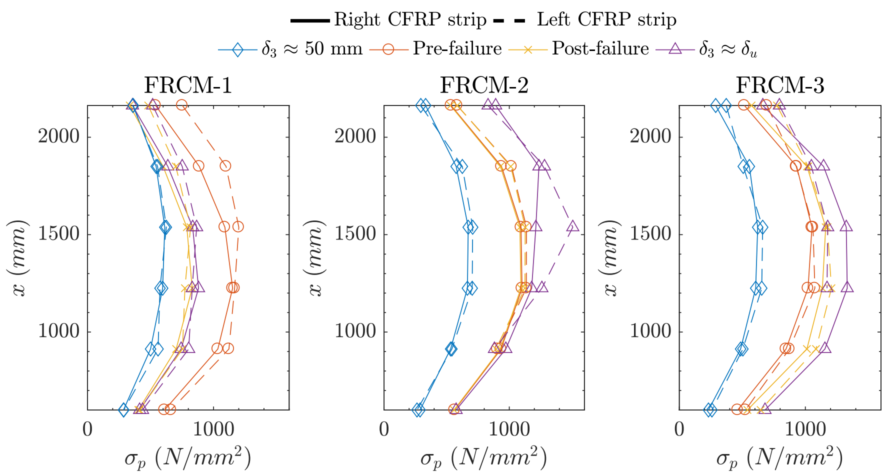

Figure 5.17: Stresses in left (dashed line) and right (solid line) CFRP strips in N/mm² over the height for all the FRCM specimens during a push cycle (FRCM in compression).

5.3.4 Internal moment - CFRP stress - curvature

The internal moment and curvature correlations for the STRIP specimens were determined using the data processing steps as mentioned in section 4.1.4. It should be noted that specimen FRCM-1 was emitted from the analysis due to incorrect installation of the CFRP mesh. The internal moment and curvature relations for the FRCM specimens are provided in Fig. 5.18. A strong linear correlation was found between stress in the CFRP strips and the internal moment: $R^2 = 0.97$ for when the FRCM layer was in tension (pull-cycle) and $R^2 = 0.98$ for when the FRCM layer was in compression (push-cycle). The internal moment and CFRP stress relations for the FRCM specimens, are provided in Fig. 21. Strong linear correlations $R^2 = 0.95$ were found between stress in the CFRP strips and the internal moment for the scenario when the FRCM layer was in tension (pull-cycle) or in compression (push-cycle).

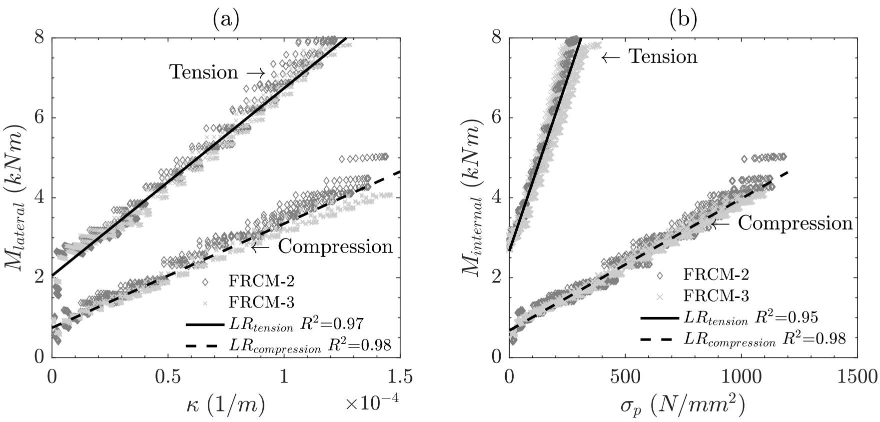

Figure 5.18: Internal moment versus: curvature (a) and CFRP stress (b) for $\frac{3}{8}h_w \leq x \leq \frac{5}{8}h_w$ of *FRCM-2* and *FRCM-3*. The solid and dashed lines show the linear regression (LR) when the FRCM overlay is in tension and in compression respectively.

5.3.5 Initial and effective stiffness

From the force displacement $(\delta_{DWS,3})$ relation per half run both the initial stiffness (k_{ini}) and effective stiffness (k_{eff}) of the tested walls were determined following the procedure presented in section 4.2.7.

The initial stiffness of the wall, k_{ini}, was taken as the slope of the F-δ loading branch within the displacement range $\delta_{DWS,3} = [-2.5mm, 2.5mm]$. The value of the slope was calculated by fitting a linear regression through the data points. The initial stiffness k_{ini} as a function of the target displacement $\delta_{DWS,3,run}$ for each run for all specimens tested with the four line load configuration *(URM, STRIP-1-2-3)* is shown in Fig. 4.26a. The same relation is shown in Fig. 4.26b for the specimens tested with the two line load configuration *(STRIP-4-5-6)*.

The initial stiffness k_{ini} as a function of the target displacement $\delta_{DWS,3,run}$ for each run *FRCM-2* and *FRCM-3* is shown in Fig. 5.19a. Looking at the power regressions line constructed for both the pull and push cycles a small difference for the initial stiffness was found between the push and pull cycles, where the pull cycle (FRCM in tension) was slightly higher. With increasing target displacement, the initial stiffness of both the pull and push cycles declined. This decline was linked to the accumulation of damage during loading repetition. The effective secant stiffness of a half run was determined in accordance with Eq. 4.14. The effective stiffness k_{eff} as a function of the target displacement $\delta_{DWS,3,target}$ is shown in Fig. 5.19b.

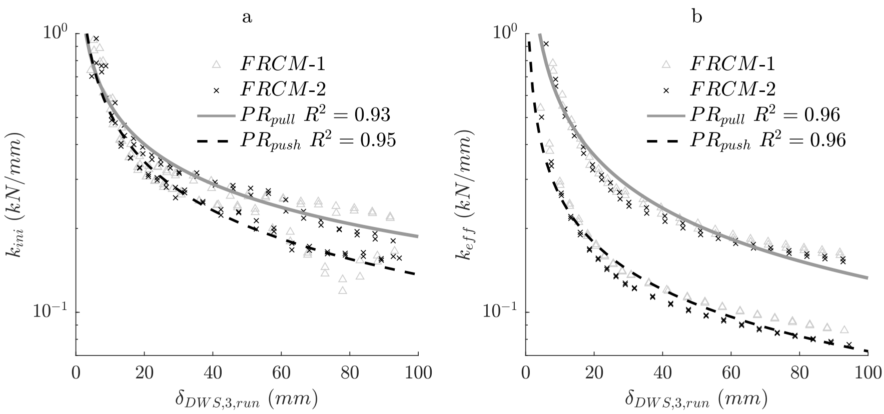

Figure 5.19: The initial stiffness k_{ini} (a) and effective stiffness k_{eff} (b) versus the target displacement $\delta_{DWS,3,target}$ for each run for *FRCM-2* and *FRCM-3*. Solid grey and black dashed lines represent the power regression for pull and push respectively.

5.4 Non-linear model

In addition to the non-linear model with the FDM CFRP strip, as was presented in section 4.4.2, the FRCM layer was included. The simplified rectangular cross section of the FDM CFRP retrofitted specimens is provided in Fig. 5.20. The FRCM layer was modelled using two components, being the CFRP mesh and the polymer-modified mortar. It is assumed that the strain profile is linear, and the CFRP strips, CFRP mesh and polymer-modified mortar are perfectly bonded without any slip until CFRP mesh rupture occurs.

The lined area in Fig. 5.20 represents the compressed region of the cross section. Two CFRP strips (z=0) generate a combined tensile force of F_p. The net force in the masonry is the sum of the masonry tensile force $(F_{m,t})$ and the masonry compression force $(F_{m,c})$. The strain distribution over height z is obtained using Eq. 4.29, where ε_A and ε_B are the maximum compressive and tensile strain respectively for the faces of the masonry wall.

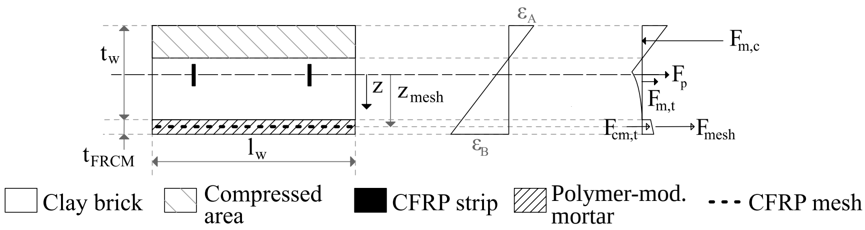

Figure 5.20: Cross section analysis of the FDM CFRP and single sided FRCM overlay retrofitted specimens.

For the maximum strain on the compressed side (ε_A), a corresponding maximum tensile strain of the masonry (ε_B) was determined where the condition as provided in Eq. 5.13 was met. It should be noted that when the FRCM layer was in compression, the contribution of the CFRP mesh was neglected. The axial load (V) on a specimen and the weight (W) of a specimen were 4.8 kN and 5.6 kN respectively. The net force in the masonry (F_m), and the tensile force in the CFRP strips (F_p) were obtained from Eq. 4.31 and 4.32 respectively. The tensile forces in the embedded CFRP mesh (F_{mesh}) and the cementitious matrix (F_{cm}) were determined using Eq. 5.10 and 5.11 respectively. The compressive behaviour of the cementitious matrix was assumed to be linear-elastic until the compressive strength $f_{CM,c}$ was reached. The moment and curvature were determined with Eqs. 5.12 and 4.34 respectively.

$$F_m + F_p + F_{cm} + F_{mesh} + V + \frac{W}{2} = 0 \tag{5.13}$$

With the material parameters for the masonry and the CFRP strip as was provided in Table 4.4 ($G_{fI} = 11.5N/m$), and the updated material parameters for the cementitious matrix and the embedded CFRP mesh as listed in Table 5.5, the moment-curvature relationship following from the model was obtained for both out-of-plane loading directions. This relationship is shown with a black dotted line in Fig. 5.21a and compared to the obtained internal moment-curvature relationships of the constant moment region ($\frac{3}{8}h_w \leq x \leq \frac{5}{8}h_w$) for specimens *FRCM-2* and *FRCM-3* (grey dots). Looking at the results for when the FRCM layer is under compression (black lines), there was a slight decline in the internal resistance after the first crack, which was not consistent with the experimental findings. This decline was also the case for the cross section analysis with no single-sided

FRCM overlay. Looking at the results for when the FRCM layer is under tension (dotted black lines) the internal moment – curvature relationships are slightly overestimated, whereas the internal moment – CFRP strip stress relationship was underestimated. The lateral moment – CFRP stress relation, as shown in Fig. 5.21b, provided a good approximation of the experimental results.

Table 5.5: Material parameters of the cementitious matrix and CFRP mesh.

Parameter	Symbol	Value	Unit
Cross sectional area of the embedded CFRP mesh	A_{mesh}	42.2	mm²
Young's modulus of the polymer-modified mortar	E_{CM}	27,680	N/mm²
Compressive strength of the polymer-modified mortar	$f_{CM,c}$	62.5	N/mm²
Tensile strength of the uncracked FRCM	$f_{CM,t}$	1.73	N/mm²
Tensile strength of the embedded CFRP mesh	f_{mesh}	1,700	N/mm²
Shape factor for tension softening curve	α	0.8	-
Ultimate tensile strain of the CFRP mesh	$\varepsilon_{FRCM,u}$	0.64	%

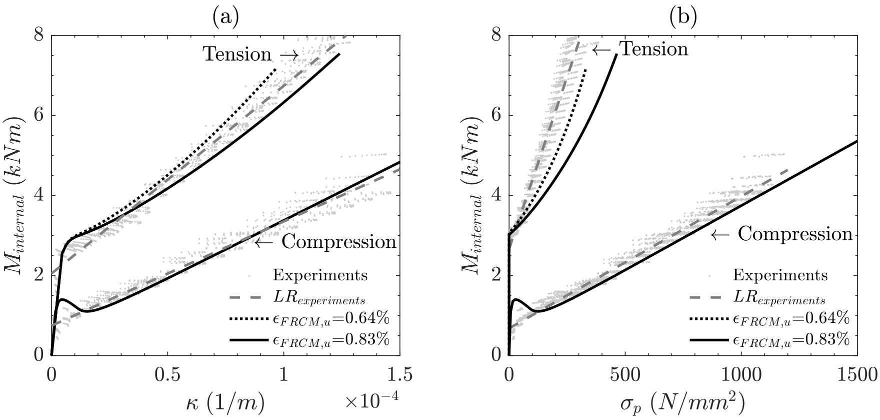

Figure 5.21: Internal moment versus: curvature (a) and CFRP strip stress (b) relationship following from the cross-section analysis with the internal moment-curvature relationships for the constant lateral moment area for *FRCM-2-3*.

Using the same procedure as mentioned in section 5.1, the non-linear material models, the cross section analysis and the lateral moment - displacement relationship were determined and compared with the experimental results. This relationship is shown in Fig. 5.22 with the dotted black line. Even though the level of maximum lateral moment resistance following from the model seemed consistent with the experimental outcome, the corresponding mid-span displacement showed a significant deviation. The reason for this deviation was linked to the value maintained for the ultimate tensile strain of the FRCM. Following the findings from section 5.1 the initial ultimate tensile strain of the FRCM was changed from $\varepsilon_{FRCM,u}$ = 1.91% (obtained from tensile slab tests) to $\varepsilon_{FRCM,u}$ = 0.64%, in order to provide a better fit between the outcome of the cross-section analysis and the results from the four-point bending tests with FRCM retrofitted beams. Increasing the value for the ultimate tensile strain of the FRCM by 30% from $\varepsilon_{FRCM,u}$ = 0.64% to $\varepsilon_{FRCM,u}$ = 0.83%, resulted in an improved fit with the experimental values, as shown in both Fig. 5.21a and Fig. 5.22 in black solid lines. Looking at Fig. 5.21b, given a value for internal moment, the model significantly overestimates the stress in the CFRP strips. The non-linear model assumed that the strain profile is linear, and that the CFRP strips are perfectly bonded without any slip. As mentioned for the cross-section analysis using only the FDM CFRP strips, the slip of the FDM CFRP strips was not negligible. Even though the tensile stresses of the CFRP strips were overestimated, the limited effect of the CFRP strips on the internal moment capacity did not affect the overall prediction of the model.

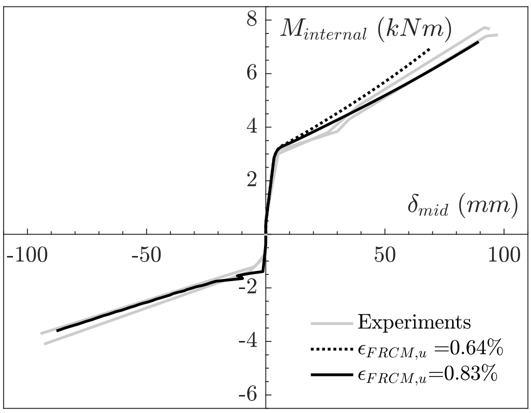

Figure 5.22: Lateral moment-displacement relationship obtained using the non-linear model, compared with specimens *FRCM2-3*.

The contribution of FRCM in compression was included. *Meriggi, de Felice and De Santis* [124] report that only in the case of composite reinforced mortar composites, which are 30-50 mm thick and whose spalling/buckling is prevented by the FRP connectors, the presence of the reinforcement on the compression side is accounted for by increasing the thickness of the wall cross section. Neglecting the contribution of FRCM in compression resulted in a significant deviation between the model outcome and the experimental result, as shown in Fig. 5.23. It is worth noting that up to a mid-span displacement of 100 mm, the dotted line had a reasonable fit with the moment-displacement relationship obtained for the STRIP-4-5 specimens. Based on these findings, the inclusion of the contribution of FRCM in compression is justified.

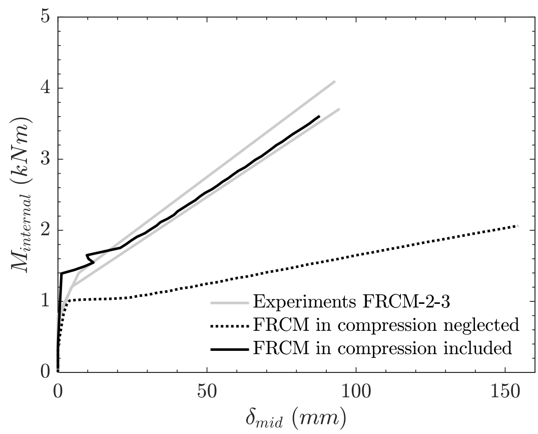

Figure 5.23: Lateral moment-displacement relationship obtained using the non-linear model, with neglected (dotted) and included (solid) FRCM in compression, compared with specimens *FRCM2-3*.

5.4.1 Comparison with existing models

Two design guidelines have been recently developed, providing acceptance criteria and design provisions for externally bonded FRCM systems for the strengthening of masonry structures: the Italian guideline CNR-DT 215 and the (at the time of writing not yet published) ACI and RILEM joint committee guideline ACI 549 0L – RILEM TC 250-CSM. *Meriggi, de Felice and De Santis* [124] report that there are still some crucial issues which need to be tackled, including the development of a simplified approach for the design of the FRCM reinforcement and the estimate of the deflection capacity. The same authors proposed an approach for the design and evaluation of the ultimate bending moment M_R and of the corresponding displacement u_d. This design approach, provided in Appendix B, was followed for a FRCM retrofitted wall with the same dimensions, axial load and CFRP mesh characteristics as the tested walls reported in this chapter. It should be noted that safety/design factors, characteristic values, the CFRP strips and second order effects were left out of the analysis. The outcome of the aforementioned approach was compared with the results obtained using the model proposed in the current study (Fig. 5.24). For the model, the parameters in Table 5.5 with $\varepsilon_{FRCM,u} =$ 0.83% and Table 4.4 ($G_{fI} = 11.5N/m$) were used.

Both the estimation for the ultimate bending moment and the corresponding displacement were in agreement with the results of the proposed model. The approach proposed by *Meriggi, de Felice and De Santis* [124] seems able to provide simple and well estimated values for both the ultimate bending moment and the corresponding displacement for the considered case.

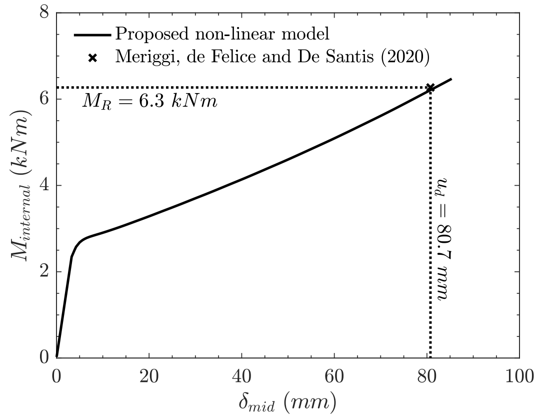

Figure 5.24: Lateral moment-displacement relationship following from the non-linear model, together with the ultimate bending moment M_R and of the corresponding displacement u_d obtained via the approach presented by *Meriggi, de Felice and De Santis* [124].

5.5 Conclusions

In the beginning of this chapter, an experimental campaign on the OOP behaviour of masonry panels retrofitted with solely a single sided FRCM overlay was discussed. From this experimental campaign and preliminary modelling efforts the following conclusions were drawn:

1. The CFRP mesh provided significant added value (especially in terms of deformation capacity) when compared to specimens reinforced with solely a polymer-modified mortar overlay. Under four-point bending, the mean moment capacity and corresponding curvature increased from 0.6 kNm and $3 \cdot 10^{-3}/m$ respectively, to 1.3 kNm and $86 \cdot 10^{-3}/m$ respectively. As no exact moment for the first crack could be determined for these specimens, no statement could be made regarding the effect of the mesh on the cracking load.

2. Loading cyclically during the out-of-plane experiments did not affect the strength, ultimate deflection or ultimate curvature when compared to the statically loaded specimens. Additionally, no significant difference was observed between the envelope of the cyclically tested specimen and the statically loaded specimens. Some permanent deflection was observed during cyclic loading due to the slippage of the mesh.

3. Using the tensile test results as input parameters for the model, there was a significant over-estimation of the cracking curvature, cracking moment and ultimate curvature.

4. Selecting lower values for the ultimate strain of the FRCM (stiffer failure mechanism) and the tensile strength of the cementitious matrix (formation of shrinkage cracks during curing), both the ultimate and cracking moment-curvature relation following from the proposed model corresponded better with the mean experimental results.

5. Introducing a factor to account for non-linear tension-softening behaviour results in an improved fit between the model and the experiments regarding the slope of the crack formation and stabilized cracking stages.

Subsequently, an additional experimental program was undertaken to assess the out-of-plane behaviour of one-way spanning full scale clay brick masonry walls retrofitted with deep and flexible adhesive mounted (FDM) carbon fiber reinforced polymer (CFRP) strips and single sided fabric reinforced cementitious matrix (FRCM) overlay. In the experimental testing program three full-scale masonry walls were tested with a four point-bending test setup. The experimental out-of-plane experiments demonstrated the effectiveness of the proposed hybrid retrofit scheme within the current study. From the experimental campaign the following conclusions were drawn:

6. All specimens failed due to CFRP mesh rupture. For one specimen, where the CFRP mesh in the FRCM layer was installed incorrectly, FRCM debonding was observed. This also resulted in two times more observed hair-line cracks over the height when compared to the other specimens.

7. For the displacement corresponding to the pre-failure cycle, the difference of the CFRP strip stresses remained significant between the pull (mean CFRP strip utilization 11.7%) and push cycles (mean 38.4%). This difference was caused due to the alternating compression zone between the FRCM layer and the masonry.

8. The mean lateral moment resistances of the FRCM specimens were found to be 3.96 kNm (FRCM under compression) and 7.67 kNm (FRCM under tension), significantly higher for the mean lateral moment resistances found for both URM (0.78 kNm) and FDM CFRP strips retrofitted specimens (1.82 kNm) tested under similar conditions (Chapter 4). The addition of a single sided FRCM overlay to form a combination of retrofit measures together with the FDM CFRP strips provides a significant surplus in terms of lateral moment resistance.

9. For the mean mid-span displacement corresponding to the maximum lateral resistance, an increase with a factor 45, from 2.1 mm (URM) to 94.2 mm, was determined with respect to unreinforced specimens.

10. Strong linear relations were $\left(R^2 \geq 0.95\right)$ were found for both the internal moment and the curvature, and the internal moment and the CFRP strip stress levels.

11. The contribution of the FRCM layer in compression was found to be significant for the lateral moment resistance, effectively resulting in an increased lever arm between the FDM CFRP strips and the resultant force of the compression zone when analysing the cross-section (over the height) of the wall.

A simple and practical applicable out-of-plane model for FDM CFRP and single sided FRCM overlay retrofitted masonry walls was proposed. A cross section analysis using non-linear and linear material models for the used components was applied. From the modelling efforts the following conclusions were drawn:

11. The cross section analysis using non-linear and linear material models provided a good approximation of both the internal moment – curvature and the lateral moment – mid span displacement relation as obtained with the experiments. This was applicable for both directions: FRCM in tension and FRCM under compression. In contrast to existing literature, the inclusion of the contribution of FRCM in compression was justified.

12. Even though the tensile stresses of the CFRP strips were overestimated with respect to the internal moment, due to the slip of the embedded CFRP strips being non-negligible, the limited effect of the CFRP strips on the internal moment capacity did not affect to overall prediction of the model.

13. Both the ultimate bending moment and the corresponding displacement following from the proposed model showed good agreement with values obtained using similar models in literature.


2
1

Chapter 6

Hybrid retrofit with FDM CFRP and FRCM: in-plane behaviour

For walls subjected to critical in-plane loading, the application of solely the flexible deep mounted (FDM) CFRP strips retrofit was not sufficient, as it was expected that the embedded CFRP strips would have an insufficient effect on the in-plane shear strength of the masonry [56]. In Chapter 1 the addition of a one-sided fabric reinforced cementitious matrix (FRCM) overlay was proposed to form a hybrid retrofit with the FDM CFRP strips, in order to enhance the strength and pseudo-ductility of masonry for in-plane loading conditions. This chapter offers insight into the in-plane (shear) behaviour of FDM CFRP strip and single sided FRCM overlay retrofitted masonry. Two different experimental campaigns are presented and the results are discussed. An existing analytical model as well as various design provisions are compared with the found failure mechanisms and failure loads. Chapter 6 is based on [79, 80].

6.1 Introduction

Past experimental programs assessing innovative strengthening systems based on cementitious mortar matrices, highlighted a significant improvement in both in-plane and/or out-of-plane lateral strengths of masonry walls [57,59–64,66,67,125–127]. Based on the response of medium-scale clay brick shear walls, beam-column type walls and beam type walls subjected to cyclic in-plane loading, Papanicolaou, Triantafillou, Karlos and Papathanasiou [57] concluded that FRCM overlays provide a substantial gain in strength and deformability. The authors reported that FRCM jacketing is much more effective than FRP. The increased effectiveness is about 15–30% in shear walls, 135% in beam-column type walls and 350% in beam type walls, on the basis of tests conducted. With an experimental campaign medium-scale walls, Babaeidarabad, De Caso and Nanni [62] showed that the increase in ultimate in-plane strength is proportional to the amount of FRCM and ranged between 2.4 and 4.7 times that of the unstrengthened specimens. The authors reported that toe-crushing failure occurred for wallettes with a calibrated reinforcement ratio higher than 4%, and therefore increments of FRCM beyond this value were claimed ineffective. Ismail [61] investigated the in-plane behaviour of medium-scale clay brick shear walls strengthened with different types of FRCM systems. The shear strength of single-sided retrofitted wallettes ranged from 113% to 148% compared with the strength of the unstrengthened wallettes, whereas the shear strength of test wallettes with a double-sided FRCM retrofit ranged from 446% to 481%. The lower increase in shear strength for the single-sided retrofitted specimens was attributed to the unrestrained boundary conditions of the diagonal compression tests, as these specimens showed out-of-plane bending behaviour. This out-of-plane bending during the diagonal compression testing of single-sided FRCM retrofitted specimens, caused by the eccentric stiffness resulting from the application of the reinforcement on a single side, was also reported in other researches [66,67]. Shabdin, Zargaran and Attari [67] tested medium-scale URM walls strengthened with FRCM under diagonal compression in order to consider the effect of strengthening on the behaviour of brick walls. The authors concluded that FRCM improved the diagonal load carrying capacity and deformation capacity, which caused the strengthened walls to fail in a ductile manner. Marcari, Basili and Vestroni [66] investigated the effectiveness of using a Basal TRM system for in-plane shear reinforcing of volcanic tuff stone masonry. The average increase in shear strength was approximately 40% for the single-side reinforced specimens, while the increase was 60% with double-side reinforced specimens. The authors also reported that the TRM system changed the failure mode of the panels from joint-sliding to diagonal cracking. Another experimental campaign carried out on medium-scale tuff-masonry walls also showed that strengthened walls did not fail under the characteristic diagonal sliding fracture, generally developing in unreinforced masonry walls at the mortar-to-brick interface [59]. The ultimate load in diagonal compression (and corresponding shear strength) for strengthened walls were reported to be between four and six times greater than the one observed for bare walls. Ismail and Ingham [64] conducted an experimental program with full scale reversed cyclic in-plane testing of FRCM strengthened URM walls. They observed the strength increment due to TRM strengthening around 130% when the URM test walls were loaded in-plane, with a notable increment in deformation capacity and ductility.

While the influence of FRCM reinforcement on the in-plane behaviour of masonry wallettes has been a popular subject of research for the past years, the influence of the aforementioned combination of retrofit measures on the in-plane shear capacity of masonry has not been investigated before. Moreover, this experimental program aims to investigate the possible degrading effect of the proposed out-of-plane strengthening system on the in-plane shear strength of masonry panels. The aim of the experimental campaign for this study was to determine the effectiveness of a one-sided FRCM reinforcement combined with FDM CFRP strips to improve the in-plane shear resistance of clay brick masonry walls. In this experimental campaign, quasi-static cyclic in-plane shear tests were performed (cantilever configuration) on full-scaled masonry walls strengthened with this combined reinforcement system. Additional pull-out experiments were conducted to gain more insight on the behaviour of foundation anchors, embedded in the same flexible adhesive as the CFRP strips. Finally, the experimental results were compared to the outcomes of existing design codes, to check the validity of these models for this combined retrofit system.

6.2 Quasi-static cyclic shear tests on walls

6.2.1 Building the test walls

The test walls for the quasi-static cyclic in-plane shear tests were built in the testing laboratory of QuakeShield in Grijpskerk, the Netherlands. The specimens were built on a reinforced concrete foundation beam by an experienced mason. The masonry walls were nominally 2450 mm high (h_w) and had a thickness (t_w) of 100 mm. The lengths of the specimens (l_w) were 1100 mm (for the S specimens), 2000 mm (for the M specimens) and 4000 mm (for the L specimens). For each configuration three specimens were built in order to test the effect of axial load (p_v) on the in-plane behaviour for each geometry. The axial loads were 0.15, 0.3 or 0.5 N/mm², with the only exception being specimen S1 (0.20 N/mm²), due to control difficulties of low axial forces. An overview of the test specimens for the quasi-static cyclic shear tests is provided in Table 6.1.

Table 6.1: Overview of the geometry of the specimens and the applied axial loads.

	Unit		S			M			L	
l_w	mm		1100			2000			4000	
h_w	mm	2450				2450			2450	
t_w	mm		100			100			100	
		S1	S2	S3	M1	M2	M3	L1	L2	L3
p_v	N/mm²	0.20	0.30	0.50	0.15	0.30	0.50	0.15	0.30	0.50

The concrete foundation beam had a height of 180 mm and a width of 180 mm. It should be noted that the reinforced concrete beam used for the M-specimens was 60 mm shorter than the length of these wall specimens.

These wall specimens therefore extended 30 mm over the foundation beam at both ends. The mortar for the masonry specimens was prepared in the laboratory and the walls were built in running bond. Both the bed and head joints had a nominal thickness of 12 mm and were fully filled. All walls cured in air in the unheated laboratory (0-10 $°C$) for at least 28 days before strengthening.

6.2.2 Reinforcing the test walls

Schematic overviews of the reinforced S, M and L walls are provided in Fig. 6.1, together with details and geometric properties. After the walls were sufficiently cured (±28 days) the strengthening process started by milling a number of vertical grooves (2, 3 and 5 for S, M and L specimens respectively) of 65 mm depth and 10 mm width, spaced 850 mm apart. The distance of the outer grooves to the side edges of the wall was 150 mm for the S and M specimens and 300 mm for the L specimens. The dust in the groove was removed with compressed air. The standard CFRP strip (20×1.4 mm^2) of the overall research was used. A layer of primer was then applied to the groove to obtain an improved bond of the adhesives to the masonry. Afterwards, the CFRP strips (cleaned with acetone) were inserted into the groove that was partially filled with the flexible adhesive. The vertical grooves at the side ends were widened to 25 mm till a depth of 35 mm over the bottom 500 mm. In each widened groove a 12 mm ribbed reinforcement bar (B500B) with a length of 650 mm was fixed with a conventional stiff adhesive (HIT-HY 100) inside a borehole of 150 mm in depth and angle of 30° in the foundation beam. The remaining part of the steel rods were embedded in the flexible adhesive within the aforementioned widened grooves over a length of 500 mm. Excess adhesive till a depth of 30 mm in the standard grooves and 10 mm in the widened grooves was removed.

After the placement of the strips and anchors, the walls were left to cure for one day before applying the single-sided FRCM overlay. The masonry surface was wetted prior to the mortar matrix application to secure proper adhesion. A thin layer of mortar was subsequently applied to the masonry surface by hand. The remaining parts of the grooves were also filled with the same mortar. The CFRP mesh was then applied on the mortar matrix surface and was pressed into the mortar matrix. After placing the CFRP mesh in the mortar a new thin layer of mortar was applied to embed the CFRP mesh, resulting in a nominal FRCM layer thickness of 15 mm. The specimens were left to cure in the laboratory environment for a minimum of 28 days before starting the experimental program.

6.2.3 Test setup and procedure

The quasi-static cyclic in-plane shear tests were performed in the test setup of QuakeShield. The test setup is illustrated in Fig. 6.2, and shown in picture

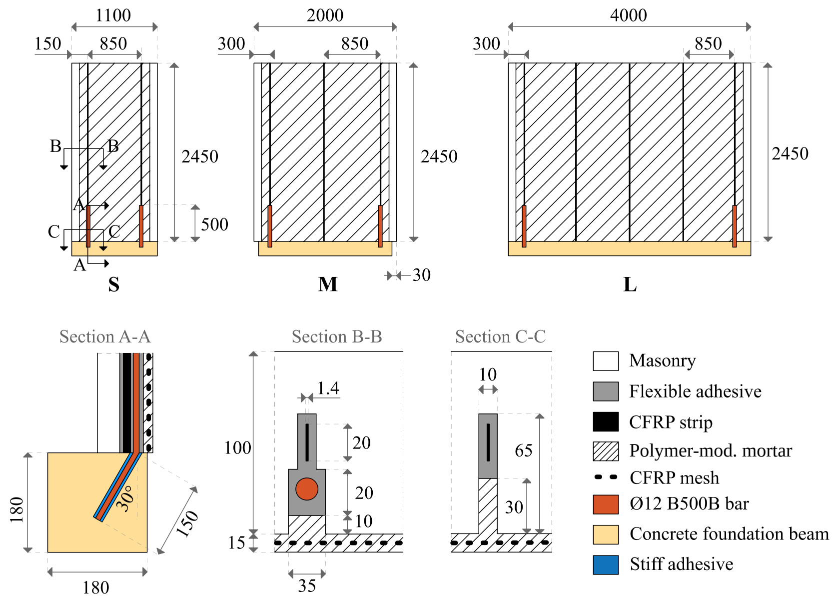

Figure 6.1: Schematic overview of the reinforced S, M, and L specimens.

in Fig. 6.3. The frame of the test setup is formed by two post-aligned steel frames which were interconnected. The basis of the frame is a rectangular closed portal frame (A in Fig. 6.2) in which the specimen was placed. The bottom beam of it passes through the portal frame and supported the steel shore (C) that connects to the portal frame at the position of the horizontal actuator. Steel beam B in Fig. 6.2 takes care of the stability of the test setup in transverse direction. All steel profiles of the test frame are interconnected by weld connections thus minimizing movement in the connections. The foundation beam was connected to a 15 mm steel plate with a fast-curing epoxy. The steel plate allowed for a connection between the specimen and the test setup. In addition to the epoxy-connection with the bottom steel plate, the foundation beam was also kept in place by a mechanical connection (steel brackets) that covered the topside of the beam.

The topside of the walls was provided with a steel plate. To ensure a uniform distribution of the vertical load, rubber pads were placed between the loading beam and the steel plate. This steel plate in turn was provided with 40 mm thick steel blocks which were positioned such that they fitted exactly between the rubber pads. These steel blocks were used to transfer the horizontal load from the loading beam to the walls (Fig. 6.2). The steel plates were attached to the walls with a fast-curing adhesive after lowering the loading beam. After curing for 24 hours (minimum), the experiment was started.

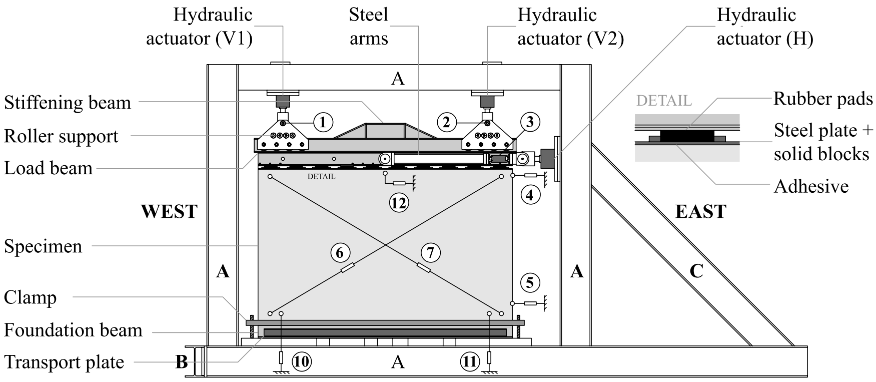

Figure 6.2: Schematic overview of the shear test setup. West direction = push; East direction = pull.

Figure 6.3: Photo of the shear test setup.

The horizontal load was generated by a horizontally positioned hydraulic actuator with a capacity of 500 kN. The horizontal load was applied in both West direction (also referred to as push direction) and East direction (also referred to as pull direction). A loading beam distributed this horizontal load over the topside of the specimen. For the sake of symmetry in the push and pull cycles the force exerted by the horizontal actuator engaged in the center of the load beam using two steel arms, on at each side of the loading beam. The load beam was stiffened at the top with an IPE-profile on which two vertically positioned hydraulic actuators with a capacity of 200 kN each, provided the desired vertical load on the test specimen. At the topside the vertical actuators were fixed in position against the frame of the test setup. Because the load beam would translate horizontally throughout the test the vertical actuators were connected to the beam by means of crane trolleys. The crane trolleys were in turn connected to the hydraulic actuator by a load pin, which also enabled rotation of the crane trolley. This load pin also monitored the load exerted by the actuators. Both load pins were calibrated to a maximum force of 120 kN and had an accuracy of 0.3%. The horizontal load which was exerted by the horizontal actuator was monitored by a load cell positioned at each of the two steel arms. In addition to these load measurement devices the horizontal and vertical loads were checked by measuring the oil pressure within the hoses of the hydraulic power pack.

Displacement and deformation measurements were conducted by laser sensors with an accuracy of 7 μm. Laser sensor 12 in Fig. 6.2 was used for controlling the test and for constructing the force-displacement plots. This sensor was connected to the steel plate on top of the specimens and displacements were measured relative to a detached frame. Vertical deformation measurements were conducted on the narrow walls (S). These deformations were measured by means of two laser sensors which were applied on telescopic tubes (8 and 9). The telescopic tubes covered nearly the complete height of the specimens and monitored the vertical deformation of the specimen. Shear deformations were measured on the medium and large specimens by laser sensors on diagonally positioned telescopic tubes (6 and 7). Slip of the wall specimens over the bottommost bed joint was measured by a laser sensor positioned on a detached measurement frame (5). The same frame was used for the positioning of a laser sensor which measured the displacement of the East top of the specimen (4). Possible vertical uplift at the position of the steel anchors was measured by two laser sensors placed on detached measurement frames (10 and 11). All measuring devices were connected to a PLC-system which processed the data in real time. This data was then forwarded by the PLC-system to a laptop and monitored by the researcher. During the tests the nature and extent of the cracking pattern was continuously observed and noted.

A cantilever configuration was chosen for this testing program, were vertical deformation and rotation of the loading beam is not restrained. The vertical force of both actuators was kept constant during the complete course of the tests. The vertical loads exerted by both actuators was therefore not depending on the exerted horizontal load nor the horizontal or eventual vertical displacement. After applying the vertical pre-compression load the wall specimens were subjected to cyclic shear loading. The cyclic shear load was applied using computer controlled displacement steps, starting from 0.26

mm with a speed of 0.2 mm/s. Each displacement step was applied two times in both loading directions forming one load cycle, before increasing the target displacement with 40%, based on the FEMA [72] protocol. This continued until a target displacement of ±40 mm, which was the maximum stroke of the horizontal actuator.

6.2.4 Direct pull test on steel anchors

The force in the anchors, especially during the rocking behaviour of a reinforced specimen, is a relevant parameter for modelling purposes. With the test setup presented in the previous paragraph and the limitations in the lab, the measurement of the force in the anchors was difficult to realize. In order to gain more understanding on the mechanical behaviour of the flexible anchor connection, additional small-scale direct pull-out tests were performed. Two possible scenarios were considered as shown in Fig. 6.4, regarding the transfer of the tensile forces in the anchor into the reinforced specimen:

- Scenario A: The tensile forces in the anchor are fully transferred to the masonry substrate via the adhesive.
- Scenario B: The tensile forces in the anchor are fully transferred to the CFRP strip, via (predominantly) the adhesive and the masonry.

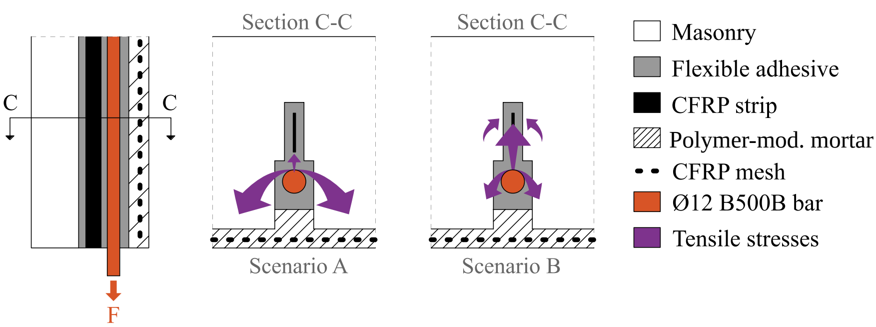

Figure 6.4: Possible stress transfer scenario's from anchor to masonry/CFRP strip.

For both configurations 3 specimens were built of 8 (Scenario A) and 12 (scenario B) bricks in height, coded DPT-A and DPT-B respectively. The installation and positioning of the anchor and strip was conducted according to the same reinforcement method as described in section 6.2.2. Only anchors were installed on the DPT-A specimens. The anchors installed in the DPT-B specimen, were bonded to the bottom 490 mm of the specimen. This was done to maintain a consistent anchorage length with the anchors of the DPT-A specimens. The installed CFRP strip on the DPT-B specimen, was bonded over the entire specimen length of 740 mm. The specimens are illustrated in Fig. 6.5. During testing, scenario A was realized by restraining the masonry prism using a steel plate. Scenario B was realized by clamping the extended piece of the CFRP strip, rather than using a steel plate. An overview of the direct pull-out test setup is provided in Fig. 6.6.

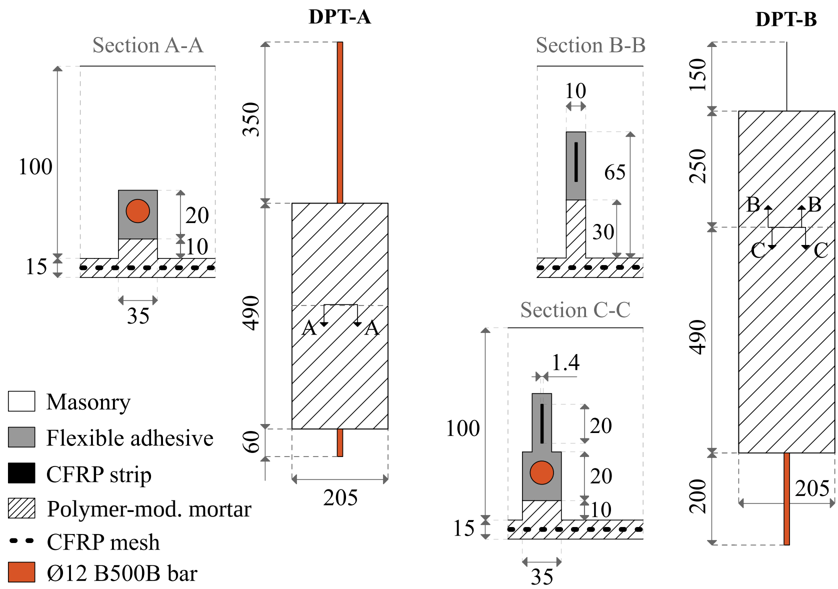

Figure 6.5: Specimens for the direct pull-out tests.

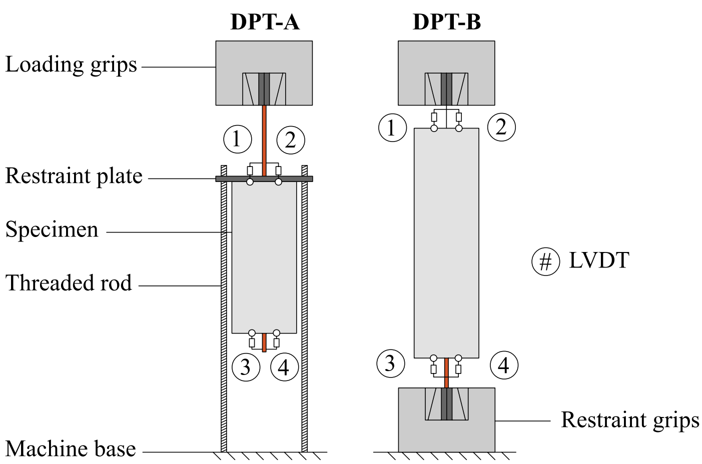

Figure 6.6: Overview direct pull-out test setup.

The direct pull-out tests were conducted on a 250 kN Instron universal testing machine (Fig. 6.7). For the DPT-A specimens, the installation process started by carefully positioning the prism under the loading grips of the testing equipment, with the specimen resting on two support blocks. Hardboard was put on the top of the prism to prevent stress concentrations due to a possible non-flat surface of the brick. Then the steel restraint plate was placed on top of the hardboard. To prevent undesirable wedge type failure modes when using partial end restraint, a full restraint in the form of a 25 mm thick solid steel plate with three openings was selected. The centrally located opening allowed the loaded end of the ribbed steel anchor to pass through. The smaller two openings allowed the LVDT sensors to rest on the specimen. The specimen was then lifted up, which made it possible for the prism to find its own balance point and thus minimize the eccentricity caused by imperfect installation of the anchor. Using M12 threaded steel rods, the steel restraint plate was bolted tightly to the base of the setup. Four LVDTs were installed prior to the load application process. The upper two LVDTs (1 and 2) measured the loaded end slip, whereas the bottom two LVDTs (3 and 4) measured the free end slip.

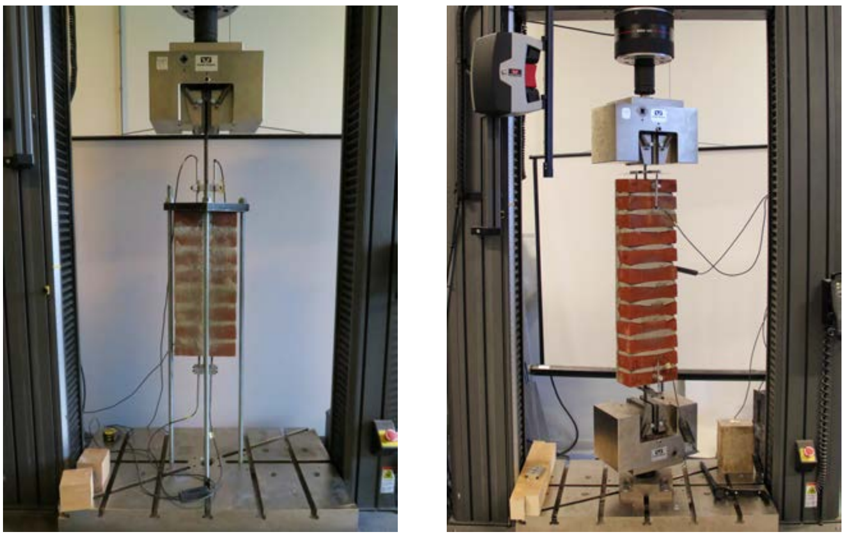

(a) Scenario A

(b) Scenario B

Figure 6.7: Test setup for scenario A and B.

The installation process of the DPT-B specimens (Fig. 6.7b) was slightly different from the DPT-A specimens (Fig. 6.7a). Aluminium plates of 100 mm in length, 20 mm in width and 2 mm in thickness were used to tab the CFRP strips. After the tabs were roughened with sandpaper and thoroughly cleaned with acetone, the tabs were glued to both sides of the extending CFRP strip using high strength and fast curing 2-component epoxy adhesive.

The prism was positioned under the loading grips of the testing equipment, with the specimen resting on two support blocks. The specimen was then lifted up via the aluminium grip plates. The extending anchor was clamped using the grips at the base of the installation. Prior to the load application process, four LVDT sensors were installed. The upper two LVDT's (1 and 2) measured the loaded end slip of the CFRP strip, whereas the bottom two LVDT's (3 and 4) measured the loaded end slip of the steel anchor. The mean of two LVDT's was used to establish the corresponding slip. The pretension load was set at 1.0 kN. After resetting the sensors, the experiment was started with a pull-out speed of 0.5 mm/min (loading grips).

6.3 Test results quasi-static shear tests

This section will provide an overview of the obtained results during the experimental campaign. The first five subsections focus on the in-plane shear experiments, covering overall results, failure modes, strength and drift values, wall response parameters and finally the uplift of the anchors. The final subsection covers the direct pull-out experiments.

6.3.1 Overview in-plane test results

A summary of the obtained in-plane test results is given in Table 6.2. The maximum forces in both the pull ($H_{max,east}$) and push cycles ($H_{max,west}$) is reported. Moreover the maximum net horizontal displacement (δ_{max}, sensor 4 in Fig. 6.2), the maximum drift (Δ_{max}, calculated in accordance with Eq. 6.1) and the failure modes are shown. These parameters are discussed in the following paragraphs.

$$\Delta_{max} = \delta_{max} / h_w \tag{6.1}$$

Table 6.2: Principal results of the cyclic in-plane shear tests.

	L (mm)	p_v (N/mm²)	$H_{max,west}$ (kN)	$H_{max,east}$ (kN)	δ_{max} (mm)	Δ_{max} (%)	Failure mode
S1	1100	0.20	13.7	11.9	± 28.6	± 1.17	rocking
S2	1100	0.30	10.8	22.3	± 40.0	± 1.63	rocking
S3	1100	0.50	20.4	22.3	± 40.0	± 1.63	rocking/crushing
M1	2000	0.15	29.4	32.0	± 40.0	± 1.63	rocking/crushing
M2	2000	0.30	41.0	41.9	± 40.0	± 1.63	rocking/crushing
M3	2000	0.50	52.6	62.6	± 40.0	± 1.63	rocking/crushing
L1	4000	0.15	88.5	94.3	± 40.0	± 1.63	rocking/sliding
L2	4000	0.30	129.1	141.6	± 28.6	± 1.17	rocking/sliding
L3	4000	0.50	174.5	174.4	± 28.6	± 1.17	rocking/sliding

6.3.2 Strength and drift

The hysteresis loops and backbone curves of all the specimens are provided in Fig. 6.8, with grey and black colored lines respectively. For all the specimens, a sudden drop in force was observed after the target displacement was reached. This sudden drop was likely a limitation in the hydraulic equipment preventing a smooth transition when changing the direction of the movement of the horizontal actuator. The test on specimen S1 was aborted due to the detachment of the foundation beam at a target displacement of 28 mm. The tests on specimens L2 and L3 were stopped due to significant damage development in the region surrounding the anchors. The test on the specimens S2, S3, M1, M2, M3 and L1 were stopped at a target displacement of 40 mm as the maximum stroke of the actuator was reached.

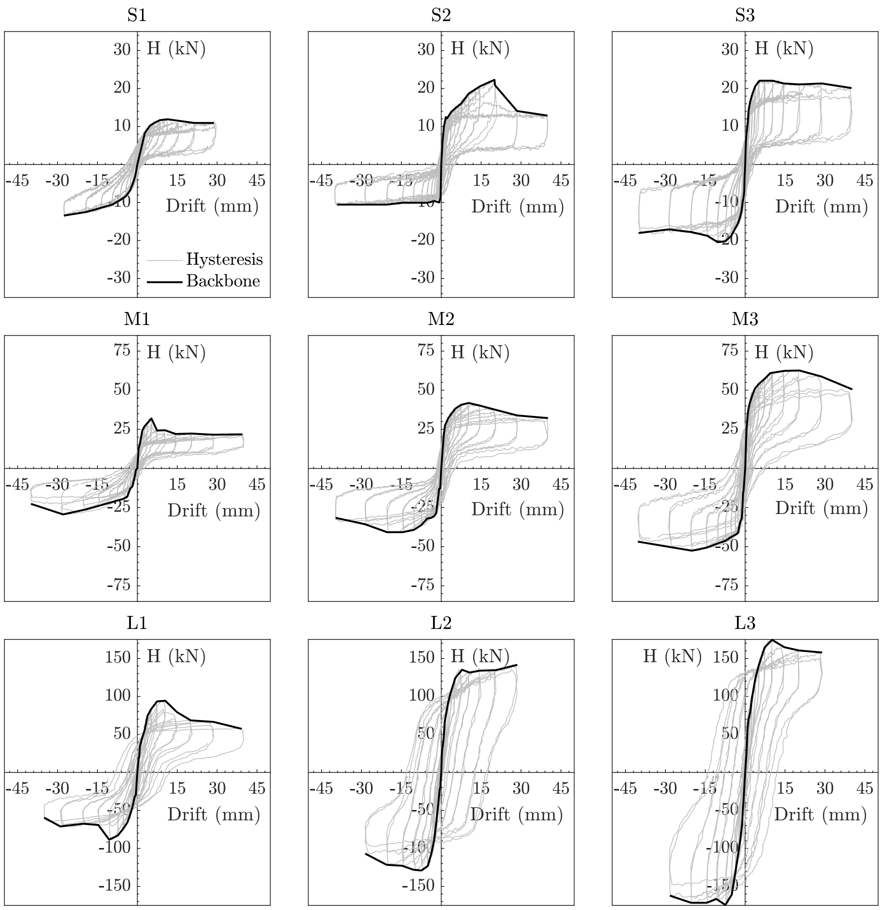

Figure 6.8: Hysteresis loops and backbone curves for the S, M and L specimens.

The difference in strength between the West and East side of the specimens, was less than 16% for all tested walls, except for S2, where the difference was over 50%. From the hysteresis loop of S2 it can be concluded that the West anchor was not activated during the push cycles. This was accompanied by a significant increase in the walls capacity in the push direction. Minimal to none activation of the anchorage occurred during the pull cycles. This is expressed in the lower capacity of the wall in the pull direction. After maximum activation of the anchor in push direction, the force in the load-uplift plot drops back to almost the same value as for the pull cycle. Faulty installation of the anchor could be a possible explanation why the West anchor was minimal to none activated for S2, and thus leading to a difference of more than 50% in strength between both sides. The east anchors of both specimens M1 and M2 were pulled out from the foundation, leading to crack formation around the initial location of the anchors in the foundation beam.

Specimens S2 and M1 showed different load-displacement behaviour between the East and West sides. Looking at the hysteresis loop of specimen S2 in the pull direction, no drop in force was monitored during the post-peak phase. This shows that the debonding process of the installed anchors was not initiated. As mentioned before, the asymmetry in the load-displacement diagram of specimen M2 was caused by the detachment of the foundation beam during the pull cycles. The West anchor did not reach full strength until a target displacement of 28 mm (versus 6.1 mm for the East anchor).

The axial load had a significant influence on the in-plane resistance of the specimens. For the M and L specimens, a linear trend was found between the applied axial load and strength of the specimen. The maximum measured bed joint sliding for the S, M and L specimens were <1mm, <2mm and >30mm respectively.

6.3.3 Failure modes

The failure modes of all specimens are illustrated in Fig. 6.9. None of the specimens showed any shear damage at the treated or untreated surfaces. As failure only occurred at the bottom side of the specimens, the upper part of the walls is not shown in the illustrations in Fig. 6.9. All tested specimens showed initial cracking at the bottom corners. These initial cracks propagated over the complete length of the specimen during subsequent loading cycles. Cracking mainly occurred at the the bottommost bed-joint of the walls. The expected formation of cracks due to the vertical shear stress concentrations caused by the deep grooves (needed for the out-of-plane reinforcement) did not occur.

All specimens started to show rocking behaviour during the tests. For specimens S3, M1, M2, M3 rocking of the specimen was followed by crushing of the specimens' bottom corners. The uplift of the specimen had the effect of reducing the compressive zone which eventually led to toe-crushing.

Due to the relatively low compression forces acting on specimen S1 and S2 these specimens did not show compressive failure.

For specimen S1, first cracking was observed at a horizontal force of about 8 kN in push direction. During the pull cycles not only similar cracking of the bed joint took place but also partial detachment of the concrete foundation beam from the steel plate occurred. Consequently some uplift of the West side of the foundation beam was observed due to rocking of the complete specimen-foundation assembly during pull cycles. This partial detachment of the foundation beam was not observed at the East side during any of the push cycles, leading to different force-displacement behaviour in push and pull cycles. It was found that the bracket at the West side of the specimen, which should keep the foundation beam in place was not tightened sufficiently. For specimen M1, uplifting of the foundation beam was observed during the pull cycles. After observing this malfunction, the brackets were tightened further. This detachment of the foundation beam was not observed during any of the push cycles. During subsequent cycles of the L-specimens, limited rocking and extensive sliding was observed. Subsequently detachment of the bottom corners next to the steel anchors occurred.

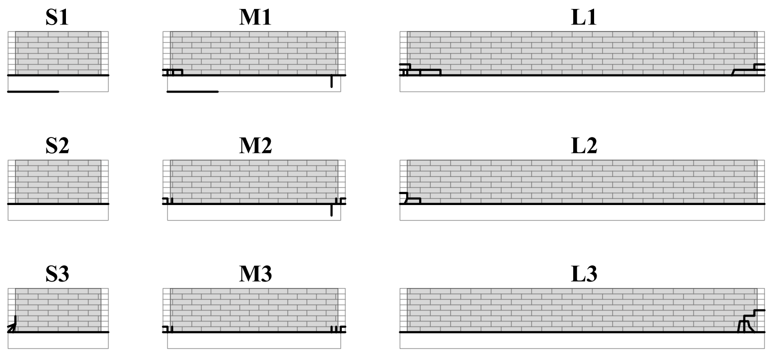

Figure 6.9: Failure patterns of the S, M and L specimens on the as-built side.

6.3.4 Wall response parameters

In-plane wall response parameters were calculated from the backbone curves in the force-displacement graphs presented in Fig. 6.8. A summary of the parameters calculated is shown in Fig. 6.10.

The bilinearised ultimate wall force H_u is determined in accordance with Eq. 6.2. The bilinearised initial stiffness K_e follows from Eq. 6.3. The wall's structural ductility factor μ, the ratio of the ultimate displacement of the wall over the bilinearised yield displacement, is obtained using Eq. 6.4.

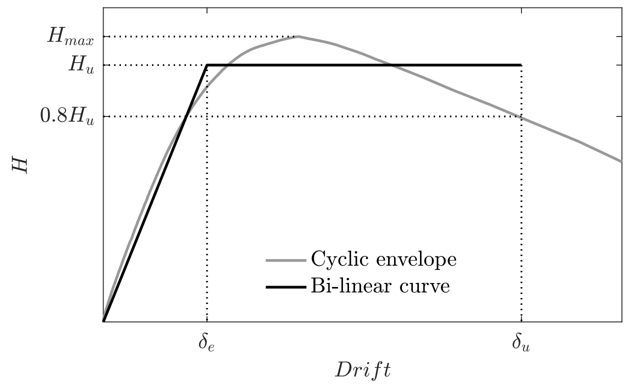

Figure 6.10: Equivalent bilinear in-plane wall response parameters [128].

$$H_u = 0.9H_{max} \tag{6.2}$$

$$K_e = \frac{H_u}{\delta_e} \tag{6.3}$$

$$\mu = \frac{\delta_u}{\delta_e} \tag{6.4}$$

where δ_e is the bilinearised yield displacement and δ_u is the wall's ultimate displacement corresponding to a 20% force drop in the post-peak phase. The wall's response parameters for the tested specimens are listed in Table 6.3.

The limited stroke of the horizontally oriented hydraulic actuator was insufficient to reach a 20% force drop in the post-peak phase for the specimens S1, S3, L2 and L3. For these specimens, the presented ductility factors in Table 6.3 are a lower boundary. For the push side of specimen S2, the wall's structural ductility factor was found to be 4.9. For the M specimens, the wall structural ductility factors were in the range of 3.7-14.7. It can be observed that higher axial loads have a positive effect on the mean ductility factor for the M specimens. For specimen L1, the mean ductility factor was found to be 4.2. Similar to the M specimens, increasing the axial load seems to increase the wall structural ductility factor. An increasing trend in bilinearised initial stiffness was observed as the axial load was increased, while keeping the geometry of the specimen constant.

Table 6.3: In-plane wall response parameters for all specimens.

		H_{max} (kN)	H_u (kN)	δ_e (mm)	δ_u (mm)	K_e (kN/mm)	μ (-)
S1	West	11.9	10.7	4.2	>28.6	2.6	>6.9
	East	-13.7	-12.3	-8.3	<-28.6	1.5	>3.5
S2	West	22.3	20.1	8.2	23.2	2.4	4.9
	East	-10.8	-9.7	-0.2	<-40.0	41.8	>25.0
S3	West	22.3	20.1	1.9	>40.0	10.7	>21.3
	East	-20.4	-18.4	-2.6	<-40.0	7.0	>15.2
M1	West	32.0	28.8	1.9	7.1	15.5	3.7
	East	-29.4	-26.4	-10.7	-38.4	2.5	3.6
M2	West	41.9	37.7	2.4	31.3	15.5	13.0
	East	-41.0	-36.9	-4.3	-36.9	8.5	8.6
M3	West	62.6	56.4	2.7	40.0	20.7	14.7
	East	-52.6	-47.3	-4.2	-40.0	11.4	9.5
L1	West	94.3	84.8	3.6	16.7	23.4	4.6
	East	-88.5	-79.7	-3.8	-14.3	20.8	3.8
L2	West	141.6	127.4	3.6	>28.6	35.8	>8.0
	East	-129.1	-116.2	-3.1	<-28.6	37.0	>9.2
L3	West	174.4	157.0	4.4	>28.6	36.0	>6.6
	East	-174.5	-157.1	-3.7	<-28.6	42.9	>7.8

6.3.5 Uplift anchors

The uplift of the walls at the moment of the maximum load is provided in Table 6.4. As the anchorage method was consistent for all specimens, the slip of the anchor (opening between foundation beam and reinforced wall) at maximum applied load was also expected to be consistent. This was not the case as a significant variation was found in the measured uplift values at the failure loads. The observed detachment of the foundation beam was a disturbing factor for the measured uplift of the West anchors of both specimen S1 and M1. The same applies for the West anchor of specimen S2 that did not enter the post-peak phase. The remaining variations in the uplift values, can be explained by the imperfect clamping of the foundation beam, the insufficient tightening of the steel transport plate to the bottom frame and/or the deformation of the used bolt and threaded rods, leading to an uplift of the foundation beam.

Table 6.4: The uplift of the anchor at maximum applied force.

	S1 (mm)	S2 (mm)	S3 (mm)	M1 (mm)	M2 (mm)	M3 (mm)	L1 (mm)	L2 (mm)	L3 (mm)
Uplift east	3.10	4.49	3.48	2.47	6.24	11.12	7.81	12.76	7.86
Uplift west	8.88	14.31	2.14	18.68	13.42	12.07	9.50	3.88	4.50

6.3.6 Overview pull-out test results

The results of the direct pull-out tests conducted on masonry prisms with embedded anchors are shown in Fig. 6.11, where the pull-out load (pre-tension force not taken into account) is plotted against the loaded end slip of the anchors. The predominant failure mechanism was adhesive failure at the anchor-adhesive interface for both scenarios.

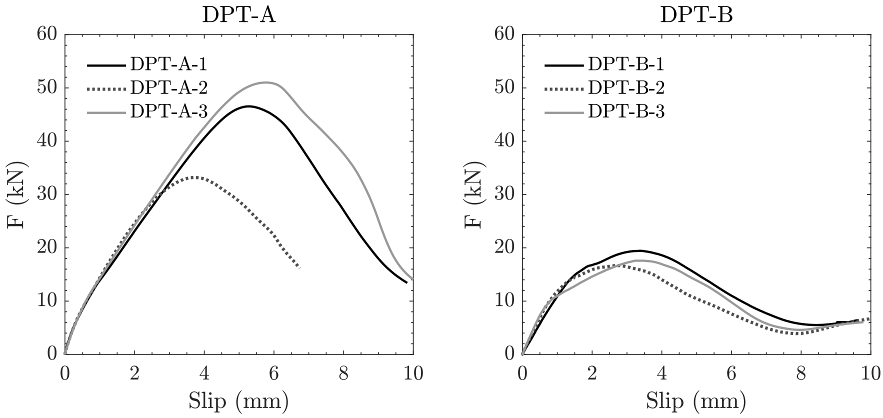

Figure 6.11: Force-slip (free end) diagrams of the direct-pull-out tests.

The anchorage strength f_{max}, mean bond strength σ_{max} and loaded end slip s_{max} at maximum pull-out load were determined at 48.78 kN, 2.59 N/mm² and 5.53 mm respectively for the DPT-A-1 and DPT-A-3 specimens. For the DPT-B specimens, these values were found to be 17.90 kN, 0.95 N/mm² and 3.1 mm respectively. The significant lower value in strength for the DPT-B specimens was likely caused by the relatively higher shear stresses in the adhesive mass between the CFRP strip and the anchor, compared to scenario A. These increased shear stresses could have expedited the crack initiation process. The mean initial stiffness $k_{50\%}$, determined at 50% of the strength and the corresponding slip, was found to be 12.30 kN/mm (DPT-A) and 12.78 kN/mm (DPT-B). For the DPT-A-1 and DPT-A-3 specimens, a reduction in stiffness was observed at a loaded end slip of approximately 4 mm (s_{damage}). For specimen DPT-A-2, the damage initiation stage was entered earlier due to incorrect surface preparation (not made dust free and not made clean with acetone), and thus leading to a significant lower anchorage strength. For the DPT-B specimens, a reduction in stiffness was observed at a significant lower slip ($\pm 1 mm$). An overview of the obtained direct pull-out test results are provided in Table 6.5. Looking at the corresponding slip values at full strength, a major difference was found between the results (Table 6.4).

Table 6.5: Overview pull-out test results.

	F_{max} kN	σ_{max} N/mm²	s_{max} mm	$k_{50\%}$ kN/mm	s_{damage} mm
DPT-A-1	46.54	2.47	5.28	11.55	±4.0
DPT-A-2	33.18*	1.76*	3.71*	13.38	±2.5
DPT-A-3	51.01	2.71	5.78	11.97	±4.0
Mean	48.78	2.59	5.53	12.30	
DPT-B-1	19.43	1.03	3.36	11.05	±1.5
DPT-B-2	16.67	0.88	2.68	13.59	±1.0
DPT-B-3	17.60	0.93	3.27	13.70	±1.0
Mean	17.90	0.95	3.10	12.78	

* Not included in the mean calculation

6.4 Comparison with design models

When out-of-plane buckling is not considered, then there are two failure modes that can occur for walls loaded in-plane: moment failure/rocking or shear failure. The governing failure mode is influenced by the aspect ratio (height divided by length) and the ratio between the vertical and horizontal loading. The moment and shear resistance of reinforced walls were modelled using modified rules from Eurocode 6 [129]. The behaviour and resistance of a reinforced wall is very much alike that of an unreinforced wall. This with the exception that a tension element (anchor) in vertical direction is present. Therefore some modifications on the existing equations for unreinforced masonry walls were made. The used mechanical model is presented in Fig. 6.12.

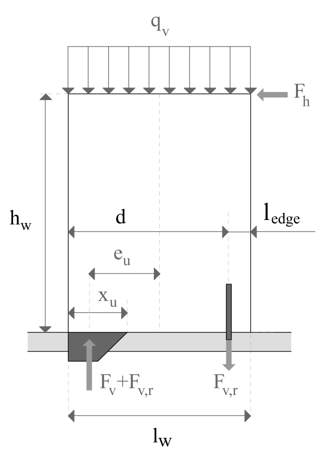

Figure 6.12: In-plane model.

6.4.1 Moment capacity

The ultimate eccentricity (e_u) is determined using Eq. 6.5. The ultimate depth of the compression zone (x_u), following Eq. 6.6, is based on a bi-linear stress-strain relation for the masonry according to the Dutch national annex to Eurocode 6 [129].

$$e_u = \frac{l_w}{2} - \frac{67}{189} x_u \tag{6.5}$$

$$x_u = \frac{14}{9} \frac{(f_v + f_{v,r})}{t_w f_m} \tag{6.6}$$

Where f_m is the compressive strength of the masonry, $F_{v,r}$ is the tensile force in the anchors and F_v is the axial force following Eq. 6.7. The own weight of the reinforced wall (γ=2.12 kN/m^2 is also taken into account for the determination of the axial force.

$$F_v = q_v l_w + (l_w h_w)\gamma \tag{6.7}$$

The moment resistance (M_R) follows from Eq. 6.8. The resistance is based on the equilibrium of the wall, which is influenced by the ultimate eccentricity (e_u) of the vertical reaction force (F_v) and the tensile force in the anchors ($F_{v,r}$):

$$M_r = (F_v + F_{v,r}) e_u + F_{v,r} \left(d - \frac{l_w}{2} \right) \tag{6.8}$$

The effective depth (d) of the anchors is determined in accordance with Eq. 6.9:

$$d = l_w - l_{edge} \tag{6.9}$$

Combing Eqs. 6.5, 6.6, 6.7, 6.8, 6.9 results in Eq. 6.10:

$$M_R = (F_v + F_{v,r}) \left\{ \frac{l_w}{2} - \frac{67}{189} \frac{14}{9} \frac{(f_v + F_{v,r})}{t_w f_m} \right\} + f_{v,r} \left(\frac{l_w}{2} - l_{edge} \right) \tag{6.10}$$

The moment resistance (M_R) that follows from the experiments is determined by Eq. 6.11:

$$M_R = F_{h,test} h_w \tag{6.11}$$

Combing and rewriting Eq. 6.10 and Eq. 6.11, results in Eq. 6.12, which can be used to determine the tensile forces in the anchors according to the proposed model. The α and β factors in 6.12 are determined using Eq. 6.13 and Eq. 6.14 respectively.

$$F_{v,r} = \frac{\beta + l_w - (2_v + l_{edge})}{2\alpha} \tag{6.12}$$

$$\alpha = \frac{67}{189}\frac{14}{9}\frac{1}{t_w f_m} \tag{6.13}$$

$$\beta = \sqrt{l_{edge}^2 - 2l_{edge}l_w + 4F_{v edge} + l_w^2 - 2F_{v w} - 4_{h,test}h} \tag{6.14}$$

With the absence of anchors ($F_{v,r}$=0), the maximum horizontal load resistance (F_{Rh}) follows from Eq. 6.15. This can be used to determine the added value of the anchors for the moment resistance of the wall.

$$F_{Rh} = \frac{M_R}{h} = \frac{f_v}{h}\left\{\frac{l_w}{2} - \frac{67}{189}\frac{14}{9}\frac{F_v}{t_w f_m}\right\} \tag{6.15}$$

6.4.2 Shear capacity

With respect to shear failure again two situations have to be considered:

- Shear failure in the masonry wall, where the resistance is based on the initial shear strength, the contribution from the normal stress and the effective depth of the compression zone.
- Sliding of the masonry wall over the base, where the resistance is based on dry friction only as no cohesive strength will be present due to the rocking behaviour.

According to Eurocode 6 [129] the shear resistance of an unreinforced masonry wall V_R is derived with Eq. 6.16. Since no shear tension failure was observed in the compressed area of the tested specimens, the upper limit for the shear resistance is not taken into account.

$$V_R = l_c t_w (f_{v0} + \mu_{ma} \sigma_v) \tag{6.16}$$

Where (l_c) is the length of the compressed area at the end section of the wall, f_{v0} is the initial shear strength, μ_{ma} is the average coefficient of friction of the masonry and σ_v is the average compressive stress in the compressed part of the cross-section determined using Eq. 6.17:

$$\sigma_v = \frac{F_v}{l_c t_w} \tag{6.17}$$

For the friction coefficient of clay brick masonry the value 0.75 was used, as determined with the triplet shear tests and proposed in NPR9998 [92]. This coefficient was also used to describe the shear resistance of the base joint between the masonry wall and the concrete base beam. It should be noted that this joint has different properties than a regular bed joint in masonry. Firstly, due to temperature effects and drying shrinkage of the mortar, the bond between concrete and masonry can be affected. Secondly, the bond will be completely gone (i.e. f_{v0}=0) when the masonry is subjected to rocking. Taking the additional compressive force into account, caused by the tensile force ($F_{v,r}$) generated by the anchor in tension, the resistance against shear sliding at the base joint is determined in accordance with Eq. 6.17. When the contribution of the anchors is not taken into account ($F_{v,r}$=0) for the resistance ($V_{R,s0}$) against shear sliding, Eq. 6.17 changes to Eq. 6.19.

$$V_{R,s} = 0.75(F_v + F_{v,r}) \tag{6.18}$$

$$V_{R,s0} = 0.75 F_v \tag{6.19}$$

6.4.3 Comparison with experimental results

By using the input parameters as provided in Table 6.6, the horizontal resistance (F_{Rh}) when neglecting the contribution of the anchorage can be determined. The calculated resistance (F_{Rh}) was compared with the maximum horizontal resistance ($F_{h,test}$) found with the experiments for the specimens (S and M) that failed due to rocking. An overview of the results of these specimens are provided in Table 6.7. It should be noted that the strongest side (West or East) is considered.

Table 6.6: Input parameters analytical model.

Description	Symbol	Value	Unit
Weight of the reinforced wall	γ	2.12	kN/m^2
Compressive strength masonry	f_m	15	N/mm^2
Average coefficient of friction of the masonry	μ_{ma}	0.75	–

Table 6.7: Overview results analytical model for the rocking specimens (S/M).

	F_v (kN)	F_{Rh} (kN) Eq. 6.15	$V_{R,s0}$ (kN) Eq. 6.19	$F_{h,test}$ (kN)	$F_{Rh}/F_{h,test}$ (–)	$F_{v,r}$ (kN) Eq. 6.12
S1	27.7	6.1	20.8	13.7	0.45	20.2
S2	38.7	8.5	29.0	22.3	0.38	37.3
S3	60.7	13.1	45.5	22.3	0.59	25.2
M1	40.4	15.7	30.3	32.0	0.51	21.3
M2	70.4	27.1	52.8	41.9	0.67	19.0
M3	110.4	41.9	82.8	62.6	0.69	27.0

The maximum horizontal load resistance (F_{Rh}) (with the absence of anchors) for the S and M specimens are presented with dashed lines in Fig. 6.13. The added value of the anchors is set as the difference between the experimental backbone curve and the analytically obtained maximum horizontal load resistance F_{Rh}. These areas are marked in light grey. It can be concluded that the effect of anchors for increasing the rocking capacity is significant for the S and M specimens, with model / experimental ratios in the range of 0.38-0.59 and 0.51-0.69 for the S and M specimens respectively. Looking at Fig. 6.13, it is observed that the rocking capacity of specimen S2 was not influenced by the West anchor. Combined with the previously mentioned absence of the post-peak phase of the anchor bond, the conducted analyses indicate that the West anchor of specimen S2 was not activated during the experiment. Faulty surface conditions of the anchor (not cleaned and made dust-free) could not be the only explanation, as the direct pull-out results indicated that there still was some significant bonding capacity left in this case. Possible explanations for the West anchor not being activated could be the insufficient confinement of the anchor in the flexible adhesive and/or the faulty preparation of the flexible adhesive.

For the specimens where sliding over the base joint occurred (L specimens), the ratio between the maximum horizontal force on the specimen and the calculated shear sliding resistance ($V_{Rs}/F_{h,test}$) is < 1.0, as shown in Table 6.8. For the L-specimens, the dark grey areas in Fig. 6.13 indicate the difference between the maximum load during the in-plane experiments

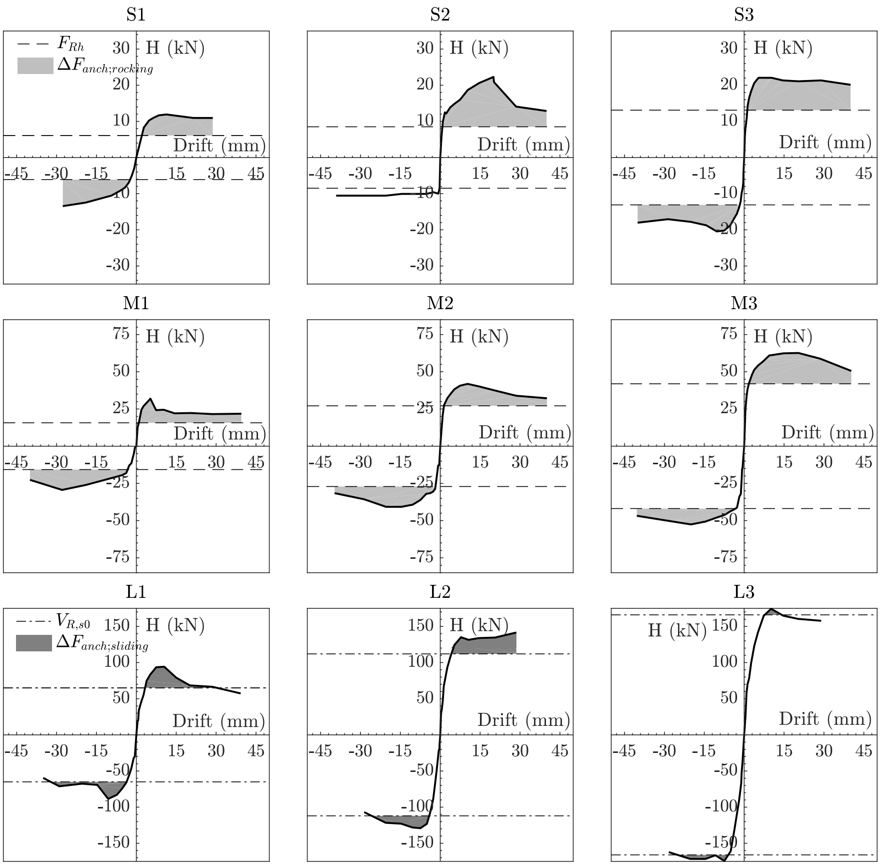

Figure 6.13: Marked backbone curves for the S, M and L specimens, with the added value of the anchors for the rocking capacity (light grey areas), and for the sliding resistance (dark grey areas).

and the sliding resistance V_{Rs} of the specimen including the extra compression force caused by the anchor (indicated by a dash-dot line). Comparing the determined values for the sliding resistance with and without the contribution of the anchors from Table 6.8, it can be observed that the additional compression force due to the anchors results in an increase of 14.8 kN (+24.5%) and 15.2 (+14.42%) in sliding shear resistance (following the analytical model) for specimens L1 and L2 respectively. For specimen L3 the sliding shear resistance for the two aforementioned cases remained the same. The contribution of the anchors in creating an additional compression force in the joint will result in an extra resistance against sliding due to friction, hence probably explaining the specimen exceeding the calculated sliding resistance V_{Rs}. Looking at the values for the rocking resistance F_{Rh} in case of no anchors and the resistance V_{Rs} against shear sliding in the base joint for specimens L1 and L2 (as provided in Table 6.8), it can be observed that the anchors first provide additional sliding resistance followed by an increased moment resistance, preventing the rocking failure of the specimen. The added value of the anchors is limited for both the rocking and sliding behaviour of specimen L3, likely caused by the high axial load.

Table 6.8: Overview results analytical model for specimens (L) failing due to sliding.

	F_v (kN)	F_{Rh} (kN)	$V_{R,s0}$ (kN)	$F_{h,test}$ (kN)	$V_{R,s0}/F_{h,test}$ (−)	$F_{v,r}$ (kN)	$V_{R,s}$ (kN)	$V_{R,s}/F_{h,test}$ (−)
Eq.		6.15	6.19			6.12	6.18	
L1	80.8	65.0	60.6	94.3	0.64	19.8	75.4	0.80
L2	140.8	111.9	105.6	141.6	0.75	20.3	120.8	0.85
L3	220.8	172.9	165.6	174.5	0.95	1.1	166.4	0.95

For the S and M specimens the determined tensile forces in the anchors using Eq. 6.12 ranged between 11.7 and 37.3 kN (Table 6.7), with a mean value of 20.1 kN (COV = 38.7%). Comparing the values for the analytically determined anchorage strength from the in-plane experiments with the conducted direct pull-out experiments, the calculated values predominantly fall between the lower bound (scenario B) and the upper bound (scenario A) as shown in Fig. 6.14. It can be concluded that scenario B, where the tensile forces are pre-dominantly transferred from the anchor to CFRP strip, provided a better approximation of the analytically determined anchorage strength. Testing conform scenario A is not advised in the current study, as the anchorage strength is significantly overestimated.

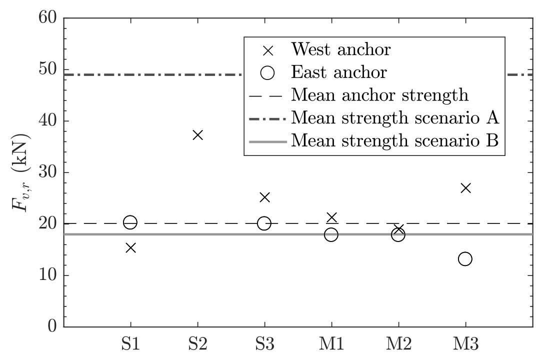

Figure 6.14: Comparison calculated and tested anchor strength.

Taking 17.9 kN as the mean strength of the anchors (following the pull-out tests conform scenario B), the (moment) resistance of the wall F_R can be determined for the S and M specimens. The results are shown in Table 6.9 and Fig. 6.15. The model/experimental ratio was in the range 0.68-1.08 and 0.90-1.07 for the S and M specimens respectively. The model/experimental ratio of 1.4 for specimen S2 (east) was not included in Fig. 6.15 as the West anchor minimally to not activated, as was shown in Fig. 6.13.

Table 6.9: Comparison analytical model ($F_{v,r}$ = 17.9kN) and experimental results for the specimens (S and M) failing predominantly due to rocking.

	$F_{h,test.east}$ (kN)	$F_{h,test.west}$ (kN)	F_{Rh} (kN)	V_{Rs} (kN)	$F_R = min(F_{Rh}; V_{Rs})$ (kN)	$F_{RM}/F_{h,test,east}$ (−)	$F_{RM}/F_{h,test,west}$ (−)
Eq.			6.15	6.19			
S1	13.7	11.9	12.8	47.6	12.8	0.94	1.08
S2	10.8	22.3	15.2	55.9	15.2	1.40*	0.68
S3	20.4	22.3	19.6	72.4	19.6	0.96	0.88
M1	29.4	32	29.5	57.1	29.5	1.00	0.92
M2	41	41.9	41.1	79.6	41.1	1.00	0.98
M3	52.6	62.6	56.1	109.6	56.1	1.07	0.90

* Anchor not activated

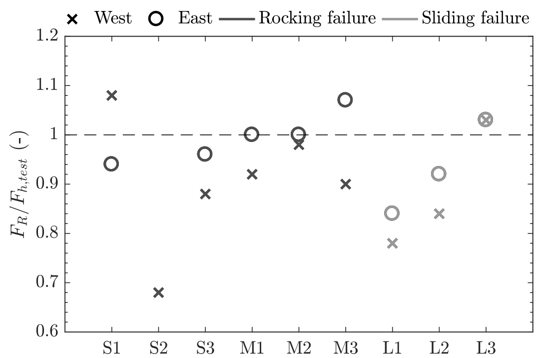

Figure 6.15: Model/experimental ratios for all specimens.

With the mean strength of the anchors (following the pull-out tests conform scenario B), the (sliding) resistance of the wall F_R can also be determined for the L specimens. The results are provided in Table 6.10 and Fig. 6.15. The model/experimental ratio was in the range 0.78-1.03 for the L specimens. The low ratios can partly be explained by the dowel effect of the anchor in the compression zone not being taken into account.

Table 6.10: Comparison analytical model ($F_{v,r}$ = 17.9kN) and experimental results for the specimens (L) failing predominantly due to sliding.

	$F_{h,test,east}$ (kN)	$F_{h,test,west}$ (kN)	F_{Rh} (kN)	V_{Rs} (kN)	$F_R = min(F_{Rh}; V_{Rs})$ (kN)	$F_R/F_{h,test,east}$ (-)	$F_R/F_{h,test,east}$ (-)
Eq.			6.15	6.19			
L1	88.5	94.3	91.5	87.4	87.4	0.84	0.78
L2	129.1	141.6	138.2	132.4	132.4	0.92	0.84
L3	174.5	174.4	198.7	192.4	192.4	1.03	1.03

6.5 Diagonal compression tests on wallettes

Within the full-scale wall experimental program rocking and sliding failure were observed, but no shear failure of the masonry was observed for any of the specimens. It was therefore considered essential to perform additional tests to determine the in-plane shear capacity of walls strengthened with this combined system. The diagonal compression test was selected for this purpose. While the influence of FRCM reinforcement on the in-plane behaviour of masonry wallettes has been a popular subject of research for the past years, the influence of the aforementioned combination of retrofit measures on the in-plane shear capacity of masonry has not been investigated before. Moreover, this experimental program aims to investigate the possible degrading effect of the proposed out-of-plane strengthening system on the in-plane shear strength of masonry panels. Finally, the experimental results will be compared to the outcomes of existing analytical models and design codes, to check the validity of these models for this combined retrofit system.

6.5.1 Building the specimens

The specimens for the diagonal compression tests were built in the testing laboratory of QuakeShield in Grijpskerk, the Netherlands. A total of 13 brick clay masonry wallettes (n_{test}) were built by an experienced mason. All specimens had a square geometry of about 700×700 mm² ($h_w \times l_w$), a nominal thickness of 95 mm and a nominal bed joint thickness of 12 mm. The panels had reduced dimensions compared to the prescriptions (1,200×1,200 mm²) of the ASTM E 519-02 [73] standard due to the geometrical limitations of the test setup. The masonry specimens were constructed against a vertical sideboard to ensure minimum horizontal deviation. Because of this construction method, the mortar layer thickness of the sideboard side seemed thicker due to the mortar flowing out in the gap between the masonry specimen and the sideboard. The masonry specimens were left to cure for at least 28 days in the unheated laboratory (8-18 °C) before retrofitting.

6.5.2 Reinforcing the specimens

A schematic overview of the different specimens in this study is provided in Fig. 6.16. Details and geometrical properties of the specimens are provided in Fig. 6.16 and Table 6.11. Four of the 13 specimens were left untreated (URM). After the walls were sufficiently cured the retrofitting process of the other specimens started, by installing one CFRP strip in the centre of each wall following the installation procedure mentioned in section 1.4.

On three specimens (coded STRIP) no FRCM layer was installed (Fig. 6.17). For the remaining specimens (coded COMB) a single-sided FRCM overlay was installed following the installation procedure mentioned in 1.5.

The nominal FRCM layer thickness (t_{FRCM}) was 10 mm and 20 mm for the COMB10 and COMB20 specimens respectively. Due to the added FRCM layer, the mass of the COMB10 and COMB20 specimens increased with approximately 10.5 kg (21.4 kg/m^2) and 21.0 kg (42.8 kg/m^2) respectively. To ensure the compression load being applied only on the masonry, the FRCM layer was bevelled close to the edges. The specimens were left to cure for an additional 28 days. Fig. 6.18 shows a photo of a COMB specimen.

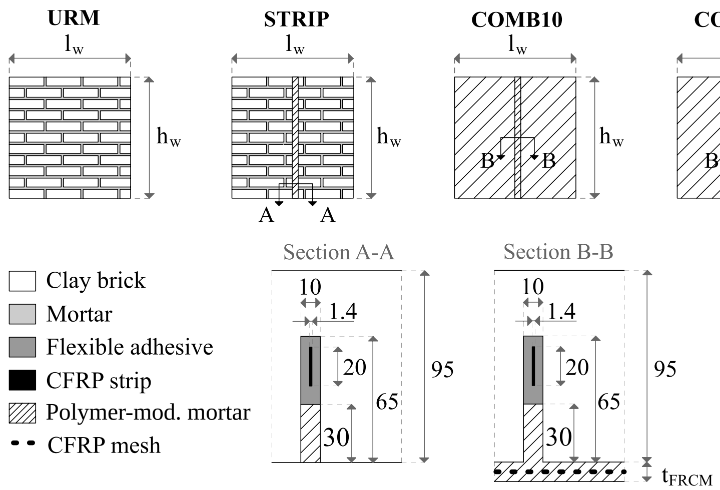

Figure 6.16: Schematic overview URM, STRIP, COMB10 and COMB20 specimens.

Table 6.11: Geometrical properties of the reinforced specimens.

	n_{test} (−)	Mean h_w (mm)	Mean l_w (mm)	FDM CFRP strip (−)	t_{FRCM} (mm)
URM	4	698.8	699.4	No	-
STRIP	3	699.0	703.3	Yes	-
COMB10	3	698.7	696.7	Yes	10
COMB20	3	696.0	699.3	Yes	20

When only the CFRP mesh, CFRP strip or the FRCM layer is considered, the specimens had a reinforcement ratio of $\rho_{r,mesh}$ = 0.046%, $\rho_{r,CFRPstrip}$ = 0.042% and $\rho_{r,FRCM}$ = 10.5% (per 10 mm layer thickness) based on the cross sectional areas. It should be noted that in practice, the reinforcement ratio of the CFRP strip is variable, as the CFRP strips can be positioned closer or further apart from each other depending on the design lateral load.

Figure 6.17: Photo STRIP specimen

Figure 6.18: Photo COMB specimen.

6.5.3 Test setup and procedure

To investigate the behaviour of the retrofit system under in-plane loading, the diagonal compression test was chosen. The diagonal compression test, as described in ASTM E 519-02 [73] is regarded as a simple procedure to determine the shear strength of masonry elements. The principle of the test is depicted in Fig. 6.19. The diagonal compression test was introduced to simulate a pure shear stress state, in accordance with the situation depicted in Fig 6.19. Under these conditions the Mohr's circle of the stress states are reduced (Fig. 6.19), leading to the corresponding value of average shear stress following Eq. 6.20:

$$\tau = \frac{P}{\sqrt{2}A_n} \tag{6.20}$$

Where P and A_n are respectively the compressive force applied to the specimen and the cross sectional area (parallel to the bed joint) of the specimen. The principal tensile stress (σ_I) is hence equal to the shear stress. Using Eq. 6.20 and the ultimate force P_u leads to the shear strength as provided in Eq. 6.21, where f_v and P_{max} are respectively the shear strength and the compressive failure load of the specimen:

$$f_v = \frac{P_{max}}{\sqrt{2}A_n} \tag{6.21}$$

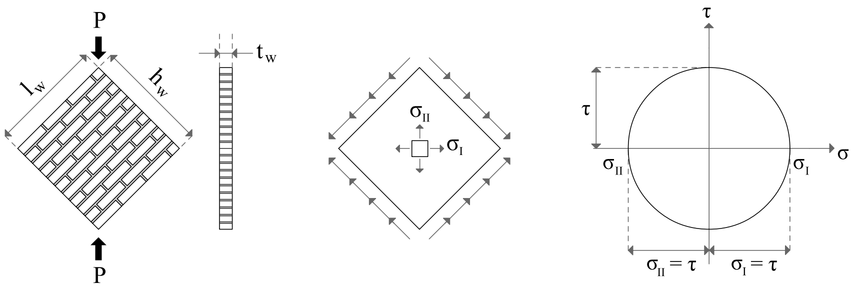

Figure 6.19: Principle of test, pure shear stress state and Mohr circle.

The diagonal compression tests were performed at the Structures Laboratory of Eindhoven University of Technology. The tests were performed on a Schenk-Trebel servo hydraulic compression machine with a maximum capacity of 2.5 MN. The test setup consisted of a data acquisition system and a monitoring system consisting of four LVDT's with a measuring range of +2 to -2 mm and an accuracy of ±1/500 mm. Vertically orientated LVDT's in the middle of both sides of the specimens measured the vertical deformation (Δ_v) over length g_v, while two horizontally positioned LVDT's (one on each side of the specimen) monitored the horizontal deformations (Δ_h) over length g_h. A schematic overview and photo of the setup are provided in Fig. 6.20 and Fig. 6.21 respectively. A steel v-shaped loading shoe at the top and bottom side of the specimens was used to apply the compressive load to the specimens. The steel shoe consisted of two 20 mm thick steel plates with two 50 mm thick steel blocks in between (attached with M16 bolts). The steel blocks were perpendicular to each other and had a length of 100 mm, as illustrated in Fig. 6.20. The steel shoes were provided with 10 mm thick softboard to prevent local stress concentrations near the supports. Fig. 6.22 shows a photo of the loading shoe. It should be noted that due to the reduced dimensions of the test specimens with respect to the ASTM E 519 [73] standard, the confining effect produced by the v-shaped steel shoes could become more prominent and, consequently, result in a greater loading capacity of the tested specimens.

Each test was performed under displacement control by using the displacement measurement system of the testing machine. A displacement rate of 0.08 mm/min was used until a compressive force of 12 kN was reached (corresponding to the force needed to close the spacing of the ball hinge of the compression machine) after which the displacement rate was lowered to 0.04 mm/min for the remainder of the test. The tests were stopped when the compressive force dropped to zero or when significant damage occurred. During the tests the crack were marked on the specimens and photographs were taken of the crack propagation.

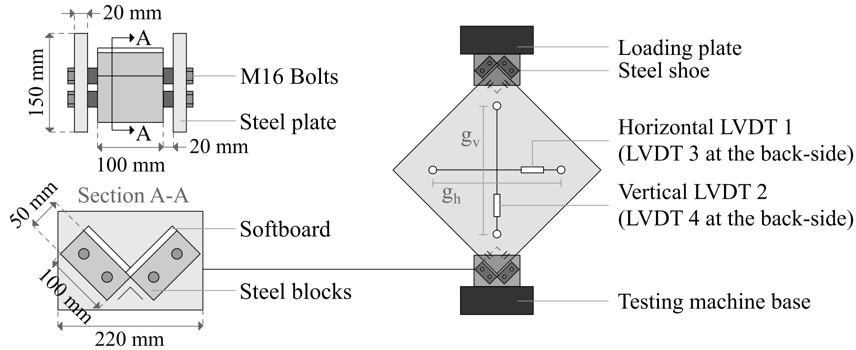

Figure 6.20: Illustrations of the test setup and loading shoe.

Figure 6.21: Photo of the test setup.

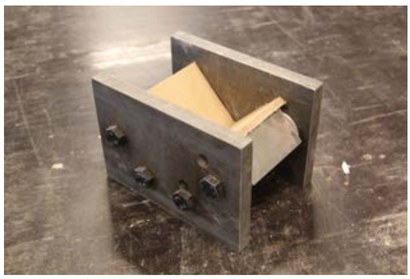

Figure 6.22: Photo of the loading shoe.

6.6 Test results diagonal compression tests

6.6.1 Overview in-plane test results

The test results are summarized in Table 6.12. The failure load P_u and shear strength will be discussed first. Failure modes, shear strains (γ), elastic shear strengths (τ_e), shear moduli (G) and pseudo-ductility factors (μ) will be covered in the following sections.

The URM specimens had an average shear strength of 0.75 N/mm², while the average shear strength of the masonry specimens reinforced with solely a DM CFRP strip was 0.77 N/mm². From these results it can be concluded that despite the deep grooves, the shear strength of a masonry element is not affected significantly by the out-of-plane reinforcement system. The average shear strength of COMB10 specimens was 1.24 N/mm², which is 1.7 times the unstrengthened specimens' shear strength. For the COMB20 the shear strength was 1.36 N/mm², resulting in a shear strength amplification factor of 1.8 compared to the URM specimens.

Table 6.12 also presents the spread of the strength values. A relatively high scatter in results was obtained for the unstrengthened specimens and the specimens reinforced with only a FDM CFRP strip, compared to the FRCM reinforced specimens. This is however expectable considering the general behaviour of the URM, and the brittle failure that occurred during these tests. For the COMB20 specimens a considerably lower scatter in results was found. Due to the significant lower FRCM layer thickness of specimen COMB10-1 compared to COMB10-2 and COMB10-3, the shear strength was also considerably lower. This indicates that the matrix mortar layer thickness has an influence on the strength. However, no strong correlation was found between the FRCM layer thickness and the failure load (R^2=0.4).

6.6.2 Failure modes

Depending on physical and mechanical properties of a wall, four possible failure modes have been identified for URM [18,62,130,131] and described by Li et al. [130] and Babaeidarabad et al. [132]:

- Shear sliding (V_{ss}): failure takes place along a single bed joint caused by bond failure between clay brick and mortar.(Fig. 6.23a)
- Shear stepped sliding (V_{sf}): failure is controlled by the loss of bond between the mortar and masonry units in the stepped-stair format. (Fig. 6.23b)
- Diagonal tension (V_{dt}): failure occurs when the principal tension stress produced by the combination of shear and compressive forces reaches the tensile strength of the wall. (Fig. 6.23c)
- Crushing (V_c): when the maximum stress on the edges of block exceeds the compressive strength of the masonry, compression failure can occur. (Fig. 6.23d)

During the diagonal compression tests several types of failure mechanisms were observed. The crack patterns of the tested specimens are illustrated in Fig. 6.24. Photos of some specimens after diagonal compression testing are provided in Fig. 6.25.

Table 6.12: Overview of the diagonal compression test results.

	t_w (mm)	t_{FRCM} (mm)	A_n mm^2	P_u (kN)	Mode*	f_v N/mm^2	γ_{max} (‰)	γ_u (‰)	γ_e (‰)	G_e (kN/mm2)	μ (-)
URM-1	95.0	-	66357	77.97	2	0.83	0.41	-	0.21	2.78	1.0
URM-2	93.8	-	65578	69.05	2	0.74	0.45	-	0.22	2.32	1.0
URM-3	94.3	-	65881	63.17	2	0.68	0.33	-	0.21	2.25	1.0
URM-4	95.0	-	66429	58.21	1&2	0.62	-	-	0.13	3.28**	1.0
Mean				67.10		0.75				2.45	
COV				11.0%		8.3%				9.5%	
STRIP-1	95.0	-	66524	81.71	1&2	0.87	0.69	-	0.18	3.29**	1.0
STRIP-2	96.0	-	67536	74.39	2	0.78	0.52	-	0.31	1.73	1.0
STRIP-3	94.3	-	65951	61.49	2	0.66	0.64	-	0.24	1.93	1.0
Mean				72.53		0.77				1.81	
COV				11.5%		11.1%				5.4%	
COMB10-1	95.0	10.3	66429	127.49	3&5	1.36	-	-	0.26	3.63	-
COMB10-2	95.0	10.8	66856	117.95	3&5	1.25	0.58	2.10	0.25	3.54	8.5
COMB10-3	95.0	6.8	66429	104.52	3&5	1.13	0.58	1.90	0.20	3.85	9.3
Mean				116.65		1.24				3.67	
COV				8.1%		7.5%				3.6%	
COMB20-1	95.0	20.8	66666	121.00	3,4 & 5	1.28	3.08	4.60	0.30	3.02	15.5
COMB20-2	95.0	20.3	66357	127.79	3&5	1.36	0.51	3.96	0.25	3.75	15.6
COMB20-3	95.0	17.6	65811	132.45	3&5	1.42	0.50	3.46	0.22	4.44	15.4
Mean				127.08		1.36				3.74	
COV				3.7%		4.2%				9.8%	

* 1 = shear failure, 2 = shear friction, 3 = diagonal tension, 4 = crushing, 5 = out-of-plane deformation;
** Not included in the mean value

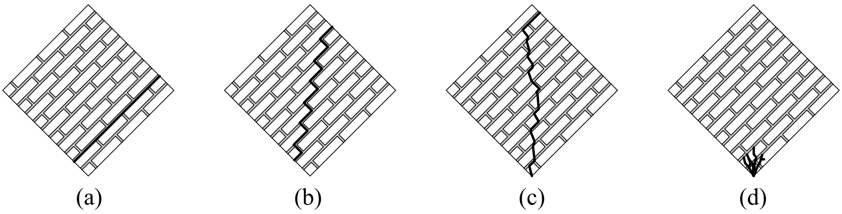

Figure 6.23: Possible failure modes: Shear sliding (A), shear stepped sliding (B), diagonal tension (C) and crushing (D).

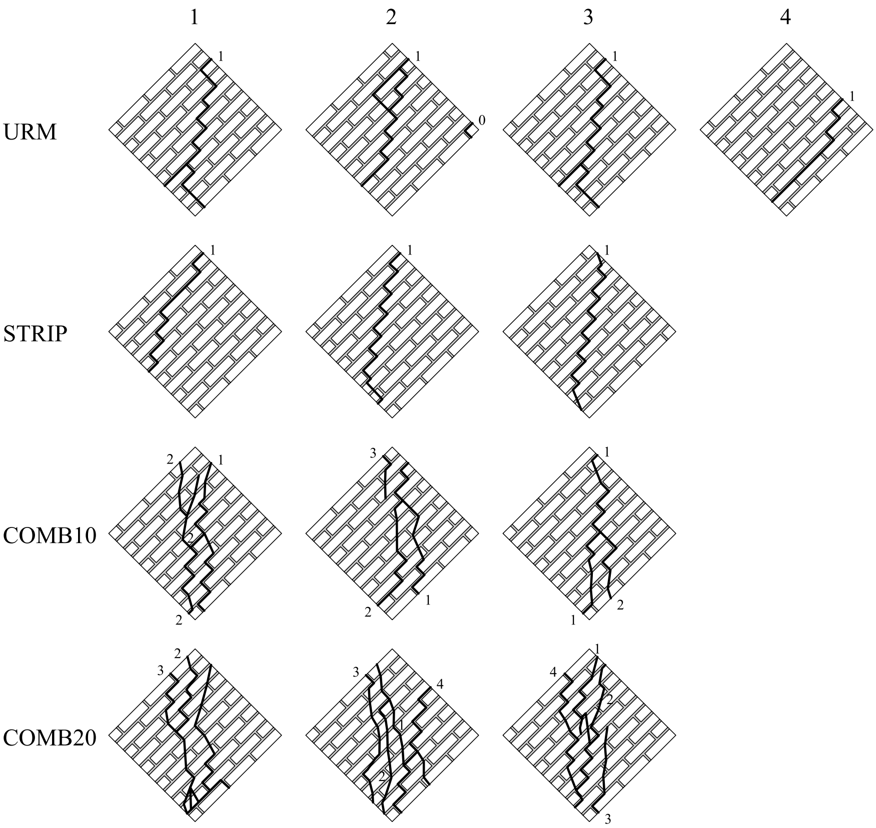

Figure 6.24: Crack patterns and propagation of the specimens (as-built side for COMB10 and COMB20)

The failure behaviour of the unstrengthened specimens was brittle. Failure of these specimens was sudden and no considerable crack development was observed prior to failure. All URM specimens except URM-4, failed by the formation of one large crack parallel to the loading direction. The crack occurred sudden and immediately propagated over the height of the specimen, leading to brittle failure. The crack mainly followed a stair-stepped pattern, where cracking predominantly occurred at the interface between the units and the mortar (i.e. shear stepped sliding failure). Unlike the other control specimens, specimen URM-4 failed by shear sliding at the bed joint located at the second layer from the bottom of the specimen.

(a) Specimen URM-2.

(b) Specimen STRIP-3.

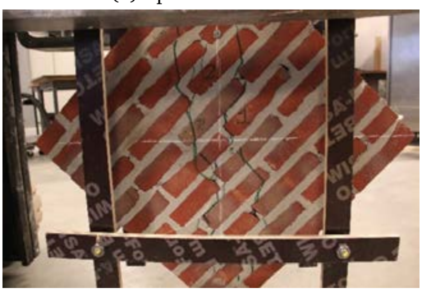

(c) Specimen COMB-20-1 as-built side.

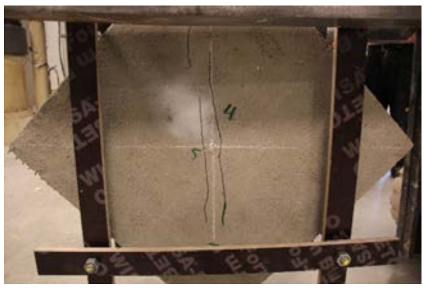

(d) Specimen COMB-20-1 reinforced side.

Figure 6.25: Photos of specimens after testing.

Specimens provided with only a DM CFRP strip showed mainly the same failure behaviour as the unstrengthened control specimens. Specimen STRIP-1 failed by shear sliding while the other two specimens, STRIP-2 and STRIP-3, showed stair-stepped diagonal cracking (shear friction failure). The STRIP specimens did not disintegrate like the unstrengthened specimens after reaching the failure load. This is attributed to the CFRP strip, holding the specimen together after failure. Specimens provided with both a DM CFRP strip and a single-sided FRCM overlay (COMB10 and COMB20) showed completely different failure behaviour. Contrary to the control specimens, these specimens behaved more ductile. When the failure load was reached a large diagonal tension crack was formed within these specimens on the as-built side, covering the complete vertical diagonal of the panels. Unlike the control specimens the strengthened specimens still possessed a considerable amount of capacity after reaching the failure load. During the course of the tests multiple cracks developed on the as-built surface of these specimens. Eventually hairline cracks were observed at the strengthened side (typical cracking displayed in Fig. 6.25d). Specimen COMB20-1 showed some additional masonry crushing near the bottom support at the final stage.

Where the COMB10-1 and COMB10-2 specimens had two diagonal cracks parallel to the vertical diagonal on the as-built side, specimen COMB10-3 (with a nominal FRCM layer thickness of only 6.8 mm) showed two diagonal cracks at the bottom half and one diagonal crack at the top half of the specimen. In contrary to the COMB10 specimens, the COMB20 specimens showed three to four diagonal cracks over a wider area. A possible explanation for this discrepancy in crack pattern may lie in the difference in thickness of the upper mortar layer of the FRCM overlay. Grande, Imbimbo & Sacco [133] conducted a parametric analysis on the interaction between the CFRP reinforcement and the mortar matrix at the level of the interface under shear bond test conditions. The researchers served that an increase of the thickness of the upper mortar layer (within certain boundaries) and thereby an increase in axial stiffness, led to an increase of the force sustained by the reinforcement. It was found that the maximum force of a coupon with an upper mortar layer of a certain thickness was 1.4 times higher than the maximum force in absence of an upper mortar layer. This effect was reported to be strictly correlated to the increase of the length of the transfer zone (effective bond length) due to the increase of the axial stiffness of the upper mortar layer [133]. The thicker upper mortar layer leading to an increased utilization of the carbon FRP mesh is in line with the experimental observations of this study of more cracks occurring at a wider area with an increased FRCM layer thickness.

Next to the mentioned failure modes, out-of-plane bending deformation on all the COMB10 and COMB20 specimens were observed towards the end of the conducted experiments. This observation is shown in Fig. 6.26a for the COMB20-3 specimen, where the dashed lines represent the specimen at initial condition and the solid lines illustrate the specimen at the end of the experiment. The out-of-plane (OOP) bending was confirmed by the difference in cracks between the reinforced side and the as-built side of the specimens. Small cracks on the strengthened side and large cracks on the as-built side are associated with out-of-plane bending deformation [126, 134] for one side strengthened specimens subjected to diagonal compression tests. The cracks on the as-built side, as shown in 6.26b for COMB10-2, closed partly as the load was removed.

6.6.3 Shear stress-strain behaviour

The vertical shortening and horizontal elongation were computed from the mean displacement readings on both sides divided by the measured length (g_h for horizontal, g_v for vertical), using Eqs. 6.22 and 6.23 respectively.

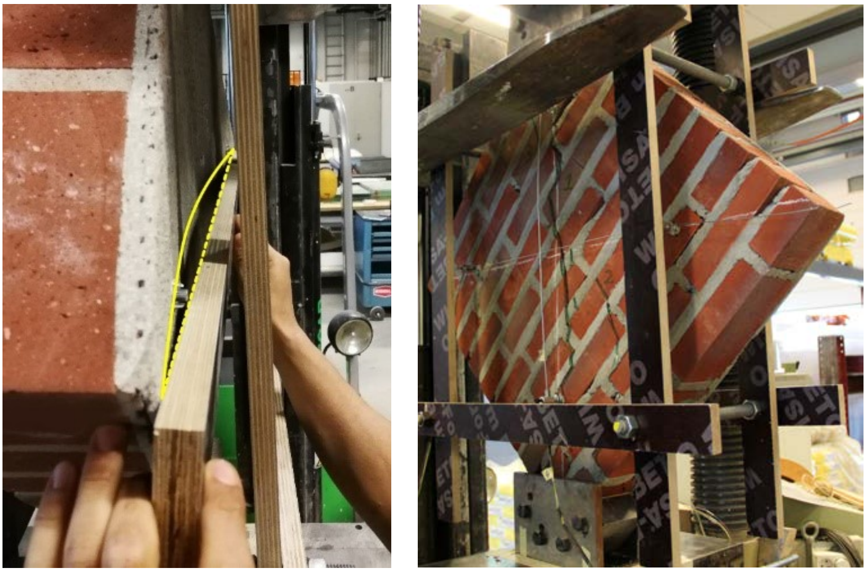

(a) (b)

Figure 6.26: Photos at the final stage of the test: OOP deformation COMB20-3 specimen (solid line) with respect to the initial condition (dashed line) (a); opening of cracks COMB10-2 specimen on the as-built side (b).

The shear stress versus strain diagrams following from the experiments are shown in Fig. 6.27. Specimen URM-4 is not presented in Fig. 18 due to measurement errors. Additionally, measurements after a 20% drop in the post-peak phase are also not shown. The averaged shear stress versus strain diagram for the different configurations is shown in Fig. 6.28. Comparing the URM and STRIP specimens, no significant differences are noticeable. Both specimen types showed linear behaviour up to the point of sudden failure. In contradiction to the absence of residual strength for the URM specimen, the STRIP specimens had a mean residual strength of 11.2 kN, as shown in Fig. 6.29. The residual strength was determined as the mean value between the point with the first positive slope after the peak (marked with o in Fig. 6.29) and the end of the diagonal compression experiment (marked with x in Fig. 6.29).

$$\epsilon_v = \frac{\Delta_{v1} + \Delta_{v2}}{2g_v} \tag{6.22}$$

$$\epsilon_h = \frac{\Delta_{h1} + \Delta_{h2}}{2g_h} \tag{6.23}$$

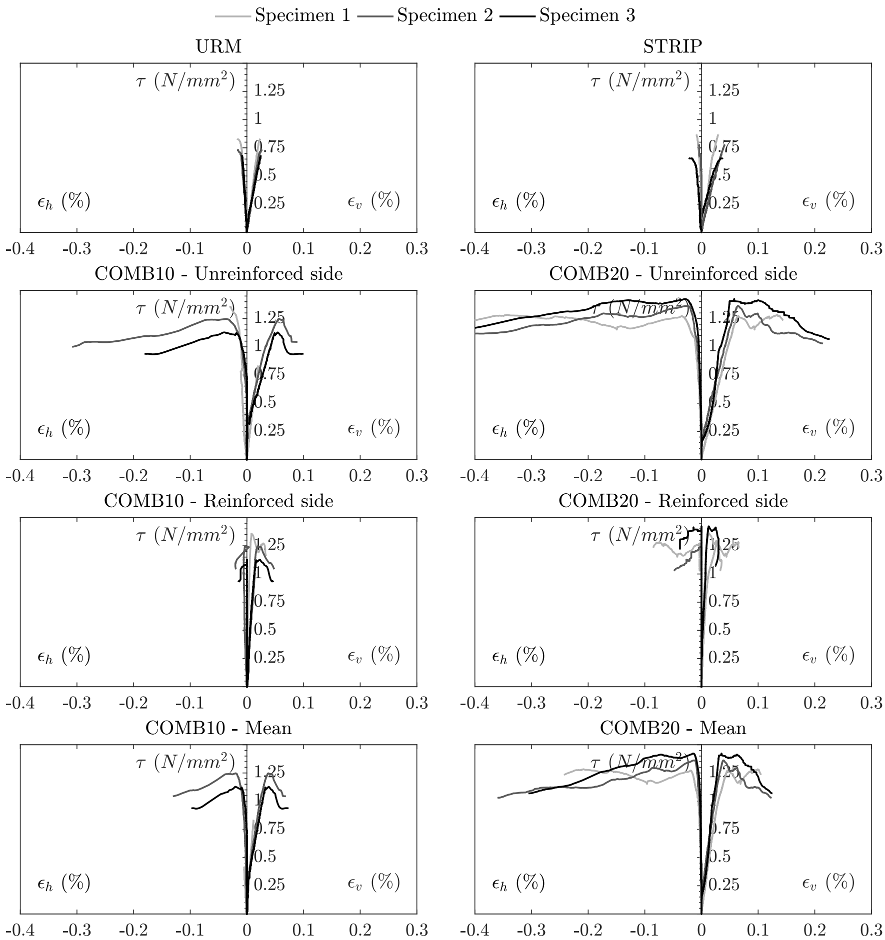

Figure 6.27: Shear stress versus strain diagrams.

For specimens COMB10 and COMB20, both the strains of the FRCM-side and the as-built side of the specimen are presented separately with an additional subscript r and u respectively (for example: $\epsilon_{h,u}$ is the axial strain in the horizontal direction of the as-built side of the specimen). The strain is defined as the mean of the strains measured on both sides of the specimens following Eq. 6.24:

$$\epsilon = \frac{\epsilon_u + \epsilon_r}{2} \tag{6.24}$$

For the specimens reinforced with a FRCM layer, the strains along the as-built side were significantly different from the opposite side where FRCM was installed. On the FRCM-side, lower deformation values were measured in both the horizontal and vertical direction. This was in line with the expectations considering the significant difference in modulus of elasticity between the mortar matrix and the masonry. For the COMB specimens it was noticed that the mean horizontal strain was higher than the mean vertical strain during the post-peak phase. This was primarily caused by the diagonal tension cracks on the as-built side of the specimens. Noticeable was the difference in strain on the as-built side of the COMB-specimens. Despite the higher mean initial stiffness (caused by the FRCM thickness), the mean strains in particular the horizontal direction was significantly higher for the COMB20 specimens when compared with the COMB10 specimens. Looking at the crack patterns that were presented in Fig. 6.24, the difference in horizontal strain can be explained with the amount of cracks that were formed, more cracks leading to higher deformation values.

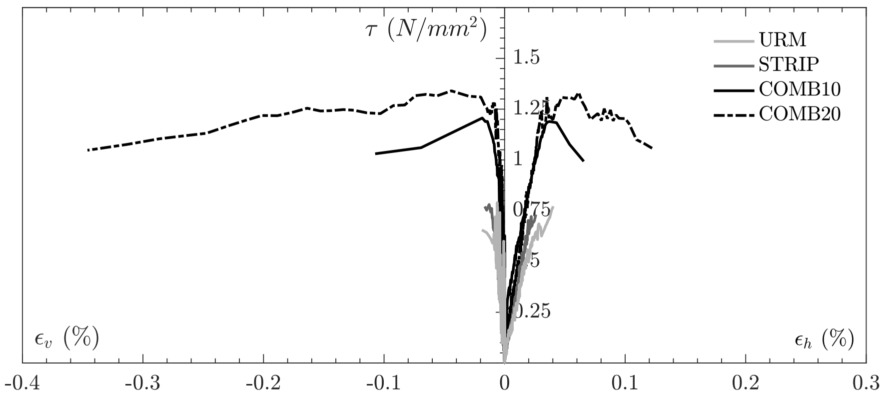

Figure 6.28: Averaged shear stress-strain diagram of the URM, STRIP, COMB10 and COMB20 specimens.

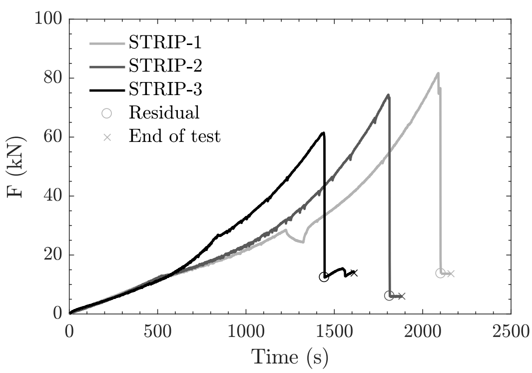

Figure 6.29: Force-time diagram of the STRIP specimens.

6.6.4 Shear modulus

The shear strain is defined in Eq. 6.25. The slope of the elastic portion of the $\tau-\gamma$ diagram is denoted as the shear modulus of rigidity, (G_e) according to ASTM E 519-02 [73], following Eq.6.26, where $\tau_e = 0.7\tau_{max}$ was assumed to be the cracking shear strength and γ_e was the corresponding cracking shear strain identified on the experimental $\tau-\gamma$ diagram.

$$\gamma = \epsilon_v + \epsilon_h \tag{6.25}$$

$$G_e = \frac{\tau_e}{\gamma_e} \tag{6.26}$$

The cracking shear strain and shear modulus are provided in columns 10 and 11 respectively of Table 6.12. Comparing the URM and STRIP specimens, considering only the cases where the predominant failure mechanism was shear stepped sliding, it can be observed that the STRIP specimens result in a 25.3% lower shear modulus. This indicates that the deep grooves resulted in a reduction in shear modulus. For the specimens where both shear sliding and shear stepped sliding occurred (URM-4 and STRIP-1), the shear modulus was found to be approximately the same, but higher than the mean value of the corresponding specimen group. This difference was likely caused by the failure plane concentrating outside the horizontal and/or vertical diagonals, where the deformation measurements were made. No significant difference in shear moduli was found between the COMB10 and COMB20 specimens, indicating that the thickness of the FRCM had limited influence on the shear modulus. A possible explanation could be the formation of shrinkage cracks during the curing stage of the FRCM layer, and that therefore the enhancement in stiffness and strength is primarily based on the presence of the CFRP mesh, and the tension stiffening effect caused by the bond between the mesh and the mortar layer. Compared with the URM specimens, the application of a single sided FRCM layer resulted in an increase of approximately 40% of the shear modulus. It was noticeable that the mean shear modulus of COMB20 specimens was more scattered (COV 15.6%) compared to the COMB10 specimens (COV 3.68%). The shear stress-shear strain diagrams are presented in Fig. 6.30. Specimen COMB10-1 is not included due to the faulty attachment of two LVDT's, leading to missing data near the failure load. For the remaining specimens, the LVDT sensors malfunctioned due to the crack development in the post-peak phase. Because of this, the shear strain relation of specimens COMB10-2, COMB10-3 and COMB20-1 have been linear extrapolated to obtain the ultimate shear strain γ_u (associated with a maximum 20% strength drop on the post-peak softening branch).

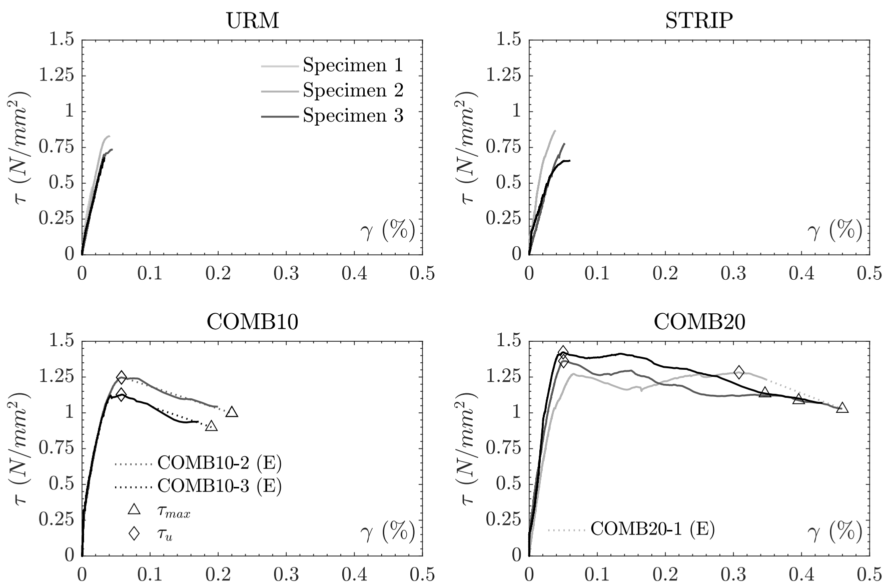

Figure 6.30: Shear stress versus shear strain diagrams.

6.6.5 Pseudo ductility

The wallette's pseudo-ductility μ (see Column 10 in Table 6.12), is calculated using Eq. 6.27, where $\gamma_u = \gamma_e$ for specimens without post peak strength.

$$\mu = \frac{\gamma_u}{\gamma_e} \tag{6.27}$$

In general, a higher pseudo-ductility ratio leads to an increased ability of strengthened masonry walls to redistribute stresses, a higher global deformation capacity and an improved energy dissipation [132]. The pseudo-ductility factors obtained were in the range 8.5-9.3 and 15.4-15.6 for the COMB10 and COMB20 specimens respectively. The out-of-plane deformations could result in optimistic factors for the pseudo-ductility.

6.7 Comparison with design models

6.7.1 Unreinfoced masonry

The in-plane shear capacity of unstrengthened walls were determined using two approaches: the analytical model developed by Li et al. [130] and the design provisions according to Eurocode 8-3 [135].

Analytical model

For wallettes subjected to a diagonal compressive force, all clamping forces are provided by the vertical component of the diagonal compression force [130], as shown in Fig. 6.31. The relationship between the v-component N_v and the u-component V_m of force P is provided by Eq. 6.28, with θ being the angle between the bed joint direction (u-axis) and the main diagonal of the wallette (y-axis).

$$N_v = \sigma_n A_n = V_m tan\theta \tag{6.28}$$

As the angle between the horizontal and the main diagonal of the wallette was kept constant at 45° during the experimental campaign, Eq. 6.28 can be reduced to Eq. 6.29:

$$N_v = \sigma_n A_n = V_m = \sqrt{2}P \tag{6.29}$$

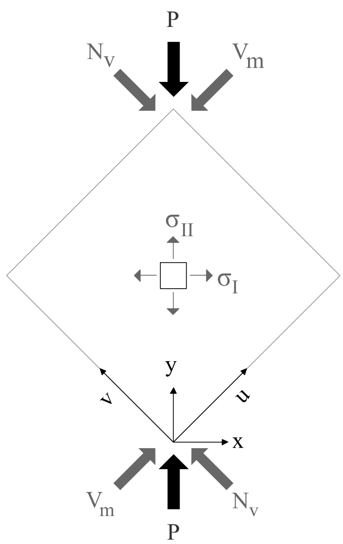

Figure 6.31: Forces acting on wallette during a diagonal compression test.

An unreinforced masonry wall fails when the value of the applied shear force reaches the minimum shear capacity, V_m, computed in accordance with Eq. 6.30:

$$V_m = min(V_{ss}; V_{sf}; V_{dt}; V_c) \tag{6.30}$$

Shear sliding (V_{ss}): Recognizing that shear strength results from the combination of bond strength and friction resistance between mortar joint and blocks [130], the shear strength is typically modelled with the Mohr-Coulomb relationship provided in Eq. 6.31.

$$f_v = f_{v,0} + \mu_{ma}\sigma_n \tag{6.31}$$

Where $f_{v,0}$ is the shear bond strength and μ_{ma} is the average coefficient of friction. The initial shear strength obtained with the triplet experiments was 0.38 N/mm². An average value for initial shear strength τ_0 of 3% of the masonry gross area compressive strength (f'_m) is suggested in various researches [18, 130–132], resulting in 0.44 N/mm² for the masonry used in this study. For the coefficient of friction μ_{ma}, a typical range from 0.3 to 1.2 is assumed, in accordance with [130], with an average of 0.75. This corresponds well with the value obtained via the triplet experiments. The shear capacity due to shear sliding failure is derived from Eq. 6.32

$$V_{ss} = (f_{v,0} + \mu_{ma}\sigma_n)A_n \tag{6.32}$$

Substituting equation Eq. 6.28 into Eq. 6.32, the horizontal resistance against shear sliding failure along a bed joint can be rewritten as:

$$V_{ss} = \frac{f_{v,0}}{1-\mu_{ma}}A_n \tag{6.33}$$

Shear stepped sliding (V_{sf}): Crisafulli, Carr, & Park [136] revised the theory of Mann & Muller [137] and presented a revised distribution of normal and shear stresses acting on a block [130]. The reduced shear strength f_{sf} is determined using a modification of Eq. 6.31, resulting in:

$$f_{sf} = f^*_{v,0} + \mu^*_{ma}\sigma_n \tag{6.34}$$

Where $f^*_{v,0}$ and $\mu^*_{v,0}$ are the reduced shear bond strength and the reduced coefficient of friction respectively, which are the confirmed determinative factors for the friction failure instead of the actual coefficients f_{v0} and μ_{ma} [137]. The shear capacity due to shear sliding failure is derived from Eq. 6.34:

$$V_{sf} = (f^*_{v,0} + \mu^*_{ma}\sigma_n)A_n \tag{6.35}$$

Substituting equation Eq. 6.28 into Eq. 6.35, the horizontal force to resist shear stepped sliding failure can be rewritten as:

$$V_{sf} = \frac{f_{v,0}}{1-\mu_{ma}}A_n \tag{6.36}$$

Diagonal tension (V_{dt}): The required force to induce diagonal tensile crack of the brick is determined using Eq. 6.37. The tensile strength of the clay brick masonry (f'_{tb}) is determined by Silva et al. [131] using Eq. 6.38:

$$V_{dt} = \frac{f'_{tb}}{2.3}\sqrt{1+\frac{\sigma_n}{f'_{tb}}}A_n \tag{6.37}$$

$$f'_{tb} = \frac{2}{3}\sqrt{f'_m} \tag{6.38}$$

Substituting Eq. 6.28 into Eq. 6.37, the expression of V_{dt} for the discussed condition and present failure mode can be rewritten as:

$$V_{dt} = 1.44 f'_{tb} A_n \tag{6.39}$$

Crushing (V_c): The shear strength to initiate crushing is evaluated as:

$$V_c = (f_m - \sigma_n)\frac{2l_b}{3h_b}A_c \tag{6.40}$$

With A_v being interface loading area between the steel shoe and the wallette, parallel to the bed joint. Substituting Eq. 6.28 into Eq. 6.40, the horizontal force to initiate crushing can be obtained:

$$V_c = \frac{2l_b}{3h_b + 2l_b} f_m A_c \tag{6.41}$$

Eqs. 6.32, 6.35, 6.37, and 6.40 completely represent the failure envelope for the shear strength of masonry. Using the relevant parameters provided in Table 6.13, the failure envelope for the unreinforced masonry used in this experimental research was determined as shown in Fig. 6.32. The failure envelope presented here is a function of the compressive stress applied to the wallette, ranging from zero to the compressive strength of the masonry.

Table 6.13: Masonry properties for the (modified) Eurocode 8-3 [135] approach.

Description	Symbol	Value	Unit
Characteristic initial shear strength of masonry [129]	$f_{v,0}$	0.3	N/mm^2
Partial factor for masonry [129]	γ_M	1.5	-
Distance between location V and edge specimen	δ	50	mm

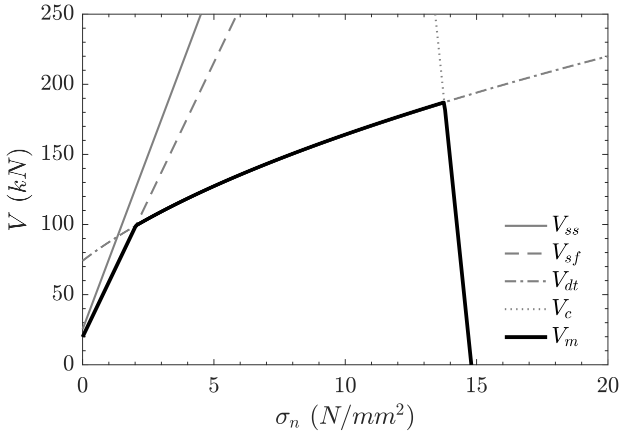

Figure 6.32: Failure envelope of the unstrengthened masonry wallete in diagonal compression, determined with the analytical model.

Eurocode 8

According to Eurocode 8-3 [135], the shear force capacity of an unreinforced masonry wall controlled by shear under an axial load N is determined with Eq. 6.42:

$$V_{sf.EC} = f_v D' t_w \tag{6.42}$$

Where D' is the depth of the compressed area of the wall and f_v is the masonry shear strength accounting for the presence of vertical load. In this study, the depth of the compressed area in the bed joints is assumed to be equal to the length of the specimen. The masonry shear strength is determined according to Eq. 6.43 per Eurocode 6 [129].

$$f_v = f_{v,0} + 0.4\frac{N}{A_n} \leq 0.065 f_b \tag{6.43}$$

Where $f_{v,0}$ is the initial shear strength in the absence of vertical load and f_b the normalized mean compressive strength of the masonry unit, obtained from either in situ tests or additional sources of information, and divided by the confidence factor (=1 for KL3). In primary seismic walls, both these material strengths are further divided by the partial factor (γ_M) for masonry in accordance with Eurocode 8-1 [5]. Characteristic initial shear strength of masonry ($f_{v,0}$) is provided as 0.3 N/mm² for clay masonry with M10-M20 mortar strength class in Eurocode 6 [129].

Substituting Eq. 6.29 in Eq. 6.42, the horizontal force to resist shear stepped sliding failure following Eurocode 8-3 [135] can be rewritten as:

$$V_{sf,EC} = \frac{f_{v,0}}{0.6} A_n \tag{6.44}$$

The upper limit $0.065 f_m$ takes care of the possibility that failure in shear tension will occur in the compression area subjected to a combination of a significant normal compressive stress and a shear stress. When failure due to shear tension will occur, cracks will run through the units. The shear force capacity for this failure mechanism is provided in Eq. 6.45:

$$V_{dt,EC} = 0.065 f_m A_n \tag{6.45}$$

Eurocode 8 [135] does not differentiate between the rocking mechanism and the toe-crushing mechanism. In Eurocode 8 [135], the shear force capacity of an unreinforced masonry wall as controlled by flexure under an axial load N is obtained via Eq. 6.46:

$$V_{fl,EC} = \frac{l_w}{h_W} \frac{N}{2} \left(1 - 1.15 \frac{N}{l_w t_w f_{mas}} \right) \tag{6.46}$$

Where f_{mas} is the compressive strength of the masonry divided by the confidence factor (=1 for KL3). Regarding the normal stress distribution, the Eurocode 8-3 [135] refers to a stress block distribution by adopting a reduction coefficient of the compressive strength (0.87=1/1.15). The mechanical scheme to obtain Eq. 6.46 is provided in Fig. 6.33.

Since during the diagonal compression experiments the axial load was not introduced at the center of the wallette, as illustrated in Fig. 6.33, a modification of Eq. 6.46 also has been considered. First, the depth of the compressed area was determined using Eq. 6.47:

$$D' = \frac{N}{0.85 t_w f_m} \tag{6.47}$$

The moment with respect to the bottom right corner in Fig. 6.33b equals:

$$(l_w - D')N = (h_w - 2\delta)V \tag{6.48}$$

With δ being the distance between the corner of the specimen and the location where the concentrated force V is assumed to be introduced. Substituting Eq. 6.47 into Eq. 6.48, the modified shear force capacity for flexural

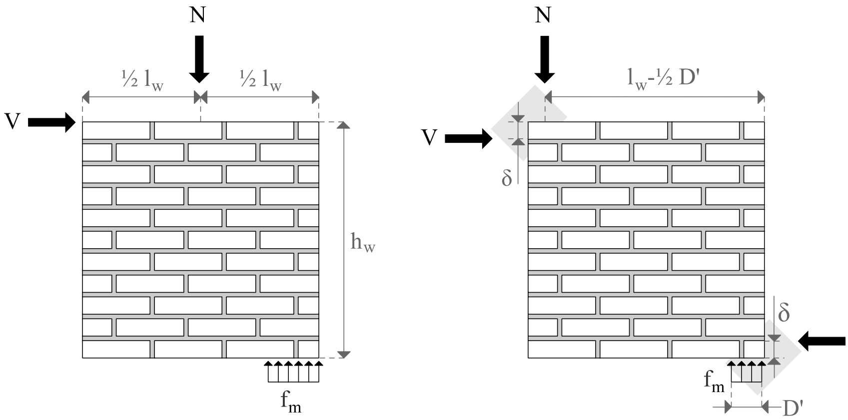

Figure 6.33: Mechanical scheme to determine the shear force capacity during flexural failure (a) and the modification for this study (b).

failure becomes:

$$V_{fl,EC'} = \frac{N}{(h_w - 2\delta)}\left(l_w - 1.15\frac{N}{t_w f_m}\right) \tag{6.49}$$

With the compressive depth during the experiments being limited to 100 mm due to the dimension of the steel shoe, combining Eq. 6.47 with Eq. 6.28 results in the shear strength needed to initiate crushing:

$$V_c = 0.85 f_m 100 t_w \tag{6.50}$$

Eqs. 6.42, 6.45 and 6.46 completely represent the failure envelope for the shear strength of masonry following Eurocode 8-3 [135]. Similar to Eq. 6.30, a wall fails when the value of the applied shear force reaches the minimum shear capacity:

$$V_{m,EC} = min(V_{ss,EC}; V_{dt,EC}; V_{fl,EC}) \tag{6.51}$$

The failure envelope including the modified shear force rocking / toe crushing is obtained with Eq. 6.52:

$$V_{m,EC'} = min(V_{ss,EC}; V_{dt,EC}; V_{fl,EC'}) \tag{6.52}$$

Using the relevant parameters provided in Table 6.14, the failure envelope for the unreinforced masonry used in this experimental research was determined as shown in Fig. 6.34. The failure envelope of the modified shear for rocking/toe crushing is also shown. It should be noted that for comparison reasons the partial factor for masonry is not taken into account.

Table 6.14: Masonry properties for the (modified) Eurocode 8-3 [135] approach.

Description	Symbol	Value	Unit
Char. initial shear strength of masonry [129]	$f_{v,0}$	0.3	N/mm²
Partial factor for masonry [129]	γ_M	1.5	–
Distance between V and the edge of the specimen	δ	50	mm

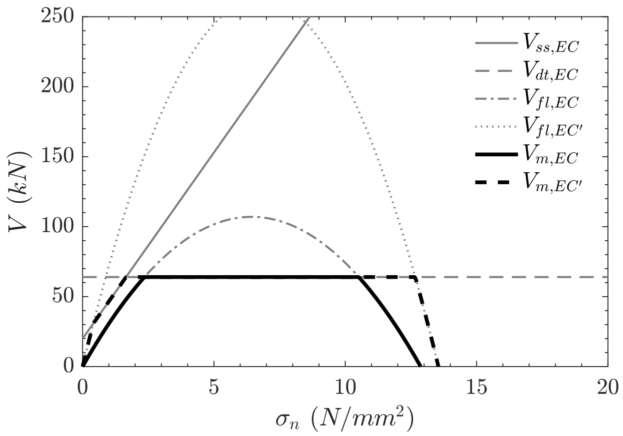

Figure 6.34: Failure envelope of URM determined with the standard Eurocode 8 design provisions (V_m) and a modified version (V'_m).

Comparing Fig. 6.32 and Fig. 6.34, it can be observed that despite leaving out the partial factors for masonry, the Eurocode 8-3 [135] approach to determine the failure envelope of unstrengthened masonry is conservative when compared to the failure envelope obtained from the analytical model. This is primarily caused by the different approaches to determine the shear strength at diagonal tension failure, where the difference builds up to 292% with respect to the Eurocode 8-3 [135] approach.

The strengths obtained with the analytical model and Eurocode 8-3 [135] are compared with the mean experimental shear strength of the URM specimens. The mean experimental shear strength is determined by using Eq. 6.28. The results are summarized in Table 6.15. The analytical model showed good correspondence with the experimental values for both the failure mechanism and the failure load, with an experimental/model ratio (ϕ) of 0.98. The Eurocode 8-3 [135] approach resulted in lower values

($\phi = 1.43$) despite leaving out the partial factor for masonry. Including this partial factor, the Eurocode approach resulted in even more conservative values ($\phi = 2.14$).

Table 6.15: Experimental and analytical results of the URM and STRIP specimens.

		Experiments	Evaluation		
			Analytical model	Eurocode 8 ($\gamma_M = 1.0$)	Eurocode 8 ($\gamma_M = 1.5$)
$V_{exp,URM}$	kN	47.4			
V_{ss}	kN		101.1	33.3	22.2
V_{sf}	kN		48.2	-	-
V_{dt}	kN		92.0	64.9	43.2
V_c	kN		102.9	119.5	79.7
V_m	kN		48.2	33.3	22.2
ϕ	-		0.98	1.43	2.14
Failure mode	-	Stepped sliding	Stepped sliding	Stepped sliding	Stepped sliding

6.7.2 Reinforced masonry

In order for the FRCM reinforcement system to be applied on a large scale for the in-plane strengthening of masonry walls, simple practitioner oriented design models are essential. However, due to the novelty of this technique and the wide variety of FRCM materials on the market, design provisions are generally not provided by international building codes [138]. Previous theoretical studies have led to various analytical formulations for determining the shear strength of FRCM reinforced masonry [132, 139–141]. Cascardi et al. [140] presented an advanced analytical model based on artificial neural network analyses. For the construction of the model a number of 75 samples were selected from previous diagonal compression tests found in scientific literature, varying in both material and geometry. The authors showed that the proposed model was competitive with the consolidated analytical formulations. However, because of the reduced specimen dimensions and the non-standard single-sided reinforcement configuration used in the current study, the model proposed by Cascardi et al. [140] was not considered.

At the end of 2013 the first design guide for FRCM reinforcement [142] was published. This guideline provides structural engineers with easily applicable design models for determining the shear resistance of FRCM reinforced masonry walls. Past studies have shown that the ACI design models show reasonable agreement with experimental data and can be considered as conservative [132, 143]. The European building codes (Eurocode), which in general differs significantly from the American design philosophy, do not provide any design models for the shear strength of FRCM reinforced masonry. Triantafillou et al. [144] and Triantafillou [141], however provided similar practitioner oriented design models in Eurocode framework.

In this research both the approach according to ACI 549-13 [142] and Triantafillou [141] to determine the FRCM contribution on the shear strength of masonry were considered. Concerning the nominal shear strength V_{RM} of FRCM reinforced masonry, both approaches pose that this is the result of the summation of the shear strength of the masonry and of the FRCM-overlay, in accordance with Eq. 6.53. It should be noted that the FRCM contribution is considered only after masonry cracking [18, 130–132, 142].

$$V_{RM} = V_m + V_t \tag{6.53}$$

The design shear strength of FRCM reinforced masonry according to Triantafillou [141] is determined using the equations provided in the second column in Table 6.16. Triantafillou defines the maximum design stress (f_{td}) allowed to the CFRP net as the lowest value between the design characteristic strength of the mesh (f_{tk}) divided by the material factor (γ_t), and the stress corresponding to the design tensile strain ϵ_{fv} where debonding is assumed to be initiated. The contribution of the FRCM ($V_{Rd,t}$) is determined with the second equation in Table 6.16, where A_f is the area of mesh per unit width (mm²/mm) and n is the number of mesh layers. It should be noted that a reduction factor of 0.9 is present. The design shear strength of FRCM reinforced masonry, including a partial factor for shear (γ_{Rd}) of 1.2 and the design shear strength of the unstrengthened masonry ($V_{Rd,m}$), is limited by a maximum value ($V_{Rd,max,c}$). This limitation corresponds to compression failure in the truss.

The design shear resistance of masonry walls strengthened with FRCM according to ACI 549-13 [142] is obtained by using the equations in the third column of Table 6.16. The ACI 549-13 [142] directly uses the design tensile strain ϵ_{fv} to determine the maximum design stress. The contribution of the FRCM is determined using the second equation in Table 6.16, where in contrast to Triantafillou [141] no reduction factor is used. The design shear strength of FRCM reinforced masonry ($V_{Rd,m}$), including a strength reduction factor for shear (Φ_v) of 0.75, is limited to 50% of the unreinforced wall's shear capacity to limit the total force transferred to the substrate of the masonry per unit width [132], as shown in Table 6.16.

Table 6.16: Approaches to determine the in-plane shear capacity of FRCM retrofitted masonry walls.

	Triantafillou [141]	ACI549-13 [142]
f_{td}	$min(\frac{f_{tk}}{\gamma_t}; E_f\epsilon_v)$	$E_f\epsilon_{fv}$
$V_{Rd,t}$	$0.9l_w(nA_f)f_{td}$	$l_w(nA_f)f_{td}$
$V_{Rd.RM}$	$\frac{1}{\gamma_{Rd}}(V_{Rd,m}+V_{Rd,t}; V*_{Rd,max,c})$	$\Phi min(V_{Rd,m}+V_{Rd,t}; 1.5V_{Rd,m})$

$V_{Rd,max,c} = 2t_w l_w$

With the parameters presented in Table 6.17, the shear strength of the masonry reinforced with a FRCM-overlay can be determined. The results are provided in Table 6.18. The contribution of the FRCM for the shear capacity $V_{Rd,t}$ was determined as 20.0 kN and 29.6 kN using the approach proposed by Triantafillou (2016) and ACI 549-13 [142] respectively. Using the experiments and the analytical model, the mean shear contribution of the FRCM reinforcement (V_{FRCM}) was estimated 38.7 kN . The approach proposed by Triantafillou [141], with an experimental / model ratio (ϕ) of 1.9, resulted in more conservative results when compared to the ACI 549-13 [142] ($\phi = 1.3$).

When taking the partial factor for shear (γ_{Rd}) and the strength reduction factor for shear (Φ_v) into account, and limiting the shear capacity of the strengthened wall to 50% of the un-strengthened wall shear capacity, the shear resistance ($V_{Rd,Rm'}$) of masonry walls strengthened with FRCM as determined with the two approaches was approximately the same (using the masonry shear strength as determined with the analytical model). This is mainly due to the design shear strength being limited to 50% of the unreinforced wall shear capacity according to ACI 549-13 [142]. The experimental/design value ratio's (ρ) for the approaches following Triantafillou [141] and ACI 549-13 [142] were 2.14 and 2.25 respectively. When for the masonry contribution the design value as obtained using Eurocode 8 is used, the experimental/design value ratios (ρ) reduce to 3.5 and 4.9 for the approaches following Triantafillou [141] and ACI 549-13 [142] respectively. It can be observed that the presented design provisions, both for the masonry part and the FRCM contribution, are conservative.

Table 6.17: Values used in the design codes to obtain the shear capacity of FRCM reinforced masonry.

Description	Symbol	Value	Unit
Number of mesh layers	n	1	–
Area of mesh reinforcement by unit width	A_f	0.044	mm^2
Tensile modulus of elasticity of the CFRP mesh	E_f	240,000	N/mm^2
Design the tensile strain of the CFRP mesh [142]	ϵ_{fv}	0.0040	mm/mm
Design characteristic strength of the mesh	f_{tk}	4.2	N/mm^2
Material factor [141]	γ_t	1.5	–
Partial factor for shear	γ_{Rd}	1.2	–
Strength reduction factor for shear [142]	Φ_v	0.75	–

Table 6.18: Experimental and analytical results of the URM and STRIP specimens.

	V_{FRCM}	$V_{Rd,t}$	$\frac{V_{FRCM}}{V_{Rd,t}}$	V_{COMB}	$V_{Rd,m}$	$V_{Rd,RM}$	$\frac{V_{COMB}}{V_{Rd,RM}}$	$V_{Rd,m,EC}$	$V_{Rd,RM'}$	$\frac{V_{COMB}}{V_{Rd,RM'}}$
Experimental	38.73	-	-	121.87	-	-	-	-	-	-
Analytical model	-	-	-	-	48.2	-	-	-	-	-
Eurocode 8 Part 3 [135]	-	-	-	-		-	-	22.2	-	-
Triantafillou [141]	-	20.0	1.9	-	-	56.8	2.1	-	35.1	3.5
ACI549-13 [142]	-	29.6	1.3	-	-	54.2	2.3	-	24.9	4.9

6.8 Conclusions

6.8.1 Quasi-static shear tests

An experimental study was presented that consisted of nine masonry walls retrofitted with a single-sided Fabric-Reinforced Cementitious Matrix (FRCM) layer, DM CFRP strips and flexible anchor connection. Three different wall geometries, with three different axial loads per geometry were tested to investigate the cyclic in-plane behaviour of the reinforced masonry walls. Additional pull-out experiments considering two stress distribution scenarios (tensile force in anchor transferred to (A) masonry or (B) CFRP strip) were performed on prisms with steel anchors to determine the anchoring strength in the flexible adhesive. The following can be concluded from the study:

1. Cracking and eventually sliding always occurred at the interface between the bottommost bed-joint and the concrete foundation beam. None of the specimens showed any shear damage at both the reinforced and as-built surfaces during the cyclic in-plane experiments.

2. The S specimen loaded by a high axial load and all M specimens had rocking and toe-crushing as pre-dominant failure mechanism. The S specimens with low and moderate axial loads only showed rocking behaviour. The large specimens showed a combined flexure and sliding failure mode.

3. For the M specimens the wall's structural ductility factors were in the range of 3.7-14.7. For specimen L1, the mean ductility factor was found to be 4.2. For the remaining specimens a lower bound (in the range 3.5-25.0) was estimated as the limited stroke of the horizontally oriented hydraulic actuator was insufficient to reach a 20% force drop in the post-peak phase. The exact value could not be determined do to the limitations of the in-plane shear test setup.

4. The mean anchor strength as determined with the direct pull-out experiments for scenario A, where the tensile forces in the anchor were transferred to the masonry, was found to be 49 kN. For scenario B, where the tensile forces in the anchor were transferred to CFRP strip (due to the chosen boundary conditions), the mean anchor strength was considerably lower at 18 kN. This was likely due to the relatively higher shear deformations of the adhesive between the CFRP strip and the anchor (scenario B) when compared to the shear deformations of the adhesive between the CFRP strip and the masonry (scenario A).

5. For the mean initial stiffness $k_{50\%}$ of the anchorage (from origin until 50% of the strength) no significant differences were found between the results obtained by direct pull-out testing with scenario A (12.3 kN/mm) and scenario B (12.8 kN/mm).

6. A mechanical model based on EC6 [129] was proposed to model the capacity of the reinforced walls during in-plane loading, covering both moment failure and shear sliding failure. The mechanical model provided a good approximation of the experimentally obtained ultimate loads, with model / experimental ratios in the range of 0.68-1.08 and 0.78-1.03 for the specimens predominantly failing due to rocking (S and M specimens) and sliding (L specimens) respectively. The sliding resistance following the model was conservative because the dowel effect of the anchor in the compression zone was not taken into account.

7. Due to the application of the anchors and the single-sided FRCM overlay, the analytical model provides moment resistance amplification factors (moment resistance reinforced masonry / moment resistance URM) in the ranges 1.5-2.1, 1.3-1.8 for the S and M specimens respectively.

8. Using the analytical model and the in-plane test results of the S and M specimens the determined tensile forces in the anchors ranged between 19.0 kN and 37.3 kN, with a mean value of 20.1 kN (COV = 38.7%). The results obtained from the direct pull-out experiments conform scenario B (mean anchorage strength 17.9 kN) provided a good approximation of the analytically determined anchorage strength. The anchorage strength is significantly overestimated when the pull-out experiments are conducted conform scenario A.

6.8.2 Diagonal compression tests

An experimental program was undertaken to assess the effectiveness of a combined retrofit method to improve the in-plane behaviour of clay brick URM walls. The diagonal compression test was used for the evaluation of the in-plane shear behaviour of these retrofitted wallettes. From the experiments the following conclusions can be drawn:

9. The out-of-plane reinforcement, which consisted of deep mounted CFRP strips embedded with a flexible adhesive in a deep groove (partly filled with mortar), did not affect the strength of masonry elements loaded under in-plane shear. It was however found that the deep grooves resulted in a 25.3% lower shear modulus compared to the unstrengthened control specimens. Moreover the experiments showed that in contrast to the unstrengthened specimens, the specimens with solely the out-of-plane reinforcement did not disintegrate after reaching the failure load. This can be attributed to the FDM CFRP strip holding the specimens together after the predominantly bed joint failure due to shear.

10. The single-sided carbon FRCM overlay increased the shear capacity with 1.7 and 1.8 times that of the unstrengthened control specimens with a 10 mm and 20 mm FRCM layer thickness respectively. The application of a single sided FRCM layer resulted in an increase of approximately 40% of the shear modulus compared to the unstrengthened control specimens.

11. No strong correlation was found between the thickness of the mortar matrix of the FRCM layer and the failure load. Additionally, FRCM layer thickness was found to have limited influence on the shear modulus. A possible explanation could be the formation of shrinkage cracks during the curing stage of the FRCM layer, and that therefore the enhancement in stiffness and strength is primarily based on the presence of the CFRP mesh and the tension stiffening effect.

12. The FRCM layer thickness did have an influence on the number of diagonal cracks that were observed on the as-built side of the combined DM CFRP and FRCM reinforced specimens. With a 20 mm FRCM layer thickness, one to two additional diagonal tensile cracks occurred over a wider area when compared to the specimens provided with a 10 mm FRCM layer. A possible explanation for this discrepancy in crack pattern is the difference in thickness of the upper mortar layer of the FRCM overlay. A thicker upper mortar layer leads to an improved utilization of the carbon FRP mesh.

13. Stiffness differences between the as-built side and the FRCM strengthened side led out-of-plane bending during the final stages of the diagonal compression experiments. With more restrained boundary conditions and superimposed vertical loads, as is the case in practice, larger shear strength increments could be achieved [61].

14. The pseudo-ductility factors obtained were in the range 8.5-9.3 and 15.4-15.6 for the reinforced specimens with a 10 mm and 20 mm FRCM layer thickness respectively. Comparison of these values with the absence of pseudo-ductility of URM showed that a one sided FRCM overlay leads to a significant improvement in ductility.

15. For the evaluation of unstrengthened masonry, the analytical model developed by Li et al. [130] showed good correspondence with the experimental values for both the failure mechanism and the failure load, with an experimental/model ratio (ϕ) of 0.98. Despite leaving out the partial factor for masonry, the Eurocode 8-3 [135] approach resulted in a lower ratio ($\phi = 1.43$). Including the partial factor for masonry, the Eurocode approach results in even more conservative values ($\phi = 2.14$). An important limitation of both approaches is that the non-uniform shear stress distribution at the center of the panel is not taken into account.

16. For the FRCM contribution on the in-plane shear capacity, the approach proposed by Triantafillou [141] (experimental/model ratio of 1.94 resulted in more conservative results when compared to the ACI 549-13 [142] ($\phi = 1.31$).

17. The obtained design values for the shear strength of FRCM reinforced masonry were conservative, especially when for the masonry contribution the design value as obtained using Eurocode 8-3 [135] was used (experimental/design value ratio (ϕ) range 3.47-4.89).

Chapter 7

Valorization

This chapter presents various flexible deep mounted (FDM) CFRP retrofit case studies in the Dutch province of Groningen carried out during the course of this doctoral research. Preliminary finite strategies for the modelling of the bond-slip and pull-out behaviour of FDM CFRP strips are provided. Furthermore, the simplified analysis procedures are presented, used to estimate the force-displacement response of vertically spanning (strengthened) masonry walls subjected to out-of-plane loading, which is required for the he implementation of the FDM CFRP strip retrofit system into structural engineering practice. Finally, the dynamic out-of-plane response of FDM CFRP strip retrofitted and vertically spanning masonry walls for different scenarios was determined by performing a series of Nonlinear Time History (NLTH) analyses on single degree of freedom (SDOF) systems.

7.1 Valorization projects

In this section, the process and challenges regarding groove cutting, FDM CFRP strip installation, and FRCM overlay installation are presented and discussed. Furthermore, five completed retrofit projects in Groningen are reviewed.

Groove cutting

In the early stages of this research, the cutting of the vertical, deep grooves was done using the dry cutting technique (Fig. 7.1). Working downwards from the top of the wall made the cutting of the slots less labor intensive as the weight of the cutting machine would predominantly rest on the wall. The machine operator needed to exert both a downward force and a force in the direction of the wall using his hands to continue the cutting process. The cutting machine was manually guided to follow the pre-determined slot position over the height of the wall. Cutting the slots was a time consuming process due to the width of the slots. Due to the radius of the saw blade and the dimensions of the cutting machine, certain parts of the masonry at the top and bottom of the vertical groove remained intact. These remaining parts were removed using a breaker machine.

Figure 7.1: Deep groove cutting.

A particular point of attention was dust development during the cutting process. Dust extraction was necessary in the early stages to prevent significant dust formation, especially when working inside the building to be retrofitted. Wet cutting was introduced as an alternative technique to prevent dust formation. As limited water was needed for the wet cutting technique, moisture content in the masonry did not reach levels where the FDM CFRP strip installation was affected. At the time of writing, the implementation of guide rails is being evaluated to further decrease the labor intensity levels of groove cutting.

FDM CFRP strip installation

After removing the dust within the grooves, a layer of primer was then applied to the groove in order to obtain an improved bond between the adhesive and the masonry. The subsequent step was the application of the flexible adhesive within the grooves. At first, this application was done manually using a spatula. As this method was to labor intensive, a manual, closed caulking gun with a slot nozzle was used to apply the flexible adhesive, as shown in Fig. 7.2.

Figure 7.2: FDM CFRP strip installation.

The fast-curing two component epoxy was prepared following the mixing ratio advised by the supplier, before scooping the adhesive in the caulking gun. As relatively high pressures needed to be exerted to inject the low viscous adhesive through the slot nozzle, the flexible adhesive would leak through the plunger. This problem was solved by putting a plastic bag in the closed frame prior the scooping in the flexible adhesive. An additional advantage of this measure was the increased service life of the caulking gun. The labor intensity was further decreased with the implementation of electric caulking guns.

After the CFRP strip was cut into the correct length and was cleaned with acetone, the strip was partially embedded by hand within the flexible adhesive. Afterwards a positioning fork was used to properly position the CFRP strip within the groove. Using this profile cut from a steel sheet, the CFRP strip was pushed to the correct depth and positioned at the center of the groove. Starting from the bottom, the positioning fork was used at multiple heights.

Once the CFRP strip was imbedded in the correct position, excess flexible adhesive till a certain depth was manually removed using a scraper. If in-plane strengthening for the retrofitted wall was not necessary, the remaining part of the groove was manually closed using polymer modified mortar (Fig. 7.3) after the flexible adhesive has cured for a minimum of 24 hours.

FRCM overlay installation

Solid preparations need to be made prior to the application of the single sided FRCM overlay. When the moisture content of the masonry wall is too low, the polymer modified mortar loses its water content too fast. This causes a significant decrease of the bond strength between the FRCM overlay

Figure 7.3: Closing the groove with the polymer modified mortar.

and the masonry. Adding more water than the supplier subscribed for the preparation of the polymer modified mortar, increases the risks of shrinkage crack formation during the curing process. To counter this moisture related problem, firstly the masonry surface was wetted a few days prior to the FRCM overlay installations. Additionally, a waterproof acrylic dispersion (Compaktuna) was added as primer layer to the masonry surface (Fig. 7.4). It should be noted that despite the mentioned preparations, the water content loss of the polymer modified mortar could not be prevented fully.

Figure 7.4: Single-sided FRCM overlay installation.

In the early stages of the research, the polymer modified mortar was applied manually using a plaster trowel. After application of the first layer of the polymer modified mortar, the CFRP mesh was pushed into position.

Neighbouring mesh sheets were provided with an overlap length of approximately 25 cm. Subsequently, a final layer of polymer modified mortar was applied to complete the FRCM overlay.

In the later stages of the research, the polymer modified mortar was applied using the mortar spraying technique to reduce the labor intensity level of FRCM application. Smoothing out the FRCM overlay remained challenging, for both the manual and spraying mortar application techniques. In most cases a levelling layer was needed, except for when a timber frame construction with insulation was placed in front of the wall.

Retrofitted masonry buildings

Over the course of this doctoral research, over a hundred buildings have been (partially) retrofitted using the FDM CFRP strip technique. The first commercial project using FDM CFRP strips and one-sided FRCM overlay as hybrid retrofit solution was realized in Usquert, Groningen (Fig. 7.5). The single leaf wall to be retrofitted could not be reached from the outside of the building due to a narrow alley. The timber strong backs solution was not preferred by the owner in order to keep the living floor space unaffected.

After the plaster layer on the wall was removed, the masonry surface was roughened. The flexible adhesive and the polymer modified mortar were applied by hand. The lessons learned presented in the previous paragraphs were mainly based on this retrofitting project.

Figure 7.5: First commercial project using FDM CFRP strip and one-sided FRCM overlay hybrid retrofit. Usquert, Groningen.

Two steel anchors were installed over the bottom 50 cm of the wall, and connected to the masonry foundation. Since the masonry foundation was limited, both the installation and engineering of the anchors was difficult.

The second project to be highlighted are the FDM CFRP strip retrofitted buildings in Zijldijk, Groningen (Fig. 7.6). As starting point the client had decided, on grounds of costs, to leave the inside of the building intact. The outer leaf of the cavity wall removed, after which the FDM CFRP strips were installed from outside the building. A major advantage was the speed with which the retrofit could be installed. Additionally, little inconvenience was caused for the residents. With retrofitting from the outside, shielding and conditioning was necessary, especially during bad weather conditions. After the installation of the retrofit system, lightweight facade elements were placed to restore the aesthetics of the buildings.

Figure 7.6: FDM CFRP strip retrofit on the inner leaf of the cavity wall, from the outside after controlled removal of the outer leaf. Zijldijk, Groningen.

The third retrofit project to be highlighted is Café Nastrovje in Zeerijp, Groningen (Fig. 7.7). The doors of this building closed in 2003, after it partially burned down. FDM CFRP strips were installed on the top facade, from the inside of the building. A single sided FRCM overlay was added to partially restore the cohesion of the masonry that was lost due to fire damage. Nowadays this building is inhabited.

Figure 7.7: FDM CFRP strip retrofit on the top facade. Zeerijp, Groningen.

The final two projects to be highlighted are in Westeremden (Fig. 7.8) and Appingedam (Fig. 7.9). For the building in Westeremden, FDM CFRP strips was selected as retrofit system in order to keep the living floor space unaffected. For the building in Appingedam, an additional single sided FRCM overlay was installed. In this project a wall containing three different types of bricks was encountered.

Figure 7.8: FDM CFRP strip retrofit. Westeremden, Groningen.

Figure 7.9: FDM CFRP strip and one-sided FRCM overlay hybrid retrofit (latter not shown). Appingedam, Groningen.

7.2 Bond related finite element modelling

In Appendix C preliminary finite element (FE) models are presented regarding the bond-slip and pull-out behaviour of flexible deep mounted (FDM) carbon fibre reinforced polymer (CFRP) strips. The modelling of the fabric reinforced cementitious matrix (FRCM) layer is not presented, as numerical modeling strategies for the evaluation of the in- and out-of-plane performance of masonry structures strengthened with FRCM are available [145]. ABAQUS FEA software was used for the numerical analysis.

The adhesive was modelled as a strain-dependent plastic. Input data in ABAQUS for the flexible adhesive was developed using the tensile stress-strain relationships presented in Fig. 2.2. Using this input data, the thick adherend shear tests presented in section 2.2.2 were simulated. The shear stress-strain relationships obtained using the FE model provided a good fit with the material test data for shear behaviour.

Two modelling strategies were maintained regarding the thick adhesive layers. In the first approach, the influence of the adhesive mass on shear deformation was neglected when determining the traction-separation parameters, while in the second approach this effect was included. The obtained local bond-slip behaviour following both strategies resulted in a close estimation of the averaged multi-linear local bond-slip behaviour (Fig. C.9, Appendix C).

As for the force-slip relationship, both finite elements strategies showed good correspondence with the force-slip relationship determined using the partial interaction (PI) model (Figs. C.12 and C.13 in Appendix C). The pull-out tests presented in section 3.3 were simulated for anchorage lengths of 340 mm, 530 mm, 730 mm and 1,000 mm. Due to symmetry, only a quarter of the pull-out specimens was modelled, as shown in Fig. C.10 (Appendix C). As both modelling strategies provided similar results in terms of force-slip relationship, strategy 1 was selected for further analyses due to the simple implementation. The shear stress distribution in the masonry right below the CFRP strip following from the finite element simulations (Fig. 7.10 for a bonded length of 1,000 mm) showed good correspondence with the stress distribution profile obtained using the PI model, as was presented in Fig. 3.33.

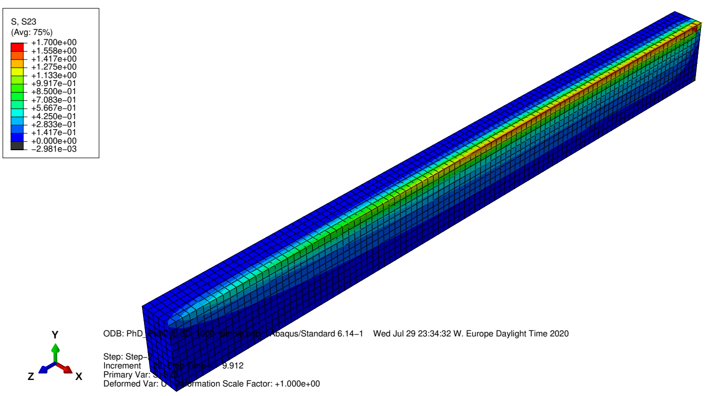

Figure 7.10: Shear stresses in the masonry (y-z plane) at the maximum pull-out resistance for an anchorage length of 1,000 mm, as obtained with the finite element simulations (strategy 1). Gradient map ranges from 0 N/mm² (blue) to 1.7 N/mm² (red).

7.3 Simplified engineering models

The implementation of the FDM CFRP strip retrofit system into structural engineering practice requires simplified analysis procedures to estimate the force-displacement response of vertically spanning (strengthened) masonry walls subjected to out-of-plane loading.

The simplified engineering model for FDM CFRP strip retrofitted walls consists of three equal height rigid masonry blocks and two discrete joints, as shown in Fig. D.1. The engineering model is explained in more detail in Appendix D. During lateral loading, the CFRP strips will be pulled out of the top and bottom rigid blocks with slip Δ_s. Additionally, the CFRP strip will elongate Δ_p over the middle block. Following the one-dimensional partial-interaction model and global bond-slip law presented in Chapter 3, a linear relation between CFRP stress and slip was assumed until σ_p = 1600 N/mm² (corresponding slip Δ_s = 3.5 mm), for rigid block heights of ≥ 750 mm. In contrast to the revised engineering model presented in section 4.3, no additional cracks occurred in the wall. Similar to the initial engineering model, the wall was treated as pre-cracked from the outset. The simplified engineering model for FDM CFRP strip retrofitted masonry walls showed acceptable agreement with the experimental findings for both axial load conditions, an meanwhile simple calculation procedures were maintained when compared to the revised engineering model.

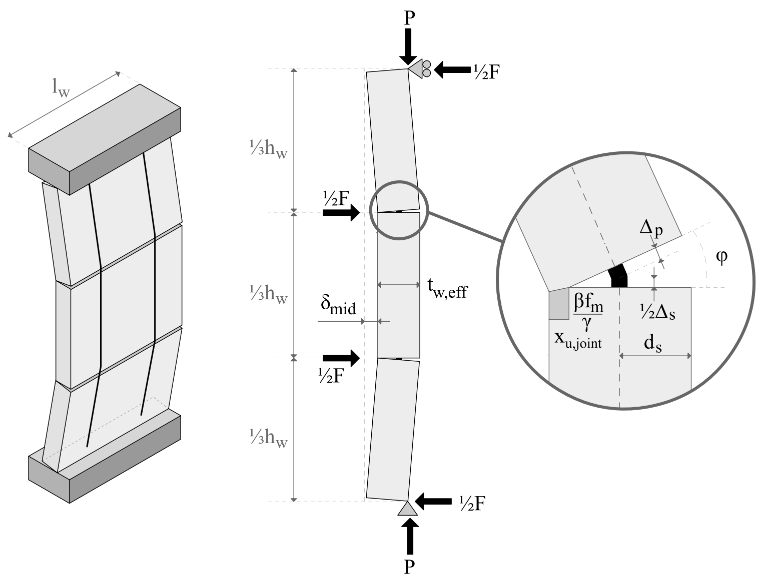

Figure 7.11: Simplified engineering model for the out-of-plane behaviour of FDM CFRP retrofitted vertically spanning masonry walls.

For the hybrid retrofit configuration containing the single-sided FRCM overlay, the simplified engineering model for FDM CFRP strip retrofitted masonry walls showed acceptable agreement with the experimental findings for the out-of-plane loading direction where the FRCM layer is in compression. For the out-of-plane loading direction where the FRCM layer is in tension, the deflection was estimated using deflection formulae for simply supported beams, again resulting in acceptable agreement with the experimental findings. For this simplified approach the tensile strength of the brick and mortar interfaces was assumed zero. The engineering model involving the single-sided FRCM overlay is explained in more detail in Appendix D.

The presented simplified engineering models are implemented and automated in a simple and easy-to-use Microsoft Excel calculation sheet (Fig. 7.12). This model is available through the website of QuakeShield. It should be noted that the Excel calculation file may not be used unless there is a thorough understanding of the principles of the underlying mechanical model.

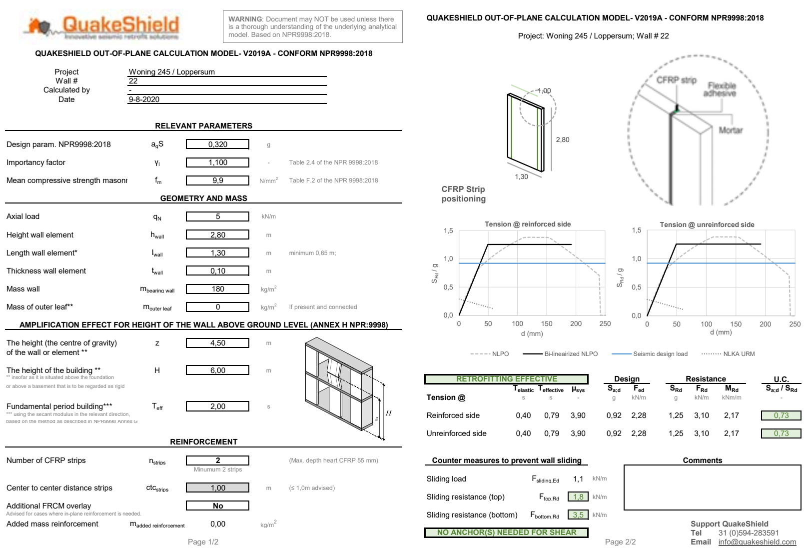

Figure 7.12: Screenshot of the Microsoft Excel calculation sheet (2018 version) for the estimation of the force-displacement response of vertically spanning, FDM CFRP strip (and optional single-sided FRCM overlay) retrofitted masonry walls subjected to out-of-plane loading. Available on the website of QuakeShield.

7.4 NLTH analyses of a SDOF system

In order to study the dynamic out-of-plane response of masonry walls that were vertically spanning and were retrofitted with FDM CFRP strips, a series of Nonlinear Time History (NLTH) analyses on single degree of freedom (SDOF) systems were performed. A suite of eleven synthetic accelerograms with ten to twelve seconds lengths (shown in Fig. 7.13) compatible with cluster A soil spectrum (NPR9998) were used as the ground motion.

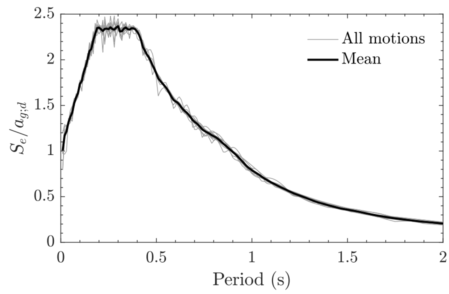

Figure 7.13: Normalized elastic acceleration response spectrum (5% damping) compatible with cluster A soil spectrum (NPR9998).

A total of ten different walls with varying retrofit configurations (illustrated in Fig. 7.14) were analysed. The walls considered had a height, length and thickness of 2,750 mm, 2,300 mm and 100 mm respectively. The mass density of a single leaf of masonry was 180 kg/m^2, which was also applicable to the outer leaf of the cavity wall if present and connected. Table F.1 (Appendix F) provides an overview of the relevant parameters of the analysed walls.

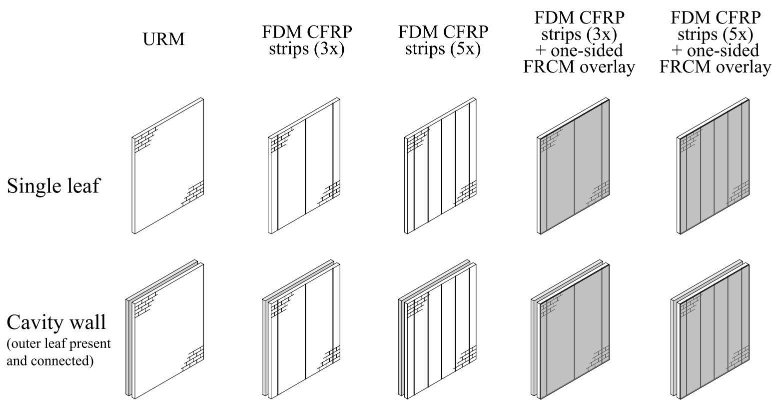

Figure 7.14: Reference walls.

In order to account for the strip spacing limit as presented in Appendix E, two scenario's were considered regarding the number of FDM CFRP strips. For the first scenario, three CFRP strips were positioned at the center-depth of the wall with a distance of 1,000 mm between the CFRP strips. For the second scenario, five CFRP strips were positioned at the center-depth of the wall with a distance of 500 mm between the CFRP strips.

The NLTH response of vertically spanning masonry walls retrofitted with FDM CFRP strips was determined as a function of the design ground acceleration $a_{g;d}$ for different axial stress levels σ_v (acting on the load bearing inner leaf for cavity walls). The NLTH calculations were performed for a scenario with no cavity wall and a scenario where a cavity wall (180 kg/m²) is present and connected. The reported maximum wall response is the maximum obtained out-of-plane displacement value from the eleven separate synthetic accelerograms.

For the lowest axial load considered (σ_v=0.05 N/mm²), the URM wall can withstand an acceleration of 0.7g, with a corresponding displacement of 46 mm. The synthetic accelerogram resulting in this displacement is presented in Fig. 7.17 together with the wall response, $\delta_{repsonse}$.

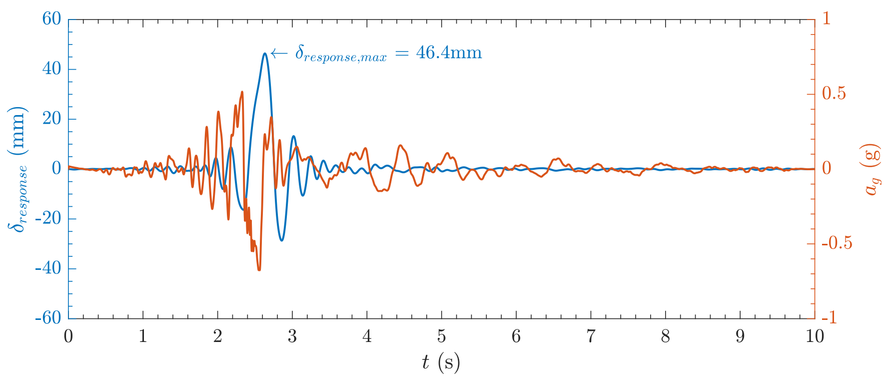

Figure 7.15: The maximum response for ground motion set # 7 (highest response of all sets) with design acceleration $a_{g;d}$ = 0.7g.

For the remaining axial loads, the out-of-plane response remains below 10 mm up to an acceleration of 1.0g, as shown in the top graph presented in Fig. 7.16a. The bottom graph in Fig. 7.16a shows the results for a URM cavity wall (outer leaf present and connected). The cavity wall fails at 0.4g (45 mm), 0.6g (46 mm) and 0.8g (26 mm) for axial stress conditions σ_v=0.05 N/mm², σ_v=0.10 N/mm² and, σ_v=0.15 N/mm² respectively. For the highest considered axial stress (σ_v=0.20 N/mm²), the URM cavity wall showed a displacement of 16 mm at 1.0 g.

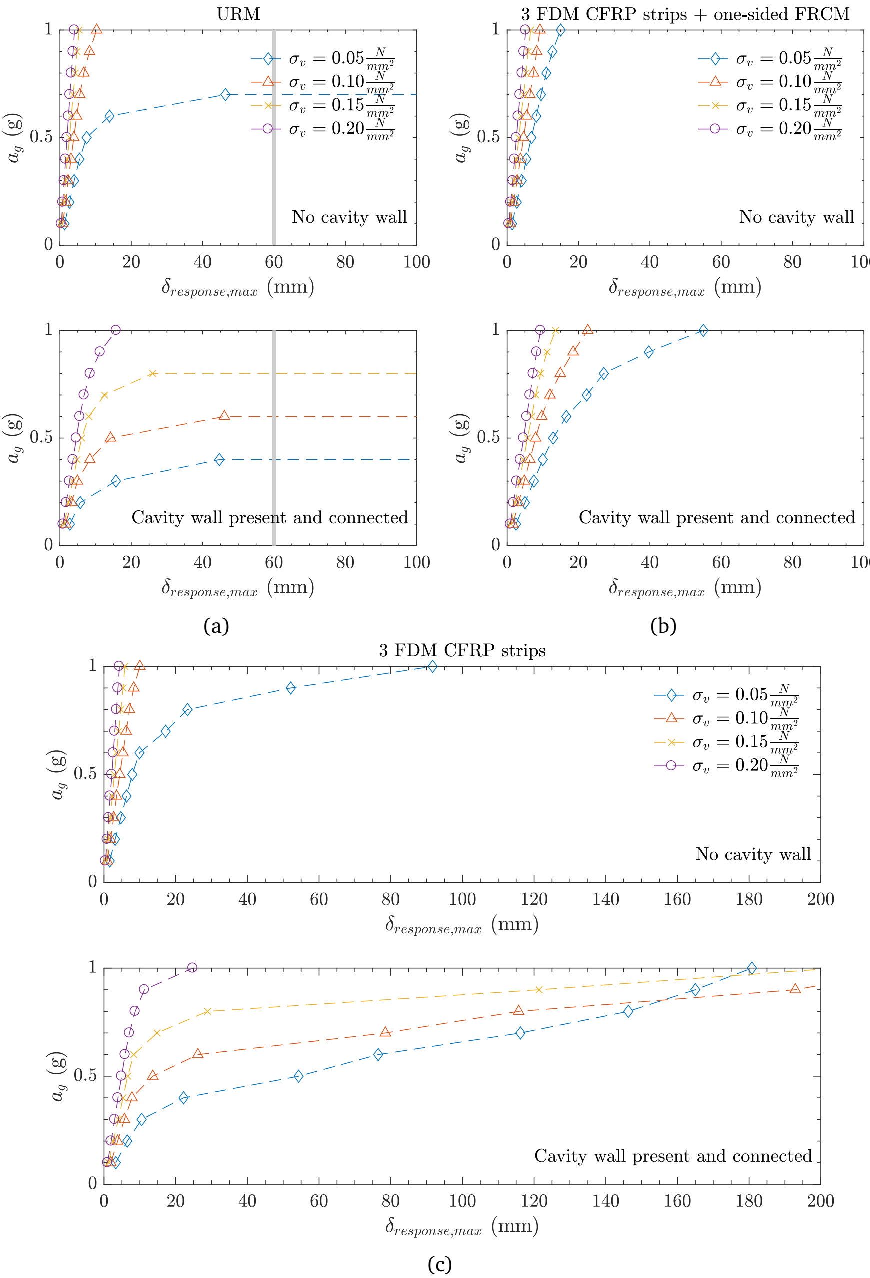

Figure 7.16: Out-of-plane displacement response following from the NLTH analyses of SDOF systems: URM (a), 3 FDM CFRP strip retrofitted masonry (b) and 3 FDM CFRP strip and one-sided FRCM overlay, hybrid retrofitted masonry (c). Four axial stress levels (σ_v) and wall configurations (single leaf and cavity wall) are included in the analysis.

The OOP displacement responses for the reference walls retrofitted with 3 FDM CFRP strips are shown in Fig. 7.16c, neglecting the limit for strip spacing (Appendix E). For the lowest axial load considered (σ_v=0.05 N/mm²), the single leaf wall can withstand an acceleration of 1.0g, with a corresponding displacement of 92 mm. The OOP displacement response for the other axial stress levels is comparable to the the OOP displacement response of single leaf retrofitted masonry walls. Considering a cavity wall, the impact of retrofitting becomes more noticeable. Where a URM cavity wall failed at 0.4g (σ_v=0.05 N/mm²), 0.6g (σ_v=0.10 N/mm²) and 0.8g (σ_v=0.15 N/mm²), the retrofitted cavity wall using 3 FDM CFRP strips showed no failure until 1.0g, with OOP displacement responses of 181 mm (σ_v=0.05 N/mm²), 226 mm (σ_v=0.10 N/mm²) and 204 mm (σ_v=0.15 N/mm²). For the highest considered axial stress (σ_v=0.20 N/mm²), the cavity wall retrofitted with 3 FDM CFRP strips showed a displacement of 25 mm for $a_{g;d}$ = 1.0 g, being slightly higher compared to the URM case.

Including an additional one-sided FRCM overlay has no significant influence of the OOP displacement response, as shown in Fig. 7.16b, but the added value of the one-sided FRCM overlay becomes significant when considering a cavity wall. The OOP displacement response corresponding to $a_{g;d}$ = 1.0 g, was significant lower: 55 mm, 23 mm and 14 mm for axial stress levels of σ_v = 0.05 N/mm², 0.10 N/mm² and 0.15 N/mm² respectively. For all NLTH analyses, the maximum displacement was reached during the loading condition where the one-sided FRCM overlay was in compression. This phenomenon is illustrated in Fig. 7.17, where the negative displacement direction represents the loading case where the one-sided FRCM overlay is in compression. The maximum reached displacement responses were 55 mm (FRCM in compression) and 22 mm (FRCM in tension).

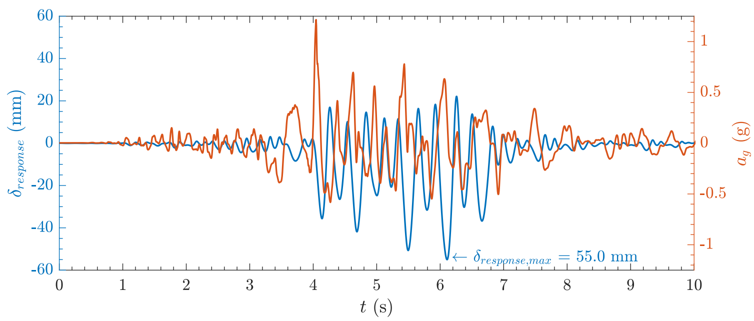

Figure 7.17: The maximum response for ground motion set # 2 (highest response of all sets) with design acceleration $a_{g;d}$ = 1.0g.

The NLTH analyses were reproduced for an increased number of CFRP strips in the reference walls. The OOP displacement response for the reference walls retrofitted with 5 FDM CFRP strips and retrofitted with an additional one-sided FRCM overlay are shown in Figs. 7.16c and 7.16a respectively.

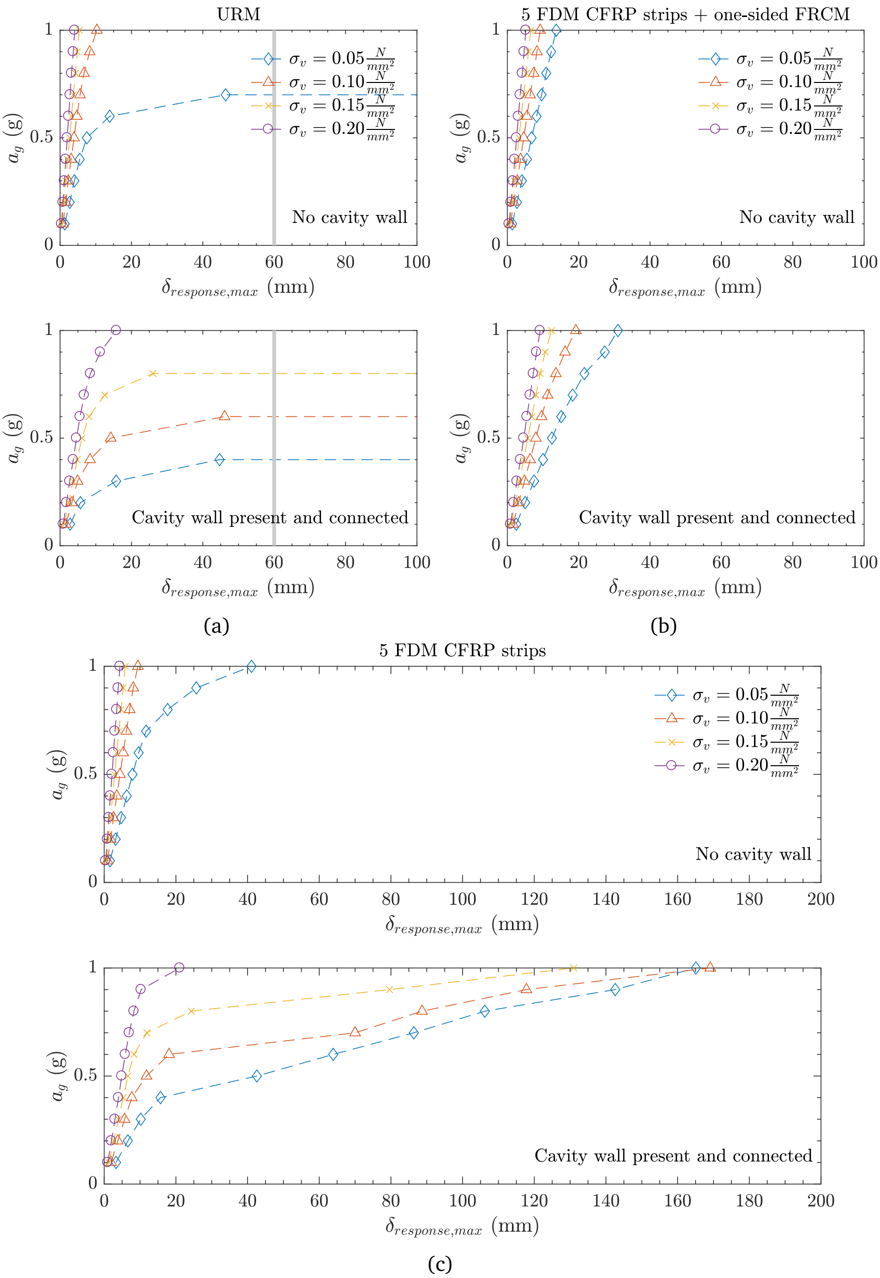

Figure 7.18: Out-of-plane response following from the NLTH analyses on SDOF systems: URM (a), 5 FDM CFRP strip retrofitted masonry (b) and 5 FDM CFRP strip and one-sided FRCM overlay, hybrid retrofitted masonry (c). Four axial stress levels (σ_v) and wall configurations (single leaf and cavity wall) are included in the analysis.

The addition of two extra FDM CFRP strips in the case of a single leaf wall, only results in a significant displacement reduction (from 91.7 to 41.1 mm at $a_{g;d}$ = 1.0g) for the low axial load case with respect to the results presented in Fig. 7.16c. For the other axial loads out-of-plane response remained at similar displacements. The retrofitted cavity wall using 5 FDM CFRP strips showed significant displacement reductions corresponding to $a_{g;d}$ = 1.0g, with out-of-plane displacement responses 165 mm (σ_v=0.05 N/mm^2), 169 mm (σ_v=0.10 N/mm^2) and 131 mm (σ_v=0.15 N/mm^2). For the highest considered axial stress (σ_v=0.20 N/mm^2), the addition of two extra FDM CFRP strip had limited effect on the out-of-plane displacement response (25 mm versus 21 mm).

The addition of two extra FDM CFRP strips in the case of a hybrid retrofit with one-sided FRCM overlay only had a significant effect for the cavity wall with the lowest considered axial stress level (σ_v=0.05 N/mm^2), where the out-of-plane response (31 mm) reduced significantly when compared to the case with three FDM CFRP strips (55 mm, Fig. 7.16b)

Chapter 8

Conclusions, recommendations and outlook

The deep mounting of Carbon Fibre Reinforced Polymer (CFRP) strips to masonry using a flexible adhesive was developed as a minimally-invasive out-of-plane seismic retrofitting technique for Unreinforced Masonry (URM) buildings. With this novel retrofitting technique deep grooves are cut in the masonry, after which CFRP strips are installed at the center of the wall using a flexible adhesive. This procedure makes the CFRP strips effective for out-of-plane lateral loading directions.

For walls subjected to in-plane (IP) loading, the application of only the flexible deep mounted (FDM) CFRP strips retrofit was expected to be insufficient to enhance the strength for in-plane loading conditions. Consequently, the addition of a one-sided fabric reinforced cementitious matrix (FRCM) overlay was proposed to form a hybrid retrofit with the FDM CFRP strips, in order to enhance the strength and pseudo-ductility of masonry for in-plane loading conditions. However, it was expected that the addition of a single-sided FRCM overlay would also have a significant influence on the out-of-plane behaviour of the retrofitted wall.

The effectiveness of this novel strengthening system, both stand-alone and in hybrid retrofit configuration, was examined in depth in this doctoral research. The primary objectives of this thesis were formulated as follows:

1. To define and model the bond behaviour between CFRP strips and masonry when the flexible adhesive is used;
2. To define and model the out-of-plane behaviour of FDM CFRP strip retrofitted masonry walls, either with or without a single-sided FRCM overlay; and
3. To define and model the in-plane behaviour of FDM CFRP strip retrofitted masonry walls with a single-sided FRCM overlay.

In this final chapter, the main conclusions and contributions of this work with regard to the research questions are presented, and general conclusions are described. Furthermore, a number of recommendations are given and suggestions for further research are presented. Finally, an outlook to the future of FDM CFRP strip retrofitting is presented.

8.1 Conclusions

Bond behaviour between CFRP strips and masonry when the flexible adhesive is used

An extensive experimental program was undertaken to assess the pull-out behaviour of deep-mounted CFRP strips bonded with a flexible, visco-elasto-plastic adhesive to clay brick masonry. Direct pull-out tests were used for the evaluation of the bond-slip behaviour of the embedded CFRP strips and a strong logarithmic correlation was found for the relation between the failure load and the displacement rate. Increasing the loading rate from 0.5 mm/min to 100 mm/min led to an increase of nearly 50% in failure strength for an embedment length of approximately 1.0 m. The governing failure mechanism for bonded lengths of < 1.0 m was cohesive failure with brick splitting, whereas for bonded lengths of ≥ 1.0 m the governing failure mechanism shifted to CFRP rupture with a few hairline cracks on the 4-5 layers of bricks at the loaded end. For both failure mechanisms, the deformation of the cohesive was dominant. A strong linear correlation was found for the relationship between the tested range of embedment lengths and the failure load up to the critical embedment length of 1.0 m, with 82 N/mm anchorage length. From the pull-out experiments multiple local bond-slip relations were obtained, which were averaged to obtain a universal local bond-slip law for the considered configuration. Using this averaged tri-linear local bond-slip model as a part of a partial-interaction analysis led to good agreement with the experimental results within the range of tested embedment lengths (0.34-1.00 m) in terms of force-slip relationship.

The research outcomes were compared to a database consisting of 124 tests on near-surface-mounted retrofits on masonry using a conventional stiff adhesive. Stiff-adhesive systems achieved considerably higher peak shear stresses compared to the flexible-adhesive system in the present study (8.2–16.5 vs. 2.2 N/mm^2). Conversely, the flexible-adhesive system achieved a much larger ultimate debonding slip of 11.6 mm compared to 0.68–2.0 mm for the stiff-adhesive systems. The flexible-adhesive system was able to achieve an overall higher fracture energy than was obtained for the stiff-adhesive systems (16.9 vs. 9.7 Nmm/mm^2). The nearly uniform distributed low-magnitude bond stresses over the embedded length obtained when using a flexible adhesive was important in preventing cohesive debonding in the masonry substrate, and thus preventing under-utilization of the CFRP.

Out-of-plane behaviour of masonry walls retrofitted with flexible deep mounted (FDM) CFRP strips

An experimental program was undertaken to assess the out-of-plane behaviour of vertically (one-way) spanning full scale clay brick masonry walls retrofitted with FDM CFRP strips. In the experimental testing program nine full-scale masonry walls were tested, from which six walls were retrofitted with two CFRP strips each using the FDM technique. Three unstrengthened specimens were tested. All wall specimens were tested with an axial load of 4.8 kN, except one wall specimen retrofitted with FDM CFRP strips, where the axial load was 20 kN.

Due to the limitations of airbag testing, a novel cyclic six or four point-bending test setup was proposed and used. The loading rate was selected at a level for which the strain rate of the embedded CFRP strips were magnitude-wise similar to the strain rate used in the quasi-dynamic pull-out campaign.

For the unreinforced masonry specimens a typical two-block rigid body behaviour was initiated after the bed-joint crack near mid-height occurred. For the retrofitted specimens, the formation of multiple bed joint cracks (14-20) and crushing of the bed joints for higher mid-span displacements were observed. In contrast to reported findings in literature regarding the out-of-plane behaviour of near-surface-mounted retrofitted masonry walls, intermediate cracking and vertical in-plane shear failure was not observed.

The average lateral moment resistance at mid-height of the unreinforced masonry specimens (three in total) was 0.78 kNm, whereas the average resistance of the FDM CFRP retrofitted specimens (five in total) was found to be 1.82 kNm. The moment capacity of the URM wall was increased by 133% with the installation of the FDM CFRP strips. For the FDM CFRP retrofitted specimen tested with a higher axial load (20 kN), the tensile forces from the CFRP strips were predominately countering the second order effects that occurred at larger deformations, rather than increasing the lateral moment resistance. The maximum utilization of the tensile capacities of the used CFRP strips was 48% within this experimental campaign.

For the mean mid-span displacement corresponding to the peak lateral resistance, an increase with a factor that was approximately 90, from 2.1 mm (URM) to 186.7 mm was determined for an axial load of 4.8 kN. The instability displacement was approximately equal to the wall thickness for the URM specimens. For the high axial load FDM CFRP retrofitted specimen, the instability displacement was estimated at approximately 200 mm. For the FDM CFRP retrofitted specimen with low axial load, the instability displacement could not be reached due to the stroke limits of the actuator used, which was 210 mm in both directions.

Another objective of the experimental study on the out-of-plane behaviour on FDM CFRP retrofitted walls, was the development of a practical and straightforward out-of-plane engineering model. The initial engineering model consisted of the force-slip behaviour of the FDM CFRP strips, two rigid masonry blocks and a discrete joint at mid-height of the wall. This engineering model provided a poor approximation of the experimentally obtained lateral moment – mid span displacement relations, the main limitation being the assumption of only one crack in the wall in the model. By performing a cross-section analysis using non-linear material models, the lateral moment capacity was overestimated after a mid-span displacement of ~120 mm. This overestimation was caused by the slip of the FDM CFRP strips being non-negligible. A revised engineering model was proposed, where multiple appending cracks over the height of the wall were introduced. The bond slip laws for FDM CFRP strips as determined using the uni-axial tensile tests were successfully implemented in the revised engineering model. Using a factor of 1.6 for reduction of the compressive strength of masonry due to degradation caused by cyclic loading with large deformations, the model provided good approximations to the experimentally obtained lateral moment – mid-span displacement relations for both the low axial load and the high axial load. The factor of 1.6 to account for masonry degradation was assumed to be a valid assumption based on the excessive damage accumulation in the bed-joints caused by the retrofit and the reached displacement levels.

Out-of-plane behaviour of masonry walls hybrid retrofitted with flexible deep mounted (FDM) CFRP strips and a single-sided FRCM overlay.

Double shear bond tests were conducted in order to investigate the bond between the FRCM system and masonry substrate, where the bond length between the masonry and the FRCM layer was varied. A strong linear correlation was found between the tested bond length range (55-250 mm) and peak stress in the mesh, where the peak stress was approximately 500 N/mm^2 per 100 mm bond length. The critical anchorage length for CFRP mesh rupture was estimated at 340 mm. The tensile behaviour between the CFRP mesh and the polymer-modified mortar was characterized by means of tensile tests.

From the experimental campaign on the OOP behaviour of masonry panels retrofitted with solely a single-sided FRCM overlay, it was observed that the CFRP mesh provided a significant added value in both resistance and deformation capacity when compared to specimens reinforced with solely a polymer-modified mortar overlay. The mean moment capacity and corresponding curvature increased from 0.6 kNm and $3 \cdot 10^{-3}$ m^{-1} respectively, to 1.3 kNm and $85 \cdot 10^{-3}$ m^{-1} respectively. Loading cyclically during the out-of-plane experiments did not affect the moment resistance, ultimate deflection or ultimate curvature when compared to the statically loaded specimens. From a cross-section analysis with partially modified material parameters, a good fit was obtained for the load-deflection relationships.

An additional experimental program was undertaken to assess the out-of-plane behaviour of one-way spanning full scale clay brick masonry walls retrofitted with deep and FDM CFRP strips and a single-sided FRCM overlay. In the experimental testing program three full-scale masonry walls were tested with a four point-bending, cyclic test configuration and an axial load of 4.8 kN. All specimens showed a significant drop in lateral moment resistance due to CFRP mesh rupture.

The mean lateral moment resistance of the FRCM specimens was found to be 4.0 kNm and 7.7 kNm for the out-of-plane loading direction where the one-sided FRCM overlay was in compression and tension respectively. The addition of a single-sided FRCM overlay to form a hyrbrid retrofit measure together with the FDM CFRP strips provides a significantly higher lateral moment resistance compared to both URM (0.8 kNm) and solely FDM CFRP strip retrofitted walls (1.8 kNm). Strong linear relations were found for both the internal moment versus the curvature, and the internal moment versus the CFRP strip stress levels. The contribution of the FRCM layer in compression was found to be significant for the lateral moment resistance, effectively resulting in an increased lever arm between the tensile force of the FDM CFRP strips and the resultant force of the compression zone when analysing the cross-section (over the height) of the wall.

A simple and practical out-of-plane model was proposed for masonry walls that are retrofitted with FDM CFRP strips and single-sided FRCM overlay. A cross section analysis using non-linear and linear material models for the used components was applied, where good approximations were obtained for both the internal moment-curvature and the lateral moment-mid span displacement relationships as determined from the experiments. This was applicable for both out-of-plane loading directions: FRCM in tension and FRCM in compression. In contrast to existing literature, the inclusion of the contribution of FRCM in compression was justified. Even though the tensile stresses of the CFRP strips were overestimated for the case when the FRCM layer is in tension, the limited effect of the CFRP strips on the internal moment capacity for this specific loading direction did not affect the overall prediction of the model. Both the ultimate bending moment and the corresponding displacement following from the proposed model (FRCM in tension) showed good agreement with values obtained using similar models reported in literature.

In-plane behaviour of masonry walls hybrid retrofitted with FDM CFRP strips and a single-sided FRCM overlay.

An experimental study was presented that consisted of nine full-scale masonry walls retrofitted with a single-sided FRCM overlay, FDM CFRP strips and flexible anchor connection. Three different wall geometries with lengths of 1.1 m (S walls), 2.0 m (M walls) and 4.0 m (L walls), with three different axial load levels (0.2, 0.4 and 0.6 N/mm^2) per geometry were tested to investigate the cyclic in-plane behaviour of the reinforced full-scale masonry walls. None of the walls showed any shear damage on either the reinforced and as-built surfaces during the cyclic in-plane experiments. The observed pre-dominant failure mechanism was rocking (low and moderate axial load S walls), a combination of rocking and toe-crushing (high axial load S specimen; M walls), and a combined flexure and sliding (L walls). The mean structural ductility factors were in the range of 3.7-14.7 (M walls), 4.2 (low axial load L wall) and 3.5-25.0 (medium and high axial load L wall). The last range represents a lower bound as the limited stroke of the horizontally oriented hydraulic actuator was insufficient to reach a 20% force drop in the post-peak phase.

A mechanical model based on EC6 [129] was proposed to determine the capacity of the reinforced walls during in-plane loading, covering both moment failure and shear sliding failure. The mechanical model provided a good approximation of the experimentally obtained ultimate loads. The sliding resistance obtained from the model was conservative because the dowel effect of the anchor in the compression zone was not taken into account. The moment resistance was a factor 1.5-2.1 (S walls) and 1.3-1.8 (M walls) higher compared to URM walls. Using the mechanical model and the in-plane test results, the calculated tensile forces in the anchors ranged between 19.0 kN and 37.3 kN.

Additional pull-out experiments considering two stress distribution scenarios were performed on prisms with steel anchors to determine the anchoring strength in the flexible adhesive. The results obtained from the direct pull-out experiments confirmed the scenario where the tensile forces in the anchor were transferred to the CFRP strip (mean anchorage strength 17.9 kN). This scenario provided a conservative but decent approximation of the analytically determined anchorage strength.

In-plane shear behaviour of masonry wallettes hybrid retrofitted with FDM CFRP strips and a single-sided FRCM overlay.

The diagonal compression test was used for the evaluation of the in-plane shear behaviour wallettes that were either unreinforced, FDM CFRP strip retrofitted, or hybrid FDM CFRP strip and single-sided FRCM overlay retrofitted. Retrofitting with solely a FDM CFRP strip did not affect the strength of masonry elements loaded for in-plane shear when compared to the URM wallettes. It was however found that the deep grooves resulted in a 25% lower shear modulus compared to the URM specimens. Moreover the experiments showed that in contrast to the URM specimens, the specimens with solely a FDM CFRP strip retrofit did not disintegrate after reaching the failure load.

Specimens retrofitted with both a FDM CFRP strip and a single-sided FRCM overlay showed an increase in shear capacity of 1.7 and 1.8 times compared to the URM specimens for both a 10 mm and 20 mm FRCM layer thickness respectively. Application of a single-sided FRCM layer resulted in an increase of approximately 40% of the shear modulus compared to the unstrengthened control specimens. No strong correlation was found between the thickness of the mortar matrix of the FRCM layer and the failure load. Additionally, the FRCM layer thickness was found to have limited influence on the shear modulus. The pseudo-ductility factors obtained were in the range of 8.5-9.3 and 15.4-15.6 for the reinforced specimens with a 10 mm and 20 mm FRCM layer thickness respectively, showing that a one sided FRCM overlay leads to a significant increase in ductility.

For the evaluation of the URM specimens for in-plane shear behaviour an existing analytical model showed good correspondence with the experimental values for both the failure mechanism and the failure load, with an experimental/model ratio (ϕ) of 0.98. Guidelines presented in the EC 8-3 [135] (ϕ=1.43), proposed by Triantafillou [141] (ϕ=1.94) and implemented in ACI-549-13 [142] (ϕ=1.31) resulted in conservative approximations.

Research objectives

The effectiveness of the FDM CFRP retrofit system, both stand-alone and in hybrid retrofit configuration with a single-sided FRCM overlay, was examined in depth in this doctoral research. The primary research objectives have been achieved. Through extensive experimental campaigns, more in-depth knowledge was obtained regarding the governing mechanics and failure mechanisms for pull-out, in-plane and out-of-plane loading conditions.

Retrofitting solely with FDM CFRP strips improved the resistance for out-of-plane loads and significantly enhanced the displacement capacity of vertically (one-way) spanning masonry walls. The addition of FDM CFRP strips did not affect the strength of masonry elements loaded under in-plane shear.

With the FDM CFRP and single-sided FRCM overlay hyrbrid retrofit, the in-plane shear behaviour of masonry walls was significantly enhaced. For out-of-plane loads, the addition of a single-sided FRCM overlay improved the performance of the FDM CFRP strips significantly.

Simple models have been proposed and validated for the bond-behaviour of FDM CFRP strips, the out-of-plane behaviour of FDM CFRP retrofitted masonry walls, the out-of-plane behaviour of FDM CFRP and single-sided FRCM overlay hyrbrid retrofitted masonry walls, and the in-plane behaviour of FDM CFRP and single-sided FRCM overlay hyrbrid retrofitted masonry walls.

8.2 Recommendations

Research into the use of flexible deep mounted (FDM) carbon fibre reinforced polymer (CFRP) strips as a seismic retrofitting technique for clay brick masonry structures is early in its development. Even though an extensive experimental campaign was reported within this thesis, some related aspects require further research.

Pull-out test involving flexible adhesives: Testing the pull-out and bond-slip behaviour of systems that include visco-elasto-plastic components should be conducted at a loading rate that is more representative for the practical application of the system. Additionally, active speed control is advised to maintain a steady loaded-end slip rate.

Cyclic pull-out test: The pull-out tests in this research were all monotonic. Performing additional tests with cyclic loading conditions can lead to a better understanding of the flexible adhesive-CFRP strip bond mechanism.

Shake table tests: Further research into the dynamic performance of FDM CFRP strip (and optional single-sided FRCM overlay) retrofitted masonry walls is recommended by means of performing shake table tests. This form of testing would allow the dynamic characterization (damping, period response etc.) of retrofitted masonry walls to be established.

Two-way spanning walls: The out-of-plane experimental campaign focused solely on vertically, one-way spanning masonry walls. With two-way spanning walls, being supported at the horizontal and vertical edges, biaxial bending occurs when the wall is subjected to out-of-plane loads. The behaviour of a FDM CFRP strip retrofitted wall when subjected to OOP two-way bending excitation can be assessed with an additional testing campaign.

Cavity walls: The walls tested in this study were made from single leaf clay brick masonry. Additional experimental investigation on cavity walls is needed to determine the load transfer across the wall ties in case of a retrofitted inner leaf. This load transfer is especially of interest for out-of-plane loads resulting in high mid-span wall displacements.

In-plane: No shear damage was observed within the applied load range on conducted static-cyclic in-plane shear tests on full-scaled masonry specimens strengthened with the hybrid reinforcement system. With these cantilever shear walls there are regions of: (a) nearly pure tension stress; (b) nearly pure compression stress; (c) combined tension and shear stresses; and (d) combined compression and shear stresses. The diagonal compression test as reported in Chapter 6 is applicable only to the latter case being the compression-shear region. Thus, the mechanical characteristics and effectiveness of the repair techniques will not be fully revealed by diagonal compression testing alone. Just like the additional experimental program for the combined compression and shear stresses covered in Chapter 6, testing other shear stress combinations are recommended to fully understand the response of reinforced masonry shear walls.

Finite element modelling: Additional finite element modelling is recommended, supported by more extensive experiments on the dynamic behaviour of the flexible adhesive and the adhesive/CFRP strip interface. The improved finite elements models can provide more insight on not only on the bond-slip and pull-out behaviour of FDM CFRP strips, but also on the out-of-plane behaviour of FDM CFRP strip retrofitted masonry walls.

Durability: When installing FDM CFRP strip strengthening on the load bearing inner leaf of cavity walls, environmental factor such as moisture and extreme temperatures do not oppose a direct problem for the retrofit system, as highlighted in section 2.2.2. Further research should be undertaken on the effects of these environmental factors on the adhesive-to-masonry and adhesive-to-CFRP interface mechanics, if the FDM CFRP strip are to be placed in less protective circumstances and/or more extreme environments.

Different masonry types: The study presented in this thesis focused solely on solid clay brick masonry walls. Special attention is needed for masonry involving perforated bricks/blocks. The presence of cores in the brick or block unit may affect the debonding resistance due to stress concentrations. It is recommended to conduct a series of pull-out experiments to assess the validity of the FDM CFRP strip retrofit for a type of brick/block that deviates significantly from the used solid clay bricks in this research.

Connection: The connection/anchoring of strengthened masonry walls to floor slabs, foundations and structural reinforced concrete elements (i.e. masonry-infilled reinforced concrete frames) deserves some extra attention.

8.3 Outlook

There is a growing awareness worldwide of the need to structurally improve the existing building stock to protect communities in the event of earthquakes. The use of flexible adhesives for the (deep) mounting of composite materials will provide new opportunities in the field of seismic retrofitting.

The application domain of flexible mounted FRP components can be expanded to different substrates such as concrete, stone masonry and calcium silicate masonry. Different composite materials could be considered to further reduce the costs, CO_2 footprint and non-renewable material usage of the total retrofitting concept. The proposed concept could also be applied for blast resistant design to resist explosive threats, where the high deformation capacity of the retrofitted wall would be beneficial in terms of blast energy dissipation.

As an alternative for the deep mounting configuration, the vertical drilling concept was developed towards the end of this doctoral research as an invisible retrofit measure. Using guided special drilling equipment, a borehole is drilled from the top of the wall. After injecting the flexible adhesive into the borehole from the top of the wall, a CFRP rod is pushed into position. An important boundary condition for this type of retrofit installation is that the topside of the wall should be easily accessible. This proposed concept with drilling could be beneficial for retrofitting monuments, where even the slightest impact on the aesthetics of the building is mostly not accepted.

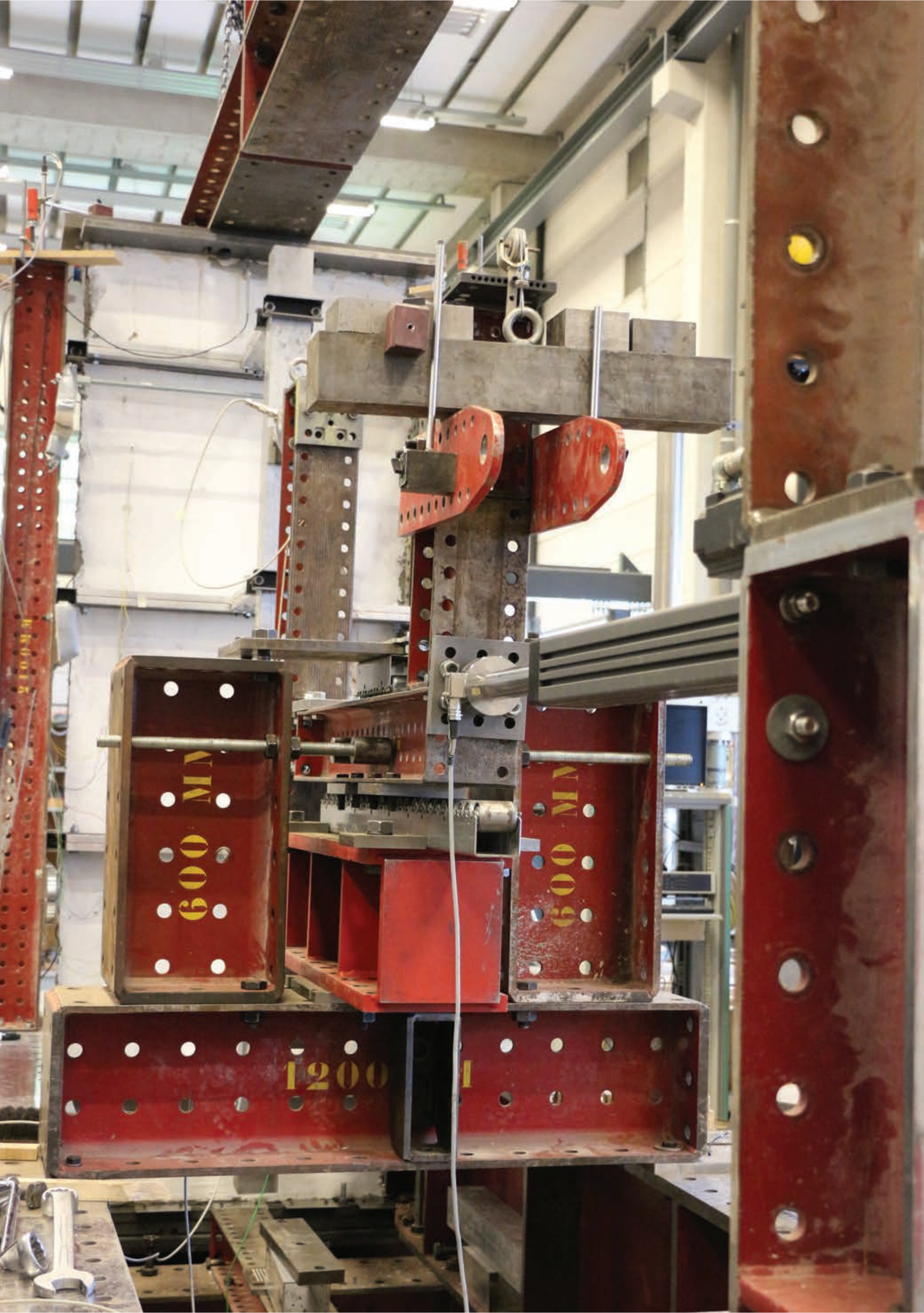
600 MN
600 MN
1200

Appendix A

Database pull-out experiments

An overview of all Near Surface Mounted (NSM) / Externally Bonded (EB) CFRP-to-masonry bond strength tests, obtained using *Vaculik et al.* [54], is presented in Table A.1. This table covers 733 pull-out experiments on CFRP-to-masonry bond strength tests found in open literature, spread over 27 separate research studies [13, 21, 28–53].

Table A.1: Database Near Surface Mounted (NSM) / Externally Bonded (EB) direct pull-out experiments for CFRP and masonry, obtained using the global database *Vaculik et al.* [54].

Reference	Configuration	Number of specimens	P_{max} (kN)	Utilization (%)	Failure mode*	$E_{adhesive}$ (N/mm²)
[28]	EB/sheet	4	16.2-28.3	-	SD	1,230
[29]	EB/sheet	8	3.2-5.9	12-33	SD	3,000
[30]	EB/sheet	18	3.2-20.4	8-50	SD	-
[31]	EB/sheet	5	15.9-20.2	56-74	SD	>3,000
[32]	NSM/strip	6	56.8-66.5	54-64	SD/AF	>2,000
[21]	NSM/strip	18	53.6-84.5	51-81	SD/AF/CR	>6,000
[33]	NSM/strip	15	17.5-50.7	53-100	SD/AF/CR	6,700
[34]	EB/sheet	64	0.8-19	14-76	SD	-
[35]	EB/sheet	3	8.5-13	29-44	SD/PF	3,300
[36]	EB/sheet	8	6.3-10.3	7-11	SD/AF	12,800
[37]	EB/sheet	5	5.1-6.1	69-82	SD	3,670
[38]	EB/sheet	9	5.3-12.1	35-87	SD	-
[39]	EB/sheet	6	14.9-32.4	34-37	SD	-
[40]	NSM/strip	14	41.0-75.3	30-75	SD	>6,700
[41]	EB/sheet	136	4.1-10.3	18-44	SD	>1,308
[42]	EB/sheet	17	4.5-14.2	4-9	SF/CR	12,800
[43]	EB/sheet	6	10.1-14.7	24-36	SD	3,300
[13]	NSM/strip	39	17.8-65.2	26-100	SD/AF/CR	>9,600
[44]	EB/sheet	6	12.5-14.9	30-36	SD/AF	3,300
[45]	EB/sheet	5	8.6-9.5	37-41	SD/PF/CR	8
[46]	EB/sheet	15	5.6-14.1	24-59	SD	7,100
[47]	EB/sheet	222	0.8-6.3	15-100	SD/CR	2,590
[48]	EB/sheet	3	5.8-13.6	24-57	SD	-
[49]	EB/sheet	28	5.0-16.2	41-99	SD/AF	12,840
[50]	EB/sheet	14	8.5-15.8	48-90	SD/AF/CR	4,500
[51]	EB/sheet	24	6.5-11.9	28-51	SD	-
[52]	EB/sheet	8	9.4-23.5	48-100	SD/CR/PF	-
[53]	EB/sheet	27	6-15.1	25-61	SD/AF/CF	15-4,500

* D = Substrate debonding; AF=Adhesive failure;
CR=CFRP rupture; PF=Prism failure (compression)

Appendix B

Flexural strength and out-of-plane displacement capacity of masonry walls with fabric reinforced cementitious matrix composites

This appendix presents an approach for the design of the out-of-plane flexural strengthening of masonry walls by FRCM systems.The content of this appendix was obtained from *Meriggi, de Felice and De Santis* [124].

According to bending theory, the flexural strength of masonry walls reinforced with externally bonded FRCM composites can be calculated by a cross-sectional analysis assuming that:

1. there is strain compatibility between FRCM and substrate;
2. plane sections remain plane after loading;
3. FRCM is assumed to be linear elastic in traction up to the attainment of the effective strain $\epsilon_{fe} \leq \epsilon_{fd}$;
4. The contribution of FRCM in compression is neglected. Only in the case of CRM composites, which are 30-50 mm thick and whose spalling / buckling is prevented by the FRP connectors, the presence of the reinforcement on the compression side is accounted for by increasing the

thickness of the wall cross section (the contribution of the FRP mesh is neglected anyway). This means that the same value of elastic modulus is assigned to both the substrate (masonry) and the matrix. From an engineering standpoint, the error associated with this simplification is negligible;

5. Masonry has no tensile strength, whereas a stress-block diagram is assumed under compression as outlined hereafter.

A wall having width L and thickness t is considered, subjected to the axial load N_{Ed}. The flexural strength can be evaluated on the basis of the following data (Fig. B.1) for textile and masonry respectively:

- FRCM textile plies (n_f), spacing between strips (s_f), width of the single strand (w_f), design thickness of each ply in the load direction (t_f), design axial strain (ϵ_{fd}) and tensile modulus of elasticity (E_f);
- Mechanical properties of masonry: a stress-block diagram is assumed in compression, in which masonry has a constant stress value of $\zeta \cdot f_{mc}$ over a depth of $\beta \cdot c_u$ (ζ and β being two scalar coefficients and c_u the neutral axis depth).

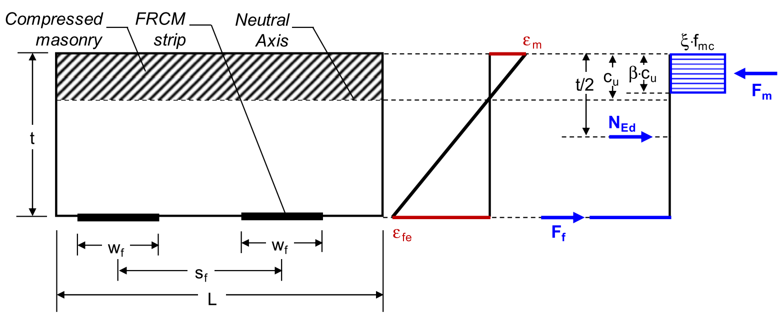

Figure B.1: Cross-section of the wall, strain and stress profiles, and load resultants assumed in the proposed assessment approach. Note that ϵ_m is the compressive strain in masonry.

The neutral axis depth (c_u) is calculated by imposing the balance of the force resultants. MR is evaluated as the sum of the contributions of masonry F_m and FRCM F_t, both calculated with respect to the centre of the cross-section (where N_{Ed} is applied).

Assuming FRCM rupture and no crushing of the masonry, c_u is provided by Eq. B.1 and the resisting bending moment is calculated in accordance with Eq. B.2, where Υ follows from Eq. B.3.

$$c_u = \frac{1}{E_m \epsilon_{fd} L} \left(-N_{Ed} - \Upsilon + \sqrt{(\Upsilon + N_{Ed})^2 + 2 E_m \epsilon_{fd} L t (N_{Ed} + \Upsilon)} \right) \tag{B.1}$$

$$M_R = \Upsilon \frac{t}{2} + E_m \frac{\epsilon_{fd}}{t - c_u} \frac{c_u^2}{2} L \left(\frac{t}{2} - \frac{c_u}{3} \right) \tag{B.2}$$

$$\Upsilon = \epsilon_{fd} E_f n_f t_f L \frac{w_f}{s_f} \tag{B.3}$$

Aiming at estimating the deflection capacity of an FRCM retrofitted wall, it is assumed that the collapse mechanism is described by two nearly-rigid blocks rotating after a crack has developed in the cross-section where the ultimate flexural strength is attained. Crack occurrence requires that FRCM detach locally from the masonry to allow composite-to-substrate relative displacement, which is assumed to occur over a development length ℓ, symmetrically distributed on the two sides of the crack (Fig. B.2). Such relative displacement is considered uniform along ℓ and null elsewhere. It is also assumed that the textile attains its design axial strain ϵ_{fd} along the whole development length, such that its elongation results $\ell\ \epsilon_{fd}$. The out-of-plane displacement (u_d) is calculated under the small displacements assumption through Eq. B.4, in which t is the thickness of the wall, h_1 and h_2 (with $h_1 \leq h_2$) are the distances between the supports and the considered cross-section and $\gamma_{u,K}$ is a statistical coefficient providing the characteristic (5% fractile) value of u_d.

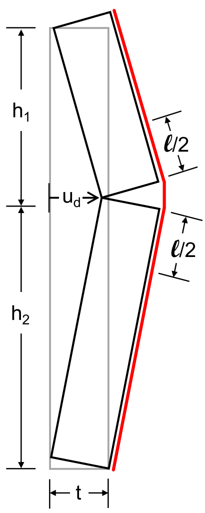

Figure B.2: Sketch of the two nearly-rigid block mechanism for out-of-plane deflection capacity estimate.

$$u_d = \gamma_{u,K} \frac{\ell \epsilon_{fd}}{t(1/h_1 + 1/h_2)} \tag{B.4}$$

A statistical coefficient of $\gamma_{u,K} = 0.4$ was recommended for the evaluation of the characteristic drift, when ultimate limit state conditions are under consideration. Based on the least squares best fit between experimental and theoretical drift values, a value of 413 mm was recommended for l. It should be noted that parameter ℓ does not coincide with the effective transfer length, which may be determined experimentally, as the bonded length needed for the full exploitation of the FRCM-to-substrate load transfer capacity. Indeed, the development length at each side of the crack ($\ell/2$) might be expected to be shorter than the effective transfer length since the strain in the CFRP mesh is assumed to attain ϵ_{fd} within ℓ, whereas it generally reduces by moving away from the FRCM loaded end (the crack).

The input parameters used to model an FRCM retrofitted wall, with similar dimensions and axial load as the tested walls in Chapter 5, are summarized in Table B.1.

Table B.1: Input parameters.

Parameter	Symbol	Value	Unit
Young's modulus of the embedded CFRP mesh	E_f	266,000	N/mm^2
Development length	ℓ	413	mm
Length of the wall	L	965	mm
Number of plies	n_f	1	-
Axial load on the wall	N_{ed}	4.8	kN
Spacing between strand of the CFRP mesh	s_f	20	mm
Thickness of the wall	t	95	mm
Design thickness of the embedded CFRP mesh	t_f	0.293	mm
Width of of a single strand of the CFRP mesh	w_f	3	mm
Ultimate tensile strain of the CFRP mesh	ϵ_{fd}	0.64	%

Appendix C

Preliminary finite element models of FDM CFRP strips

In this Appendix preliminary finite element models are presented regarding the bond-slip and pull-out behaviour of flexible deep mounted (FDM) carbon fibre reinforced polymer (CFRP) strips. The modelling of the fabric reinforced cementitious matrix (FRCM) layer is not presented, as numerical modeling strategies for the evaluation of the in- and out-of-plane performance of masonry structures strengthened with FRCM are available [145]. ABAQUS FEA software was used for the numerical analysis.

C.1 Flexible adhesive

The rate dependent tensile behaviour of the adhesive is modelled as a strain-dependent plastic. The load application is assumed non-cyclic and moving in a single direction. For more accurate representation of the visco elasto-plastic adhesive, the use of a two-layer viscoplasticity model is suggested as numerical modeling strategy. The material test data (as was presented in Fig. 2.2) can be converted to ABAQUS input. The strains provided in material test data are the total strains in the material, which need to be decomposed into the elastic ϵ_e and plastic strain ϵ_p components (Fig. C.1). The plastic strain is obtained by subtracting the elastic strain, defined as the value of true stress σ divided by the Young's modulus E, from the value of total strain (Eq. C.1).

$$\epsilon_p = \epsilon_t - \epsilon_e = \epsilon_t - \frac{\sigma}{E} \tag{C.1}$$

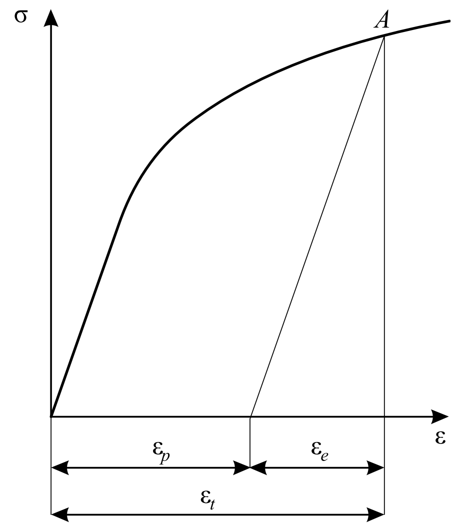

Figure C.1: Decomposition of the total strain into elastic and plastic components.

The nominal stress and nominal strain are converted to true stress and true strain following Eqs. C.2 and C.3 respectively. Once these values are known, the equation relating the plastic strain to the total and elastic strains (Eq. C.1) can be used to determine the plastic strains associated with each yield stress value.

$$\sigma = \sigma_{nom}(1+\epsilon_{nom}) \tag{C.2}$$

$$\epsilon = ln(1+\epsilon_{nom}) \tag{C.3}$$

ABAQUS approximates the smooth stress-strain behaviour of the material with a series of straight lines joining the given data points. Any number of points can be used to approximate the actual material behaviour; therefore, it is possible to use a very close approximation of the actual material behaviour. The test data are entered as tables of yield stress values versus equivalent plastic strain at different equivalent plastic strain rates. The yield stress must be given as a function of the equivalent plastic strain. The yield stress at a given strain and strain rate is interpolated directly from these tables. The input data in ABAQUS for the tensile behaviour of the flexible adhesive (Young's modulus 66.67 N/mm^2, Poisson's ratio = 0.48), determined using Fig. 2.2, is provided in Table C.1.

A 2D-planar shell element was used to model a stroke of the flexible adhesive (Fig. C.2. The top of the geometry was fixed against displacement

Table C.1: Input data in ABAQUS for the flexible adhesive (Young's modulus 66.67 N/mm^2, Poisson's ratio = 0.48).

Yield stress	Plastic strain	Rate
0.02	0	0
5	0.5	0
0.0200	0.0000	0.00276
0.6000	0.0160	0.00276
0.9500	0.0358	0.00276
1.6200	0.0757	0.00276
2.2700	0.1160	0.00276
3.0000	0.1550	0.00276
3.7000	0.1945	0.00276
4.4000	0.2340	0.00276
5.1000	0.2735	0.00276
5.7200	0.3142	0.00276
6.3000	0.3555	0.00276
6.9000	0.3965	0.00276
7.4500	0.4383	0.00276
0.0200	0.0000	0.05259
1.2000	0.0070	0.05259
1.9300	0.0211	0.05259
2.9500	0.0558	0.05259
3.8400	0.0924	0.05259
4.7500	0.1288	0.05259
5.6000	0.1660	0.05259
6.4000	0.2040	0.05259
7.1000	0.2435	0.05259
7.6500	0.2853	0.05259
8.2000	0.3270	0.05259
8.7000	0.3695	0.05259
9.2500	0.4113	0.05259
10.1500	0.4678	0.05259

in the y-direction. At the bottom of the geometry a displacement boundary condition (in the y direction) was set to be reached within a certain time, resulting in a specific strain rate. Four-node plane stress elements (CP4SR) were chosen to mesh the selected geometry. Reduced integration and enhanced hourglass control were employed for all the elements to decrease computation time and improve convergence.

The tensile stress-strain relationships of the flexible adhesive following from the material test data are compared with the obtained tensile stress-strain relationships from the finite element model (Fig. C.3). Two strain rates $\dot{\epsilon}$ of 0.46 %/s and = 10.33 %/s, are presented. The results of the finite element model are cut off at the plastic strain levels provided in Table C.1. For both strain rates levels, the tensile stress-strain relationships obtained using the finite element model provided a good fit with the material test data for tensile behaviour.

Using the same input data as presented in Table C.1, the thick adherend shear test presented in section 2.2.2 was simulated. A 2D-planar shell element with a length and height of 10 mm and 1.75 mm respectively, was used to model the flexible adhesive under shear loading (Fig. C.4. The bottom of the geometry was pinned (U1=U2=U3=0), whereas the top of the geometry was fixed against displacement in the y-direction. At the top of the geometry, an additional displacement boundary condition (in the x direction) was set to reach a displacement of 2.1 mm within 12.6 seconds (similar to the crosshead rate of 10 mm/min presented in section 2.2.2). Again, four-node plane stress elements (CP4SR) were chosen to mesh the selected geometry, with reduced integration and enhanced hourglass control. The result of the finite element simulation is provided in Fig. C.5.

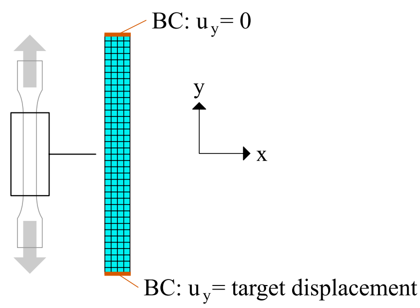

Figure C.2: Geometry used to model the tensile behaviour of the flexible adhesive.

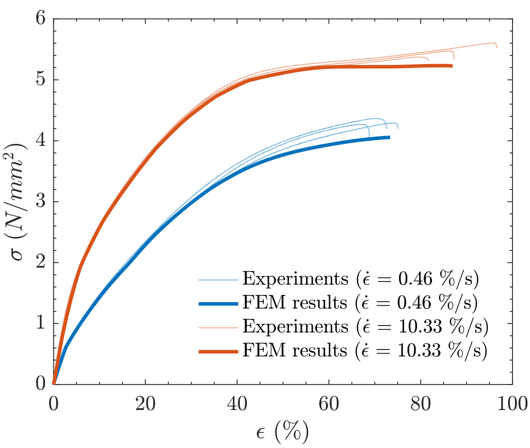

Figure C.3: Comparison tensile stress-strain relationships obtained using the finite element model with the material test data for tensile behaviour.

The shear stress-strain relationships of the flexible adhesive following from the material test data are compared with the obtained tensile stress-strain relationships from the finite element model (Fig. C.6). The shear stress-strain relationships obtained using the finite element model provided a good fit with the material test data for shear behaviour.

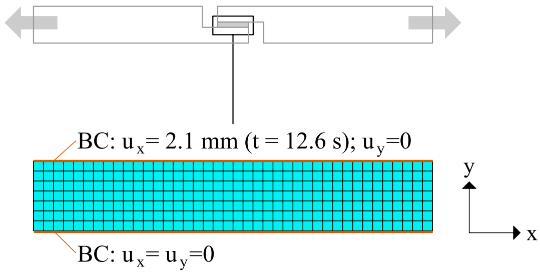

Figure C.4: Geometry used to model the shear behaviour of the flexible adhesive.

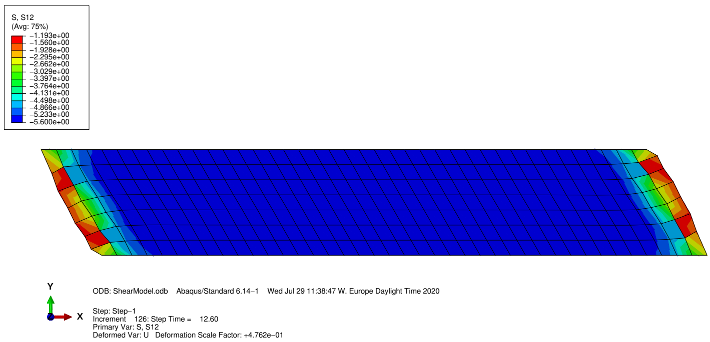

Figure C.5: Result finite element model regarding shear stresses.

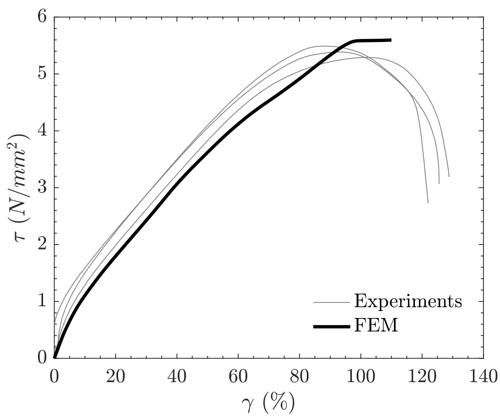

Figure C.6: Comparison shear stress-strain relationships obtained using the finite element model with the material test data for shear behaviour.

C.2 Bond-slip behaviour FDM CFRP strip

The available traction-separation model in ABAQUS assumes initially linear elastic behaviour followed by degradation. Damage modeling allows the simulation of the degradation and eventual failure of the bond between two cohesive surfaces. The failure mechanism consists of two components: a damage initiation criterion and a damage evolution law. Damage initiation refers to the beginning of degradation of the cohesive response at a contact point. A typical cohesive traction-separation law with damage evolution is shown in Fig. C.7. For more background information regarding the traction-separation model in ABAQUS, the ABAQUS user manual can be consulted [146]. Figure C.7 shows a damage model in three directions, but likely only the longitudinal shear direction along the CFRP strip is important in this analysis, whereas the interface normal properties and the interface shear properties for the other direction do not play a role. A simple axial truss element with a simple line-interface element including just the bond-slip shear traction curve can also be sufficient.

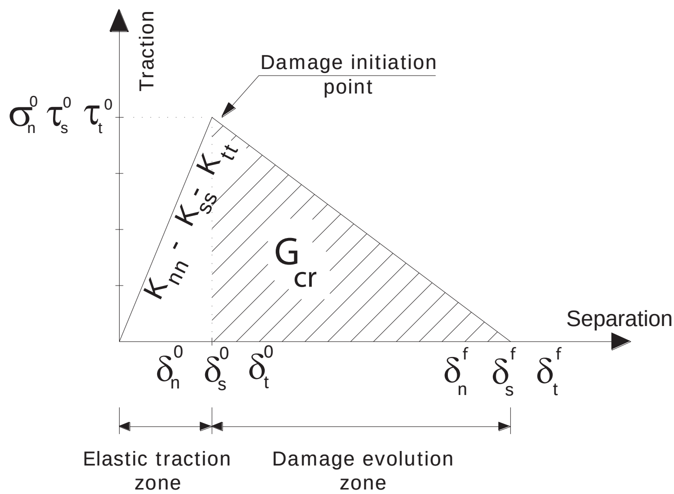

Figure C.7: Typical cohesive traction-separation law with damage evolution.

Two modelling strategies were maintained regarding the thick adhesive layer. In the first approach, the influence of the adhesive mass on shear deformation was neglected in determining the traction-separation parameters. The analysed geometry with a length of 200 mm is shown in Fig. C.8. Due to symmetry of the proposed 2D approach, only half of the cross-section A-A as was illustrated in Fig. 3.1 is modelled. The adhesive (4.3 mm in thickness) was assigned a Young's Modulus of 1,000,000 N/mm² and a Poisson ratio of 0. The CFRP strip (0.7 mm thickness) was modelled as a linear elastic material (Young's modulus 198,000 N/mm², Poisson's ratio = 0.23). The top edge of the CFRP strip was assigned to be symmetrical in the y-direction, and the bottom of the adhesive was encastered.

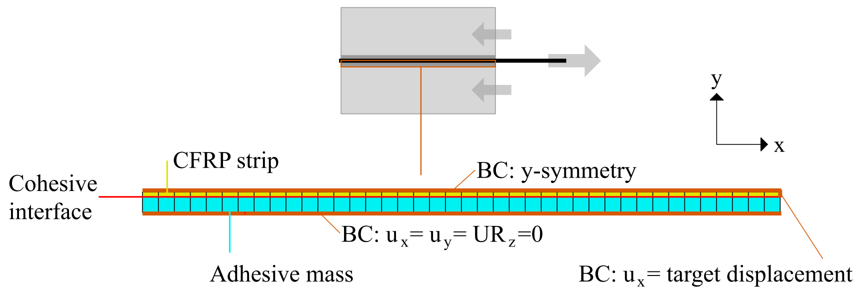

Figure C.8: Geometry used to model the traction-separation behaviour.

A surface to surface contact with small sliding was assigned between the CFRP strip and the adhesive. The contact interaction property for this interface included a traction-separation model. Maximum separation was selected as damage initiation criterion based using the maximum separation value of $\delta = 2.8$ (assumed the same for all directions), following the global bond-slip law presented in section 3.4. The uncoupled stiffness coefficient, which was assumed to be same in all three directions, was assigned a value of $\tau_f/\delta_1 = 2.2 / 2.8 = 0.79$ (τ_f and δ_1 obtained from Table 3.4). Using the uncoupled stiffness coefficient and the maximum separation value, the displacement-based damage variables and corresponding plastic displacement were determined.

The second approach included the effect of the adhesive mass in shear deformation in determining the traction-separation parameters. The strategy and assigned properties remained the same as mentioned in the previous paragraph, except the flexible adhesive was now assigned the input parameters presented in Table C.1. As the shear deformation of the adhesive is now present, the traction-separation parameters needed modification. The traction-separation related input data in ABAQUS are provided in Table C.2 for both strategies. The obtained local bond-slip behaviours following both strategies resulted in a close estimation of the averaged multi-linear local bond-slip behaviour (Table 3.4), as shown Fig. C.9.

Table C.2: Traction-separation related input data in ABAQUS for strategy 1 (adhesive mass neglected) and strategy 2 (adhesive mass included).

Strategy 1 (adhesive mass neglected)		Strategy 2 (adhesive mass included)	
Uncoupled stiffness coefficients		Uncoupled stiffness coefficients	
Knn	0.786	Knn	1.375
Kss	0.786	Kss	1.375
Ktt	0.786	Ktt	1.375
Maximum separation criterion for damage initiation		Maximum separation criterion for damage initiation	
Normal only	2.8	Normal only	1.6
Shear-1 only	2.8	Shear-1 only	1.6
Shear-2 only	2.8	Shear-2 only	1.6
Displacement based damage evolution		Displacement based damage evolution	
Softening	Tabular	Softening	Tabular
Damage variable	Total/Plastic displacement	Damage variable	Total/Plastic displacement
0.000	0.0	0.000	0.0
0.176	0.6	0.200	0.4
0.300	1.2	0.333	0.8
0.391	1.8	0.429	1.2
0.462	2.4	0.500	1.6
0.606	3.4	0.556	2.0
0.711	4.4	0.620	2.4
0.789	5.4	0.736	3.4
0.851	6.4	0.814	4.4
0.901	7.4	0.869	5.4
0.956	8.8	0.911	6.4
0.963	10.9	0.943	7.4
0.968	13.0	0.969	8.4
0.972	15.2	0.974	9.4
0.975	17.2	0.977	10.9
-	-	0.979	12.4
-	-	0.981	13.9
-	-	0.983	15.4
-	-	0.984	16.9
-	-	0.985	18.4

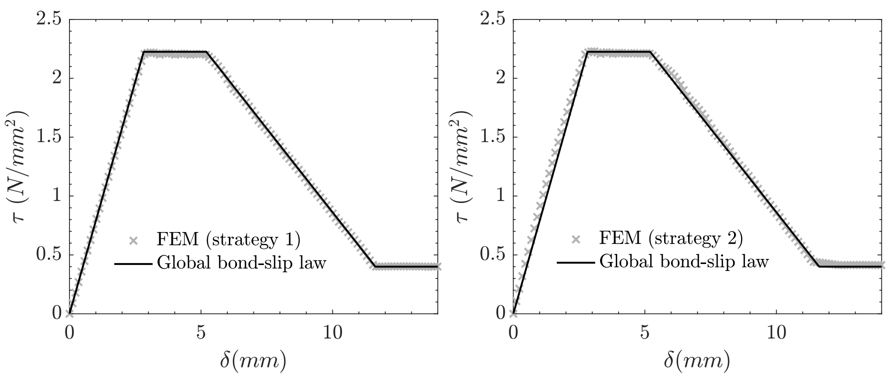

Figure C.9: Comparison local bond-slip behaviour following from both FEM strategies with the averaged multi-linear local bond-slip behaviour.

C.3 Pull-out behaviour FDM CFRP strip

The pull-out tests presented in section 3.3 were simulated for anchorage lengths 340 mm, 530 mm, 730 mm and 1,000 mm. Due to symmetry, only a quarter of the pull-out specimens were modelled, as shown in Fig. C.10. The masonry (100 mm height en 50 mm width) was modelled as a homogeneous, linear elastic material (Young's modulus 3,100 N/mm², Poisson's ratio = 0.25). The CFRP strip (0.7 mm thickness) was modelled as a homogeneous, linear elastic material (Young's modulus 198,000 N/mm², Poisson's ratio = 0.23). Based on the selected strategy, two different geometries were analysed, as shown in Fig. C.11.

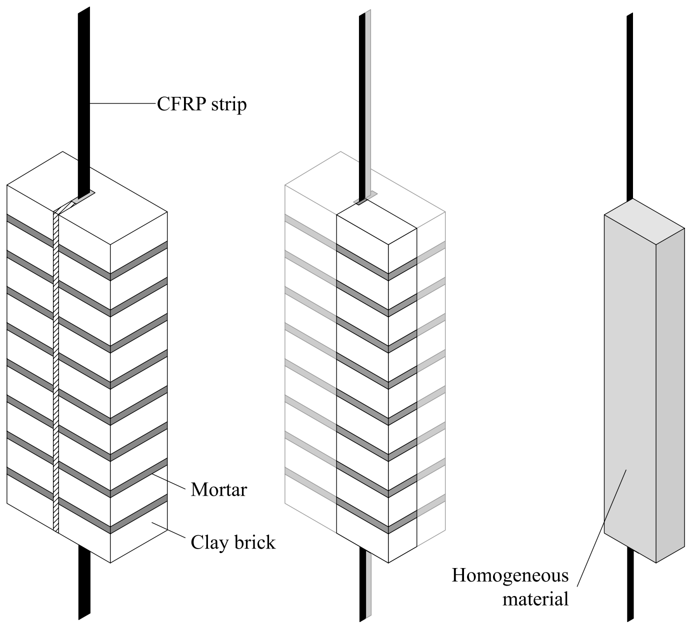

Figure C.10: Simplification of the pull-out specimen for finite element modelling.

For strategy 1, where the influence of the adhesive mass was neglected, the analysed geometry was simplified to a rectangular block masonry with a CFRP attached on top of it, as shown in Fig. C.11. The top surface of the CFRP strip and masonry were again assigned to be symmetrical in the y-direction. The left surfaces of the CFRP strip and masonry were assigned to be symmetrical in the x-direction. The left surface of the masonry was restricted movement in the z-direction. The contact interaction property for the interface between the CFRP strip and the masonry included the previously presented traction-separation model (strategy 1, Table C.2).

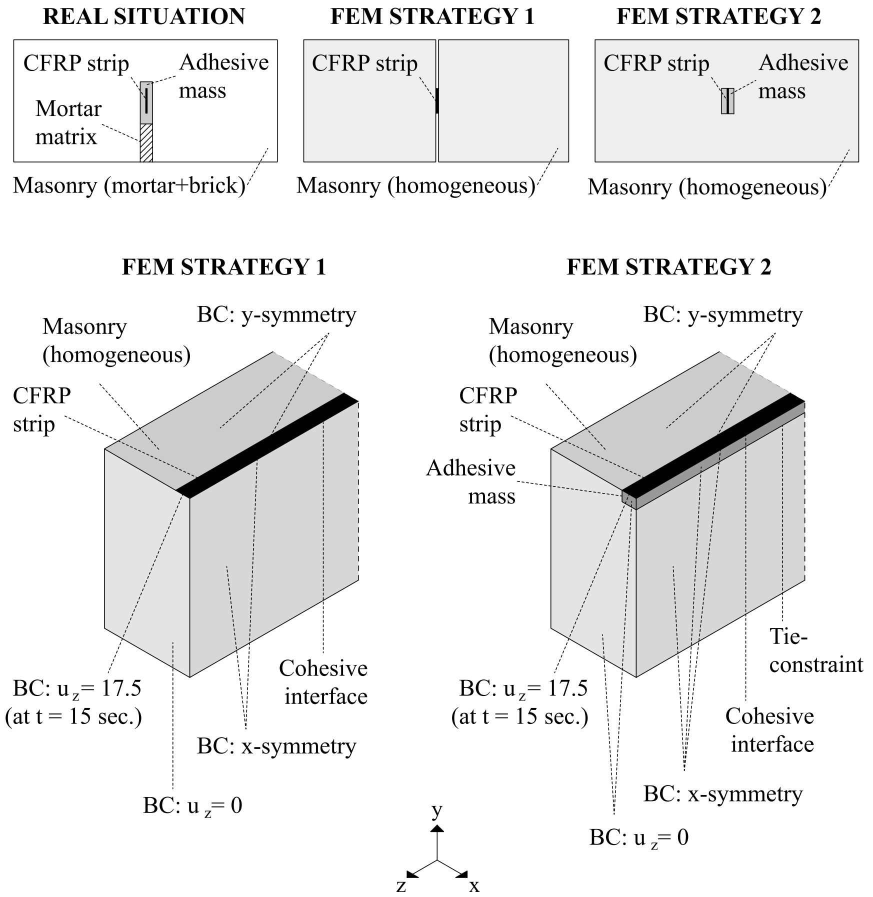

Figure C.11: Geometries and boundary conditions (BC) of the two proposed FEM strategies.

For strategy 2, where the influence of the adhesive mass was included, the adhesive mass was simplified, as shown in Fig. C.11. Between the adhesive mass and the masonry interface, only a tie constraint was assigned for the interface with the normal pointing in the y direction. The top surface of the CFRP strip and masonry were assigned to be symmetrical in the y-direction, whereas the left surfaces of the CFRP strip, adhesive mass and masonry were assigned to be symmetrical in the x-direction. The left surface of the masonry was restricted movement in the z-direction. The contact interaction property for the interface between the CFRP strip and the adhesive mass included the previously presented traction-separation model (strategy 2, Table C.2). No interaction properties or constraints were applied for the interface between the masonry and the CFRP strip.

For both strategies, a displacement boundary condition (in the z direction) was set at the left surface of the CFRP strip, to reach a displacement of 17.5 mm within 15 seconds (similar to the pull-out speed of 70 mm/min in section 3.3). Four-node plane stress elements (CP4SR) were chosen to mesh the selected geometry (maximum mesh size 10 x 10 mm), with reduced integration and enhanced hourglass control.

The force-slip results of the finite element simulations were plotted together with the experimental outcomes (section 3.3) and the prediction made with the partial interaction model (section 3.4) in Figs. C.12 (strategy 1) and C.13 (strategy 2). Both finite elements strategies resulted in force-slip relationship that showed good correspondence with the force-slip relationship determined using the partial interaction model.

As both modelling strategies provide similar results in terms of force-slip relationship, strategy 1 was selected for further analyses due to the simple implementation. The shear stress distribution in the masonry (y-z plane) and the axial stress distribution in the masonry (z-direction) are provided in Figs. C.14 and C.15 respectively for masonry lengths L= 340 (a), 530 (b), 730 (c) and 1,000 mm (d). The shear stress distribution in the masonry right below the CFRP strip following from the finite element simulations (Fig. C.14) showed good correspondence with the stress distribution profile obtained using the partial interaction model, as was presented in Fig. 3.33.

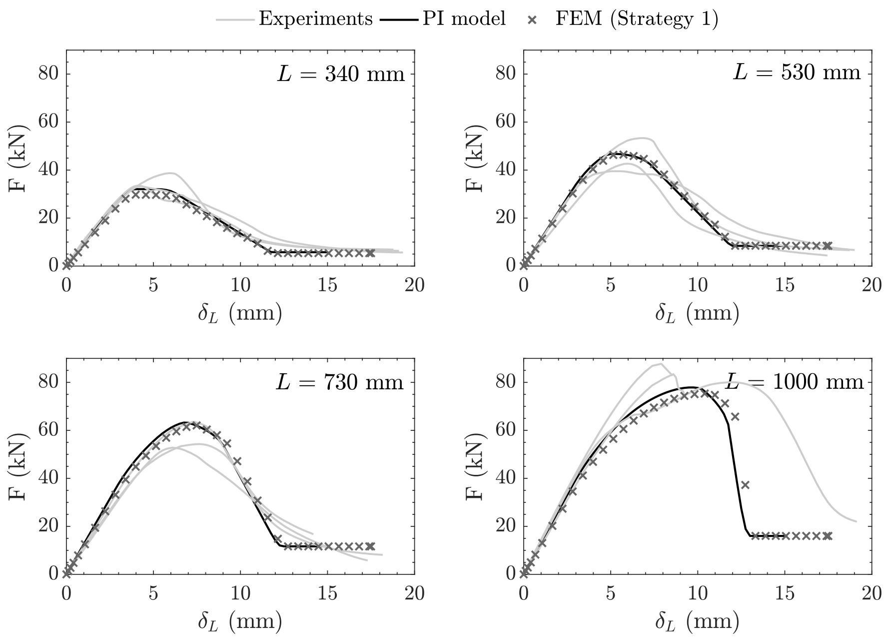

Figure C.12: Comparison force-slip relationship: finite element simulations (strategy 1) with the and partial interaction (PI) model.

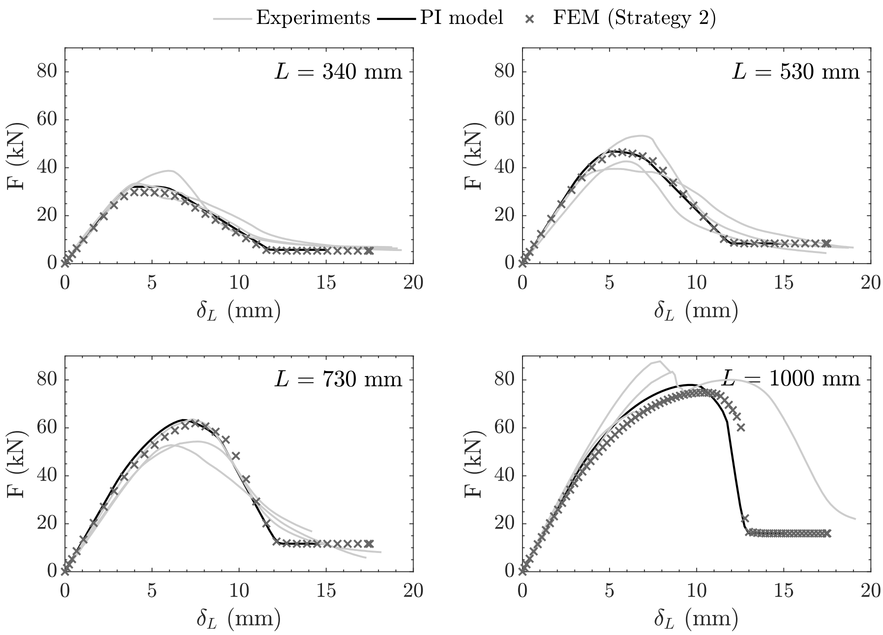

Figure C.13: Comparison force-slip relationship: finite element simulations (strategy 2) with the and partial interaction (PI) model.

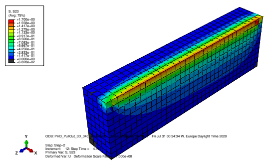

(a) L = 340 mm

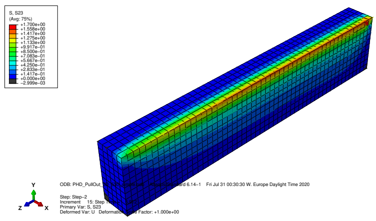

(b) L = 530 mm

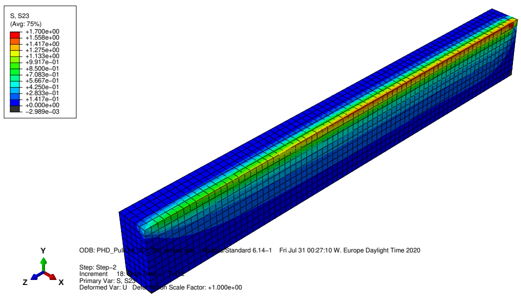

(c) L = 730 mm

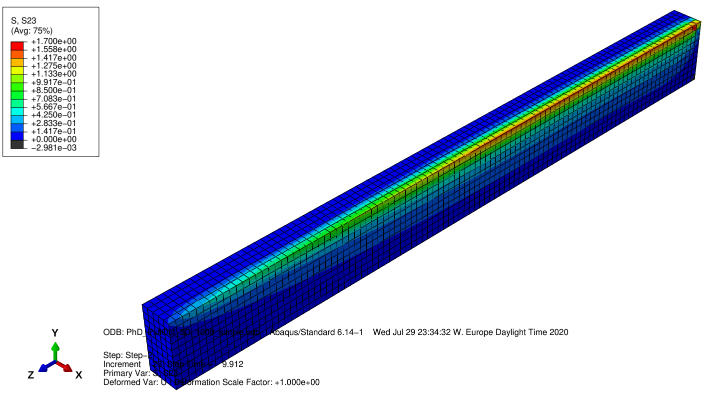

(d) L = 1000 mm

Figure C.14: Shear stresses in the masonry (y-z plane) at the maximum pull-out resistance, as obtained with the finite element simulations (strategy 1). Gradient map ranges from 0 N/mm² (blue) to 1.7 N/mm² (red).

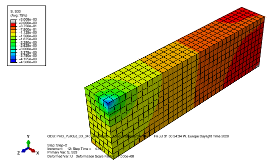

(a) L = 340 mm

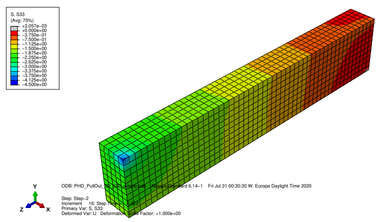

(b) L = 530 mm

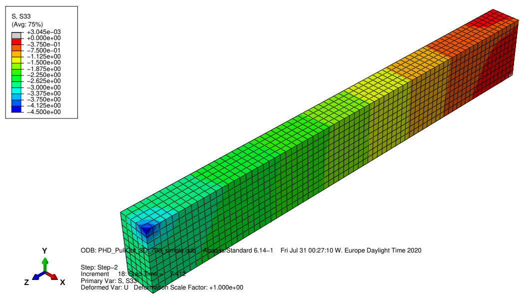

(c) L = 730 mm

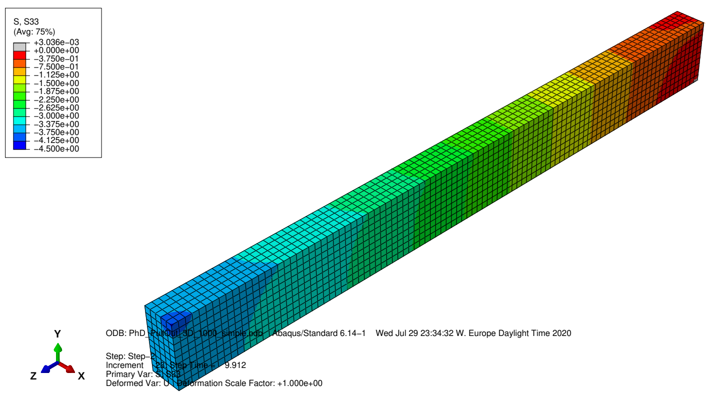

(d) L = 1000 mm

Figure C.15: Axial stresses in the masonry (z-direction) at the maximum pull-out resistance, as obtained with the finite element simulations (strategy 2). Gradient map ranges from -4.5 N/mm² (blue) to 0 N/mm² (red).

Appendix D

Simplified models describing the force-displacement response of vertically spanning (strengthened) masonry walls subjected to out-of-plane loading

This appendix presents simplified models describing the force-displacement response of vertically (one-way) spanning (strengthened) masonry walls subjected to out-of-plane loading. The considered strengthening systems are flexible and deep mounted (FDM) CFRP strips (also considered stand-alone), and a single sided FRCM overlay. The simplified models presented in this Appendix ignore any bond strength that the wall may have prior to cracking, thus effectively treating the wall as pre-cracked from the outset.

D.1 Flexible deep mounted CFRP strips

The simplified engineering model consists of three rigid masonry blocks and two discrete joints, as shown in Fig. D.1. During lateral loading, the CFRP strips will be pulled out of the top and bottom rigid blocks. Additionally, the CFRP strip will elongate over the middle block.

For a rigid block length with a minimum of 750 mm, the the relation between between CFRP stress σ_p and slip Δ_s of the CFRP strip follows from

D. Simplified models describing the force-displacement response of vertically spanning (strengthened) masonry walls subjected to out-of-plane loading

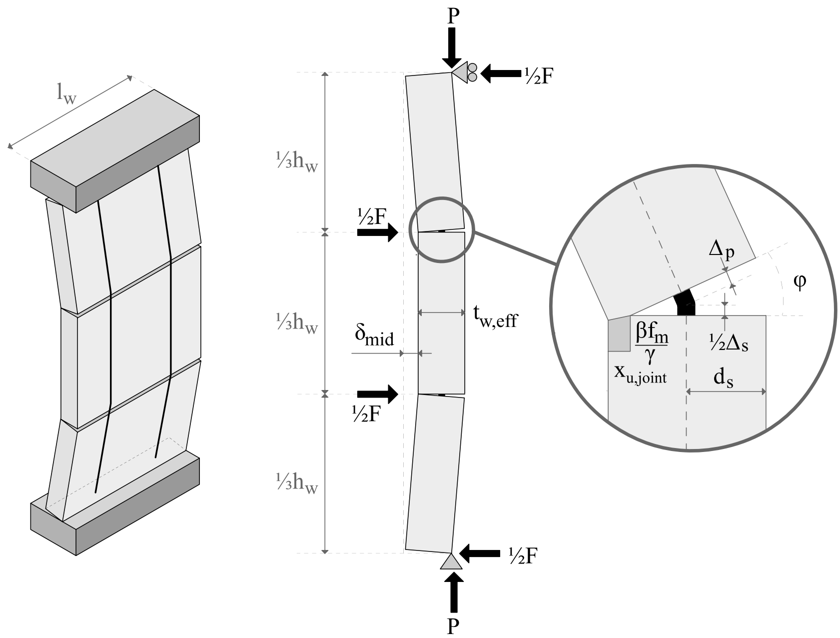

Figure D.1: Simplified engineering model for the out-of-plane behaviour of FDM CFRP retrofitted vertically spanning masonry walls.

Eq. D.1. This relation was obtained using the one-dimensional partial-interaction model and global bond-slip law presented in Chapter 3. It should be noted that the CFRP stress σ_p may not exceed the maximum stress level of 1,600 N/mm^2, which is an acceptable limit when compared to the CFRP stress level limit of 1,300 N/mm^2 as determined with the out-of-plane experimental campaign presented in Chapter 4. The force in a single CFRP strip can be determined using Eq. D.2, where b_p and t_p are the width and thickness of the CFRP strip respectively.

$$\Delta_s = \frac{\sigma_p}{1,600} \times 3.5 \tag{D.1}$$

$$F_s = min(1,600; \sigma_p) \times b_p \times t_p \tag{D.2}$$

The depth of the compression zone $x_{u,joint}$ at the discrete joint can be determined using Eq. D.16, where the actual stress block was replaced by a fictitious rectangular block of intensity β times the masonry compressive strength (f_m). The degradation in masonry is covered by factor $\gamma_m = 1.5$.

$$x_{u,joint} = \frac{n_s \times F_s + P}{\frac{\beta \times f_m}{\gamma_m} \times l_w} \tag{D.3}$$

The number of CFRP strips and the length of the wall is represented by n_s and l_w respectively. The effective axial load P is defined using Eq. D.4, where V and W are the axial load and weight of the wall respectively.

$$P = \frac{1}{2}W + V \tag{D.4}$$

The total elongation of the CFRP strip within the middle rigid block (Δ_p), follows from Eq. D.5, where E_p is the Young's modulus of the CFRP strip.

$$\Delta_p = \frac{\sigma_p}{E_p} \times \frac{1}{3}h_w \tag{D.5}$$

The displacement difference between the CFRP strip and the masonry (Δ_s) and half of the elongation of the CFRP strip in the middle block (Δ_p), results in a rotation in the joint, and is obtained in accordance with Eq. D.6, where here d_s is the effective depth of the CFRP strip and x_u is the ultimate depth of the compression zone.

$$\varphi = \frac{\Delta_s + \frac{1}{2}\Delta_p}{d_s - x_u} \tag{D.6}$$

The displacement of the wall at mid-height δ_{mid} is obtained using

$$\delta_{mid} = \varphi \times \frac{1}{3}h_w \tag{D.7}$$

The internal moment in the discrete joint is determined using Eq. D.8

$$M_{int} = n_s \times F_s \times \left(d_s - \frac{x_u}{2}\right) \tag{D.8}$$

The external moment in the discrete joint follows from Eq. D.9.

$$M_{ext} = \frac{h_w}{3} \times \frac{F}{2} - z_N \times P \tag{D.9}$$

where z_N is the distance between the point of gravity of the compression force in the masonry at the discrete joint and the point of gravity of the compression force at the top of the masonry. z_N is determined using Eq. D.19, where the depth of the compression zone $x_{u,top}$ at the top of the masonry follows from Eq. D.11.

$$z_N = t_{w,eff} - \frac{x_{u,joint}}{2} - \frac{x_{u,top}}{2} - \delta_{mid} \tag{D.10}$$

$$x_{u,top} = \frac{P}{\frac{\beta \times f_m}{\gamma} \times l_w} \tag{D.11}$$

Since the internal and external moment in the discrete joint are in equilibrium, the lateral force F follows from combing Eqs. D.8 and D.9:

$$F = \frac{z_N \times P + M_{int}}{\frac{1}{6} h_w} \tag{D.12}$$

The maximum lateral moment with the two-point loading scheme follows from Eq. D.13, whereas the maximum lateral moment with an equivalent distributed load is determined using Eq. D.14

$$M_{max,lat,two-point} = \frac{1}{2} F \times \frac{1}{3} h_w \tag{D.13}$$

$$M_{max,lat,distributed} = \frac{1}{8} q_{eq} \times h_w^2 \tag{D.14}$$

Combining Eqs. Eq. D.13 and D.14, the distributed load equivalent for force F is obtained:

$$q_{eq} = \frac{4}{3} \frac{F}{h_w}. \tag{D.15}$$

The normalized lateral moment over the normalized height is presented in Fig. D.2 for both the two-line load and the equivalent distributed load configuration. The two-line load results in a reasonable approximation of the equivalent distributed load.

Using the presented calculation steps the lateral moment - displacement relation of the simplified engineering model was determined and compared with the experiments in Fig. D.3, for axial loads V = 4.8 and 20 kN. The simplified engineering model showed acceptable agreement with the experimental findings for both axial load conditions.

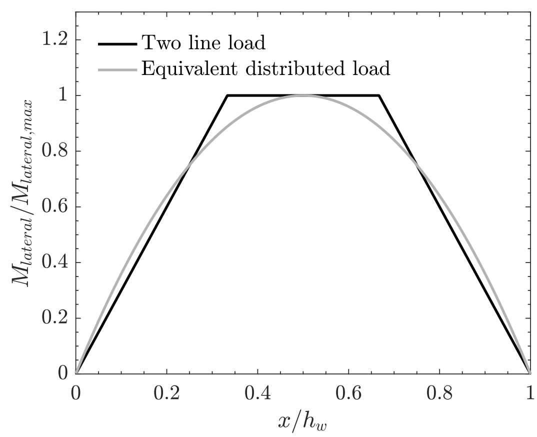

Figure D.2: The normalized lateral moment over the normalized height for both the two-line load and the equivalent distributed load configuration.

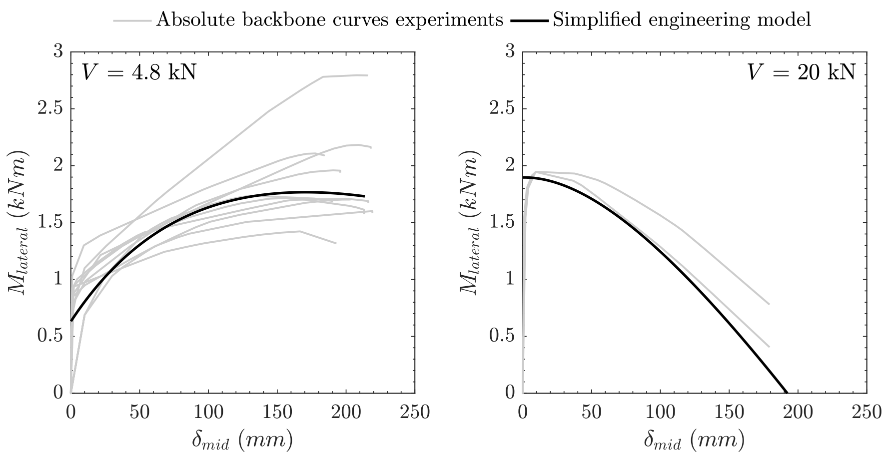

Figure D.3: Comparison outcome simplified engineering model with the absolute backbone curves from the experimental campaign in 4.

D.2 Flexible deep mounted CFRP strips and single-sided FRCM overlay: FRCM in compression

When considering flexible deep mounted CFRP strips and single-sided FRCM overlay, and the FRCM overlay is compression due to the lateral loadign direction, the model is similar to the three rigid blocks and two discrete joints model presented in the previous section. The simplified engineering model for this retrofit combination is shown in Fig. D.4.

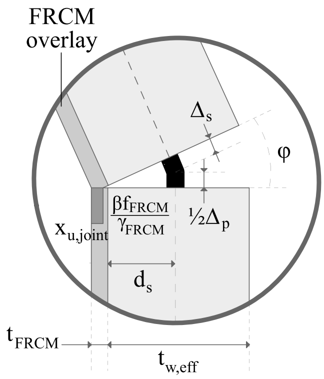

Figure D.4: Detail of the simplified engineering model for the out-of-plane behaviour of the combined FDM CFRP and one-sided FRCM overlay sretrofitted vertically spanning masonry walls, when the lateral loading direction is such that the FRCM layer is in compression.

The depth of the compression zone $x_{u,joint}$ at the discrete joint was modified Eq. D.16, where the actual stress block was replaced by a fictitious rectangular block of intensity β times the FRCM compressive strength $\left(f_m\right)$. The correction in the FRCM overlay is covered by factor γ_{FRCM}.

$$x_{u,joint} = \frac{n_s \times F_s + P}{\frac{\beta \times f_{FRCM}}{\gamma_{FRCM}} \times l_w} \tag{D.16}$$

The number of CFRP strips and the length of the wall is represented by n_s and l_w respectively. P is the effective axial load determined with Eq. D.4. It should be noted that the additional mass of the FRCM layer (36 kg/m² for a 15 mm thick FRCM layer) needs to be taken into account when determining the weight W of the wall.

The rotation in the joint is modified to Eq. D.17, where here d_s is the effective depth of the CFRP strip and x_u is the ultimate depth of the compression zone.

$$\varphi = \frac{\Delta_s + \frac{1}{2}\Delta_p}{d_s - x_u + t_{FRCM}} \tag{D.17}$$

The internal moment in the disrete joint is determined using Eq. D.18

$$M_{int} = n_s \times F_s \times \left(d_s - \frac{x_u}{2} + t_{FRCM}\right) \tag{D.18}$$

where z_N is the distance between the point of gravity of the compression force in the masonry at the discrete joint and the point of gravity of the compression force at the top of the masonry. z_N is determined using Eq. D.19, where the depth of the compression zone $x_{u,top}$ at the top of the masonry follows from Eq. D.11.

$$z_N = t_{w,eff} + t_{FRCM} - \frac{x_{u,joint}}{2} - \frac{x_{u,top}}{2} - \delta_{mid} \tag{D.19}$$

Using the presented calculation steps the lateral moment - displacement relation of the simplified engineering model was determined and compared with the experiments in Fig. D.5, for the loading case where the FRCM overlay is in compression. The simplified engineering model showed acceptable agreement with the experimental findings. Increasing the FRCM degradation factor from 1 to 4 results in a slightly improved fit, but does not have a significant influence on the outcome.

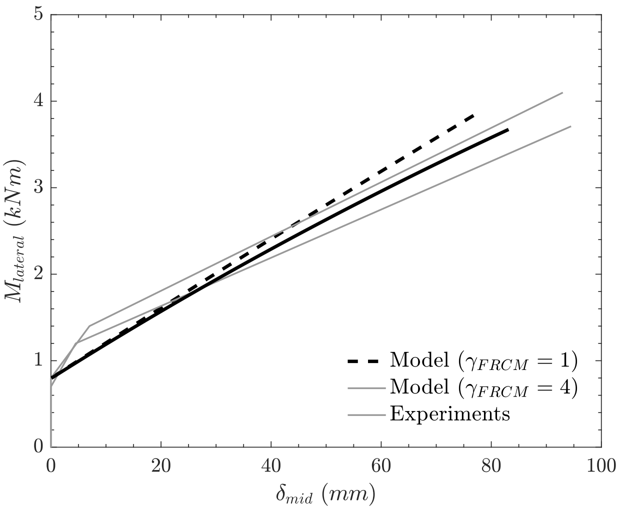

Figure D.5: Comparison outcome simplified engineering model with the absolute backbone curves from the experimental campaign in 5 for the loading case where the FRCM overlay is in compression.

D.3 FRCM overlay in tension

In the out-of-plane calculations for walls with the deep-mounted CFRP strips and FRCM overlay combination, no capacity is assigned to the deep mounted CFRP strips when the FRCM layer is under tension. In reality these CFRP strips would take over post FRCM failure. However, as the out-of-plane failure of the FRCM layer also reduces the in-plane capacity, the out-of-plane failure of the FRCM layers is considered determinant for the design out-of-plane failure for the considered wall. The simplified engineering model for this retrofit combination is shown in Fig. D.6.

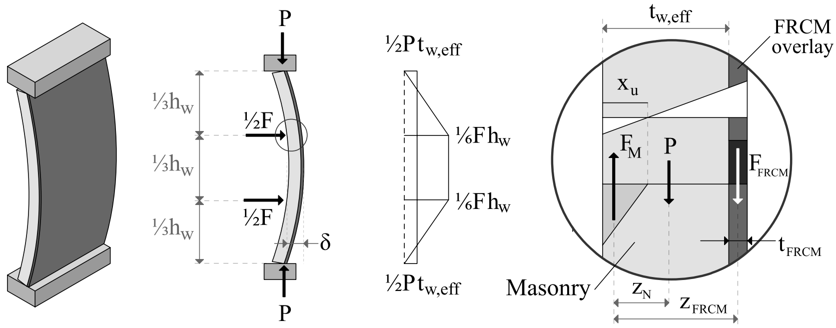

Figure D.6: Simplified engineering model for the out-of-plane behaviour of the combined FDM CFRP and one-sided FRCM overlay sretrofitted vertically spanning masonry walls, when the lateral loading direction is such that the FRCM layer is in compression. The influence of the FDM CFRP is neglected.

The stress-strain curves for the cementitious matrix and the embedded CFRP mesh were determined using Eqs. D.20 and D.21 respectively, where E_{CM}, and $E_{mesh,em}$ are the Young's moduli cementitious matrix and the embedded CFRP mesh respectively.

$$\sigma_{CM} = \begin{cases} 0 & \varepsilon < 0, \\ \varepsilon \cdot E_{CM} & 0 < \varepsilon \leq \varepsilon_{CM}, \\ \varphi(\varepsilon) \cdot E_{CM} & \varepsilon_{CM} < \varepsilon \leq \varepsilon_{FRCM,u}, \\ 0 & \varepsilon > \varepsilon_{FRCM,u}, \end{cases} \tag{D.20}$$

$$\sigma_{mesh} = \begin{cases} 0 & \varepsilon < 0, \\ \varepsilon \cdot E_{FRCM,u} & 0 < \varepsilon \leq \varepsilon_{FRCM,u}, \\ 0 & \varepsilon > \varepsilon_{FRCM,u}, \end{cases} \tag{D.21}$$

The tensile forces in the embedded CFRP mesh and the cementitious matrix were determined in accordance with Eqs. D.22 and D.23 respectively.

$$F_{CM} = \sigma_{CM} \times l_w \times t_{FRCM} \tag{D.22}$$

$$F_{mesh} = \sigma_{mesh} \times A_{mesh} \tag{D.23}$$

The total force F_{FRCM} in the FRCM overlay follows from D.24:

$$F_{FRCM} = F_{CM} + F_{mesh} \tag{D.24}$$

The depth of the compression zone in the masonry was approximated with D.25, where P is the effective axial load P as defined using Eq. D.4, and f_m is the compressive strength of the masonry. It should be noted that the additional mass of the FRCM layer (36 kg/m² for a 15 mm thick FRCM layer) needs to be taken into account when determining the weight W of the wall.

$$x_u = 2\frac{F_{FRCM} + P}{l_w \times f_m} \tag{D.25}$$

The sum of the internal moment was obtained using Eq. D.26, where z_N is the distance between the centre of the cross section and the point of gravity of the compression force in the masonry, determined using Eq. D.27. The distance between the centre of the cross section of the FRCM layer and the point of gravity of the compression force in the masonry, z_{FRCM}, is obtained with Eq. D.28.

$$M_{int} = F_{FRCM} \times z_{FRCM} + F_M \times z_N \tag{D.26}$$

$$z_N = \begin{cases} \left(\frac{t_w}{2} - \frac{x_u}{3}\right)\frac{\varepsilon_{FRCM}}{7E-4} & \varepsilon_{FRCM} < 7E-4, \\ \frac{t_w}{2} - \frac{x_u}{3} & \varepsilon_{FRCM} \geq 7E-4 \end{cases} \tag{D.27}$$

$$z_{FRCM} = \begin{cases} \left(t_w - \frac{x_u}{3} + \frac{t_{FRCM}}{2}\right)\frac{\varepsilon_{FRCM}}{7E-4} & \varepsilon_{FRCM} < 7E-4, \\ t_w - \frac{x_u}{3} + \frac{t_{FRCM}}{2} & \varepsilon_{FRCM} \geq 7E-4 \end{cases} \tag{D.28}$$

It is obvious that when the displacement δ is equal to 0, the point of gravity of the compression force in the masonry is in the centre of the cross section, so z_N equals 0. In the model it is assumed that both z_N and z_{FRCM} increases linear from 0 to $\frac{t_w}{2} - \frac{x_u}{3}$ and $t_w - \frac{x_u}{3} + \frac{t_{FRCM}}{2}$ respectively when ε_{FRCM} increases from 0 to 0.0007 mm/mm. After this both z_N and z_{FRCM} remain constant.

The moment at the top and foot of the wall is determined using Eq. D.29. Based on the ultimate moment resistance, the maximum horizontal load on the specimen follows from Eq. D.30. The distributed load equivalent for force F is obtained with Eq. D.15, where the curvature follows from Eq. D.31

$$M_{top} = V \times \frac{t_w}{2} \tag{D.29}$$

$$F = \frac{6}{h_w}\left(M_{int} + M_{top}\right) \tag{D.30}$$

$$\kappa_R = \frac{\varepsilon_{FRCM}}{t_w - x_u + \frac{t_{FRCM}}{2}} \tag{D.31}$$

For a simply supported beam with two point loads at at a distance of $\frac{1}{3}h_w$ from the supports, the mid-span deflection is provided by $\delta = \frac{23}{216}\frac{Mh_w^2}{EI}$. With the curvature being $\kappa_R = \frac{M}{EI}$, the mid-span deflection becomes $\delta = \frac{23}{216}\kappa_R h_w^2$. Based on the distribution of the moment over the height (as shown in Fig. D.6) the mid-height displacement can be estimated with Eq. D.32

$$\delta_{mid} = \frac{23}{216}\kappa_R h_w^2 \left(\frac{M_{int}}{M_{int} + M_{top}}\right) \tag{D.32}$$

Using the presented calculation steps the lateral moment - displacement relation of the simplified engineering model was determined and compared with the experiments in Fig. D.7, for the loading case where the FRCM overlay is in tension. The simplified engineering model showed acceptable agreement with the experimental findings.

D.4 Unreinforced masonry

The tri-linear $F-\delta$ curve illustrated in Figure D.8 is constructed from the rigid bi-linear curve defined by F_0 and δ_0. This bi-linear idealisation relies on the assumption of wall responding as an assembly of two rigid bodies with an infinite initial stiffness and strength, representing an upper bound of the real OOP static resistance of a one-way vertical spanning strip wall. Equations D.33 and D.34 define F_0 and δ_0 respectively, where ζ describes the position of the middle crack along the height of the wall. For clamped-clamped walls the middle crack does not necessarily form at the wall midheight but at $(1-\zeta)h_w$ from the base support, with ζ given by Eq. D.35.

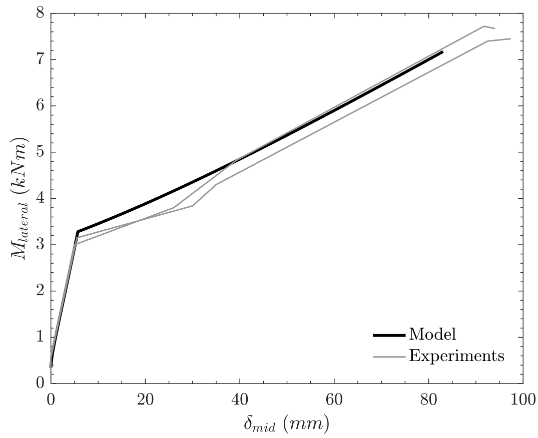

Figure D.7: Comparison outcome simplified engineering model with the absolute backbone curves from the experimental campaign in 5 for the loading case where the FRCM overlay is in tension.

.

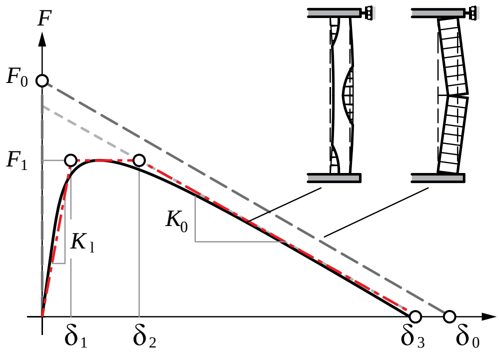

Figure D.8: Derivation of the trilinear model (dotted-dashed line) from the bilinear model (dashed line) and the pushover curve (solid line) [147].

$$F_0 = 2\frac{\zeta W + V}{\zeta(1-\zeta)}\frac{t_w}{h_w} \tag{D.33}$$

$$\delta_0 = \frac{1}{2}\frac{t_w}{1-\zeta} \tag{D.34}$$

$$\zeta = \frac{\sqrt{(W+V)V} - V}{W} \tag{D.35}$$

The key parameters of the tri-linear relationship are $\delta_1 = a_1\delta_0$ controlling the wall's initial cracked stiffness, $F_1 = b_1 F_0$ identifying a force plateau and $\delta_2 = a_2\delta_0$. The tri-linear idealisations proposed in literature beyond δ_2 (second corner displacement of the trilinear curve), generally located along the bi-linear curve ($\delta_2 = \delta_0 - F_1/K_0 = a_2\delta_0$), in some cases, drop to zero matching the bi-linear idealisation ($\delta_3 = \delta_0$); in some other cases, taking into account the masonry compressive strength and the physical dimension of the hinges [148], the third branch presents a backward translation (with negative stiffness equal to K_0) of the last tri-linear branch ($\delta_3 = a_3\delta_0$). This latter case, leads to a reduction of the δ_2 value ($\delta_2 = \delta_3 - F_1/K_0$). K_0 ($= F_0/\delta_{ins}$) represents the negative stiffness of the system.

The values for a_1, a_3 and b_1 are strongly affected by aspects such as wall thickness, acting vertical overburden force and masonry mechanical properties [148]. Doherty [149] identified three stages of degradation: new, moderate and severe damage corresponding to b_1 values of 0.72, 0.60 and 0.50 and a_1 values of 0.06, 0.13 and 0.20 respectively. Other researchers later suggested a_1 values of 0.04 [150] and 0.05 [151] based on both experimental results of air-bag quasi static tests and successful numerical modelling of the dynamic behaviour of one-way vertical spanning strip wall systems. Derakhshan et al. [150] showed that an a_2 value of 0.25 represents an upper bound level for this parameter. A refined work on the characterisation of the F-u relationship can be found in [148]. The contents of this paragraph were taken from [116].

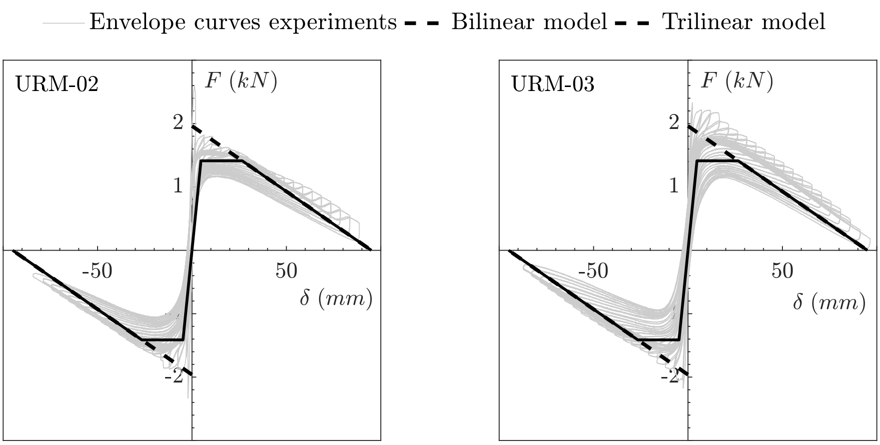

Figure D.9: Comparison of the determined bilinear (dashed black line) and trilinear (solid black line) $F-u$ relations with the cyclic envelopes (grey lines) of specimens URM-02 and URM-03.

With a_1 selected at 0.05, $\delta_3 = \delta_0$, $b_1 = 0.72$, and $\zeta = 0.5$, the tri-linear $F-\delta$ curve of the unreinforced masonry walls from Chapter 4 was estimated. Both the obtained bilinear (dashed black line) and trilinear model (solid black line) outcomes were compared with the cyclic envelopes (grey lines) of specimens URM-02 and URM-03, as shown in Fig. D.9.

From the comparison in Fig. D.9 it was observed that the trilinear $F-\delta$ relation was within acceptable agreement between the experiments. The initial stiffness following from the model was (F_1/δ_1) 0.3 kN/mm, whereas the experimentally determined value started at approximately 0.8 kN/mm and reduced to around 0.15 kN/mm throughout the course of the experiments. The initial stiffness following from the trilinear model was also acceptable for the (hybrid) retrofitted specimens. The initial stiffness (F_1/δ_1) following from the URM model was used as an estimate of the initial stiffness for the simplified engineering model, as the initial stiffness parameter was not determined for these models.

Appendix E

FDM CFRP strip spacing

The horizontal spacing s of the FDM CFRP reinforcement must be selected such that the strengthened URM wall does not fail in horizontal bending between the strips due to the inertial load caused by the demand acceleration $a_{g;d}$ [122]. Unreinforced masonry walls subjected to out-of-plane horizontal bending can fail by two alternate modes: stepped failure along the brick-mortar bond, or line failure cutting directly through the bricks [152].

Over a single masonry course, the ultimate moment capacity with respect to stepped failure is obtained using Eq. E.1, where τ_u is the ultimate shear bond stress of a bed joint, following from Eq. E.2.

$$M_{h,u,stepped} = \tau_u \cdot k_b \cdot t_u^3 \tag{E.1}$$

$$\tau_u = 1.6 f_{mt} + 0.9 f_d \tag{E.2}$$

In the equations above, f_{mt} is the flexural tensile strength of masonry (=0.85 N/mm² for post 1945 masonry according to NPR9998 [92]), t_u is the thickness of a brick unit, and k_b is a dimensionless coefficient relating the maximum shear stress in a rectangular section to the applied torsion and is equal to 0.208 for square overlap [152]. It should be noted that the presented analytical expressions are applicable specifically to single-leaf stretcher bond masonry [152].

The moment capacity with respect to line failure is is calculated using Eq. E.3, where h_u is the height of a brick unit, f_{ut} is the flexural tensile strength of the brick unit, υ is the Poisson's ratio of the brick units (typically taken as 0.2), and f_d is the vertical stress in the wall at its mid-height.

$$M_{h,u,stepped} = \frac{1}{2}\left[(f_{ut} - \upsilon \cdot f_d) \cdot h_u \frac{t_u^2}{6}\right] \tag{E.3}$$

The moment capacity of the mixed failure mode over a single course $M_{h,u,mixed}$ is taken as the lesser of equations E.1 and E.3 [152], that is:

$$M_{h,u,mixed} = min(M_{h,u,line}, M_{h,u,stepped}) \tag{E.4}$$

Once the horizontal bending capacity of the URM wall ($M_{h,u,mixed}$) is determined, the upper limit for the strip spacing follows from Eq. E.5 [122], where γ_{wall} is the specific mass density of the masonry wall per m² surface area.

$$s < \sqrt{\frac{8M_{h,u,mixed}}{a_{g;d} \cdot \gamma_{wall} \cdot g}} \tag{E.5}$$

The limit FDM CFRP strip spacing s as a function of demand acceleration $a_{g;d}$, is provided in Fig. E.1 for both γ_{wall} = 180 kg/m² (single leaf-masonry wall) and γ_{wall} = 360 kg/m² (cavity wall with a present and connected outer leaf) single-leaf stretcher bond masonry walls. The maximum strip spacing was set as 1.5 m.

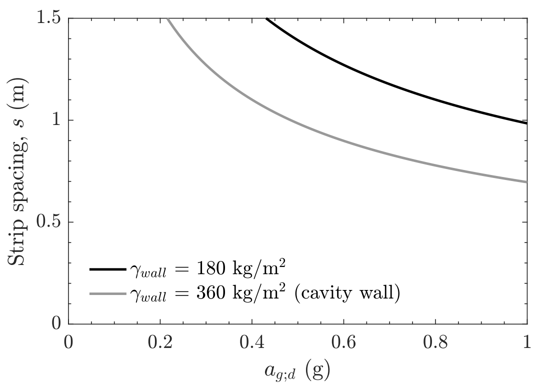

Figure E.1: Limit FDM CFRP strip spacing s (to prevent horizontal bending failure between the strips) as a function of demand acceleration $a_{g;d}$.

Using Fig. E.1, the strip spacing must be selected before conducting either a non-linear pushover (NLPO) analysis or a non-linear time history (NLTH) analysis.

Appendix F

Modelling the dynamic one-way OOP response of strengthened masonry walls

In order to study the dynamic behaviour of a reinforced masonry wall for out-of-plane loading, the simplest oscillating model to be considered is the singular degree of freedom (SDOF) system. Under the hypothesis of no sliding, no bouncing effect and assuming both top and bottom supports moving simultaneously, the generic SDOF equation of motion of vertically spanning masonry wall subjected to out-of-plane loading is given by Eq. F.1, where m_{eq} is the equivalent mass of the wall, $c(t)$ is the damping coefficient and $f_{bi}(u,t)$ is the bi-linear rigid restoring force relationship assuming a uniformly distributed lateral face load.

$$m_{eq}\ddot{u}(t) + c(t)\dot{u}(t) + f_{bi}(u,t) = -m_{eq}\ddot{u}_g(t) \tag{F.1}$$

When a beam with a constant mass is schemed as a beam with a concentrated mass, the equivalent mass m_{eq} equals half the total mass of the beam. The damping coefficient $c(t)$ was determined using the constant damping ratio (CDR) damping model. This damping model acts on the instantaneous secant frequency $\omega(t)$ defined by the instantaneous secant stiffness $K_{sec}(t)$ of the system (Eq. F.2), where the secant frequency $\omega(t)$ follows from Eq. F.3.

$$c(t) = 2 \cdot m_{eff} \cdot \omega(t) \cdot \zeta_{sys} \tag{F.2}$$

$$\omega(t) = \sqrt{\frac{K_{sec}(t)}{m_{eff}}} \tag{F.3}$$

Following the Dutch Practice NPR 9998 for earthquake resistant design [92], the effective equivalent viscous damping ζ_{sys} for a system follows from F.4. It should be noted that the radiation damping was not included.

$$\zeta_{sys} = \zeta_0 + \zeta_{hys} \tag{F.4}$$

The inherent damping ζ_0 was estimated at 0.05, whereas the hysteretic damping ζ_{hyst} was obtained from Fig. 4.25. The mean value for hysteretic damping for the specimens retrofitted with FDM CFRP (axial load V = 4.8 kN), was determined at 0.036. It should be noted that ζ_{hyst} = 0.036 is a conservative assumption for higher axial loads, as illustrated in Fig. 4.25. The effective equivalent viscous damping ζ_{sys} was set at 0.086.

A self-centering model with limited hysteretic energy dissipation capacity (flag-shaped model, Fig. F.1), was used as hysteretic model to compute the non-linear spring response $f_{bi}(u,t)$. In Fig. F.1, K is the initial stiffness of the system (F_y/u_y), u_y is the yield displacement, F_y is the yield strength and α the post-yield stiffness ratio, defined by the ratio of the post-yield stiffness to the initial stiffness K. The post-yield stiffness ratio is determined using Eq. F.5, and is dependent on the target history $u_{his}(t)$, which is the maximum reached displacement level until time t, as shown in Eq. F.6

$$\alpha(u(t), u_{his}(t)) = \begin{cases} 1 & u(t) < u_y, \\ \frac{f_{bi}(u_{his}(t)) - F_e}{K(u_{his}(t) - u_e)} & u_y \leq u(t) < u_{his}(t), \\ \frac{f_{bi}(u(t)) - F_e}{K(u(t) - u_e)} & u(t) \geq u_{his}(t) \end{cases} \tag{F.5}$$

$$u_{his}(t) = \begin{cases} u_{his}(t-1) & u_{his}(t-1) \geq u(t), \\ u(t) & u_{his}(t-1) < u(t) \end{cases} \tag{F.6}$$

An example of the non-linear spring response is provided with the blue path with arrows in Fig. F.1. The spring is assumed to have a displacement history until time $t = t_1$, marked with an orange circle in Fig. F.1. Starting from $u(t_1) = 0$ the spring builds up a force of F_y until a displacement of u_y, with stiffness K. If the positive displacement is further increased, the force increases with a stiffness of αK (following from Eq. F.5) until a displacement level of $u(t_2)$. Further increasing the positive displacement from this point on reduces the stiffness once again (following from Eq. F.5) since the new displacement levels exceed the target history u_{his} (orange circle in

Fig. F.1). Additionally, a new value is continuously assigned to the target history following Eq. F.6 between displacements $u(t_2)$ and $u(t_3)$, ending at $u_{his}(t) = u(t_3)$. The non-linear spring follows the shape of the bounding envelope between $u(t_2)$ and $u(t_3)$. When the non-linear spring moves in the opposite direction ($u(t_3)$), the stiffness follows again from Eq. F.5 with the updated target history ($u_{his}(t) = u(t_3)$). This slope continues until the displacement reaches the level u_y, where the value for the post-yield stiffness ratio α reduced to 1 following Eq. F.5.

The yield displacement of the hysteretic curve (u_y) was determined as 50% of the yield displacement of the bounding envelope ($u_{y,be}$) when FDM CFRP strips are considered in the calculation. When the FRCM layer is in tension (influence of the FDM CFRP strips neglected) the yield displacement of the hysteretic curve u_y was to 0. Both yield displacements of the hysteretic curve were roughly estimated using the cyclic envelopes presented in Chapters 4 and 5.

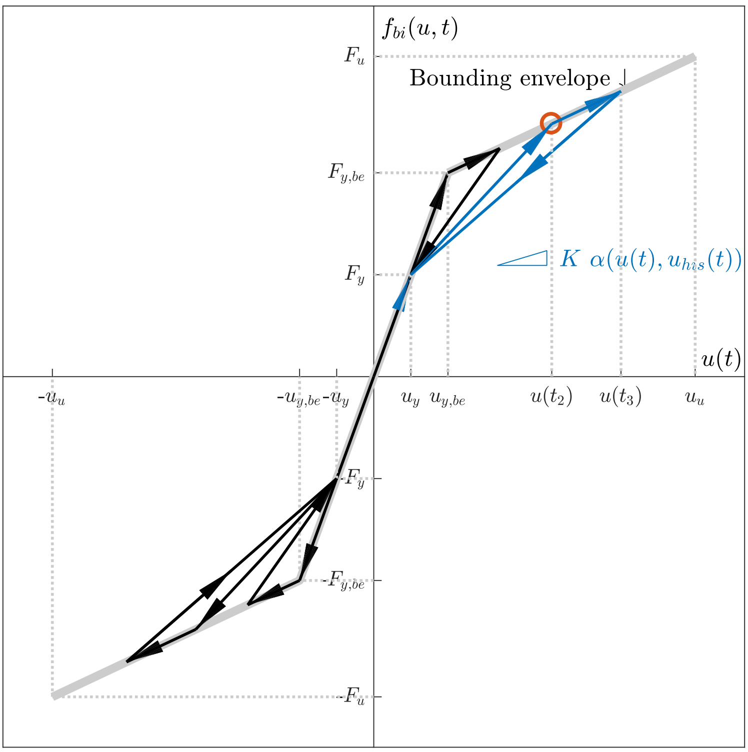

Figure F.1: Flag shaped hysteretic model for retrofitted walls, with the bounding envelope (solid grey line) loading - unloading paths (black lines) and a highlighted example of the loading and unloading path until $u(t_3)$ (blue lines) with a displacement history (orange circle).

For URM walls with a ductile response, the hysteretic damping ζ_{hyst} was taken as 0.05 as a conservative assumption for out-of-plane loaded walls [92]. The effective equivalent viscous damping ζ_{sys} for URM was set at 0.1. The hysteretic curve for URM was determined as the tri-linear force-displacement behaviour as was presented in Appendix D.4. The hysteretic model for URM did not include a displacement history, resulting in the same loading and unloading paths for a given displacement.

F.1 Reference walls

A total of ten different walls with varying retrofit configurations (illustrated in Fig. F.2) were analysed. The walls considered had a height h_w, length l_w, thickness t_w and effective thickness of $t_{w,eff}$ of 2,750 mm, 2,300 mm, 100 mm and 95 mm respectively. The masonry compression strength and Young's modulus were assumed at 10 N/mm^2 and 6,000 N/mm^2 respectively (post 1945 clay brick masonry as mentioned in in the Dutch Practice NPR 9998 for earthquake resistant design [92]). The mass density of a single leaf of masonry was 180 kg/m^2, which was also applicable to the outer leaf of the cavity wall if present and connected. Table F.1 provides overview of the relevant parameters of the analysed walls.

In order to account for the strip spacing limit as presented in Appendix E, two scenario's were considered regarding the number of FDM CFRP strips. For the first scenario, three n_s CFRP strips were positioned at the center-depth of the wall with a distance of 1,000 mm between the CFRP strips. As for the second scenario, five n_s CFRP strips were positioned at the center-depth of the wall with a distance of 500 mm between the CFRP strips.

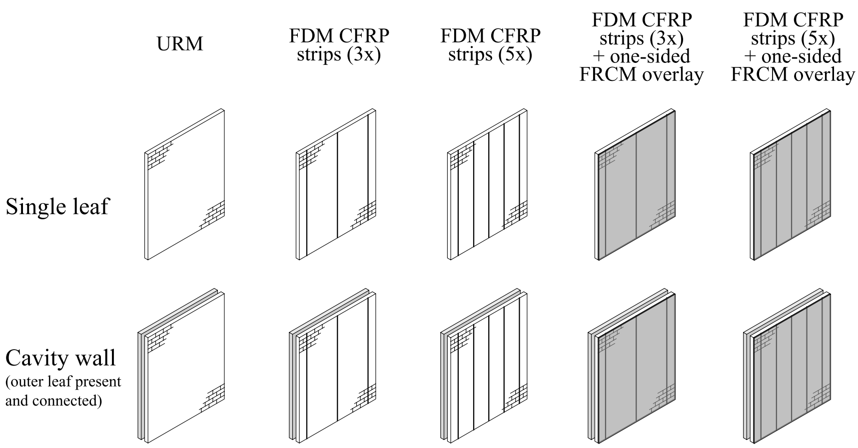

Figure F.2: Reference walls.

Table F.1: Properties of the reference walls

Parameter	Symbol	Value	Unit
Length of the wall	l_w	2,750	mm
Height of the wall	h_w	2,300	mm
Effective thickness of the wall	$t_{w,eff}$	95	mm
Mass density of the wall	ρ_m	180	kg/m²
Mass density of the outer leaf of the cavity wall (if presented and connected)	ρ_{leaf}	180	kg/m²
Compressive strength masonry	f_m	10	N/mm²
Young's Modulus masonry	E_m	6,000	N/mm²
Degradation factor of masonry	γ_m	1.5	–
Number of CFRP strips (scenario A)	n_s	3	–
Number of CFRP strips (scenario B)	n_s	5	–
Thickness FRCM layer (if applicable)	t_{FRCM}	15	mm
Mass density of the FRCM overlay	ρ_{FRCM}	36	kg/m²
Cross sectional area CFRP mesh (if applicable)	A_{mesh}	101.2	mm²

F.2 Bounding envelopes

The bounding envelopes for the different retrofitting combinations and axial loads were determined using the simplified engineering models presented in Appendix D. For simple implementation in the hysteretic model, the bounding envelope was bilinearized using the yield point ($u_{y,be}$,$F_{y,be}$) of the bounding envelope and the ultimate displacement u_u and corresponding force F_u, as shown in Fig. F.3.

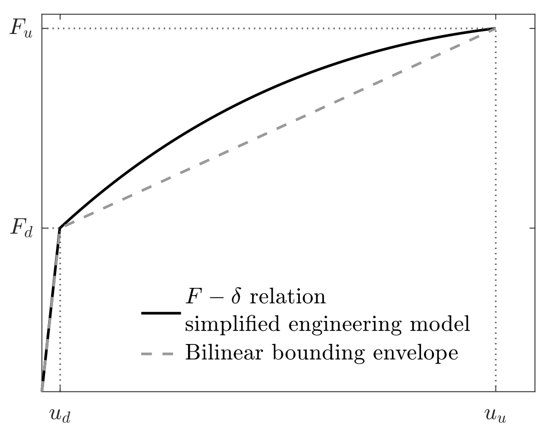

Figure F.3: Bilinear bounding envelope for retrofitted walls.

The bounding envelopes were determined for axial stress levels σ_V of 0.05, 0.10, 0.15 and 0.20 N/mm^2, for URM (Fig. F.4), the FDM CFRP strip retrofitted (Fig. F.5) and the FDM CFRP strip and single-sided FRCM overlay combined retrofitted (Fig. F.6) walls. The relaxation path starting from the ultimate displacement u_u is provided with dashed black lines in Figures F.5 and F.6. For the analysis involving the single-sided FRCM overlay (Fig. F.6), the positive and negative displacements correspond to the loading direction where the FRCM layer is in tension and in compression respectively.

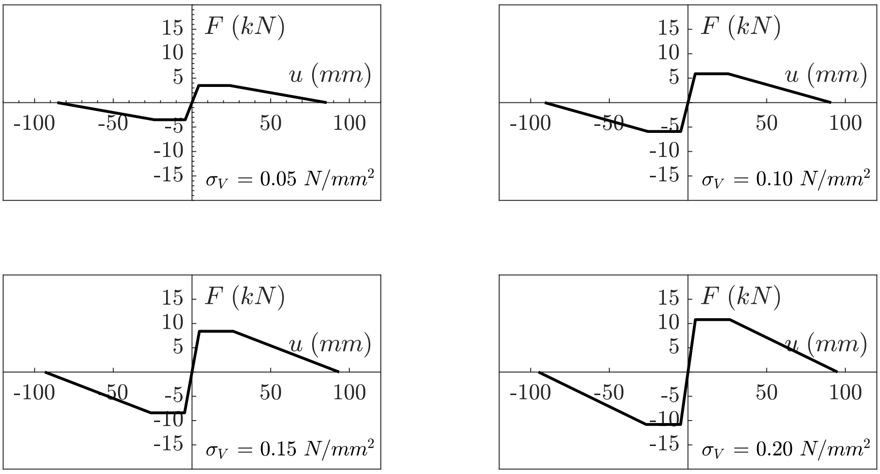

Figure F.4: Bounding envelopes for a URM wall conform Table F.1, for different axial stress levels σ_V.

An overview of the relevant parameters of the hysteretic models of the reference walls for different axial stress levels are given in Tables F.2, F.3 and F.4 for URM, FDM CFRP strip retrofit and FDM CFRP strip with one-sided FRCM overlay hybrid retrofit respectively.

Table F.2: Parameters for the hysteretic model of URM conform Table F.1, for four different axial stress levels σ_V.

σ_V (N/mm²)	F_1 (kN)	K_1 (kN/mm)	u_1 (mm)	u_2 (mm)	u_u (mm)
0.05	3.5	0.8	4.3	24.0	85.6
0.10	5.9	1.3	4.6	25.5	91.0
0.15	8.4	1.8	4.7	26.2	93.5
0.20	10.8	2.3	4.7	26.6	94.9

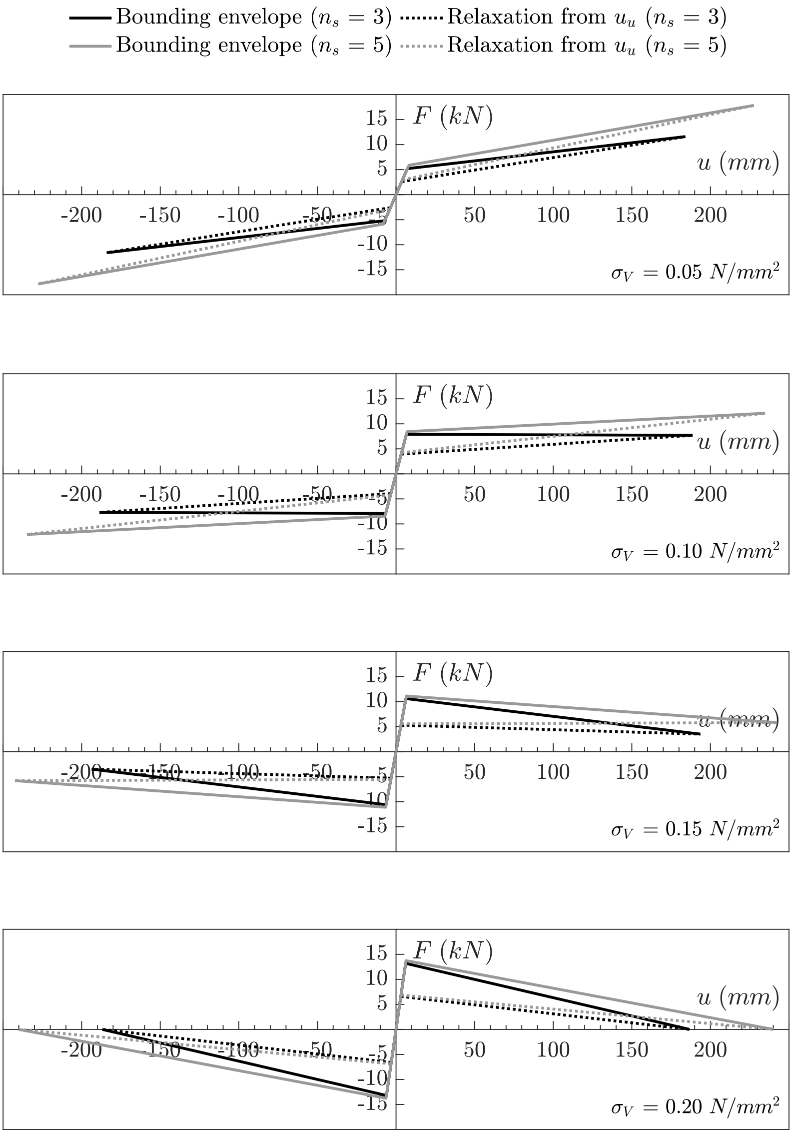

Figure F.5: Bounding envelopes for a masonry wall retrofitted with FDM CFRP strips conform Table F.1, for different axial stress levels σ_V and number of FDM CFRP strips (n_s=3 , black; n_s=5, grey). The relaxation path starting from the ultimate displacement u_u is provided with dashed lines.

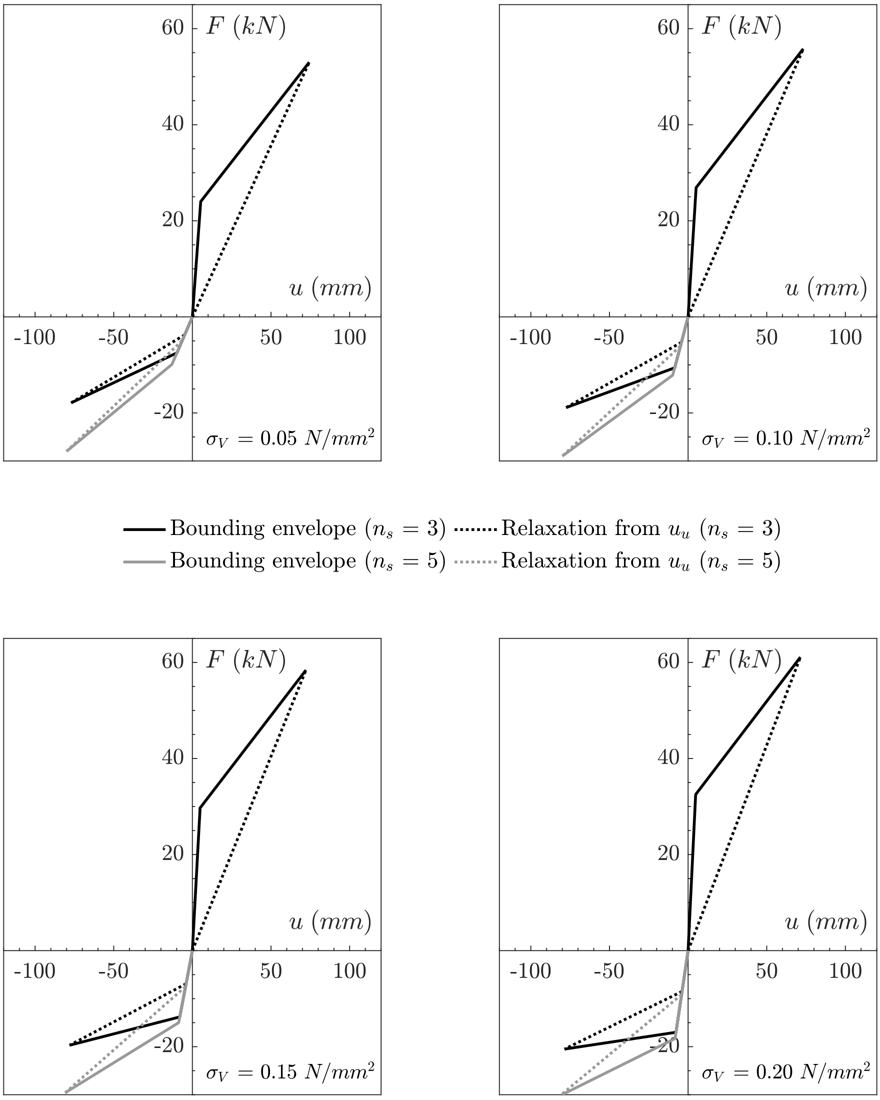

Figure F.6: Bounding envelopes for a masonry wall retrofitted with FDM CFRP strips and single-sided FRCM overlay conform Table F.1, for different axial stress levels σ_V and number of FDM CFRP strips (n_s=3 , black; n_s=5, grey). The relaxation path starting from the ultimate displacement u_u is provided with dashed black lines. The positive and negative displacements correspond to the loading direction where the single-sided FRCM layer is in tension and in compression respectively.

Table F.3: Parameters for the hysteretic model of three ($n_s = 3$) FDM CFRP strips (and optional one-sided FRCM overlay) retrofitted wall conform Table F.1, for four different axial stress levels σ_V.

Retrofit	σ_V (N/mm²)	F_y (kN)	u_y (mm)	K (kN/mm)	$F_{y,be}$ (kN)	$u_{y,be}$ (mm)	F_u (kN)	u_u (mm)
FDM CFRP	0.05	2.6	3.6	0.7	5.2	7.2	11.6	184.1
	0.10	4.0	3.3	1.2	7.9	6.6	7.7	188.7
	0.15	5.3	3.1	1.7	10.6	6.3	3.5	193.6
	0.20	6.6	3.1	2.2	13.2	6.1	0.0	186.8
FDM CFRP	0.05	3.7	4.9	0.8	7.5	9.8	17.9	77.1
FRCM	0.10	5.3	4.2	1.2	10.6	8.5	18.8	77.6
compression	0.15	6.9	4.0	1.7	13.8	8.0	19.7	78.1
	0.20	8.5	3.9	2.2	17.0	7.7	20.5	78.6
FRCM	0.05	0.0	0.0	4.5	24.0	5.3	53.0	74.3
tension	0.10	0.0	0.0	5.3	26.9	5.1	55.8	73.2
	0.15	0.0	0.0	6.1	29.7	4.9	58.4	72.2
	0.20	0.0	0.0	6.8	32.5	4.8	61.1	71.4

Table F.4: Parameters for the hysteretic model of five ($n_s = 5$) FDM CFRP strips (and optional one-sided FRCM overlay) retrofitted wall conform Table F.1, for four different axial stress levels σ_V.

Retrofit	σ_V (N/mm²)	F_y (kN)	u_y (mm)	K (kN/mm)	$F_{y,be}$ (kN)	$u_{y,be}$ (mm)	F_u (kN)	u_u (mm)
FDM CFRP	0.05	2.9	4.1	0.7	5.9	8.2	17.8	227.7
	0.10	4.2	3.5	1.2	8.4	7.0	12.11	234.8
	0.15	5.6	3.3	1.7	11.1	6.6	5.8	242.4
	0.20	6.9	3.2	2.2	13.7	6.4	0.0	240
FDM CFRP	0.05	5.0	6.5	0.8	9.9	13.0	28.2	79.8
FRCM	0.10	6.1	4.9	1.2	12.1	9.8	28.9	80.4
compression	0.15	7.5	4.4	1.7	15.1	8.7	29.6	80.9
	0.20	9.2	4.1	2.2	18.3	8.3	30.2	81.4

F.3 Numerical method

An analytical solution of the equation of motion for a single-degree of freedom system is usually not possible if the ground acceleration $\ddot{g}(t)$ varies arbitrarily with time or if the system is nonlinear. Such problems can be tackled by numerical time-stepping methods for integration of differential equations. The differential equation presented in F.1 was solved using the Newmark 'linear acceleration method'.

References

[1] M. Kortekaas and B. Jaarsma, "Improved definition of faults in the Groningen field using seismic attributes," *Netherlands Journal of Geosciences*, vol. 96, no. 5, pp. s71–s85, 2017. (Cited on page 1.)

[2] K. Van Thienen-Visser and J. N. Breunese, "Induced seismicity of the Groningen gas field: History and recent developments," *Leading Edge*, vol. 34, no. 6, pp. 664–671, 2015. (Cited on page 1.)

[3] KNMI, "Aardbevingscatalogus: Geïnduceerde bevingen." Retrieved April 4, 2020, from http://cdn.knmi.nl/knmi/map/page/seismologie/all_induced.pdf. (Cited on page 2.)

[4] R. Esposito, F. Messali, G. J. P. Ravenshorst, H. R. Schipper, and J. G. Rots, "Seismic assessment of a lab-tested two-storey unreinforced masonry Dutch terraced house," *Bulletin of Earthquake Engineering*, vol. 17, no. 8, pp. 4601–4623, 2019. (Cited on page 2.)

[5] CEN, *Eurocode 8: Design of structures for earthquake resistance-part 1: General rules, seismic actions and rules for buildings*. Brussels: European Committee for Standardization, 2005. (Cited on pages 2, 10, and 210.)

[6] M. Sintubin, "The Groningen case: When science becomes part of the problem, not the solution," *Seismological Research Letters*, vol. 89, no. 6, pp. 2001–2007, 2018. (Cited on page 2.)

[7] Government of The Netherlands, "Natural gas production reduced and funds earmarked for Groningen." Retrieved from https://www.government.nl/latest/news/2014/01/17/natural-gas-production-reduced-and-funds-earmarked-for-groningen, 2014. (Cited on page 2.)

[8] Government of The Netherlands, "Dutch Cabinet: termination of natural gas extraction in Groningen." Retrieved from https://www.government.nl/latest/news/2018/03/29/dutch-cabinet-termination-of-natural-gas-extraction-in-groningen, 2018. (Cited on page 2.)

[9] M. C. Griffith, J. Kashyap, and M. S. Mohamed Ali, "Flexural displacement response of NSM FRP retrofitted masonry walls," *Construction and Building Materials*, vol. 49, pp. 1032–1040, 2013. (Cited on page 3.)

[10] J. Ingham and M. Griffith, "Performance of unreinforced masonry buildings during the 2010 Darfield (Christchurch, NZ) earthquake," *Australian Journal of Structural Engineering*, vol. 11, pp. 207–224, 9 2011. (Cited on page 3.)

[11] D. Dizhur, J. Ingham, L. Moon, M. Griffith, A. Schultz, I. Senaldi, G. Magenes, J. Dickie, S. Lissel, J. Centeno, C. Ventura, J. Leite, and P. Lourenco, "Performance of masonry buildings and churches in the 22 February 2011 Christchurch earthquake," *Journal of the Structural Engineering Society of New Zealand*, vol. 24, pp. 47–57, 12 2011. (Cited on page 3.)

[12] S. Bhattacharya, S. Nayak, and S. C. Dutta, "A critical review of retrofitting methods for unreinforced masonry structures," *International Journal of Disaster Risk Reduction*, vol. 7, pp. 51–67, 2014. (Cited on page 3.)

[13] D. Dizhur, M. C. Griffith, and J. M. Ingham, "Pullout strength of NSM CFRP strips bonded to vintage clay brick masonry," *Engineering Structures*, vol. 69, pp. 25–36, 2014. (Cited on pages 3, 4, 5, 6, 37, 45, 74, 75, 76, 79, 80, 257, and 258.)

[14] D. Dizhur, M. Giaretton, I. Giongo, and J. Ingham, "Seismic retrofit of masonry walls using timber strong-backs," vol. 30, pp. 30–44, 1 2017. (Cited on page 4.)

[15] M. Miglietta, N. Damiani, L. Grottoli, G. Guerrini, and F. Graziotti, "Shake-table investigation of a timber retrofit solution for unreinforced masonry cavity-wall buildings," 9 2019. (Cited on page 4.)

[16] U. Ianniruberto and Z. Rinakdi, "Influence of FRP reinforcement on the local ductility of RC elements," *FRP Composites in Civil Engineering. Proceedings of the International Conference on FRP composites in Civil EngineeringHong Kong Institution of Engineers, Hong Kong Institution of Steel Construction*, no. Volume 1, 2001. (Cited on page 4.)

[17] C. G. Papanicolaou, T. C. Triantafillou, M. Papathanasiou, and K. Karlos, “Textile reinforced mortar (TRM) versus FRP as strengthening material of URM walls: Out-of-plane cyclic loading,” *Materials and Structures/Materiaux et Constructions*, vol. 41, no. 1, pp. 143–157, 2008. (Cited on pages 4 and 8.)

[18] R. B. Petersen, “In-plane shear behaviour of unreinforced masonry panels strengthened with fibre reinforced polymer strips,” 2009. (Cited on pages 4, 197, 208, and 215.)

[19] S. Banijamali, M. Esfahani, S. Nosratollahi, M. Sohrabi, and S. Mousavi, “Reviewing the FRP Strengthening Systems,” *American Journal of Civil Engineering*, vol. 3, p. 38, 1 2015. (Cited on page 4.)

[20] R. Seracino, N. M. Jones, M. S. Ali, M. W. Page, and D. J. Oehlers, “Bond strength of near-surface mounted FRP strip-to-concrete joints,” *Journal of Composites for Construction*, vol. 11, no. 4, pp. 401–409, 2007. (Cited on page 4.)

[21] R. B. Petersen, M. J. Masia, and R. Seracino, “Bond behavior of near-surface mounted FRP strips bonded to modern clay brick masonry prisms: Influence of strip orientation and compression perpendicular to the strip,” 2009. (Cited on pages 4, 6, 74, 75, 76, 257, and 258.)

[22] O. S. Türkmen, A. T. Vermeltfoort, and D. R. Martens, “Seismic retrofit system for single leaf masonry buildings in Groningen,” *Brick and Block Masonry: Trends, Innovations and Challenges - Proceedings of the 16th International Brick and Block Masonry Conference, IBMAC 2016*, 2016. (Cited on pages 5 and 38.)

[23] I. A. Sharaky, L. Torres, M. Baena, and C. Miàs, “An experimental study of different factors affecting the bond of NSM FRP bars in concrete,” *Composite Structures*, vol. 99, pp. 350–365, 2013. (Cited on page 5.)

[24] A. Rizzo and L. De Lorenzis, “Behavior and capacity of RC beams strengthened in shear with NSM FRP reinforcement,” *Construction and Building Materials*, vol. 23, no. 4, pp. 1555–1567, 2009. (Cited on page 5.)

[25] W. Derkowski, A. Kwiecień, and B. Zajac, “CFRP strengthening of bent RC beams using stiff and flexible adhesives,” *Technical Transactions Civil Engineering*, vol. 1, pp. 37–52, 2013. (Cited on page 5.)

[26] J. G. Dai, T. Ueda, Y. Sato, and T. Ito, “Flexural strengthening of RC beams using externally bonded FRP sheets through flexible adhesive bonding,” *International symposium on bond behavior of FRP in structures (BBFS 2005), Hong Kong*, pp. 7–9, 2005. (Cited on page 5.)

[27] A. Kwiecień, "Stiff and flexible adhesives bonding CFRP to masonry substrates-Investigated in pull-off test and Single-Lap test," *Archives of Civil and Mechanical Engineering*, vol. 12, no. 2, pp. 228–239, 2012. (Cited on page 6.)

[28] S. Xia and D. Oehlers, "Debonding Mechanisms in FRP Plated Unreinforced Masonry under Out-Of-Plane Loading," *Advances in Structural Engineering*, vol. 9, no. 5, pp. 619–637, 2006. (Cited on pages 6, 257, and 258.)

[29] U. S. Camli and B. Binici, "Strength of carbon fiber reinforced polymers bonded to concrete and masonry," *Construction and Building Materials*, vol. 21, no. 7, pp. 1431–1446, 2007. (Cited on pages 6, 257, and 258.)

[30] R. Capozucca, "Behaviour of CFRP sheets bonded to historical masonry," in *Proceedings, Asia-Pacific Conference on FRP in Structures*, pp. 723–728, 2007. (Cited on pages 6, 257, and 258.)

[31] M. Panizza, E. Garbin, M. Valluzzi, and C. Modena, "Bond behaviour of CFRP and GFRP laminates on brick masonry," pp. 763–770, 2008. (Cited on pages 6, 257, and 258.)

[32] K. M. C. Konthesingha, M. J. Masia, R. B. Petersen, and A. W. Page, "Bond behaviour of NSM FRP strips to modern clay brick masonry prisms under cyclic loading," in *Proceedings of the 11th Canadian Masonry Symposium, Toronto, Canada*, vol. 31, 2009. (Cited on pages 6, 74, 75, 76, 257, and 258.)

[33] C. R. Willis, Q. Yang, R. Seracino, and M. C. Griffith, "Bond behaviour of FRP-to-clay brick masonry joints," *Engineering Structures*, vol. 31, no. 11, pp. 2580–2587, 2009. (Cited on pages 6, 74, 75, 76, 257, and 258.)

[34] S. Briccoli Bati and M. Fagone, "An analysis of CFRP-brick bonded joints," in *XVIII Convegno Italiano di Meccanica Computazionale. Siracusa, Italy*, pp. 1–4, 2010. (Cited on pages 6, 257, and 258.)

[35] R. Capozucca, "Experimental FRP/SRP–historic masonry delamination," *Composite Structures*, vol. 92, no. 4, pp. 891–903, 2010. (Cited on pages 6, 257, and 258.)

[36] E. Grande, M. Imbimbo, and E. Sacco, "Bond behaviour of CFRP laminates glued on clay bricks: Experimental and numerical study," *Composites Part B: Engineering*, vol. 42, no. 2, pp. 330–340, 2011. (Cited on pages 6, 257, and 258.)

[37] D. Oliveira, I. Basilio, and P. Lourenco, "Experimental Bond Behavior of FRP Sheets Glued on Brick Masonry," *Journal of Composites for Construction - J COMPOS CONSTR*, vol. 15, 2010. (Cited on pages 6, 257, and 258.)

[38] C. Carloni and K. Subramaniam, "FRP-Masonry Debonding: Numerical and Experimental Study of the Role of Mortar Joints," *Journal of Composites for Construction*, vol. 16, pp. 581–589, 2012. (Cited on pages 6, 257, and 258.)

[39] C. Faella, G. Camorani, E. Martinelli, F. Perri, and S. Paciello, "Bond behaviour of FRP strips glued on masonry: Experimental investigation and empirical formulation," *Construction and Building Materials*, vol. 31, p. 353–363, 2012. (Cited on pages 6, 257, and 258.)

[40] J. Kashyap, C. R. Willis, M. C. Griffith, J. M. Ingham, and M. J. Masia, "Debonding resistance of FRP-to-clay brick masonry joints," *Engineering Structures*, vol. 41, pp. 186–198, 2012. (Cited on pages 6, 37, 74, 75, 76, 257, and 258.)

[41] M. R. Valluzzi, D. V. Oliveira, A. Caratelli, G. Castori, M. Corradi, G. de Felice, E. Garbin, D. Garcia, L. Garmendia, E. Grande, U. Ianniruberto, A. Kwiecień, M. Leone, G. P. Lignola, P. B. Lourenço, M. Malena, F. Micelli, M. Panizza, C. G. Papanicolaou, A. Prota, E. Sacco, T. C. Triantafillou, A. Viskovic, B. Zając, and G. Zuccarino, "Round Robin Test for composite-to-brick shear bond characterization," *Materials and Structures*, vol. 45, no. 12, pp. 1761–1791, 2012. (Cited on pages 6, 257, and 258.)

[42] P. Carrara, D. Ferretti, and F. Freddi, "Debonding behavior of ancient masonry elements strengthened with CFRP sheets," *Composites Part B: Engineering*, vol. 45, no. 1, pp. 800–810, 2013. (Cited on pages 6, 257, and 258.)

[43] C. Caggegi, V. Pensée, M. Fagone, M. Cuomo, and L. Chevalier, "Experimental global analysis of the efficiency of carbon fiber anchors applied over CFRP strengthened bricks, Construction and Building Materials," *Construction and Building Materials*, vol. 53, p. 203–212, 2014. (Cited on pages 6, 257, and 258.)

[44] M. Fagone, G. Ranocchiai, C. Caggegi, S. B. Bati], and M. Cuomo, "The efficiency of mechanical anchors in CFRP strengthening of masonry: An experimental analysis," *Composites Part B: Engineering*, vol. 64, pp. 1–15, 2014. (Cited on pages 6, 257, and 258.)

[45] A. Kwiecień, "Shear bond of composites-to-brick applied with highly deformable, in relation to resin epoxy, interface materials," *Materials and Structures*, vol. 47, 2014. (Cited on pages 6, 257, and 258.)

[46] H. Maljaee, B. Ghiassi, P. Lourenco, and D. Oliveira, “BOND PERFORMANCE IN NSM-STRENGTHENED MASONRY BRICK,” vol. 32, no. 8, pp. 2432–2439, 2014. (Cited on pages 6, 257, and 258.)

[47] T. Rotunno, L. Rovero, U. Tonietti, and S. Briccoli Bati, “Experimental Study of Bond Behavior of CFRP-to-Brick Joints,” *Journal of Composites for Construction*, vol. 19, p. 4014063, 2014. (Cited on pages 6, 257, and 258.)

[48] G. Barbieri, L. Biolzi, M. Bocciarelli, and S. Cattaneo, “Pull out of FRP reinforcement from masonry pillars: Experimental and numerical results,” *Composites Part B: Engineering*, vol. 69, pp. 516–525, 2015. (Cited on pages 6, 257, and 258.)

[49] F. G. Carozzi, P. Colombi, and C. Poggi, “Calibration of end-debonding strength model for FRP-reinforced masonry,” *Composite Structures*, vol. 120, pp. 366–377, 2015. (Cited on pages 6, 257, and 258.)

[50] A. Hosseini, D. Mostofinejad, and M. Emami, “Influence of bonding technique on bond behavior of CFRP-to-clay brick masonry joints: Experimental study using particle image velocimetry (PIV),” *International Journal of Adhesion and Adhesives*, vol. 59, pp. 27–39, 2015. (Cited on pages 6, 257, and 258.)

[51] G. Felice, M. Aiello, A. Bellini, F. Ceroni, S. De Santis, E. Garbin, M. Leone, G. P. Lignola, M. Malena, C. Mazzotti, M. Panizza, and M. Valluzzi, “Experimental characterization of composite-to-brick masonry shear bond,” *Materials and Structures*, 2015. (Cited on pages 6, 257, and 258.)

[52] Anıl, C. Durucan, and S. W. Din, “Experimental study on the stress distribution at the interface between CFRP and three different types of masonry units,” *Composites Part B: Engineering*, vol. 92, pp. 63–73, 2016. (Cited on pages 6, 257, and 258.)

[53] A. Kwiecień, G. de Felice, D. V. Oliveira, B. Zając, A. Bellini, S. De Santis, B. Ghiassi, G. P. Lignola, P. B. Lourenço, C. Mazzotti, and A. Prota, “Repair of composite-to-masonry bond using flexible matrix,” *Materials and Structures*, vol. 49, no. 7, pp. 2563–2580, 2016. (Cited on pages 6, 257, and 258.)

[54] J. Vaculik, P. Visintin, and N. G. Burton, “Global database of FRP-to-masonry bond strength tests,” *Data in Brief*, vol. 20, pp. 2065–2071, 2018. (Cited on pages 6, 56, 73, 74, 76, 257, and 258.)

[55] O. S. Türkmen, S. N. M. Wijte, A. T. Vermeltfoort, and D. R. W. Martens, “Experiments to determine the out-of-plane behavior of CFRP and ductile adhesive reinforced clay brick masonry walls,”

in *Proceedings of the 13th Canadian Masonry Symposium*, (Halifax), pp. 1–11, 2017. (Cited on page 6.)

[56] K. M. C. Konthesingha, M. J. Masia, R. B. Petersen, N. Mojsilovic, G. Simundic, and A. W. Page, "Static cyclic in-plane shear response of damaged masonry walls retrofitted with NSM FRP strips – An experimental evaluation," *Engineering Structures*, vol. 50, pp. 126–136, 2013. (Cited on pages 8 and 167.)

[57] C. Papanicolaou, T. Triantafillou, K. Karlos, and M. Papathanasiou, "Textile-reinforced mortar (TRM) versus FRP as strengthening material of URM walls: In-plane cyclic loading," *Materials and Structures/-Materiaux et Constructions*, vol. 40, pp. 1081–1097, 1 2007. (Cited on pages 8 and 167.)

[58] G. Mantegazza, A. Gatti, and A. Barbieri, "Retrofitting concrete and masonry building: FRCM (fiber reinforced cementitious matrix) a new emerging technology," *XII Konferencja Naukowo-Techniczna Problemy Remontowe W Budownictwie Ogólnym i Obiektach Zabytkowych REMO*, pp. 6–8, 2006. (Cited on page 8.)

[59] C. Faella, E. Martinelli, E. Nigro, and S. Paciello, "Shear capacity of masonry walls externally strengthened by a cement-based composite material: An experimental campaign," *Construction and Building Materials*, vol. 24, no. 1, pp. 84–93, 2010. (Cited on pages 8, 167, and 168.)

[60] M. Maalej, V. W. Lin, M. P. Nguyen, and S. T. Quek, "Engineered cementitious composites for effective strengthening of unreinforced masonry walls," *Engineering Structures*, vol. 32, no. 8, pp. 2432–2439, 2010. (Cited on pages 8 and 167.)

[61] N. Ismail, "Selected strengthening techniques for the seismic retrofit of unreinforced masonry buildings," 2012. (Cited on pages 8, 167, 168, and 219.)

[62] S. Babaeidarabad, F. De Caso, and A. Nanni, "URM walls strengthened with fabric-reinforced cementitious matrix composite subjected to diagonal compression," *Journal of Composites for Construction*, vol. 18, no. 2, 2014. (Cited on pages 8, 167, 168, and 197.)

[63] F. Parisi, I. Iovinella, A. Balsamo, N. Augenti, and A. Prota, "In-plane behaviour of tuff masonry strengthened with inorganic matrix-grid composites," *Composites Part B: Engineering*, vol. 45, no. 1, pp. 1657–1666, 2013. (Cited on pages 8 and 167.)

[64] N. Ismail and J. M. Ingham, "In-plane and out-of-plane testing of unreinforced masonry walls strengthened using polymer textile reinforced mortar," *Engineering Structures*, vol. 118, pp. 167–177, 2016. (Cited on pages 8, 167, and 168.)

[65] A. Bilotta, F. Ceroni, E. Nigro, and M. Pecce, "Experimental tests on FRCM strengthening systems for tuff masonry elements," *Construction and Building Materials*, vol. 138, pp. 114–133, 2017. (Cited on page 8.)

[66] G. Marcari, M. Basili, and F. Vestroni, "Experimental investigation of tuff masonry panels reinforced with surface bonded basalt textile-reinforced mortar," *Composites Part B: Engineering*, vol. 108, pp. 131–142, 2017. (Cited on pages 8, 167, and 168.)

[67] M. Shabdin, M. Zargaran, and N. K. Attari, "Experimental diagonal tension (shear) test of Un-Reinforced Masonry (URM) walls strengthened with textile reinforced mortar (TRM)," *Construction and Building Materials*, vol. 1264, pp. 704–715, 2018. (Cited on pages 8, 167, and 168.)

[68] A. Nanni, "A New Tool for Concrete and Masonry Repair," *Concrete International*, vol. 34, no. 4, pp. 1–7, 2012. (Cited on page 8.)

[69] J. Vaculik, P. Visintin, N. G. Burton, M. C. Griffith, and R. Seracino, "State-of-the-art review and future research directions for FRP-to-masonry bond research: Test methods and techniques for extraction of bond-slip behaviour," *Construction and Building Materials*, vol. 183, pp. 325–345, 2018. (Cited on pages 8, 35, 38, and 73.)

[70] G. de Felice, M. A. Aiello, C. Caggegi, F. Ceroni, S. De Santis, E. Garbin, N. Gattesco, Hojdys, P. Krajewski, A. Kwiecień, M. Leone, G. P. Lignola, C. Mazzotti, D. Oliveira, C. Papanicolaou, C. Poggi, T. Triantafillou, M. R. Valluzzi, and A. Viskovic, "Recommendation of RILEM Technical Committee 250-CSM: Test method for Textile Reinforced Mortar to substrate bond characterization," *Materials and Structures*, vol. 51, no. 4, p. 95, 2018. (Cited on pages 10 and 24.)

[71] I. C. C. AC434, "Acceptance criteria for masonry and concrete strengthening using fiber-reinforced cementitious matrix (FRCM) composite systems," *ICC-Evaluation Service, Whittier, CA*, 2013. (Cited on pages 10, 27, and 31.)

[72] FEMA, *FEMA 461: Interim Testing Protocols for Determining the Seismic Performance Characteristics of Structural and Nonstructural Components*. Washington: Federal Emergency Management Agency, 2007. (Cited on pages 10 and 174.)

[73] ASTM, *E519/E519M-10: Standard test method for diagonal tension (shear) in masonry assemblages*. West Conshohocken: American Society for Testing and Materials, 2010. (Cited on pages 10, 192, 194, 195, and 205.)

[74] O. S. Türkmen, B. T. de Vries, and S. N. M. Wijte, "Mechanical characterization and out-of-plane behavior of fabric-reinforced cementitious matrix overlay on clay brick masonry," *Civil Engineering Design*, vol. 1, pp. 131–147, 12 2019. (Cited on pages 12, 17, and 137.)

[75] O. S. Türkmen, S. N. M. Wijte, J. M. Ingham, and A. T. Vermeltfoort, "Bond slip behaviour of deep mounted carbon fibre reinforced polymer strops confined with a ductile adhesive in clay brick masonry," *Proceedings of 10th Australasian masonry conference: masonry today and tomorrow, blz*, pp. 672–686, 2018. (Cited on pages 12 and 35.)

[76] O. S. Türkmen, S. N. M. Wijte, J. Vaculik, B. T. De Vries, and J. M. Ingham, "High-speed pullout behavior of deep-mounted CFRP strips bonded with a flexible adhesive to clay brick masonry," *Structures*, vol. 28, pp. 1153–1172, 2020. (Cited on pages 12 and 35.)

[77] O. S. Türkmen, S. N. M. Wijte, B. T. De Vries, and J. M. Ingham, "Out-of-plane behaviour of clay brick masonry walls retrofitted with flexible deep mounted CFRP strips," *Engineering Structures (in press)*. (Cited on pages 12 and 87.)

[78] O. S. Türkmen, B. T. De Vries, S. N. M. Wijte, and J. M. Ingham, "Out-of-plane behaviour of clay brick masonry walls retrofitted with deep and flexible mounted CFRP strips and additional single-sided FRCM overlay," *Structures (Manuscript submitted for publication)*. (Cited on pages 12 and 137.)

[79] O. S. Türkmen, B. T. De Vries, S. N. M. Wijte, and A. T. Vermeltfoort, "Quasi-static cyclic in-plane testing of masonry walls strengthened with a single-sided fabric-reinforced cementitious matrix overlay and flexible anchorage," *Journal of Building Pathology and Rehabilitation*, vol. 4, no. 1, p. 8, 2019. (Cited on pages 12 and 167.)

[80] O. S. Türkmen, B. T. De Vries, S. N. Wijte, and A. T. Vermeltfoort, "In-plane behaviour of clay brick masonry wallettes retrofitted with single-sided fabric-reinforced cementitious matrix and deep mounted carbon fibre strips," *Bulletin of Earthquake Engineering*, vol. 18, pp. 725–765, 2019. (Cited on pages 12 and 167.)

[81] ASTM, *ASTM C67-03a: Standard Test Methods for Sampling and Testing Brick and Structural Clay Tile*. West Conshohocken: American Society for Testing and Materials, 2003. (Cited on pages 17 and 18.)

[82] ASTM, *C1006-07: Standard Test Method for Splitting Tensile Strength of Masonry Units*. West Conshohocken: American Society for Testing and Materials, 2007. (Cited on pages 17 and 18.)

[83] CEN, *EN 772-1:2011+A1:2015: Methods of test for masonry units — Part 1: Determination of compressive strength*. Brussels: European Committee for Standardization. (Cited on pages 17 and 18.)

[84] Eurocode, "1015-11: Methods of test for mortar for masonry–Part 11: Determination of flexural and compressive strength of hardened mortar," 1999. (Cited on pages 17, 18, and 23.)

[85] E. N. HRN, "1052-1, Methods of test for masonry–Part 1: Determination of of compressive strength," *European Committee for Standardization, Bruxelles*, 1998. (Cited on pages 18 and 19.)

[86] B. S. EN, "1052-2." Methods of test for masonry-part 2: determination of flexural strength," *Brussels: CNE*, 1999. (Cited on page 18.)

[87] C. E. d. Normalisation, "EN 1052–3. Methods of Test for Masonry. Part 3: Determination of Initial Shear Strength," 2002. (Cited on pages 18 and 19.)

[88] R. G. Drysdale, A. A. Hamid, and L. R. Baker, *Masonry structures: behavior and design*. 1994. (Cited on page 18.)

[89] A. H. P. Maurenbrecher, *Effect of test procedures on compressive strength of masonry prisms*. National Research Council of Canada, Division of Building Research, 1980. (Cited on page 18.)

[90] J. A. Thamboo and M. Dhanasekar, "Correlation between the performance of solid masonry prisms and wallettes under compression," *Journal of Building Engineering*, vol. 22, pp. 429–438, 2019. (Cited on page 19.)

[91] S. Jafari, J. G. Rots, R. Esposito, and F. Messali, "Characterizing the Material Properties of Dutch Unreinforced Masonry," *Procedia Engineering*, vol. 193, pp. 250–257, 2017. (Cited on pages 20, 119, and 120.)

[92] NEN, *NPR 9998:2017: Beoordeling van de constructieve veiligheid van een gebouw bij nieuwbouw, verbouw en afkeuren – Grondslagen voor aardbevingsbelastingen: geïnduceerde aardbevingen*. Delft: Nederlands Normalisatie Instituut, 2017. (Cited on pages 20, 111, 187, 291, 294, and 296.)

[93] CEN, *EN ISO 527-1:2012: Plastics - Determination of tensile properties - Part 1: General principles*. Brussels: European Committee for Standardization, 2012. (Cited on page 21.)

[94] C. A. Harper, *Handbook of plastics, elastomers, and composites*, vol. 4. McGraw-Hill New York, 2002. (Cited on page 22.)

[95] "Chapter 10 - Durability of Adhesive Bonds," pp. 231–272, Norwich, NY: William Andrew Publishing, 2009. (Cited on page 22.)

[96] H. O. Sugo, A. W. Page, and B. Moghtaderi, "A comparative study of the thermal performance of cavity and brick veneer construction," (Cited on page 23.)

[97] P. Valeri, M. Fernández Ruiz, and A. Muttoni, "Experimental research on Textile Reinforced Concrete for the development of design tools," 8 2018. (Cited on page 23.)

[98] J. Donnini and V. Corinaldesi, "Mechanical characterization of different FRCM systems for structural reinforcement," *Construction and Building Materials*, vol. 145, pp. 565–575, 2017. (Cited on page 27.)

[99] K. Al-lami, T. D'Antino, and A. Colombi, "Durability of Fabric-Reinforced Cementitious Matrix (FRCM) Composites: A Review," *Applied Sciences*, vol. 10, p. 1714, 3 2020. (Cited on page 31.)

[100] D. Arboleda, S. Babaeidarabad, C. DiLaurenzio Hays, and A. Nanni, "Durability of fabric reinforced cementitious matrix (FRCM) composites," in *Proceedings of the 7th international conference on FRP composites in civil engineering* (R. El-Hacha, ed.), 2014. (Cited on page 31.)

[101] K. Benzarti, S. Chataigner, M. Quiertant, C. Marty, and C. Aubagnac, "Accelerated ageing behaviour of the adhesive bond between concrete specimens and CFRP overlays," *Construction and Building Materials*, vol. 25, no. 2, pp. 523–538, 2011. (Cited on page 31.)

[102] N. Williams Portal, M. Flansbjer, P. Johannesson, K. Malaga, and K. Lundgren, "Tensile behaviour of textile reinforcement under accelerated ageing conditions," *Journal of Building Engineering*, vol. 5, pp. 57–66, 2016. (Cited on page 31.)

[103] D. O. Adams and D. F. Adams, "Tabbing guide for composite test specimens Technical report," *Washington, DC: Office of Aviation Research*, 2002. (Cited on pages 41 and 52.)

[104] F. Ceroni, H. Darban, and R. Luciano, "Analysis of bond behavior of injected anchors in masonry elements by means of Finite Element Modeling," *Composite Structures*, vol. 241, p. 112099, 2020. (Cited on page 56.)

[105] J. Vaculik, A. B. Sturm, P. Visintin, and M. C. Griffith, "Modelling FRP-to-substrate joints using the bilinear bond-slip rule with allowance for friction—Full-range analytical solutions for long and short bonded

lengths," *International Journal of Solids and Structures*, vol. 135, pp. 245–260, 2018. (Cited on pages 62, 64, 78, and 79.)

[106] H. Maljaee, B. Ghiassi, and P. B. Lourenço, "Bond behavior in NSM-strengthened masonry," *Engineering Structures*, vol. 166, pp. 302–313, 2018. (Cited on page 74.)

[107] M. Haskett, D. J. Oehlers, and M. S. Mohamed Ali, "Local and global bond characteristics of steel reinforcing bars," *Engineering Structures*, vol. 30, no. 2, pp. 376–383, 2008. (Cited on pages 77 and 78.)

[108] A. A. Costa, A. Arêde, F. Garcia, and C. S. Quintela, "Out-of-Plane Cyclic Experimental Testing of Traditional Stone Masonry Walls with Distributed Loads," 2012. (Cited on page 89.)

[109] M. Griffith and J. Vaculik, "Out-of-Plane Flexural Strength of Unreinforced Clay Brick Masonry Walls," *TMS Journal*, vol. 25, pp. 53–68, 9 2007. (Cited on page 89.)

[110] H. Derakhshan, W. Lucas, P. Visintin, and M. C. Griffith, "Out-of-plane Strength of Existing Two-way Spanning Solid and Cavity Unreinforced Masonry Walls," *Structures*, vol. 13, pp. 88–101, 2018. (Cited on page 89.)

[111] D. Dizhur, R. Lumantarna, H. Derakhshan, and J. Ingham, *In-situ testing of a residential unreinforced masonry building in Wellington, New Zealand*. 7 2010. (Cited on page 89.)

[112] M. C. Griffith, J. Vaculik, N. T. K. Lam, J. Wilson, and E. Lumantarna, "Cyclic testing of unreinforced masonry walls in two-way bending," *Earthquake Engineering & Structural Dynamics*, vol. 36, pp. 801–821, 5 2007. (Cited on page 89.)

[113] J. Vaculik, "Unreinforced masonry walls subjected to out-of-plane seismic actions.," 2012. (Cited on pages 89 and 98.)

[114] M. Damiola, R. Esposito, F. Messali, and J. G. Rots, "Quasi-static cyclic two-way out-of-plane bending tests and analytical models comparison for URM walls," in *Proceedings of the International Masonry Society Conferences*, vol. 0, pp. 1003–1016, 2018. (Cited on page 89.)

[115] F. Messali, R. Esposito, G. J. P. Ravenshorst, and J. G. Rots, "Experimental investigation of the in-plane cyclic behaviour of calcium silicate brick masonry walls," *Bulletin of Earthquake Engineering*, vol. 18, no. 8, pp. 3963–3994, 2020. (Cited on page 93.)

[116] U. Tomassetti, F. Graziotti, A. Penna, and G. Magenes, *ENERGY DISSIPATION INVOLVED IN THE OUT-OF-PLANE RESPONSE OF UNREINFORCED MASONRY WALLS*. 6 2017. (Cited on pages 103 and 288.)

[117] J. Kashyap, "Out-of-Plane Strengthening of Unreinforced Masonry Walls Using Frp," 2014. (Cited on pages 105 and 130.)

[118] D. Dizhur, "Performance of Masonry Buildings in the Canterbury Earthquakes and Corresponding Strengthening Using NSM CFRP Strips," 2013. (Cited on page 105.)

[119] K. H. B., R. D. C., and J. S. K., "Stress-Strain Characteristics of Clay Brick Masonry under Uniaxial Compression," *Journal of Materials in Civil Engineering*, vol. 19, pp. 728–739, 9 2007. (Cited on page 118.)

[120] R. Van der Pluijm, "Out-of-plane bending of masonry: behaviour and strength," 1999. (Cited on page 119.)

[121] A. T. Vermeltfoort and R. van der Pluijm, "Materiaalparameters voor constructief metselwerk," 1999. (Cited on page 119.)

[122] D. Dizhur, M. Griffith, and J. Ingham, "Out-of-plane strengthening of unreinforced masonry walls using near surface mounted fibre reinforced polymer strips," *Engineering Structures*, vol. 59, pp. 330–343, 2014. (Cited on pages 130, 291, and 292.)

[123] G. Mininno, "Modelling of the behaviour of TRM-strengthened masonry walls," 2016. (Cited on page 151.)

[124] P. Meriggi, G. de Felice, and S. De Santis, "Design of the out-of-plane strengthening of masonry walls with fabric reinforced cementitious matrix composites," *Construction and Building Materials*, vol. 240, p. 117946, 2020. (Cited on pages 158, 159, 160, and 259.)

[125] N. Augenti, F. Parisi, A. Prota, and G. Manfredi, "In-plane lateral response of a full-scale masonry subassemblage with and without an inorganic matrix-grid strengthening system," *Journal of Composites for Construction*, 2011. (Cited on page 167.)

[126] A. Prota, G. Marcari, G. Fabbrocino, G. Manfredi, and C. Aldea, "Experimental in-plane behavior of tuff masonry strengthened with cementitious matrix-grid composites," *Journal of Composites for Construction*, vol. 10, no. 3, pp. 223–233, 2006. (Cited on pages 167 and 201.)

[127] S. L. Sagar, V. Singhal, D. C. Rai, and P. Gudur, "Diagonal shear and out-of-plane flexural strength of fabric-reinforced cementitious matrix-strengthened masonry walletes," *Journal of Composites for Construction*, vol. 21, no. 4, 2017. (Cited on page 167.)

[128] G. Magenes and G. M. Calvi, "In-plane seismic response of brick masonry walls," *Earthquake Engineering and Structural Dynamics*, vol. 26, no. 11, pp. 1091–1112, 1997. (Cited on page 181.)

[129] CEN, *Eurocode 6: Design of masonry structures — Part 1-1: General rules for reinforced and unreinforced masonry structures*. Brussels: European Committee for Standardization, 2006. (Cited on pages 184, 185, 187, 209, 210, 213, 218, and 250.)

[130] T. Li, N. Galati, J. G. Tumialan, and A. Nanni, "Analysis of unreinforced masonry concrete walls strengthened with glass fiber-reinforced polymer bars," *ACI Structural Journal*, vol. 102, no. 4, pp. 569–577, 2005. (Cited on pages 197, 206, 207, 208, 215, and 219.)

[131] P. F. Silva, P. Yu, and A. Nanni, "Monte Carlo simulation of shear capacity of URM walls retrofitted by polyurea reinforced GFRP grids," *Journal of Composites for Construction*, vol. 12, no. 4, pp. 405–415, 2008. (Cited on pages 197, 208, 209, and 215.)

[132] S. Babaeidarabad, D. Arboleda, G. Loreto, and A. Nanni, "Shear strengthening of un-reinforced concrete masonry walls with fabric-reinforced-cementitious-matrix," *Construction and Building Materials*, vol. 65, pp. 243–253, 2014. (Cited on pages 197, 206, 208, 214, and 215.)

[133] E. Grande, M. Imbimbo, and E. Sacco, "Numerical investigation on the bond behavior of FRCM strengthening systems," *Composites Part B: Engineering*, vol. 145, pp. 240–251, 2018. (Cited on page 201.)

[134] F. Parisi, C. Menna, and A. Prota, "Fabric-Reinforced Cementitious Matrix (FRCM) composites: Mechanical behavior and application to masonry walls," in *Failure Analysis in Biocomposites, Fibre-Reinforced Composites and Hybrid Composites*, pp. 199–227, Woodhead Publishing, 2019. (Cited on page 201.)

[135] CEN, *Eurocode 8: design of structures for earthquake resistance —Part 3: Assessment and retrofitting of buildings*. Brussels: European Committee for Standardization, 2005. (Cited on pages 206, 209, 210, 211, 212, 213, 216, 219, 220, and 251.)

[136] F. Crisafulli, A. Carr, and R. Park, "Shear strength of unreinforced masonry panels," in *Proceedings of Pacific Coference on Earthquake Engineering*, pp. 77–86, 1995. (Cited on page 208.)

[137] W. Mann and H. Muller, "Failure of Shear-Stressed Masonry — An Enlarged Theory, Tests and Application to Shear Walls," in *Proc. Br. Ceram. Soc.*, pp. 223–235, 1982. (Cited on page 208.)

[138] F. Ceroni and P. Salzano, "Design provisions for FRCM systems bonded to concrete and masonry elements," *Composites Part B: Engineering*, 2018. (Cited on page 214.)

[139] N. Gattesco and I. Boem, "Experimental and analytical study to evaluate the effectiveness of an in-plane reinforcement for masonry walls using GFRP meshes," *Construction and Building Materials*, vol. 88, pp. 94–104, 2015. (Cited on page 214.)

[140] A. Cascardi, F. Micelli, and M. A. Aiello, "Analytical model based on artificial neural network for masonry shear walls strengthened with FRM systems," *Composites Part B: Engineering*, vol. 95, pp. 252–263, 2016. (Cited on page 214.)

[141] T. Triantafillou, "16 - Strengthening of existing masonry structures: Design models," pp. 375–388, Woodhead Publishing, 2016. (Cited on pages 214, 215, 216, 220, and 251.)

[142] ACI Committee 549, *Guide to Design and Construction of Externally Bonded Fabric-Reinforced Cementitous Matrix (FRCM) Systems for Repair and Strengthening Concrete Structures*. 2013. (Cited on pages 214, 215, 216, 220, and 251.)

[143] J. A. Almeida, E. B. Pereira, and J. A. Barros, "Assessment of overlay masonry strengthening system under in-plane monotonic and cyclic loading using the diagonal tensile test," *Construction and Building Materials*, vol. 94, pp. 851–865, 2015. (Cited on page 214.)

[144] T. Triantafillou, C. Kolyvas, I. Bal, and A. Bernakos, "Design examples of a textile mortar system for strengthening of historical masonry structures," in *10th International Congress on Advances in Civil Engineering.*, 2012. (Cited on page 214.)

[145] E. Bertolesi, G. Milani, and B. Ghiassi, "Chapter 20 - Advanced finite element modeling of textile-reinforced mortar strengthened masonry," *Woodhead Publishing Series in Civil and Structural Engineering*, pp. 713–743, 2019. (Cited on pages 231 and 263.)

[146] H. D. Hibbit, B. I. Karlsson, and E. P. Sorensen, "ABAQUS user manual, version 6.12," *Simulia, Providence, RI*, 2012. (Cited on page 268.)

[147] G. Michele and B. Katrin, "Trilinear Model for the Out-of-Plane Seismic Assessment of Vertically Spanning Unreinforced Masonry Walls," *Journal of Structural Engineering*, vol. 145, p. 4019159, 12 2019. (Cited on page 287.)

[148] D. Hossein, G. M. C., and I. J. M., "Out-of-Plane Behavior of One-Way Spanning Unreinforced Masonry Walls," *Journal of Engineering Mechanics*, vol. 139, pp. 409–417, 4 2013. (Cited on page 288.)

[149] K. T. Doherty and F.-A.-U. Erlangen-Nürnberg, *An Investigation of the Weak Links in the Seismic Load Path of Unreinforced Masonry Buildings*.

Friedrich-Alexander-Universität Erlangen-Nürnberg, 2000. (Cited on page 288.)

[150] H. Derakhshan, M. C. Griffith, and J. M. Ingham, “Airbag testing of multi-leaf unreinforced masonry walls subjected to one-way bending,” *Engineering Structures*, vol. 57, pp. 512–522, 2013. (Cited on page 288.)

[151] L. Sorrentino, R. Masiani, and M. Griffith, “The vertical spanning strip wall as a coupled rocking rigid body assembly,” *Structural Engineering and Mechanics*, vol. 29, 7 2008. (Cited on page 288.)

[152] V. Jaroslav and G. M. C., “Probabilistic Analysis of Unreinforced Brick Masonry Walls Subjected to Horizontal Bending,” *Journal of Engineering Mechanics*, vol. 143, p. 4017056, 8 2017. (Cited on pages 291 and 292.)

List of publications

Journal publications

TÜRKMEN, Ö. S., DE VRIES, B. T., WIJTE, S. N. M. AND VERMELTFOORT, A. T. Quasi-static cyclic in-plane testing of masonry walls strengthened with a single-sided fabric-reinforced cementitious matrix overlay and flexible anchorage. *Journal of Building Pathology and Rehabilitation* 4, 8 (2019).
https://doi.org/10.1007/s41024-019-0043-y

TÜRKMEN, Ö. S., DE VRIES, B. T. AND WIJTE, S. N. M. Mechanical characterization and out-of-plane behavior of fabric-reinforced cementitious matrix overlay on clay brick masonry. *Civil Engineering Design* 1, 131– 147 (2019).
https://doi.org/10.1002/cend.201900021

TÜRKMEN, Ö. S., DE VRIES, B. T., WIJTE, S. N. M. AND VERMELTFOORT, A. T. In-plane behaviour of clay brick masonry wallettes retrofitted with single-sided fabric-reinforced cementitious matrix and deep mounted carbon fibre strips. *Bulletin of Earthquake Engineering* 18, 725–765 (2020).
https://doi.org/10.1007/s10518-019-00596-2

TÜRKMEN, Ö. S., WIJTE, S. N. M., VACULIK, J., DE VRIES, B. T. AND INGHAM, J.M. High-speed pullout behavior of deep-mounted CFRP strips bonded with a flexible adhesive to clay brick masonry. *Structures* 28, 1153-1172 (2020).
https://doi.org/10.1016/j.istruc.2020.09.026

TÜRKMEN, Ö. S., WIJTE, S. N. M., DE VRIES, B. T. AND INGHAM, J.M. Out-of-plane behavior of clay brick masonry walls retrofitted with flexible deep mounted CFRP strips. *Engineering Structures.* In press.

TÜRKMEN, Ö. S., DE VRIES, B. T., WIJTE, S. N. M. AND INGHAM, J.M. Out-of-plane behavior of clay brick masonry walls retrofitted with deep and flexible mounted CFRP strips and additional single-sided FRCM overlay. *Structures*. Manuscript submitted for publication.

Conference proceedings

Türkmen, Ö. S., Vermeltfoort, A. T. and Martens, D. R. W. Seismic retrofit system for single leaf masonry buildings in Groningen. In *Proceedings of 16th international brick and block masonry conference*, pp. 26-30 (2016).

Türkmen, Ö. S., Wijte, S. N. M., Vermeltfoort, A. T. and Martens, D. R. W. Experiments to determine the out-of-plane behavior of CFRP and ductile adhesive reinforced clay brick masonry wall. In *13th Canadian Masonry Symposium*, pp. 1-11 (2017).

Wijte, S. N. M., Türkmen, Ö. S., Vermeltfoort, A. T. and Martens, D. R. W. Analytical modelling of the out-of-plane behavior of CFRP and ductile adhesive reinforced clay brick masonry walls. In *13th Canadian Masonry Symposium* (2017).

Türkmen, Ö. S., Wijte, S. N. M., Ingham, J.M. and Vermeltfoort, A. T. Bond slip behaviour of deep mounted carbon fibre reinforced polymer strops confined with a ductile adhesive in clay brick masonry. In *Proceedings of 10th Australasian masonry conference: masonry today and tomorrow*, pp. 672-686 (2018).

Türkmen, Ö. S., De Vries, B. T., Wijte, S. N. M. and Vermeltfoort, A.T. Static-cyclic in-plane tests on clay brick masonry retrofitted with a single sided fabric-reinforced cementitious matrix layer, deep mounted CFRP strips and flexible anchor connection. In *10th International Masonry Conference*, pp. 1668-1683 (2018)

Türkmen, Ö. S., De Vries, B. T., Wijte, S. N. M. and Vermeltfoort, A.T. Evaluation of the in-plane shear strength of a combined retrofit system for masonry walls. In *10th International Masonry Conference*, pp. 1953-1962 (2018)

Curriculum Vitae

Ömer Serhat Türkmen

Education

PhD Research *2016 - 2020*
Department of the Built Environment
Eindhoven University of Technology

M.Sc.Ba General Management *2012 - 2013*
Rotterdam School of Management

M.Sc. Sustainable Process & Energy Technologies *2009 - 2012*
Department of Mechanical, Maritime and Materials Engineering
Delft University of Technology

B.Sc. Mechanical Engineering *2006 - 2010*
Department of Mechanical, Maritime and Materials Engineering
Delft University of Technology

Voorbereidend Wetenschappelijk Onderwijs (VWO) *2000 - 2006*
Wolfert van Borselen

Work experience

CTO *2016 - Present*
QuakeShield

Engineer *2012 - Present*
Koninklijke Oosterhof Holman

Bouwstenen is een publicatiereeks
van de Faculteit Bouwkunde,
Technische Universiteit Eindhoven.
Zij presenteert resultaten van
onderzoek en andere activiteiten op
het vakgebied der Bouwkunde,
uitgevoerd in het kader van deze
Faculteit.

Bouwstenen en andere proefschriften van de
TU/e zijn online beschikbaar via:
https://research.tue.nl/

Reeds verschenen in de serie
Bouwstenen

nr 1
Elan: A Computer Model for Building Energy Design: Theory and Validation
Martin H. de Wit
H.H. Driessen
R.M.M. van der Velden

nr 2
Kwaliteit, Keuzevrijheid en Kosten: Evaluatie van Experiment Klarendal, Arnhem
J. Smeets
C. le Nobel
M. Broos
J. Frenken
A. v.d. Sanden

nr 3
Crooswijk: Van 'Bijzonder' naar 'Gewoon'
Vincent Smit
Kees Noort

nr 4
Staal in de Woningbouw
Edwin J.F. Delsing

nr 5
Mathematical Theory of Stressed Skin Action in Profiled Sheeting with Various Edge Conditions
Andre W.A.M.J. van den Bogaard

nr 6
Hoe Berekenbaar en Betrouwbaar is de Coëfficiënt k in x-ksigma en x-ks?
K.B. Lub
A.J. Bosch

nr 7
Het Typologisch Gereedschap: Een Verkennende Studie Omtrent Typologie en Omtrent de Aanpak van Typologisch Onderzoek
J.H. Luiten

nr 8
Informatievoorziening en Beheerprocessen
A. Nauta
Jos Smeets (red.)
Helga Fassbinder (projectleider)
Adrie Proveniers
J. v.d. Moosdijk

nr 9
Strukturering en Verwerking van Tijdgegevens voor de Uitvoering van Bouwwerken
ir. W.F. Schaefer
P.A. Erkelens

nr 10
Stedebouw en de Vorming van een Speciale Wetenschap
K. Doevendans

nr 11
Informatica en Ondersteuning van Ruimtelijke Besluitvorming
G.G. van der Meulen

nr 12
Staal in de Woningbouw, Korrosie-Bescherming van de Begane Grondvloer
Edwin J.F. Delsing

nr 13
Een Thermisch Model voor de Berekening van Staalplaatbetonvloeren onder Brandomstandigheden
A.F. Hamerlinck

nr 14
De Wijkgedachte in Nederland: Gemeenschapsstreven in een Stedebouwkundige Context
K. Doevendans
R. Stolzenburg

nr 15
Diaphragm Effect of Trapezoidally Profiled Steel Sheets: Experimental Research into the Influence of Force Application
Andre W.A.M.J. van den Bogaard

nr 16
Versterken met Spuit-Ferrocement: Het Mechanische Gedrag van met Spuit-Ferrocement Versterkte Gewapend Betonbalken
K.B. Lubir
M.C.G. van Wanroy

nr 17
De Tractaten van Jean Nicolas Louis Durand
G. van Zeyl

nr 18
Wonen onder een Plat Dak: Drie Opstellen over Enkele Vooronderstellingen van de Stedebouw
K. Doevendans

nr 19
Supporting Decision Making Processes: A Graphical and Interactive Analysis of Multivariate Data
W. Adams

nr 20
Self-Help Building Productivity: A Method for Improving House Building by Low-Income Groups Applied to Kenya 1990-2000
P. A. Erkelens

nr 21
De Verdeling van Woningen: Een Kwestie van Onderhandelen
Vincent Smit

nr 22
Flexibiliteit en Kosten in het Ontwerpproces: Een Besluitvormingondersteunend Model
M. Prins

nr 23
Spontane Nederzettingen Begeleid: Voorwaarden en Criteria in Sri Lanka
Po Hin Thung

nr 24
Fundamentals of the Design of Bamboo Structures
Oscar Arce-Villalobos

nr 25
Concepten van de Bouwkunde
M.F.Th. Bax (red.)
H.M.G.J. Trum (red.)

nr 26
Meaning of the Site
Xiaodong Li

nr 27
Het Woonmilieu op Begrip Gebracht: Een Speurtocht naar de Betekenis van het Begrip 'Woonmilieu'
Jaap Ketelaar

nr 28
Urban Environment in Developing Countries
editors: Peter A. Erkelens
George G. van der Meulen (red.)

nr 29
Stategische Plannen voor de Stad: Onderzoek en Planning in Drie Steden
prof.dr. H. Fassbinder (red.)
H. Rikhof (red.)

nr 30
Stedebouwkunde en Stadsbestuur
Piet Beekman

nr 31
De Architectuur van Djenné: Een Onderzoek naar de Historische Stad
P.C.M. Maas

nr 32
Conjoint Experiments and Retail Planning
Harmen Oppewal

nr 33
Strukturformen Indonesischer Bautechnik: Entwicklung Methodischer Grundlagen für eine 'Konstruktive Pattern Language' in Indonesien
Heinz Frick arch. SIA

nr 34
Styles of Architectural Designing: Empirical Research on Working Styles and Personality Dispositions
Anton P.M. van Bakel

nr 35
Conjoint Choice Models for Urban Tourism Planning and Marketing
Benedict Dellaert

nr 36
Stedelijke Planvorming als Co-Produktie
Helga Fassbinder (red.)

nr 37
Design Research in the Netherlands
editors: R.M. Oxman
M.F.Th. Bax
H.H. Achten

nr 38
Communication in the Building Industry
Bauke de Vries

nr 39
Optimaal Dimensioneren van Gelaste Plaatliggers
J.B.W. Stark
F. van Pelt
L.F.M. van Gorp
B.W.E.M. van Hove

nr 40
Huisvesting en Overwinning van Armoede
P.H. Thung
P. Beekman (red.)

nr 41
Urban Habitat: The Environment of Tomorrow
George G. van der Meulen
Peter A. Erkelens

nr 42
A Typology of Joints
John C.M. Olie

nr 43
Modeling Constraints-Based Choices for Leisure Mobility Planning
Marcus P. Stemerding

nr 44
Activity-Based Travel Demand Modeling
Dick Ettema

nr 45
Wind-Induced Pressure Fluctuations on Building Facades
Chris Geurts

nr 46
Generic Representations
Henri Achten

nr 47
Johann Santini Aichel: Architectuur en Ambiguiteit
Dirk De Meyer

nr 48
Concrete Behaviour in Multiaxial Compression
Erik van Geel

nr 49
Modelling Site Selection
Frank Witlox

nr 50
Ecolemma Model
Ferdinand Beetstra

nr 51
Conjoint Approaches to Developing Activity-Based Models
Donggen Wang

nr 52
On the Effectiveness of Ventilation
Ad Roos

nr 53
Conjoint Modeling Approaches for Residential Group preferences
Eric Molin

nr 54
Modelling Architectural Design Information by Features
Jos van Leeuwen

nr 55
A Spatial Decision Support System for the Planning of Retail and Service Facilities
Theo Arentze

nr 56
Integrated Lighting System Assistant
Ellie de Groot

nr 57
Ontwerpend Leren, Leren Ontwerpen
J.T. Boekholt

nr 58
Temporal Aspects of Theme Park Choice Behavior
Astrid Kemperman

nr 59
Ontwerp van een Geïndustrialiseerde Funderingswijze
Faas Moonen

nr 60
Merlin: A Decision Support System for Outdoor Leisure Planning
Manon van Middelkoop

nr 61
The Aura of Modernity
Jos Bosman

nr 62
Urban Form and Activity-Travel Patterns
Daniëlle Snellen

nr 63
Design Research in the Netherlands 2000
Henri Achten

nr 64
Computer Aided Dimensional Control in Building Construction
Rui Wu

nr 65
Beyond Sustainable Building
editors: Peter A. Erkelens
Sander de Jonge
August A.M. van Vliet
co-editor: Ruth J.G. Verhagen

nr 66
Das Globalrecyclingfähige Haus
Hans Löfflad

nr 67
Cool Schools for Hot Suburbs
René J. Dierkx

nr 68
A Bamboo Building Design Decision Support Tool
Fitri Mardjono

nr 69
Driving Rain on Building Envelopes
Fabien van Mook

nr 70
Heating Monumental Churches
Henk Schellen

nr 71
Van Woningverhuurder naar Aanbieder van Woongenot
Patrick Dogge

nr 72
Moisture Transfer Properties of Coated Gypsum
Emile Goossens

nr 73
Plybamboo Wall-Panels for Housing
Guillermo E. González-Beltrán

nr 74
The Future Site-Proceedings
Ger Maas
Frans van Gassel

nr 75
Radon transport in Autoclaved Aerated Concrete
Michel van der Pal

nr 76
The Reliability and Validity of Interactive Virtual Reality Computer Experiments
Amy Tan

nr 77
Measuring Housing Preferences Using Virtual Reality and Belief Networks
Maciej A. Orzechowski

nr 78
Computational Representations of Words and Associations in Architectural Design
Nicole Segers

nr 79
Measuring and Predicting Adaptation in Multidimensional Activity-Travel Patterns
Chang-Hyeon Joh

nr 80
Strategic Briefing
Fayez Al Hassan

nr 81
Well Being in Hospitals
Simona Di Cicco

nr 82
Solares Bauen: Implementierungs- und Umsetzungs-Aspekte in der Hochschulausbildung in Österreich
Gerhard Schuster

nr 83
Supporting Strategic Design of Workplace Environments with Case-Based Reasoning
Shauna Mallory-Hill

nr 84
ACCEL: A Tool for Supporting Concept Generation in the Early Design Phase
Maxim Ivashkov

nr 85
Brick-Mortar Interaction in Masonry under Compression
Ad Vermeltfoort

nr 86
Zelfredzaam Wonen
Guus van Vliet

nr 87
Een Ensemble met Grootstedelijke Allure
Jos Bosman
Hans Schippers

nr 88
On the Computation of Well-Structured Graphic Representations in Architectural Design
Henri Achten

nr 89
De Evolutie van een West-Afrikaanse Vernaculaire Architectuur
Wolf Schijns

nr 90
ROMBO Tactiek
Christoph Maria Ravesloot

nr 91
External Coupling between Building Energy Simulation and Computational Fluid Dynamics
Ery Djunaedy

nr 92
Design Research in the Netherlands 2005
editors: Henri Achten
Kees Dorst
Pieter Jan Stappers
Bauke de Vries

nr 93
Ein Modell zur Baulichen Transformation
Jalil H. Saber Zaimian

nr 94
Human Lighting Demands: Healthy Lighting in an Office Environment
Myriam Aries

nr 95
A Spatial Decision Support System for the Provision and Monitoring of Urban Greenspace
Claudia Pelizaro

nr 96
Leren Creëren
Adri Proveniers

nr 97
Simlandscape
Rob de Waard

nr 98
Design Team Communication
Ad den Otter

nr 99
Humaan-Ecologisch Georiënteerde Woningbouw
Juri Czabanowski

nr 100
Hambase
Martin de Wit

nr 101
Sound Transmission through Pipe Systems and into Building Structures
Susanne Bron-van der Jagt

nr 102
Het Bouwkundig Contrapunt
Jan Francis Boelen

nr 103
A Framework for a Multi-Agent Planning Support System
Dick Saarloos

nr 104
Bracing Steel Frames with Calcium Silicate Element Walls
Bright Mweene Ng'andu

nr 105
Naar een Nieuwe Houtskeletbouw
F.N.G. De Medts

nr 106 and 107
Niet gepubliceerd

nr 108
Geborgenheid
T.E.L. van Pinxteren

nr 109
Modelling Strategic Behaviour in Anticipation of Congestion
Qi Han

nr 110
Reflecties op het Woondomein
Fred Sanders

nr 111
On Assessment of Wind Comfort by Sand Erosion
Gábor Dezsö

nr 112
Bench Heating in Monumental Churches
Dionne Limpens-Neilen

nr 113
RE. Architecture
Ana Pereira Roders

nr 114
Toward Applicable Green Architecture
Usama El Fiky

nr 115
Knowledge Representation under Inherent Uncertainty in a Multi-Agent System for Land Use Planning
Liying Ma

nr 116
Integrated Heat Air and Moisture Modeling and Simulation
Jos van Schijndel

nr 117
Concrete Behaviour in Multiaxial Compression
J.P.W. Bongers

nr 118
The Image of the Urban Landscape
Ana Moya Pellitero

nr 119
The Self-Organizing City in Vietnam
Stephanie Geertman

nr 120
A Multi-Agent Planning Support System for Assessing Externalities of Urban Form Scenarios
Rachel Katoshevski-Cavari

nr 121
Den Schulbau Neu Denken, Fühlen und Wollen
Urs Christian Maurer-Dietrich

nr 122
Peter Eisenman Theories and Practices
Bernhard Kormoss

nr 123
User Simulation of Space Utilisation
Vincent Tabak

nr 125
In Search of a Complex System Model
Oswald Devisch

nr 126
Lighting at Work: Environmental Study of Direct Effects of Lighting Level and Spectrum on Psycho-Physiological Variables
Grazyna Górnicka

nr 127
Flanking Sound Transmission through Lightweight Framed Double Leaf Walls
Stefan Schoenwald

nr 128
Bounded Rationality and Spatio-Temporal Pedestrian Shopping Behavior
Wei Zhu

nr 129
Travel Information: Impact on Activity Travel Pattern
Zhongwei Sun

nr 130
Co-Simulation for Performance Prediction of Innovative Integrated Mechanical Energy Systems in Buildings
Marija Trčka

nr 131
Niet gepubliceerd

nr 132
Architectural Cue Model in Evacuation Simulation for Underground Space Design
Chengyu Sun

nr 133
Uncertainty and Sensitivity Analysis in Building Performance Simulation for Decision Support and Design Optimization
Christina Hopfe

nr 134
Facilitating Distributed Collaboration in the AEC/FM Sector Using Semantic Web Technologies
Jacob Beetz

nr 135
Circumferentially Adhesive Bonded Glass Panes for Bracing Steel Frame in Façades
Edwin Huveners

nr 136
Influence of Temperature on Concrete Beams Strengthened in Flexure with CFRP
Ernst-Lucas Klamer

nr 137
Sturen op Klantwaarde
Jos Smeets

nr 139
Lateral Behavior of Steel Frames with Discretely Connected Precast Concrete Infill Panels
Paul Teewen

nr 140
Integral Design Method in the Context of Sustainable Building Design
Perica Savanović

nr 141
Household Activity-Travel Behavior: Implementation of Within-Household Interactions
Renni Anggraini

nr 142
Design Research in the Netherlands 2010
Henri Achten

nr 143
Modelling Life Trajectories and Transport Mode Choice Using Bayesian Belief Networks
Marloes Verhoeven

nr 144
Assessing Construction Project Performance in Ghana
William Gyadu-Asiedu

nr 145
Empowering Seniors through Domotic Homes
Masi Mohammadi

nr 146
An Integral Design Concept for Ecological Self-Compacting Concrete
Martin Hunger

nr 147
Governing Multi-Actor Decision Processes in Dutch Industrial Area Redevelopment
Erik Blokhuis

nr 148
A Multifunctional Design Approach for Sustainable Concrete
Götz Hüsken

nr 149
Quality Monitoring in Infrastructural Design-Build Projects
Ruben Favié

nr 150
Assessment Matrix for Conservation of Valuable Timber Structures
Michael Abels

nr 151
Co-simulation of Building Energy Simulation and Computational Fluid Dynamics for Whole-Building Heat, Air and Moisture Engineering
Mohammad Mirsadeghi

nr 152
External Coupling of Building Energy Simulation and Building Element Heat, Air and Moisture Simulation
Daniel Cóstola

nr 175
Modeling Recreation Choices over the Family Lifecycle
Anna Beatriz Grigolon

nr 176
Experimental and Numerical Analysis of Mixing Ventilation at Laminar, Transitional and Turbulent Slot Reynolds Numbers
Twan van Hooff

nr 177
Collaborative Design Support: Workshops to Stimulate Interaction and Knowledge Exchange Between Practitioners
Emile M.C.J. Quanjel

nr 178
Future-Proof Platforms for Aging-in-Place
Michiel Brink

nr 179
Motivate: A Context-Aware Mobile Application for Physical Activity Promotion
Yuzhong Lin

nr 180
Experience the City: Analysis of Space-Time Behaviour and Spatial Learning
Anastasia Moiseeva

nr 181
Unbonded Post-Tensioned Shear Walls of Calcium Silicate Element Masonry
Lex van der Meer

nr 182
Construction and Demolition Waste Recycling into Innovative Building Materials for Sustainable Construction in Tanzania
Mwita M. Sabai

nr 183
Durability of Concrete with Emphasis on Chloride Migration
Przemysław Spiesz

nr 184
Computational Modeling of Urban Wind Flow and Natural Ventilation Potential of Buildings
Rubina Ramponi

nr 185
A Distributed Dynamic Simulation Mechanism for Buildings Automation and Control Systems
Azzedine Yahiaoui

nr 186
Modeling Cognitive Learning of Urban Networks in Daily Activity-Travel Behavior
Şehnaz Cenani Durmazoğlu

nr 187
Functionality and Adaptability of Design Solutions for Public Apartment Buildings in Ghana
Stephen Agyefi-Mensah

nr 188
A Construction Waste Generation Model for Developing Countries
Lilliana Abarca-Guerrero

nr 189
Synchronizing Networks: The Modeling of Supernetworks for Activity-Travel Behavior
Feixiong Liao

nr 190
Time and Money Allocation Decisions in Out-of-Home Leisure Activity Choices
Gamze Zeynep Dane

nr 191
How to Measure Added Value of CRE and Building Design
Rianne Appel-Meulenbroek

nr 192
Secondary Materials in Cement-Based Products: Treatment, Modeling and Environmental Interaction
Miruna Florea

nr 193
Concepts for the Robustness Improvement of Self-Compacting Concrete: Effects of Admixtures and Mixture Components on the Rheology and Early Hydration at Varying Temperatures
Wolfram Schmidt

nr 194
Modelling and Simulation of Virtual Natural Lighting Solutions in Buildings
Rizki A. Mangkuto

nr 195
Nano-Silica Production at Low Temperatures from the Dissolution of Olivine - Synthesis, Tailoring and Modelling
Alberto Lazaro Garcia

nr 196
Building Energy Simulation Based Assessment of Industrial Halls for Design Support
Bruno Lee

nr 197
Computational Performance Prediction of the Potential of Hybrid Adaptable Thermal Storage Concepts for Lightweight Low-Energy Houses
Pieter-Jan Hoes

nr 198
Application of Nano-Silica in Concrete
George Quercia Bianchi

nr 199
Dynamics of Social Networks and Activity Travel Behaviour
Fariya Sharmeen

nr 200
Building Structural Design Generation and Optimisation including Spatial Modification
Juan Manuel Davila Delgado

nr 201
Hydration and Thermal Decomposition of Cement/Calcium-Sulphate Based Materials
Ariën de Korte

nr 202
Republiek van Beelden: De Politieke Werkingen van het Ontwerp in Regionale Planvorming
Bart de Zwart

nr 203
Effects of Energy Price Increases on Individual Activity-Travel Repertoires and Energy Consumption
Dujuan Yang

nr 204
Geometry and Ventilation: Evaluation of the Leeward Sawtooth Roof Potential in the Natural Ventilation of Buildings
Jorge Isaac Perén Montero

nr 205
Computational Modelling of Evaporative Cooling as a Climate Change Adaptation Measure at the Spatial Scale of Buildings and Streets
Hamid Montazeri

nr 206
Local Buckling of Aluminium Beams in Fire Conditions
Ronald van der Meulen

nr 207
Historic Urban Landscapes: Framing the Integration of Urban and Heritage Planning in Multilevel Governance
Loes Veldpaus

nr 208
Sustainable Transformation of the Cities: Urban Design Pragmatics to Achieve a Sustainable City
Ernesto Antonio Zumelzu Scheel

nr 209
Development of Sustainable Protective Ultra-High Performance Fibre Reinforced Concrete (UHPFRC): Design, Assessment and Modeling
Rui Yu

nr 210
Uncertainty in Modeling Activity-Travel Demand in Complex Uban Systems
Soora Rasouli

nr 211
Simulation-based Performance Assessment of Climate Adaptive Greenhouse Shells
Chul-sung Lee

nr 212
Green Cities: Modelling the Spatial Transformation of the Urban Environment using Renewable Energy Technologies
Saleh Mohammadi

nr 213
A Bounded Rationality Model of Short and Long-Term Dynamics of Activity-Travel Behavior
Ifigeneia Psarra

nr 214
Effects of Pricing Strategies on Dynamic Repertoires of Activity-Travel Behaviour
Elaheh Khademi

nr 215
Handstorm Principles for Creative and Collaborative Working
Frans van Gassel

nr 216
Light Conditions in Nursing Homes: Visual Comfort and Visual Functioning of Residents
Marianne M. Sinoo

nr 217
Woonsporen: De Sociale en Ruimtelijke Biografie van een Stedelijk Bouwblok in de Amsterdamse Transvaalbuurt
Hüseyin Hüsnü Yegenoglu

nr 218
Studies on User Control in Ambient Intelligent Systems
Berent Willem Meerbeek

nr 219
Daily Livings in a Smart Home: Users' Living Preference Modeling of Smart Homes
Erfaneh Allameh

nr 220
Smart Home Design: Spatial Preference Modeling of Smart Homes
Mohammadali Heidari Jozam

nr 221
Wonen: Discoursen, Praktijken, Perspectieven
Jos Smeets

nr 222
Personal Control over Indoor Climate in Offices: Impact on Comfort, Health and Productivity
Atze Christiaan Boerstra

nr 223
Personalized Route Finding in Multimodal Transportation Networks
Jianwe Zhang

nr 224
The Design of an Adaptive Healing Room for Stroke Patients
Elke Daemen

nr 225
Experimental and Numerical Analysis of Climate Change Induced Risks to Historic Buildings and Collections
Zara Huijbregts

nr 226
Wind Flow Modeling in Urban Areas Through Experimental and Numerical Techniques
Alessio Ricci

nr 227
Clever Climate Control for Culture: Energy Efficient Indoor Climate Control Strategies for Museums Respecting Collection Preservation and Thermal Comfort of Visitors
Rick Kramer

nr 228
Fatigue Life Estimation of Metal Structures Based on Damage Modeling
Sarmediran Silitonga

nr 229
A multi-agents and occupancy based strategy for energy management and process control on the room-level
Timilehin Moses Labeodan

nr 230
Environmental assessment of Building Integrated Photovoltaics: Numerical and Experimental Carrying Capacity Based Approach
Michiel Ritzen

nr 231
Performance of Admixture and Secondary Minerals in Alkali Activated Concrete: Sustaining a Concrete Future
Arno Keulen

nr 232
World Heritage Cities and Sustainable Urban Development: Bridging Global and Local Levels in Monitoring the Sustainable Urban Development of World Heritage Cities
Paloma C. Guzman Molina

nr 233
Stage Acoustics and Sound Exposure in Performance and Rehearsal Spaces for Orchestras: Methods for Physical Measurements
Remy Wenmaekers

nr 234
Municipal Solid Waste Incineration (MSWI) Bottom Ash: From Waste to Value Characterization, Treatments and Application
Pei Tang

nr 235
Large Eddy Simulations Applied to Wind Loading and Pollutant Dispersion
Mattia Ricci

nr 236
Alkali Activated Slag-Fly Ash Binders: Design, Modeling and Application
Xu Gao

nr 237
Sodium Carbonate Activated Slag: Reaction Analysis, Microstructural Modification & Engineering Application
Bo Yuan

nr 238
Shopping Behavior in Malls
Widiyani

nr 239
Smart Grid-Building Energy Interactions: Demand Side Power Flexibility in Office Buildings
Kennedy Otieno Aduda

nr 240
Modeling Taxis Dynamic Behavior in Uncertain Urban Environments
Zheng Zhong

nr 241
Gap-Theoretical Analyses of Residential Satisfaction and Intention to Move
Wen Jiang

nr 242
Travel Satisfaction and Subjective Well-Being: A Behavioral Modeling Perspective
Yanan Gao

nr 243
Building Energy Modelling to Support the Commissioning of Holistic Data Centre Operation
Vojtech Zavrel

nr 244
Regret-Based Travel Behavior Modeling: An Extended Framework
Sunghoon Jang

nr 245
Towards Robust Low-Energy Houses: A Computational Approach for Performance Robustness Assessment using Scenario Analysis
Rajesh Reddy Kotireddy

nr 246
Development of sustainable and functionalized inorganic binder-biofiber composites
Guillaume Doudart de la Grée

nr 247
A Multiscale Analysis of the Urban Heat Island Effect: From City Averaged Temperatures to the Energy Demand of Individual Buildings
Yasin Toparlar

nr 248
Design Method for Adaptive Daylight Systems for buildings covered by large (span) roofs
Florian Heinzelmann

nr 249
Hardening, high-temperature resistance and acid resistance of one-part geopolymers
Patrick Sturm

nr 250
Effects of the built environment on dynamic repertoires of activity-travel behaviour
Aida Pontes de Aquino

nr 251
Modeling for auralization of urban environments: Incorporation of directivity in sound propagation and analysis of a framework for auralizing a car pass-by
Fotis Georgiou

nr 252
Wind Loads on Heliostats and Photovoltaic Trackers
Andreas Pfahl

nr 253
Approaches for computational performance optimization of innovative adaptive façade concepts
Roel Loonen

nr 254
Multi-scale FEM-DEM Model for Granular Materials: Micro-scale boundary conditions, Statics, and Dynamics
Jiadun Liu

nr 255
Bending Moment - Shear Force Interaction of Rolled I-Shaped Steel Sections
Rianne Willie Adriana Dekker

nr 256
Paralympic tandem cycling and handcycling: Computational and wind tunnel analysis of aerodynamic performance
Paul Fionn Mannion

nr 257
Experimental characterization and numerical modelling of 3D printed concrete: Controlling structural behaviour in the fresh and hardened state
Robert Johannes Maria Wolfs

nr 258
Requirement checking in the building industry: Enabling modularized and extensible requirement checking systems based on semantic web technologies
Chi Zhang

nr 259
A Sustainable Industrial Site Redevelopment Planning Support System
Tong Wang

nr 260
Efficient storage and retrieval of detailed building models: Multi-disciplinary and long-term use of geometric and semantic construction information
Thomas Ferdinand Krijnen

nr 261
The users' value of business center concepts for knowledge sharing and networking behavior within and between organizations
Minou Weijs-Perrée

nr 262
Characterization and improvement of aerodynamic performance of vertical axis wind turbines using computational fluid dynamics (CFD)
Abdolrahim Rezaeiha

nr 263
In-situ characterization of the acoustic impedance of vegetated roofs
Chang Liu

nr 264
Occupancy-based lighting control: Developing an energy saving strategy that ensures office workers' comfort
Christel de Bakker

nr 265
Stakeholders-Oriented Spatial Decision Support System
Cahyono Susetyo

nr 266
Climate-induced damage in oak museum objects
Rianne Aleida Luimes

nr 267
Towards individual thermal comfort: Model predictive personalized control of heating systems
Katarina Katic

nr 268
Modelling and Measuring Quality of Urban Life: Housing, Neighborhood, Transport and Job
Lida Aminian

nr 269
Optimization of an aquifer thermal energy storage system through integrated modelling of aquifer, HVAC systems and building
Basar Bozkaya

nr 270
Numerical modeling for urban sound propagation: developments in wave-based and energy-based methods
Raúl Pagán Muñoz

nr 271
Lighting in multi-user office environments: improving employee wellbeing through personal control
Sanae van der Vleuten-Chraibi

nr 272
A strategy for fit-for-purpose occupant behavior modelling in building energy and comfort performance simulation
Isabella I. Gaetani dell'Aquila d'Aragona

nr 273
Een architectuurhistorische waardestelling van naoorlogse woonwijken in Nederland: Het voorbeeld van de Westelijke Tuinsteden in Amsterdam
Eleonore Henriette Marie Mens

nr 274
Job-Housing Co-Dependent Mobility Decisions in Life Trajectories
Jia Guo

nr 275
A user-oriented focus to create healthcare facilities: decision making on strategic values
Emilia Rosalia Catharina Maria Huisman

nr 276
Dynamics of plane impinging jets at moderate Reynolds numbers – with applications to air curtains
Adelya Khayrullina

nr 277
Valorization of Municipal Solid Waste Incineration Bottom Ash - Chemical Nature, Leachability and Treatments of Hazardous Elements
Qadeer Alam

nr 278
Treatments and valorization of MSWI bottom ash - application in cement-based materials
Veronica Caprai

nr 279
Personal lighting conditions of office workers - input for intelligent systems to optimize subjective alertness
Juliëtte van Duijnhoven

nr 280
Social influence effects in tourism travel: air trip itinerary and destination choices
Xiaofeng Pan

nr 281
Advancing Post-War Housing: Integrating Heritage Impact, Environmental Impact, Hygrothermal Risk and Costs in Renovation Design Decisions
Lisanne Claartje Havinga

nr 282
Impact resistant ultra-high performance fibre reinforced concrete: materials, components and properties
Peipeng Li

nr 283
Demand-driven Science Parks: The Perceived Benefits and Trade-offs of Tenant Firms with regard to Science Park Attributes
Wei Keat Benny Ng

nr 284
Raise the lantern; how light can help to maintain a healthy and safe hospital environment focusing on nurses
Maria Petronella Johanna Aarts

nr 285
Modelling Learning and Dynamic Route and Parking Choice Behaviour under Uncertainty
Elaine Cristina Schneider de Carvalho

nr 286
Identifying indoor local microclimates for safekeeping of cultural heritage
Karin Kompatscher

nr 287
Probabilistic modeling of fatigue resistance for welded and riveted bridge details. Resistance models and estimation of uncertainty.
Davide Leonetti

nr 288
Performance of Layered UHPFRC under Static and Dynamic Loads: Effects of steel fibers, coarse aggregates and layered structures
Yangyueye Cao

nr 289
Photocatalytic abatement of the nitrogen oxide pollution: synthesis, application and long-term evaluation of titania-silica composites
Yuri Hendrix

nr 290
Assessing knowledge adoption in post-disaster reconstruction: Understanding the impact of hazard-resistant construction knowledge on reconstruction processes of self-recovering communities in Nepal and the Philippines
Eefje Hendriks

nr 291
Locating electric vehicle charging stations: A multi-agent based dynamic simulation
Seheon Kim

nr 292
De invloed van Lean Management op de beheersing van het bouwproces
Wim van den Bouwhuijsen

nr 293
Neighborhood Environment and Physical Activity of Older Adults
Zhengying Liu

nr 294
Practical and continuous luminance distribution measurements for lighting quality
Thijs Willem Kruisselbrink

nr 295
Auditory Distraction in Open-Plan Study Environments in Higher Education
Pieternella Elizabeth Braat-Eggen

nr 296
Exploring the effect of the sound environment on nurses' task performance: an applied approach focusing on prospective memory
Jikke Reinten

nr 297
Design and performance of water resistant cementitious materials– Mechanisms, evaluation and applications
Zhengyao Qu

nr 298
Design Optimization of Seasonal Thermal Energy Storage Integrated District Heating and Cooling System: A Modeling and Simulation Approach
Luyi Xu

nr 299
Land use and transport: Integrated approaches for planning and management
Zhongqi Wang

nr 300
Multi-disciplinary optimization of building spatial designs: co-evolutionary design process simulations, evolutionary algorithms, hybrid approaches
Sjonnie Boonstra

nr 301
Modeling the spatial and temporal relation between urban land use, temperature, and energy demand
Hung-Chu Chen